

# **Synthesis, Photophysical and Photoisomerization Properties of Stilbene-Appended Terpyridine Complexes of Iron and Zinc**

**A Thesis**

**Submitted for the Degree of  
Doctor of Philosophy (Science)  
of  
Jadavpur University**

**by**

**Shruti Mukherjee**



**DEPARTMENT OF CHEMISTRY  
JADAVPUR UNIVERSITY  
JADAVPUR, KOLKATA 700032  
INDIA**

**2022**

**Dr. Sujoy Baitalik**  
**Professor**  
**Department of Chemistry**  
**Inorganic Chemistry**  
**Section**



**JADAVPUR UNIVERSITY**  
**KOLKATA – 700 032, INDIA**  
**Telephone: 91-033-2414-6666**  
**Facsimile : 91-033-2414-6584**  
**E-mail: sbaitalik@hotmail.com**

### **To whom it may concern**

This is to certify that Smt. Shruti Mukherjee who got her name registered on 23.04.2015 and having index No. 38/15/Chem./23, has submitted her thesis entitled “Synthesis, Photophysical and Photoisomerization Properties of Stilbene-Appended Terpyridine Complexes of Iron and Zinc” on 16/03/2022 for the award of Ph.D. (Science) degree of Jadavpur University. The work embodied in the thesis is absolutely based upon her own work under my supervision and that neither this thesis nor any part of it has been submitted for any degree/diploma or any other academic award anywhere before.

*Sujoy Baitalik*  
16/03/2022  
(SUJOY BAITALIK)

Signature of the Supervisor

& Date with official seal

*Professor Sujoy Baitalik*  
*Department of Chemistry*  
*Jadavpur University*  
*Kolkata- 700 032, India*

***Dedicated  
to  
My Family***

## PREFACE

The work embodied in the thesis entitled “Synthesis, Photophysical and Photoisomerization Properties of Stilbene-Appended Terpyridine Complexes of Iron and Zinc” have been carried out in the Department of Chemistry of Jadavpur University during the period between 2015 and 2022. The thesis is composed of six chapters.

In [Chapter 1](#), an overview of the synthetic strategy and photophysical as well as photoisomerization behaviours of stilbene conjugates as well as their Fe(II) and Zn(II) complexes with tridentate ligands have been given. Stimuli-responsive behaviours of selected systems were also presented. A concise review on photoisomerization studies of noble metal complexes incorporating stilbene units was also performed. Finally, objective and scope of this dissertation has been discussed at the end of the chapter.

[Chapter 2](#) deals with the synthesis and characterization of a series of terpyridine ligands, tpy-pvp-X (where X = H, Me, Cl, NO<sub>2</sub>, Ph) covalently coupled with styrylbenzene and thorough investigation of their photophysical and reversible *trans-cis* photoisomerization behaviours. The photochromic behaviours of the compounds were also explored and modulated in presence of acid. The "on-off" and "off-on" emission switching was made possible upon alternate interaction of the compounds with UV and visible light. Computation work were performed on both the *trans* and *cis* forms of the compounds by employing DFT and TD-DFT methods to acquire deeper insight about their electronic structures as well as for proper assignment of the experimentally observed absorption and emission bands.

[Chapter 3](#) deals with synthesis, characterization, photophysics, and reversible *trans-cis* photoisomerization behaviours of three homoleptic Fe(II)-terpyridine complexes,  $[\text{Fe}(\text{tpy-pvp-X})_2]^{2+}$  where X = H, Me, and NO<sub>2</sub>) covalently coupled with photo-active styrylbenzene moiety. The complexes undergo *trans-trans* to *cis-cis* isomerization upon treating with both visible and UV light with substantial alteration of their absorption and emission spectral profiles. The reverse process (*cis-cis* to *trans-trans* isomerization) also proceeds, albeit very slowly, on keeping and can be accelerated upon heating. The isomerization studies were performed in different solvents of varying polarity to tune the thermodynamic and kinetic aspects of the isomerization process. The rate, rate constant and quantum yield of photoisomerization were determined in all the



solvents. Computational investigations involving DFT and TD-DFT methods were also carried out in their *trans-trans*, *trans-cis* and *cis-cis* forms to understand the electronic structures and correctly assign the experimental optical spectral bands.

In chapter 4, the anion sensing properties of a bis-terpyridine Fe(II) complex,  $[\text{Fe}(\text{tpy-pvp-Cl})_2]^{2+}$  has been thoroughly investigated in both acetonitrile and water-acetonitrile (100:1, v/v) media through multiple optical channels and spectroscopic techniques. Interestingly, the complex acts as chromogenic and fluorogenic receptor for cyanide (among the other studied anions such as  $\text{F}^-$ ,  $\text{Cl}^-$ ,  $\text{Br}^-$ ,  $\text{I}^-$ ,  $\text{CN}^-$ ,  $\text{OAc}^-$ ,  $\text{H}_2\text{PO}_4^-$ ,  $\text{SCN}^-$ ,  $\text{BF}_4^-$  and  $\text{ClO}_4^-$ ) in predominantly aqueous medium with very low detection limit.

Synthesis, characterization, photophysics, and photo-isomerization behaviours of three Zn(II)-terpyridine complexes of the type  $[\text{Zn}(\text{tpy-pvp-X})_2]^{2+}$  ( $\text{X} = \text{H}$ ,  $\text{Me}$ , and  $\text{NO}_2$ ) are reported in chapter 5. The stilbene motifs in the complexes undergo *trans* to *cis* isomerization upon irradiating with UV and visible light accompanied by significant alteration of their absorption, emission, and  $^1\text{H}$  NMR spectral profiles. The rate, rate constant and quantum yield of isomerization were estimated in three different solvents. The reverse process (*cis* to *trans*) also occurs very slowly on keeping but could be accelerated upon heating. The emission spectral responses upon successive action of photonic and thermal input were utilized to mimic the function of INHIBIT and IMPLICATION logic gates.

In chapter 6, the terpyridine-stilbene system was utilized to demonstrate multiple advanced logic functions. Upon using the optical response profile of the receptor in presence of selected cations as well as light of specific wavelength, we are able to demonstrate multiple Boolean logic functions such as INHIBIT, IMPLICATION, OR, NOR and NAND as well as the functions of security keypad locks and memory devices. The present system has also been used to demonstrate fuzzy logic operations for building an infinite-valued logic scheme based the emission spectral responses upon varying the concentration of cationic ( $\text{Fe}^{2+}$  and/or  $\text{Zn}^{2+}$ ) and anionic ( $\text{CN}^-$ ) inputs.

\*\*\*\*\*

## ACKNOWLEDGEMENTS

*Firstly, I would like to express my special appreciation and thanks to my supervisor Professor Sujoy Baitalik for continuous support during my Ph. D study and related research. His guidance helped me in all the time of research and writing of this thesis.*

*I am very much thankful to the Department of Chemistry of Jadavpur University for giving me the scope to carry out my research work. I would like to thank the present Dean, Faculty Council of Science, Prof. Subenoy Chakraborty and the Head of the department, Prof. Swapan Kumar Bhattacharya, for providing the departmental and laboratory facilities. All the faculty members and non-teaching staffs of this department deserve warm regards for their help. I would like to acknowledge specially Prof. Samarendra Bhattacharya, Prof. Nitin Chattopadhyay, Prof. Chittaranjan Sinha, Prof. Subrata Mukhopadhyay, Prof. Jnan Prakash Naskar, Dr. Tapan Kumar Mondal, Prof. Md Ali, Dr. Partha Roy, Dr. Bibhuti Bhusan Shaw, Prof. Debajyoti Ghoshal, Dr. Sourav Das, Dr. Suman Das, and Prof. Kalyan Kumar Mukherjee for their excellent cooperation and help.*

*I am also very thankful to my former lab-mates Dr. Debasish Saha, Dr. Chanchal Bhaumik, Dr. Shyamal Das, Dr. Dinesh Maity, Dr. Srikanta Karmakar, Dr. Sourav Mardanya, Dr. Debiprasad Mondal and Dr. Manoranjan Bar who have already completed their doctoral degree from our lab. My senior lab mates taught me all the things I required to pursue my research work and they helped me always to get the perfection. An extensive help from my present lab-mates, Poulami di, Sourav, Animesh, Tanusree, Anik, Tousique, Soumi and Sohini is very much praiseworthy and deserves my heartfelt acknowledgement. All the moments we spent together during the research activities and others became a memory for the whole life. Without their help it would be difficult to complete my doctoral degree.*

*I am thankful to UGC for the financial support at the very beginning and also thankful to CSIR for giving me SRF fellowships. I would like to acknowledge DST for providing Time-Resolved Nanosecond Spectrofluorimeter in PURSE programme to the Department of Chemistry, Jadavpur University.*

*My Ph. D thesis will be incomplete without acknowledging my family members. It was impossible to complete my doctoral degree without the continuous encouragement, help and blessings from my father Mr. Phalguni Mukherjee and Mother Mrs. Manjusri Mukherjee.*

*My parent-in-law also deserve a big thank for their blessings and unconditional support. I would specially like to thank my husband Tanmay, for his enormous support and uncountable efforts to help me during writing and formatting of dissertation as much as he can.*

*Last but not the least; I would like to thank everybody who has played a role in the successful completion of my thesis.*

*Finally, I would like to thanks the almighty for his blessing through the journey of completion of my thesis.*

*Now I am expressing my apology if I have failed to mention personally each and everyone.*

*Shruti Mukherjee*  
*16/3/22*  
**(Shruti Mukherjee)**

*Department of chemistry,  
Inorganic Chemistry Section,  
Jadavpur University,  
Kolkata-700032, India*

# CONTENTS

	Page No.
<b>Chapter 1: Review on photophysical, photoisomerization behaviors of Fe(II)- and Zn(II)-terpyridine type of complexes along with <i>trans-cis</i> aspects of stilbene and substituted stilbene appended noble metal complexes and objective and scope of the present work</b>	1-50
1.1. General introduction	1
1.2. An overview of photophysical properties of Fe(II) and Zn(II) poly-pyridine complexes	2
1.3. Overview of photoisomerization behaviors of stilbene and substituted stilbene units	3
1.4. An overview of photophysical properties of styrylbenzene-terpyridine conjugate	5
1.5. Brief survey on tridentate ligand along with their iron and zinc complexes	6
1.5.1. Common synthetic strategy of tridentate ligand and their metal complexes	6
1.5.2. Brief literature survey on Fe(II)-terpyridine-type complexes	7
1.5.3. Brief literature survey on Zn(II)-terpyridine-type complexes	18
1.6. A brief survey on the photoisomerization behaviors of stilbene-appended polypyridine complexes of noble metals	26
1.7. Objective and scope of the present work	33
1.8. References	38
 <b>Chapter 2: Photophysics and luminescence switching properties of a series of photochromic styrylbenzene-terpyridine conjugate:experimental and DFT/TD-DFT investigation</b>	 51-100
2.1. Introduction	51
2.2. Experimental	52
2.2.1 Materials	52
2.2.2 Synthesis of the styrylbenzene-terpyridine conjugate	52
2.2.3 Physical measurements	54
2.3. Results and discussion	56
2.3.1 Synthesis and characterization	56
2.3.2 Computational investigations	56
2.3.3 Experimental absorption and emission spectra	71
2.3.4 Proton binding studies of the compounds	76
2.3.5 Photo-isomerization studies	81
2.4. Conclusions	93
2.5. References	93

<b>Chapter 3: Photo-switchable iron-terpyridine complexes functionalized with styrylbenzene Unit</b>	101-138
3.1. Introduction	101
3.2. Experimental	102
3.2.1 Materials	102
3.2.2 Synthesis of the metal complexes	103
3.2.3 Physical measurements	104
3.3. Results and discussions	105
3.3.1 Synthesis and characterization	105
3.3.2 Computational investigations	106
3.3.3 Absorption and emission spectra	106
3.3.4 Photo-isomerization behaviours	115
3.4. Conclusions	131
3.5. References	132
 <b>Chapter 4: Chromogenic and fluorogenic detection of selected anions by bis-terpyridine Fe(II) complex through displacement approach</b>	 139-159
4.1. Introduction	139
4.2. Experimental	141
4.2.1 Materials	141
4.2.2 Synthesis of the Fe(II) complex, $[Fe(tpy-pvp-Cl)_2](ClO_4)_2 (1)$	141
4.2.3 Physical measurements	142
4.3. Results and discussions	142
4.3.1 Synthesis and characterization	142
4.3.2 Absorption and emission spectral properties	143
4.3.3 Anion sensing studies of the metalloreceptor through different optical channels and spectroscopic techniques	144
4.4. Conclusions	155
4.5. References	155
 <b>Chapter 5: Low cost photo-switches based on stilbene-appended Zn(II)-terpyridine complexes</b>	 160-213
5.1. Introduction	160
5.2. Experimental	162
5.2.1 Materials	162
5.2.2 Synthesis of the metal complexes	163
5.2.3 Physical measurements	164

<b>5.3. Results and discussion</b>	164
5.3.1. <i>Synthesis and characterization</i>	164
5.3.2. <i>NMR spectra</i>	164
5.3.3. <i>Mass spectra</i>	164
5.3.4. <i>Computational investigations</i>	165
5.3.5. <i>Absorption and emission spectra</i>	172
5.3.6. <i>Photo-isomerization studies of the complexes</i>	178
5.3.7. <i>IMPLICATION Gate</i>	202
5.3.8. <i>INHIBIT Gate</i>	204
<b>5.4. Conclusions</b>	205
<b>5.5. References</b>	206

<b>Chapter 6: Light and cation driven optical switch based on a stilbene appended terpyridine system for the design of molecular-scale logic devices</b>	214-242
<b>6.1. Introduction</b>	214
<b>6.2. Materials and methods</b>	216
<b>6.3. Results and discussion</b>	216
6.3.1 <i>Synthesis, characterization and overview of photoisomerization and complextion-decomplextion process</i>	216
6.3.2 <i>Key-pad lock</i>	219
6.3.3 <i>Combination of IMPLICATION and INHIBIT logic gates</i>	220
6.3.4 <i>Construction of set-reset flip-flop circuit (memory devices)</i>	221
6.3.5 <i>Combination of NOR and INHIBIT logic gates</i>	222
6.3.6 <i>Combination of OR and INHIBIT logic gates</i>	223
6.3.7 <i>Combination of OR and NOR logic gates</i>	224
6.3.8 <i>Construction of NAND logic gate</i>	226
6.3.9 <i>Construction of INHIBIT logic gate</i>	227
6.3.10 <i>Fuzzy logic operations</i>	229
<b>6.4. Conclusions</b>	235
<b>6.5. References</b>	236

# ***Chapter 1***

**Review on photophysical, photoisomerization behaviors of Fe(II)- and Zn(II)-terpyridine type of complexes along with *trans-cis* aspects of stilbene and substituted stilbene appended noble metal complexes and objective and scope of the present work**



## 1.1 General introduction

There is widespread interest for the design of task-specific materials which could respond to different external stimuli such as light, heat or chemical species [1-5]. Among the stimuli, light is considered to be most convenient source as the materials could be excited at any wavelength of choice encompassing within a wide spectral range (UV to IR). The interaction between light and matter induces different performances, viz. emission of light, electron or energy transfer, conformational changes or chemical transformation which can lay the foundations for many applications [6-15]. An optical stimulus is very loyal to user and switching off the source gives rise to immediate turn-off of the signal. Additionally, the light source could be remote-controlled over a long distance that can facilitate the fabrication of optical information storage, high density optical memory and optical switches [6-16].

The compounds containing stilbene, azobenzene and spiropyran unit undergo reversible *trans/cis* photo-isomerization and lead to the generation of a wide range of photo-responsive materials [17-21]. The conformational change accompanied with remarkable alteration of their photophysical behaviors were utilized for this purpose. Although lots of studies were reported with purely organic stilbene derivatives, but similar studies with their coordination complexes are relatively sparse in the literature [17-21]. The metal complexes could offer a wide range of electronic structures with regard to coordination sphere, electronic configuration and redox state of the metal [22-31]. In order to utilize the coordination complexes for the fabrication of photo switching materials, one of the most effective strategies is to reversibly alter their properties by inducing conformational changes on the photo-responsive component appended on the ligands. The major reports in this regard are mainly focused on the noble metals (such as Ru, Re, Ir, and Pt) which are very expensive as well as synthetically challenging [5, 22-31]. The main objective of the dissertation is to design suitable base-metal complexes which could demonstrate similar behavior and can lead to the design of a new class of low-cost and easily synthesizable photo-switches.

In order to achieve our objective, we designed a series of terpyridine derivatives {2-(6-(pyridin-2-yl)-4-(4-styrylphenyl)pyridin-2-yl)pyridine} appended with substituted stilbene units (tpy-pvp-X) and synthesized a wide range of homoleptic bis-terpyridine

complexes of  $\text{Fe}^{2+}$  and  $\text{Zn}^{2+}$  metals ( $[\text{M}(\text{tpy-pvp-X})_2]^{2+}$ ). The terpyridine (tpy) offer an excellent coordinating motif compared with bipyridine (bpy) unit for the design of linear achiral architectures as functionalization at the 4'-position of tpy unit is quite easy.

We will thoroughly investigate the photo-isomerization behaviors of the free ligands as well as their Fe(II) and Zn(II) complexes through different spectroscopic tools. In this dissertation, we also address the influence of solvents, excitation wavelength and the effect of electron donating/withdrawing substituent (X) on the thermodynamic and kinetic aspects of isomerization process. Substantial alteration of the optical properties along with switching of emission spectral characteristics of the complexes was made possible upon isomerization. Moreover, the absorption and emission spectral output as a function of photonic, thermal and ionic inputs was utilized for the fabrication of several advanced Boolean and Fuzzy logic functions. The processing of information at the molecular level is now a very active area of research and proper utilization of sequential logic functions exhibited by molecular and supramolecular species is a huge challenge in research field of information technology [32-36]. In conjunction with experiment, theoretical studies employing DFT and TD-DFT methods are also performed to acquire insight about the electronic structures of the complexes, correct assignment of the spectral bands, and to understand the actual mode of isomerization process.

### 1.2 An overview of photophysical properties of Fe(II) and Zn(II) polypyridine complexes

Iron is the most abundant low-cost metal in Earth's covering and plays a vital role in transport and storage of oxygen in living organisms [37-39]. Fe(II)-polypyridine complexes are generally less effective sensitizers with respect to its higher analogues like  $\text{Ru}^{2+}$  and  $\text{Os}^{2+}$  (low spin  $d^6$  complexes). The Fe(II)-polypyridine complexes usually possess low lying  $^3/5\text{MC}$  states which gives rise to very fast non-radiative deactivation and reduce the excited state lifetime dramatically [40-47]. Although the terpyridine complexes of Fe(II) don't display Fe(II)-centered emission, they exhibit strong metal-to-ligand charge transfer ( $^1\text{MLCT}$ ) absorption band at higher wavelength (at  $\sim 575\text{nm}$ ) compared with analogous Ru(II) and Os(II) complexes. In addition, Fe(II)-terpyridine

complexes display emission due to ligand-centered intra-ligand charge transfer transition (ILCT) at shorter wavelength.[44-46,48].

Bivalent Zn also constitutes an important class of low-cost Zn(II) complexes. Because of its  $d^{10}$  electronic configuration, Zn(II) complexes do not show much preference of their coordination geometries. Zn(II)-polypyridine complexes show intense intra-ligand charge transfer (LLCT) absorption and emission band at low energy [49-52]. Due to absence of MLCT as well as d-d bands, the zinc complexes are optically more transparent than other  $d^n$  metal complexes. The main objective of the dissertation is to design base-metal (such as Fe and Zn) complexes of terpyridine ligands which could show alike response as those of other costly metal co-ordinated species (such as Ru, Re, Ir and Pt) and can promote a series of low-cost photo responsive switches.

### 1.3 Overview of photoisomerization behaviors of stilbene and substituted stilbene units

It is well known that the stilbene unit is capable of undergoing reversible *trans/cis* isomerization upon irradiation with light of appropriate wavelength (Fig. 1.1). Upon photo-irradiation, the stilbene is raised to the S1 excited state with a C=C bond slightly shorter compared to the ground state species and leads to free turn around the ethylenic

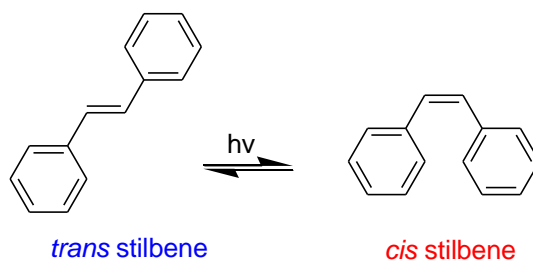


**Fig. 1.1**

unit within very short timescale. One of the most acknowledged processes of the isomerization includes the involvement of the phantom  $p^*$  state [17] having incredibly short lifetime of  $\sim 1$  ps. The C=C bond twist about  $90^\circ$  around its axis in the phantom state in electronically excited *trans* and *cis* forms (Fig. 1.2). Statistical formation of both *cis* and *trans* isomers is also proposed in recent time upon deactivation of the upper lying

excited state. Another proposed mechanism of isomerization involves inter system crossing process. The intersecting point between the singlet and the lowest triplet state is believed to be the reason for *trans*→*cis* isomerization. ISC from S1 state→ triplet state can be ignored in liquid state at RT.

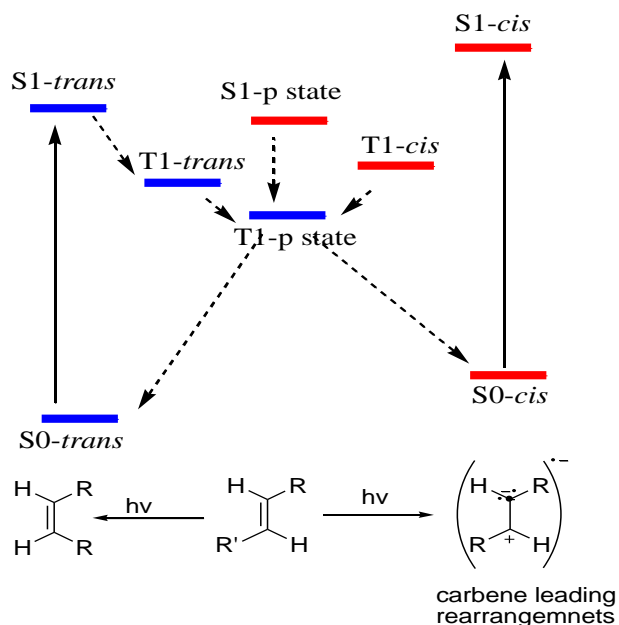


**Fig. 1.2**

The *trans/cis* isomerization of ethylene derivatives are studied thoroughly both via experiment as well as by theoretical calculations. The outcomes of the study propose some novel mechanisms [53-55]. Geometric isomerization is a major mode of reaction of polyenes in their excited singlet state and the prevailing theory is “one bond-flip (OBF)”, which involves the torsional relaxation of the perpendicular excited state via an adiabatic mechanism (Fig. 1.3).

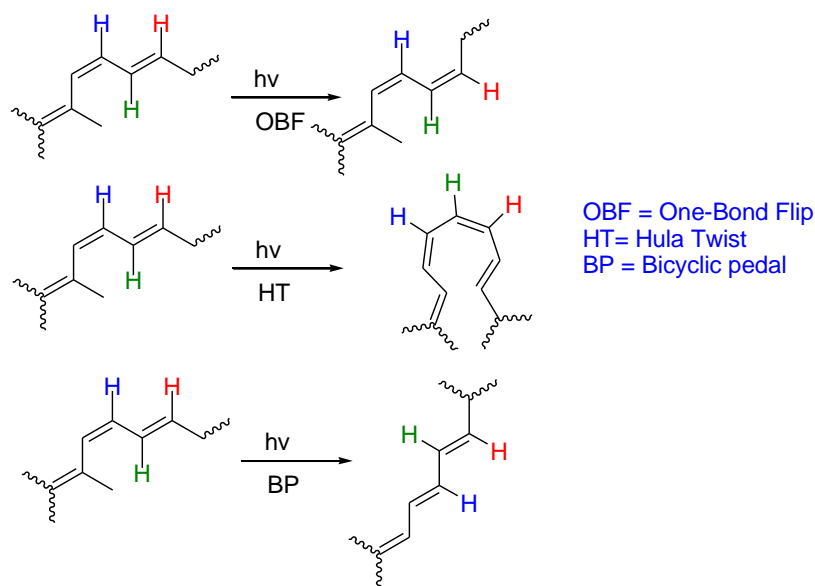


Fig. 1.3

However, such a phenomenon is not consistent with large polyenes such as retinyl chromophores which are confined inside a protein structure. Therefore, the Hula-Twist (HT) mechanism as depicted in Fig. 1.3 was proposed [56]. The HT mechanism postulates that a C-H unit can undergo a 180° translocation via an adiabatic mechanism that is in apparent violation of non-equilibration of excited isomers (NEER) theories (Fig. 1.3). However, the HT mechanism has been primarily validated with carotenoids in particular in the vitamin D series and later with diene triplets and simple trienes.

#### 1.4 An overview of photophysical properties of styrylbenzene-terpyridine conjugate

Since the first use of 2,2':6',2''-terpyridine (tpy) in 1932, a wide variety of terpyridine derivatives functionalized at different positions have been designed and found to be very useful building blocks in both organic and inorganic supramolecular chemistry [57-66]. In this dissertation, a series of stilbene-appended terpyridine derivatives have been designed. The stilbene unit is capable of undergoing reversible *trans/cis* isomerization upon irradiation with light of appropriate wavelength. Thus, the present stilbene-terpyridine conjugate can act as photo-switches by changing its geometrical conformation [67-74]. The experimental results show that the *trans* form of the compounds are highly fluorescent compared to their *cis* counterpart. Interestingly, isomerization from

*trans* to *cis* or vice-versa leads to emission switching. So, the compounds could display "on-off" and "off-on" emission switching upon alternate interaction with different light source. This kind of switching leads to the formation of various kinds of logic gate like NOR, AND, OR, INHIBIT, IMPLICATION etc.

### 1.5 Brief survey on tridentate ligand along with their iron and zinc complexes

Synthesis, structural features and physicochemical properties of a wide range of Fe(II) and Zn(II) complexes with tridentate ligands have been studied by various research groups. In this section, we have mainly focused on the synthesis and physicochemical properties of the tridentate ligands and their monometallic complexes of Fe(II) and Zn(II).

#### 1.5.1 Common synthetic strategy of tridentate ligand and their metal complexes

The terpyridine ligands incorporating styrylbenzene unit are synthesized by modification of the literature procedures adopted by Schmehl [75] and Magennis [76] research groups. The synthetic strategies of homoleptic complexes of Fe(II) and Zn(II) with tridentate ligands are well known in the literature and can be obtained by treating appropriate metal precursor and terpyridine ligand in 1:2 ratio (Fig. 1.4). Purification of the complexes is usually done by column chromatography and recrystallization techniques. The metal complexes of the type  $[M(tpy)_2]^{2+}$  (M=Fe and Zn) usually possess distorted octahedral geometry.

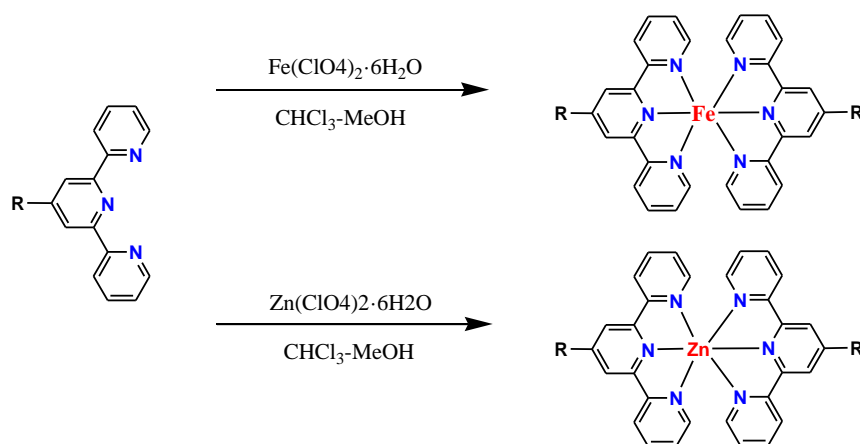


Fig. 1.4

### 1.5.2 Brief literature survey on Fe(II)-terpyridine-type complexes

With the development of supramolecular chemistry [77,78] and the utilization of metal complexes for the development of noncovalently bound architectures [79,80], the 2,2':6,2''- terpyridine (tpy) ligand has turned into a widely utilized receptor unit for metal-ligand mediated self-assembly because of its simple accessibility and its anticipated complexation behavior. The terpyridine subordinates together with buildups at the 4'-position are of special significance as they permit the course of action of two units in a precisely collinear fashion. In the last decade, an expanding number of models for supramolecular structures bearing tpy ligand have been reported, combined with an increase in complexity and functionality of the systems. An impressive example of the potential metal-terpyridine self-assembly was reported by Newkome and coworkers [81-82], who invented the development of the cyclic hexamers of six  $[M(tpy)_2]^{2+}$  units using  $Fe^{2+}$  and  $Ru^{2+}$  metals. Various research groups are working on the development of coordination polymers involving the tpy ligand, a field which was further developed by the work of Constable [83], and widely explored by a few other groups [84-85]. Another important class of supramolecular frameworks built by tpy-metal complexes is dendrimers [86], matrix like structures [87] and helicates [88]. Due to their good luminescence properties, especially the  $Ru^{2+}$  and  $Os^{2+}$  complexes of terpyridine ligands have been widely used to construct functional supramolecular systems, for example molecular rods with tpy complexes acting as energy donor and/or acceptor units. Extensive as well as very interesting research has been done in this field by the research groups of Sauvage, Balzani, and Ziessel [89-91]. Furthermore, terpyridine is used as a receptor unit in fluorescence sensors for the recognition of metal ions [92-93] and amino acids [94-95]. Recently, even more complicated supramolecular systems, so-called molecular muscles, based on catenanes and rotaxanes have been introduced [96]. These systems have been designed by taking advantage of the different stability of tpy and phenanthroline complexes along with the metals in different oxidation states. Among all the metal ions, iron is most abundant in the Earth's crust and plays very important role in biological systems. Iron is very low-cost metal ion which also plays vital role for storage



and transport of oxygen in living systems and also gives high response in various metalloenzymes [37-39]. It was already beendiscussed that iron-terpyridine complexes are unable to function as good sensitizerslike its higher homologues (such as  $\text{Ru}^{2+}$  and  $\text{Os}^{2+}$ ). The low lying  $^3/5\text{MC}$  states confined on Fe(II) unit undergo very fast non-radiative deactivation leading to remarkable lowering of excited state lifetime [40-47]. Although the Fe-terpyridine complexes have no iron-centered emission but it shows singlet MLCT absorption at lower energy region ( $\sim 575\text{nm}$ )[44-46,48].

During last few decades, a great variety of the bridging ligandshas also been designed for the development of polynuclear metal complexes with well-defined properties. Properties of complexes are strongly influenced by the nature of the ligand such as their  $\sigma$  and  $\pi$  donor/acceptor capacities, length and rigidity as well as the type of chelating motifs (bidentate vs tridentate coordination sites). The literature on the polypyridine complexes of Fe(II) is quite exhaustive and discussion on the properties of the individual complex is much difficult. Th early works in this field are nicely summarized in several reviews and monographs [16,23-25,41-44,46-47,97]. Therefore, only a few selected systems that are related to our work will be discussed here.

The first example of the kinetics of formation and dissociation of complexes of Mn-Zn and Cd with 2,6-bis(2'-pyridyl)pyridine (2,2',2''-terpyridine) was measured by the stopped-flow method by R. G. Wilkins and group[98]. The stability constants were calculated from these results and the thermodynamic and kinetic data were compared with those for bipyridine and phenanthroline complexes.

Elena Jakubikova and coworkers designed two series of compounds of composition  $[\text{Fe}(\text{tpy})_2]^{2+}$  ( $\text{tpy}=2,2';6',2''\text{-terpyridine}$ ) and  $[\text{Fe}(\text{dcpp})_2]^{2+}$  ( $\text{dcpp}=2,6\text{-bis}(2\text{-carboxypyridyl})\text{pyridine}$ ). The focal pyridine was replaced by some five membered and/or six membered rings to tune the ligand filed energy. The N-heterocyclic carbene, pyrrole and furan were used as five membered moieties whereas aryl, thiazine-1,1-dioxide and 4-pyrone were used as six membered units (Fig. 1.5) [99]. The singlet, triplet and quintet state of theFe(II) center were optimized by DFT calculation through the use of B3LYP+D2 level, 6-311G\* and SDD(Fe) basis set in water (using PCM model) to know the effect of different kind of ligating units on the physico-chemical properties in the

complexes. It was observed that the dcpp ligand framework gives rise to geometry which is closer to ideal octahedral coordination compared to the tpy-type ligand scaffold. Additionally, it is observed that the six-membered central unit induces geometry that are closer to ideal octahedral compared with the five-membered unit. They also showed that the LF strength of Fe(II)-polypyridine could be modulated by replacing its donor atom in the order O→N→C.

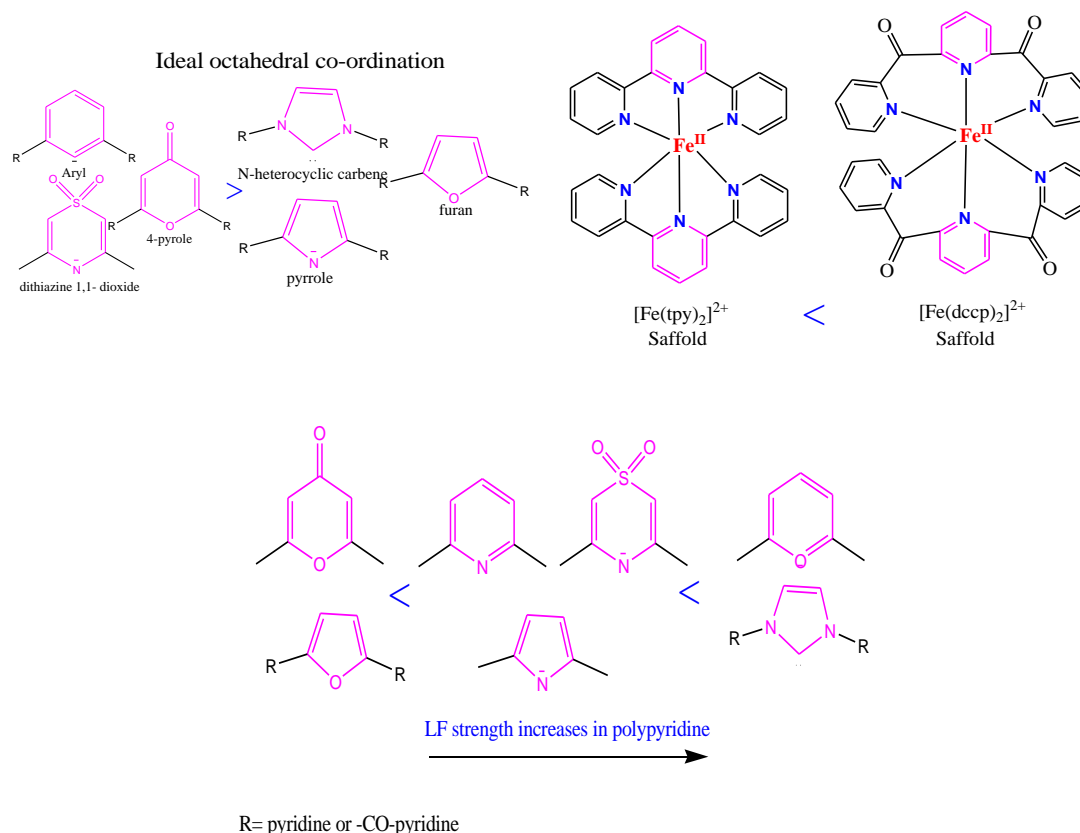


**Fig. 1.5**

C.A. Mirkin *et al* reported one-pot synthesis of Fe(II) bis-terpyridine building blockscoupled with two peripheral square-planar Pt(II) bis phosphinoalkylthioether motif (Fig. 1.6) [100]. The complex architectures show allosterically controllable electronic properties induced by two symmetrical Pt(II) building units. The initial and final forms of the allosteric framework have been characterized by single-crystal X-ray diffraction and NMR, UV-vis, and  $^{57}\text{Fe}$  Mossbauer spectroscopy.

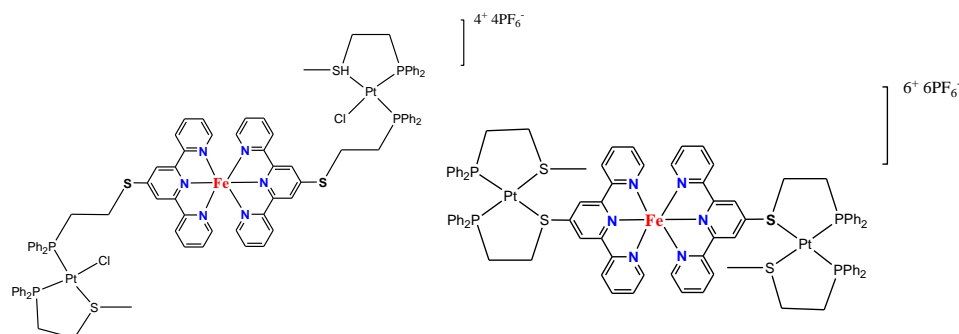


Fig. 1.6

Lallan Mitra and his group synthesized a benzimidazolyl terpyridyl ligand (BIT) which acts as a sensor for  $Fe^{2+}$ ,  $F^-$  and  $CN^-$  ions in acetonitrile (Fig. 1.7). The  $Fe(II)$  complex of the BIT ligand exhibits high response towards 2,4,6-trinitrophenol (TNP) with very low detection limit ( $1.4 \times 10^{-7}$  M) [101]. The prominent color change from purple to red, yellow, and green upon sequential addition of 2,4,6-trinitrophenol and tetrabutylammonium salts of fluoride and cyanide, respectively is utilized to mimic the function of a traffic signal.

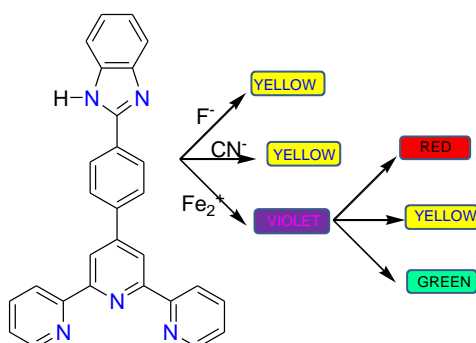


Fig. 1.7

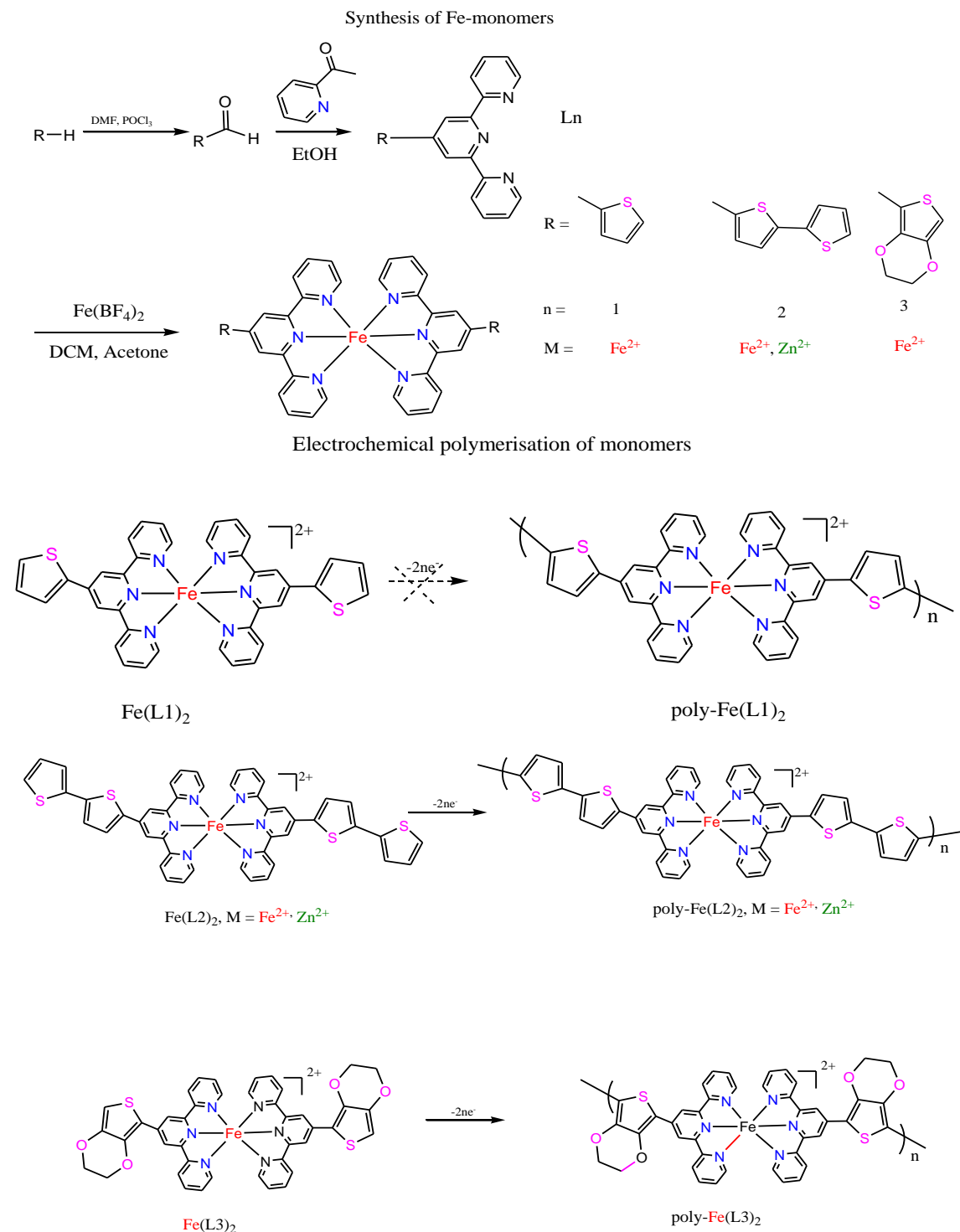
The research group of Richard A. Jones designed three  $Fe(II)$  bis(terpyridine)-based compounds by incorporating thiophene, bithiophene, and 3,4-ethylenedioxythiophene side chain to provide two terminal sites suitable for electrochemical polymerization (Fig. 1.8) [102]. The metallopolymer were synthesized on ITO-covered glass substrates via oxidative electro-polymerization of the thiophene-substituted monomers. They used thin film of poly- $Fe(bithiophene)_2$  for electrochromic

switching properties and constructed electrochromic (EC) device by utilizing the strong MLCT absorption band at 596nm without any applied voltage. The electro-polymerization and electro-chromic conductance of Fe(bithiophene)<sub>2</sub> gives a helpful and controllable method of film formation and forming solid state device.

Manna *et al.* synthesized a series of heteroleptic compounds of 4'-functionalized terpyridyl derivatives with Fe<sup>2+</sup> and Ru<sup>2+</sup> (d<sup>6</sup> metal ions) [103]. Furthermore, they investigated the impact of both electron donating (-NH<sub>2</sub>) and electron withdrawing (-NO<sub>2</sub>) group on the photophysical and electrochemical behaviors of the complexes (Fig. 1.9). The electron donating group induces red-shift of the MLCT band maximum together with increase in the molar extinction coefficient.

G. Hanan and co-workers synthesized homoleptic first and second row transition metal complexes with terpyridine ligands covalently connected with a 3-pyridyl unit (Fig. 1.10) [104]. UV-vis absorption spectroscopy displays spin-allowed <sup>1</sup>MLCT absorption band for Fe(II) and Ru(II) complexes whereas Co(II) and Cu(II) exhibit spin-forbidden d-d transitions. These compounds show their potential for the design of “metallo-ligands as building blocks” in the field of supramolecular chemistry.

Philippe C. Gross and coworkers synthesized two iron(II) complexes using pyridyl-NHC and pyridylquinoline type ligands forming almost perfect octahedral coordination around the metal center (Fig. 1.11). The internal properties of these complexes were investigated by ultrafast spectroscopy and TD-DFT calculations [105]. It was observed that the excited state deactivation was faster than the parent pseudo-octahedral complex in case of pyridyl-NHC containing complexes. This unprecedented result is because of the increased ligand flexibility which may lower the energy barrier for the relaxation of <sup>3</sup>MLCT into the <sup>3</sup>MC state. For iron-pyridylquinoline type complexes, the ligand field was increased but it was not strong enough to shutdown the prominent deactivation channel into the metal-centered quintet state, as for other Fe-polypyridine complexes.



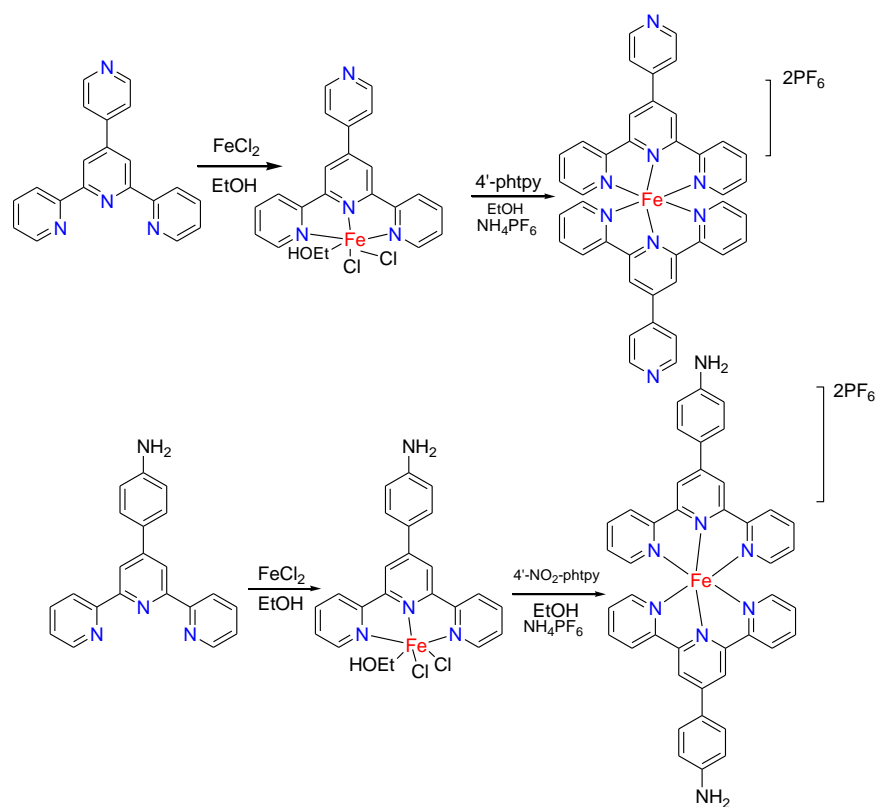


Fig. 1.9

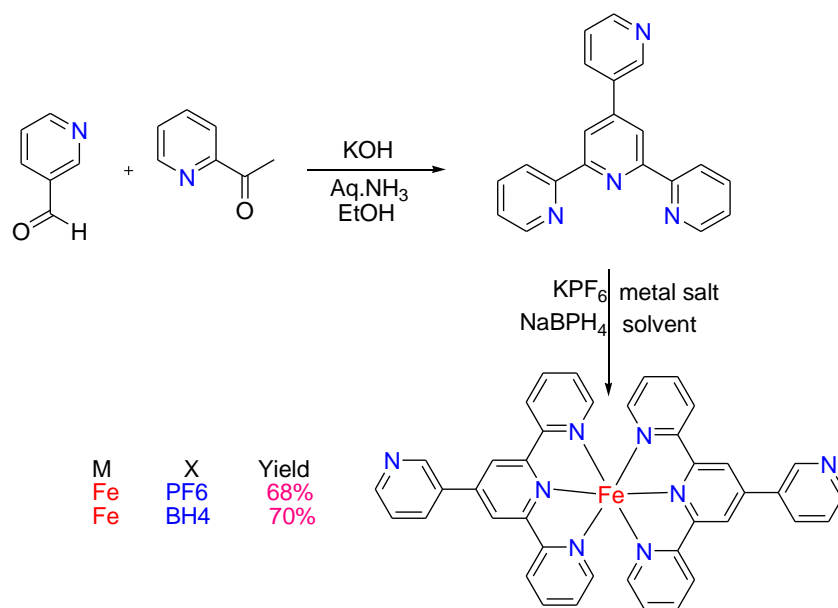


Fig. 1.10

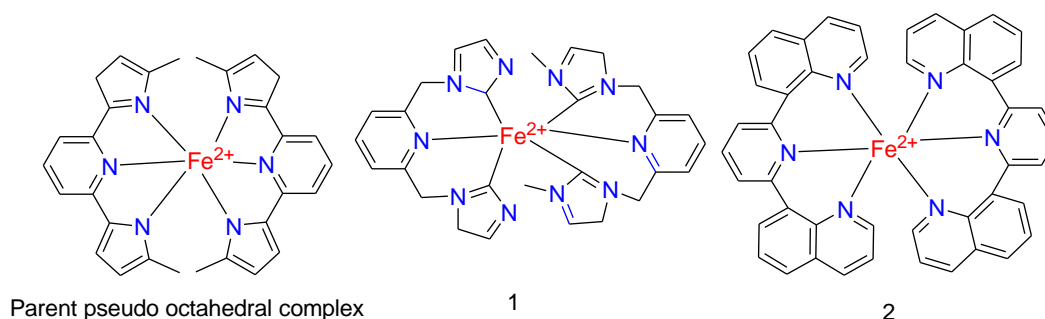
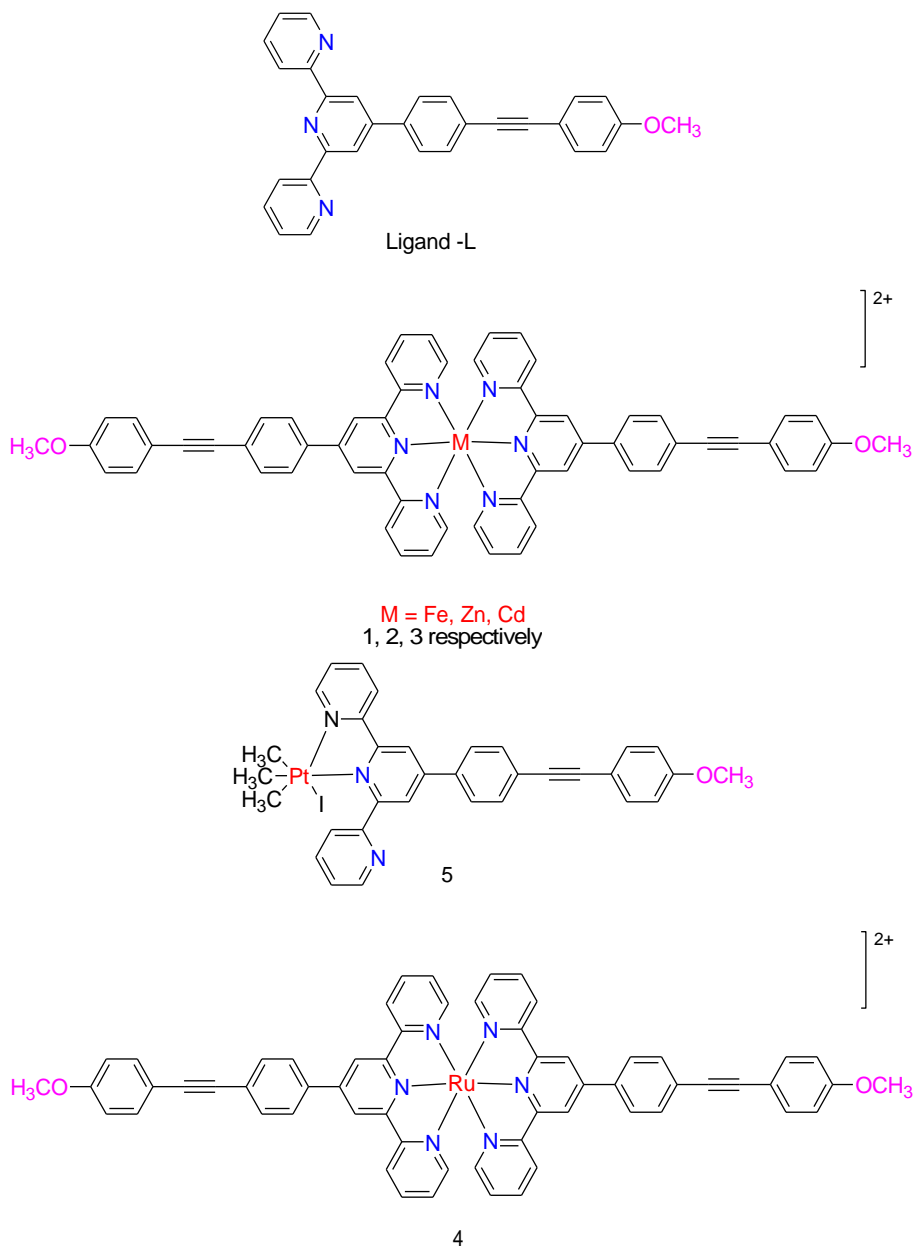


Fig. 1.11

Kari Rissanen and coworkers synthesized a new type of fluorescent terpyridine ligand covalently connected with alkyne spacer (L) following Sonogashira cross-coupling reaction in the presence of  $\text{Pd}(\text{PPh}_3)_4/\text{CuI}$  catalyst [106]. Five transition metal complexes of compositions,  $\{[\text{FeL}_2](\text{CF}_3\text{SO}_3)_2$  (**1**),  $[\text{ZnL}_2](\text{ClO}_4)_2$  (**2**),  $[\text{CdL}_2](\text{ClO}_4)_2$  (**3**),  $[\text{RuL}_2](\text{PF}_6)_2$  (**4**), and  $\text{PtMe}_3\text{IL}$  (**5**), were synthesized and characterized by standard analytical tools as well as by single crystal X-ray diffraction analysis (Fig. 1.12). It was shown that complexes **1,2** and **3** exhibit distorted octahedral geometry with two terpyridine units connected via tridentate fashion, while in complex **5**, the terpyridine unit is coordinated to  $\text{Pt(IV)}$  center via bidentate manner. The  $\text{Fe(II)}$ ,  $\text{Ru(II)}$  and  $\text{Pt(IV)}$  complexes were found to be non-emissive, whereas both  $\text{Zn(II)}$  and  $\text{Cd(II)}$  complexes display strong green emission through their ILCT states. Complexes **2** and **3** also showed red-shifted emission as the polarity of the solvent is increased gradually.

Koiti Araki and coworkers performed the photochemical *cis-trans* isomerization of a styryl-benzene conjugated terpyridine ligand (vpytpy) through UV-vis and NMR spectroscopy as well as via travelling wave ion mobility mass spectrometry (TWIM-MS)[73]. The vpytpy ligand has a very high affinity for transition metal ions, particularly for  $\text{Fe}^{2+}$  ions ( $K_a \sim 10^{21}$ ). The addition of excess of  $\text{Fe}^{2+}$  ion leads to the formation of  $[\text{Fe}(\text{vpytpy})_2]^{2+}$  complex due to high ligand field stabilization brought about by high-low spin transition (Fig. 1.13). The isomerization process became extremely slow for the  $\text{Fe(II)}$  complex compared with the free ligand because of the generation of low-lying excited



**Fig. 1.12**

states which in turn drove away the electronic excitation outside the isomerization pathways. They performed the photoisomerization of the free *trans*vpypyligand upon optical excitation and quenched the products upon complexation with  $\text{Fe}^{2+}$  ions, and determined the relative contributions of the respective *cis-cis*, *cis-trans* and *trans-trans* isomers through the use of TWIM-MS spectrometry.

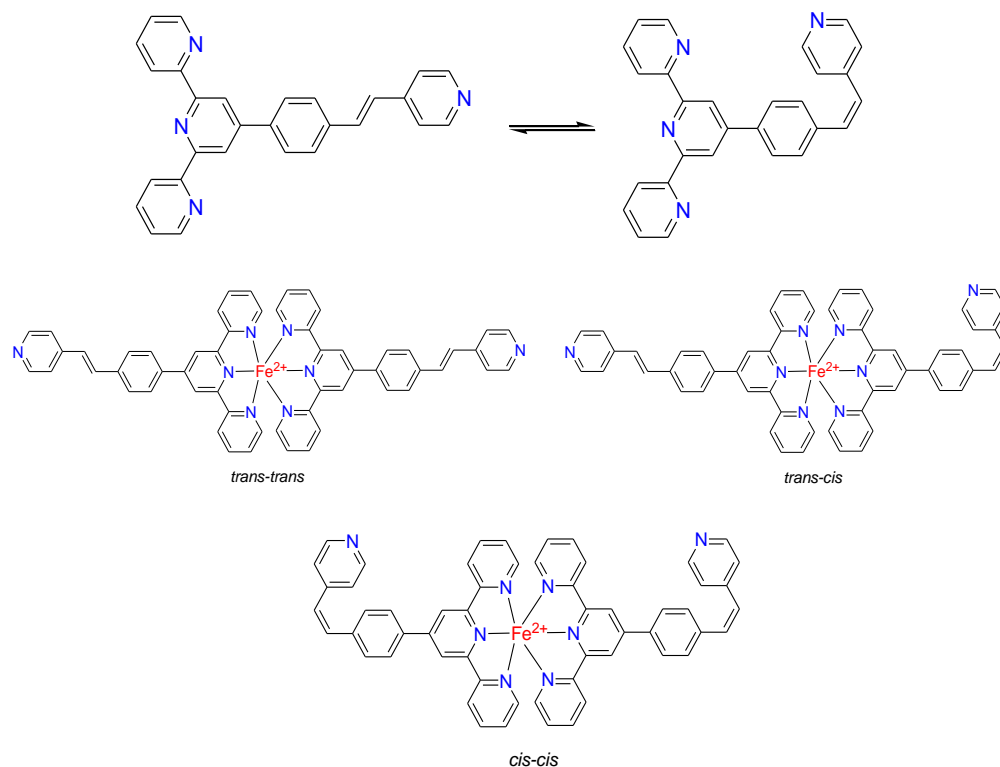


**Fig. 1.13**

H.Nishihara and coworkers studied the photo-isomerization behaviors of iron(II) complexes based on 2,6-di(1H-pyrazol-1-yl)-4-styrylpyridine both in solution and in solidphase [74] (Fig. 1.14). The *cis*-form remains in the high-spin state over the full temperaturerange studied, whereas the *trans*-isomer displays a spin crossoverphenomenon inthe temperature range of 100-300 K. Thus, they demonstrated the change in magnetic properties of the complexes upon irradiation with visible light in both solution and solid states.

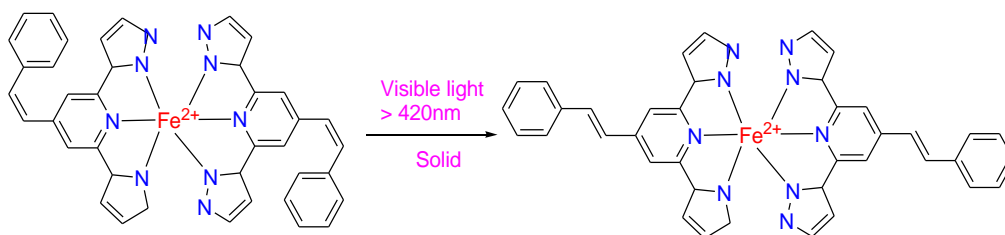


**Fig. 1.14**

Russell H. Schmehl and his group reported a variety of phenylene-vinylene-substituted terpyridyl ligands and their mono-, bi-, and trimetallic complexes incorporating Fe(II) and Ru(II) metals [107]. In these complexes the lowest-energy absorption transition is MLCT; intersystem crossing leads to a long-lived triplet excited-state localized on the ligand ( $^3\text{IL}$ ) that serves as the reactive excited state for energy- and electron-transfer reactions [64]. Interestingly, they designed trimetallic complexes of the type RuFeRu which possess long-lived excited state. (Fig. 1.15) [44].

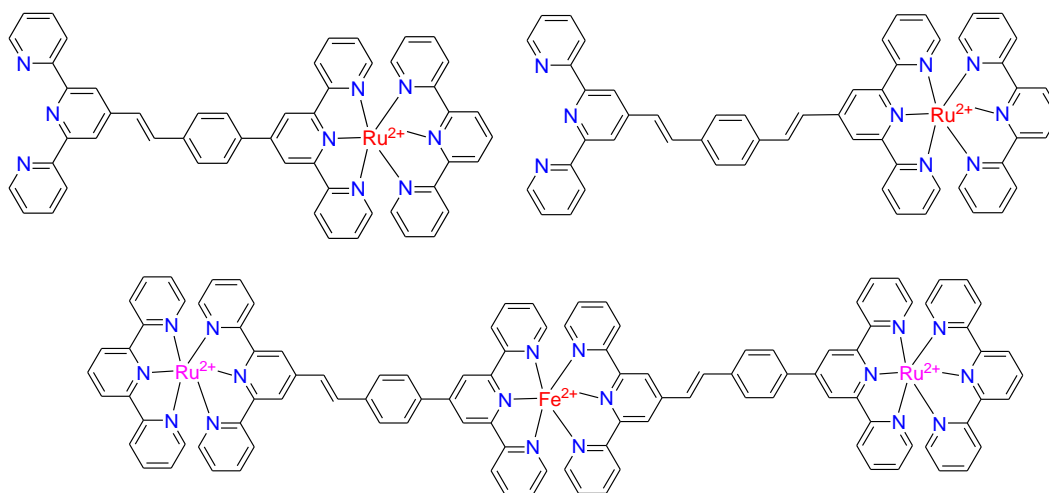


**Fig. 1.15**

Hiroshi Nishihara and coworkers thoroughly studied and reviewed the photoisomerization behaviors of various photochromic and photosensitive metal complexes based on terpyridine ligands covalently attached with azo-moiety. Incorporation of metals leads to enormous change in the isomerization behaviors of pure organic azobenzenes. The photoisomerization behaviors were found to be highly dependent on the type of metals, counter-ions and solvents. The rate as well as quantum yield of the photoisomerization of Rh(III) and Co(III) complexes was found to be much faster compared with Ru(II) and Fe(II) complexes due to energy transfer from the  $\pi\text{-}\pi^*$  excited state to the MLCT state in the complexes. They also investigated the photoisomerization behaviors of several azo-ferrocenyl complexes upon irradiating with both UV and green light (Fig. 1.16) [23]. Interestingly, 3-ferrocenylazobenzene undergoes reversible *trans*–*cis* photoisomerization accompanied with remarkable change in  $\text{Fe}^{\text{III}}/\text{Fe}^{\text{II}}$  redox potential. Thus, the

research group of Nishihara contributed significantly for the design of various types of multi-photo-functionalities based on azo-terpyridine moiety and by incorporating different type of metal units in the complex architecture.

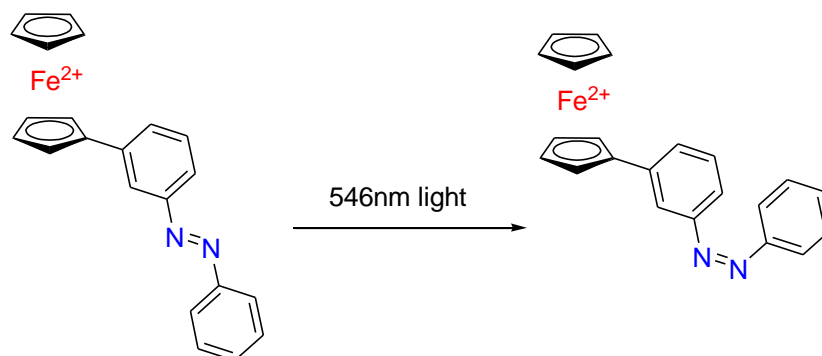


**Fig. 1.16**

### 1.5.3 Brief literature survey on Zn(II)-terpyridine-type complexes

As already mentioned in the previous section, Zn(II) constitutes an important class of low-cost and photophysically rich complexes. Because of its  $d^{10}$  electronic configuration, the Zn(II) complexes are optically more transparent than other  $d^n$  metal complexes. Zn(II)- complexes usually display intense intra-ligand charge transfer (LLCT) absorption and emission band at relatively low energy [49-52].

Over last few decades, a great variety of Zn(II) complexes have been designed with well-defined structures and properties. The properties of the complexes are strongly influenced by the nature of the ligands, such as their  $\sigma$  and  $\pi$  donor/acceptor capacities, length and rigidity, type of chelating motifs as well as the coordinating atoms. The literature on the polypyridine complexes of Zn(II) is quite large and discussion on the properties of every individual complex is very difficult. Early works in this field are nicely summarized in several reviews and monographs. Therefore, only a few selected systems which are somehow related to our work will be presented here.

K. Uvdal and co-workers reported four Zn(II)-terpyridine complexes for the fabrication of two-photon excited fluorescent bioimaging probes with intense emission, high photo-stability and low cytotoxicity (Fig. 1.17) [108]. The compounds were thoroughly investigated both by experiment and theoretical calculations to justify their

potentiality as efficient two-photon probes for bioimaging. Notably, the experimental outcomes indicate that complexes **1** and **2** display upgraded two-photon absorption (2PA) cross sections compared to the free ligand. Additionally, complex **1** has the benefits of moderate 2PA cross section in the near-infrared region with enhanced two-photon excited fluorescence, longer fluorescence lifetime, higher quantum yield and good biocompatibility. Complex **1** also acts as a bioimaging probe for in vitro imaging of HepG2 cells.

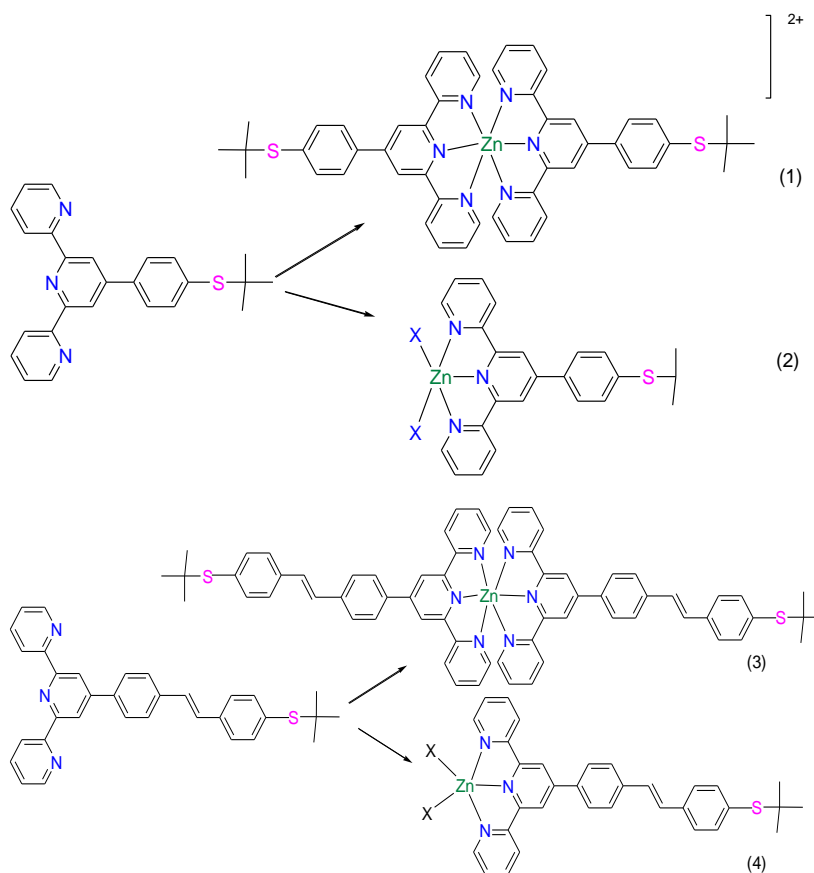


**Fig. 1.17**

M. Pizzotti and co-workers designed novel terpyridine systems by incorporating substituted stilbene units. By using the ligand, they synthesized bis-terpyridine complexes of Zn(II), Ru(II), and Ir(III) metals to investigate their second order nonlinear optical (NLO) properties. They employed electric field induced second harmonic generation technique (Fig 1.18). The second-order non-linear optical response was found to shift

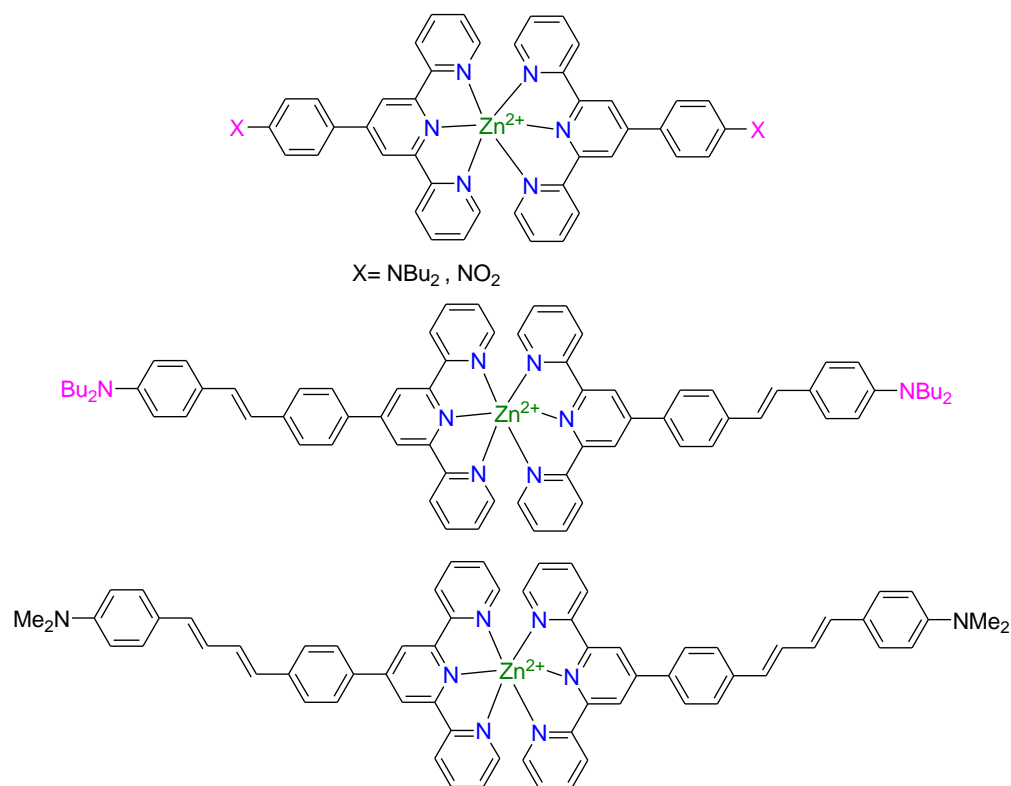


Fig. 1.18

from positive to negative upon variation of the metal center [50]. This type of shift was due to various kinds of charge-transfer (such as MLCT, LMCT or LLCT) transitions.

Hiroshi Nishihara and group designed tripodal bridging terpyridine ligands {1,3,5-tris[4-(4'-2,2':6',2''-terpyridyl)phenyl]benzene} and synthesized different Zn-terpyridine complexes upon varying the counter anions in the Zn-salt for the fabrication of photoactive nanosheets (Fig. 1.19) [51]. Zn(BF<sub>4</sub>)<sub>2</sub> forms a cationic coordination nanosheets incorporating the Zn(tpy)<sub>2</sub> unit. But when counter ion of Zn(II) was substituted by SO<sub>4</sub><sup>2-</sup>, a different type of charge-neutral coordination nanosheet as shown in Fig. 1.19 was formed. The effect of the counter anions is also reflected in the photophysical and in particular the luminescence spectral properties of the nanosheet (Fig. 1.19). Another type of Zn(II) complex was also synthesized with triarylamine-centered terpyridine ligand for further modulation of luminescence properties of the nanosheet. Thus, this new class of coordination nanosheets having tpy-Zinc(II) units can act as a promising potential photo-functional nanomaterials.

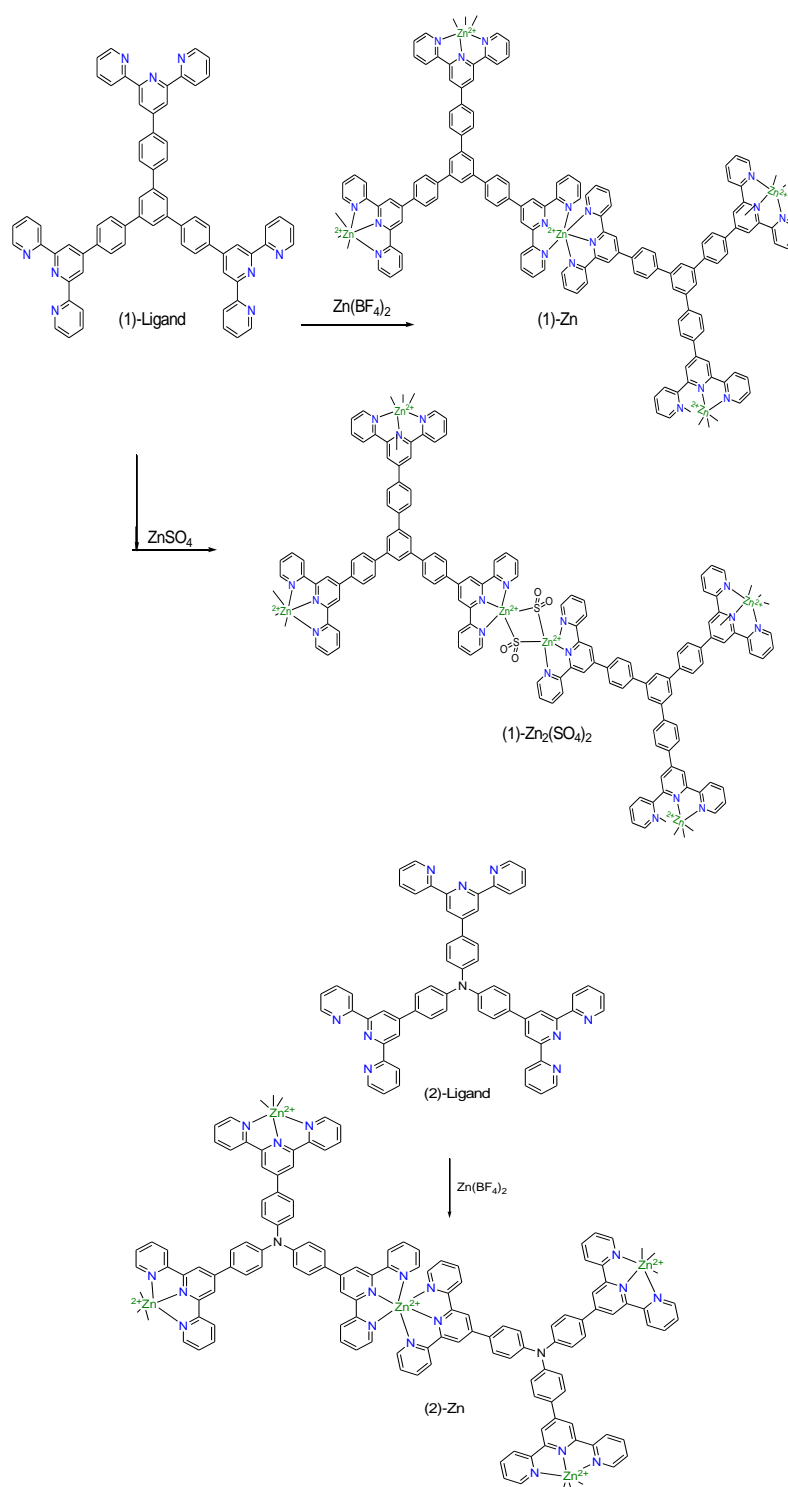
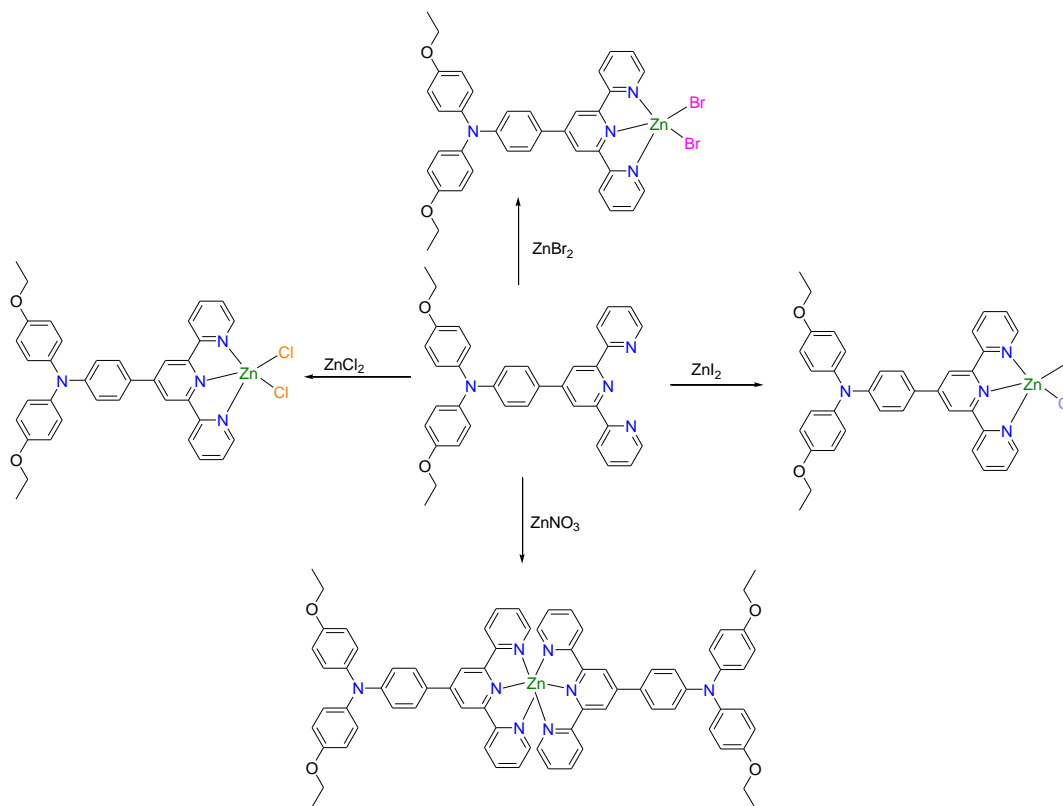


Fig. 1.19



Yupeng Tian *et al.* synthesized and characterized a terpyridine ligand possessing both donor and acceptor unit and four zinc(II) complexes which are two-photon activated nonlinear optical (NLO) materials [109]. In view of their precise photophysical characters, it was observed that the third-order non-linear optical response in the near-infrared (NIR) region was significantly enhanced for the symmetrical complex compared with the other asymmetric complexes. The symmetrical Zn(II) complex also acts as a two-photon probe in cellular lipid membrane (Fig. 1.20). The fluorescence intensity was substantially enhanced in presence of selected bioactive liposomes. In essence, the present metal complexes can act as lipid membrane targeting probes in biological systems.



**Fig. 1.20**

Y. Pang and coworkers designed various terpyridine ligands with electron donating substituent and synthesized their different types of Zn(II) complexes [110]. The ligands react readily with  $\text{ZnCl}_2$  and yield Zn(II) complexes with a 2:1 (ligand-to-metal) ratio when the concentration of Zn(II) ion is less, while 1:1 complex in presence of excess  $\text{Zn}^{2+}$  salt (Fig. 1.21). The photophysical characteristics of the compounds were examined by various spectroscopic techniques at RT as well as at low temperature. Lowering of temperature gives rise to significant enhancement of emission intensity due to enhanced charge transfer characteristics (ICT) brought about by restricting non-radiative channels at frozen state.

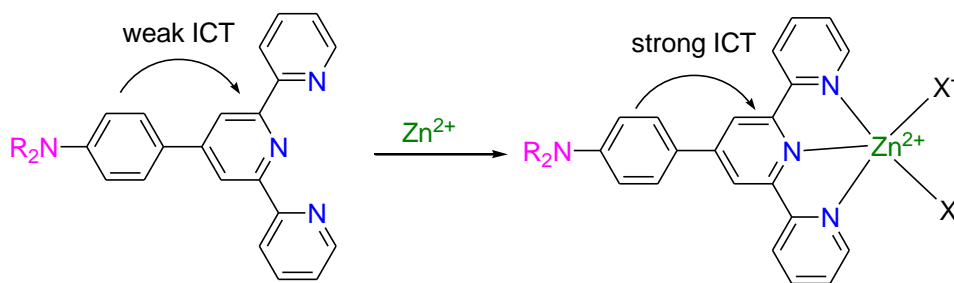


Fig. 1.21

Zhen Ma and coworkers synthesized a wide variety of Zn(II) complexes derived from 4'-(substituted-phenyl)-2,2':6',2''-terpyridine ligands and thoroughly studied their antiproliferative activities against tumor cells via various spectrochemical tools (Fig. 1.22). The complexes possess interesting and tunable photophysical properties, dependent on the electronic nature of substituent. The compounds have excellent antiproliferative activity against four human carcinoma cells. The complexes also possess strong affinity to bind with DNA via intercalation [111].

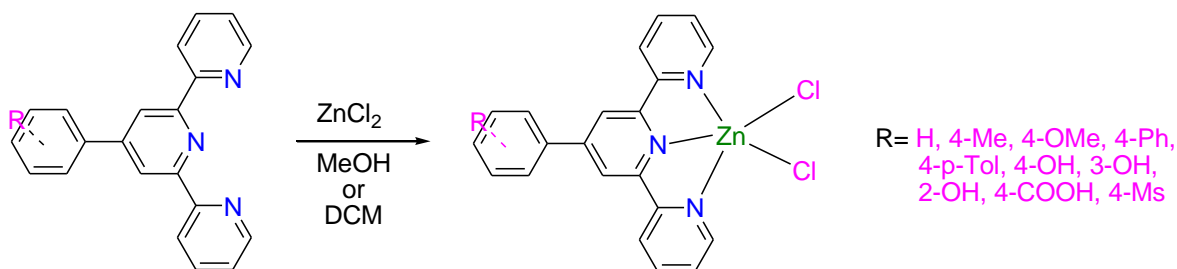
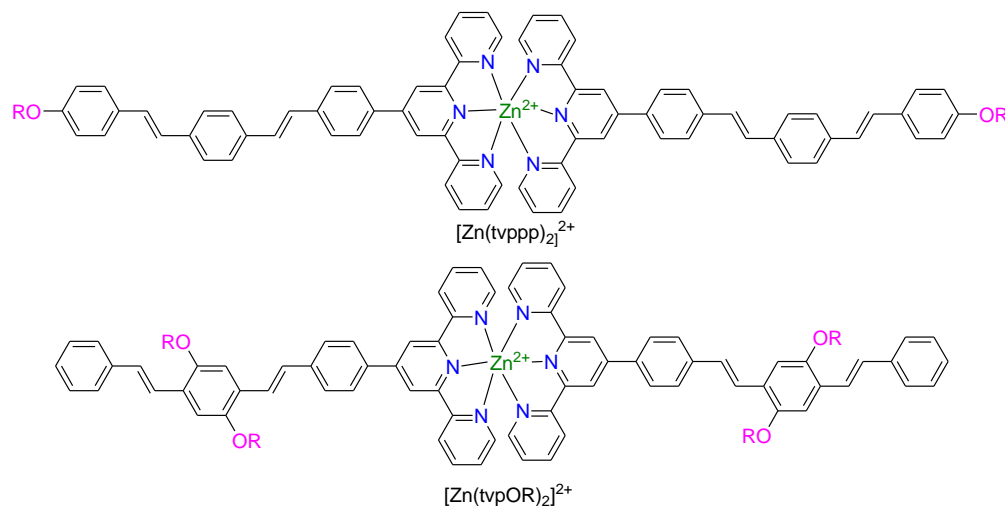


Fig. 1.22

R.H. Schmehl and co-workers worked on a large number of terpyridine derivatives incorporating varying number of phenylene vinylene units which show bright emission from their singlet  $\pi$ - $\pi^*$  state (Fig. 1.23)[63]. Coordination of the ligands with Zn(II) ion increases electron delocalization in the complex backbone which is reflected by the red-shift of the emission maximum compared with the free ligands. They proposed that the emitting excited state of the Zn(II) complexes possess significant charge transfer character. The luminescence properties of the metal complexes are highly solvent dependent and displayed significant solvochromism.



**Fig. 1.23**

U.S Schubert and coworkers synthesized ethynylphenyl-substituted terpyridine ligand and its Zinc (II) complex and thoroughly investigated their photophysical behaviors (Fig. 1.24). DFT calculations suggest substantial  $\pi$ -electron delocalization between ethynylphenyl and pyridine units upon complexation with Zn(II) ion. They utilized the Zn(II) complex as the model for the design of various photoluminescent and electroluminescent devices [112].

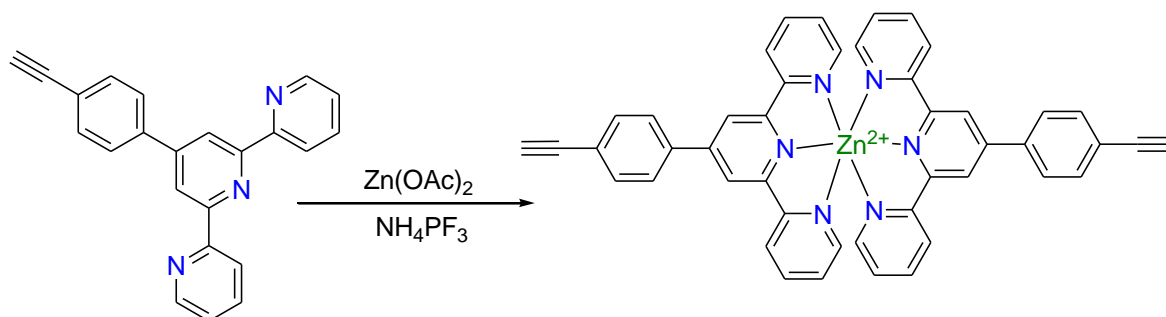


Fig. 1.24

L. Wang and co-workers synthesized and characterized five Zn(II) complexes based on 4'-phenyl-2,2':6',2''-terpyridine (ptpy) ligands (Fig. 1.25). The *para*-position of phenyl group in ptpy was substituted by various electron-donating groups to modulate the photophysical properties of the complexes. They demonstrated that the emission color of complexes gradually changes from violet (392 nm) to reddish orange (604 nm) upon increasing the electron donating ability of the group. The emitting excited state is predominantly ILCT in nature. They utilized the complexes for the fabrication of electroluminescent devices [49].

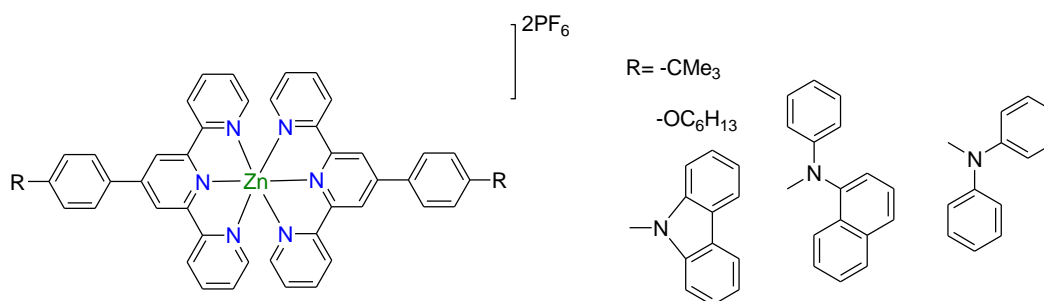


Fig. 1.25

Yunjun Wu and coworkers synthesized a new series of Zn(II) complexes based on terpyridine derivative ligand upon varying the counter anion (halides) (Fig. 1.26). Single crystal diffraction studies indicate the structure became coplanar as the size of the halide ion increases. [113]. The lowest energy absorption maximum undergoes gradual red-shift along with quenching of emission intensity. The Zn(II) complexes also act as biological imaging agents. The Zn(II) complexes have low cytotoxicity, good membrane

permeability and good photostability and they show strong fluorescence in the cytosolic space in living Hela cells.

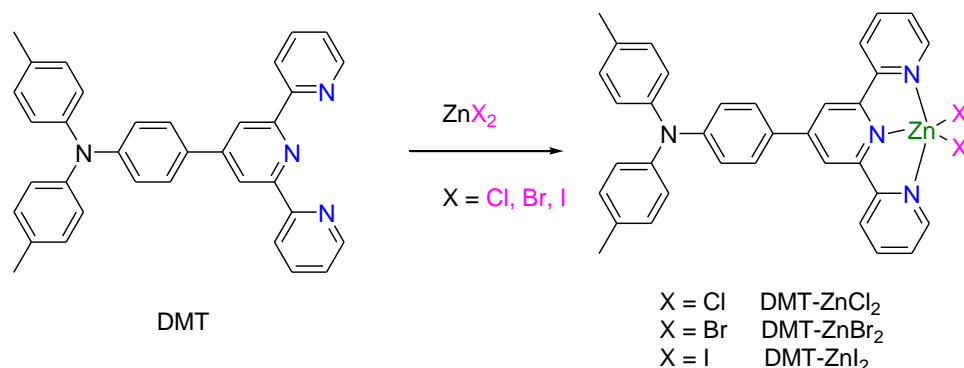
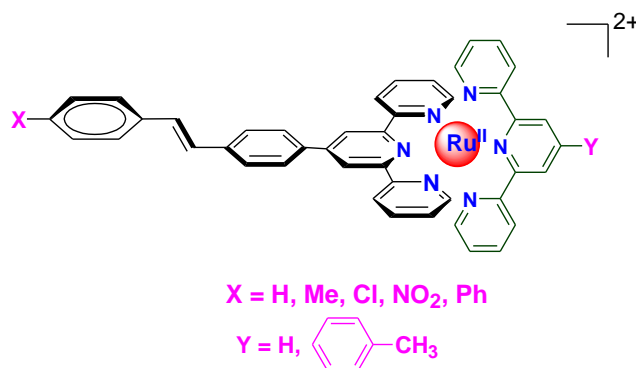


Fig. 1.26

### 1.6 A brief survey on the photoisomerization behaviors of stilbene-appended polypyridine complexes of noble metals

Light-induced reversible *trans/cis* isomerization across the stilbene unit has received great attention in the field of photo-responsive functional materials. The photoisomerization studies of different organic molecules incorporating stilbene moiety are well documented in literature. Similar studies dealing with coordination complexes are relatively less in the literature. Among the coordination complexes, most of the reports are based on noble metals because of their very rich photophysical and electrochemical behaviors. The research groups of Baitalik, Yam, Nishihara, Lees, Iha and some other researchers thoroughly investigated the photo-isomerization behaviors of various transition metal complexes involving Re, Rh, Ir, Pt, Ru and Os metals covalently coupled with the stilbene-, azo-, spirooxazine-, and diarylethylene units [4, 23,26-31,51-52,71,114-128]. In this dissertation, our target is to investigate the photo-isomerization behaviors of low cost and easily synthesizable photo-switches based on 3d metals such as Fe and Zn which are very rare in the literature. In the previous sections, we made a brief survey of the polypyridine complexes Fe(II) and Zn(II) metals appended with stilbene moiety. Among the reviewed complexes, we observed only a limited number of systems exhibiting photo-isomerization behaviors. Herein, we will present a brief survey on photo-isomerization behaviors of some selected noble metal complexes incorporating stilbene moiety in the complex architecture.

Baitalik and coworkers designed a new array stilbene-appended hetero- and homoleptic Ru(II) and Os(II) terpyridine complexes and thoroughly investigated their photophysical, electrochemical and photoisomerization behaviors (Fig. 1.27-1.30) [28-31]. All the complexes exhibit strong absorption in the visible region due to M(II)→tpy charge transfer transitions and several intense bands in the UV region because of intra-ligand charge transfer as well as  $\pi \rightarrow \pi^*$  transitions. The Os(II) complexes exhibit a weak and broad absorption in the longer wavelength region because of spin-forbidden electronic transition to the  $^3\text{MLCT}$  state. The complexes display emission at room temperature due to radiative deactivation of their  $^3\text{MLCT}$  state with reasonably long lifetime. The Ru(II) complexes usually exhibit emission within 650-700 nm, depending upon the nature of co-ligand. For the Os(II) complexes, the emission band stretched beyond 700 nm because of the energy gap law. All the complexes also undergo reversible trans/cis isomerization in presence of either UV or visible light with substantial change in the absorption and emission spectral behaviors. Solvent- and wave-length dependent modulation of photo-isomerization behaviors of the complexes was also explored. They calculated the rate constants and quantum yield of isomerization for the studied complexes.



**Fig. 1.27**

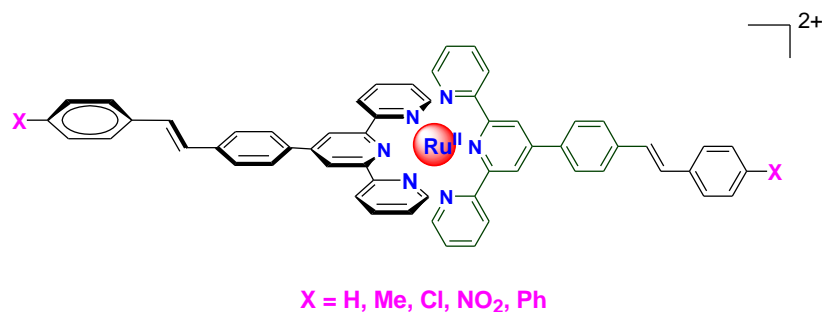


Fig. 1.28

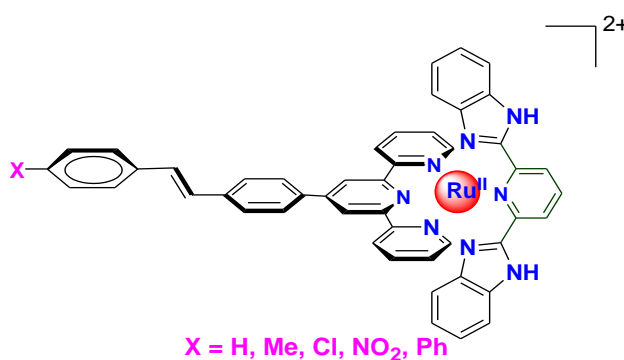


Fig. 1.29

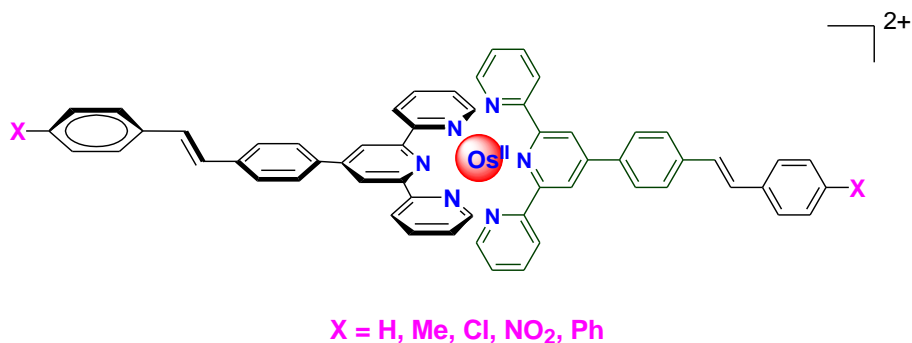


Fig. 1.30

There are quite a sizeable number of reports dealing with photo-isomerization behaviors of Re(I)-polypyridyl complexes appended with stilbene moiety. Wrington and coworkers first reported the isomerization studies of a series of Re(I) complexes of composition  $\text{XRe}(\text{CO})_3\text{L}_2$  [where  $\text{X} = \text{Cl, Br}$ ;  $\text{L} = \text{trans-3-styrylpyridine}$  and  $\text{trans-4-styrylpyridine}$ ] (Fig. 1.31)[47]. When irradiated with UV light (313 or 366nm), the complexes underwent *trans* to *cis* photoisomerization with higher quantum yield. The

photo-stationary states were believed to be generated through triplet sensitization and the quantum yields of isomerization processes were close to those of the free ligands.

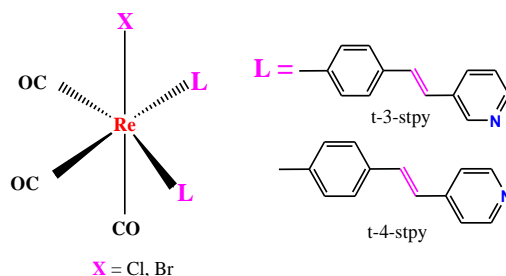


Fig. 1.31

H. Gray and coworkers reported the photo-isomerization behaviors of  $[\text{Re}(\text{diimine})(\text{CO})_3(\text{dpe})](\text{PF}_6)$  ( $\text{dpe}$  = 1,2-di(4-pyridyl)-ethylene) complexes in dichloromethane (Fig. 1.32) [128]. The forward *trans* to *cis* conversion proceeds smoothly upon irradiation with 350 nm light and the quantum yield of the process being 0.2. 70% of the *cis* and 30% of the *trans* form exit at the photostationary state. The

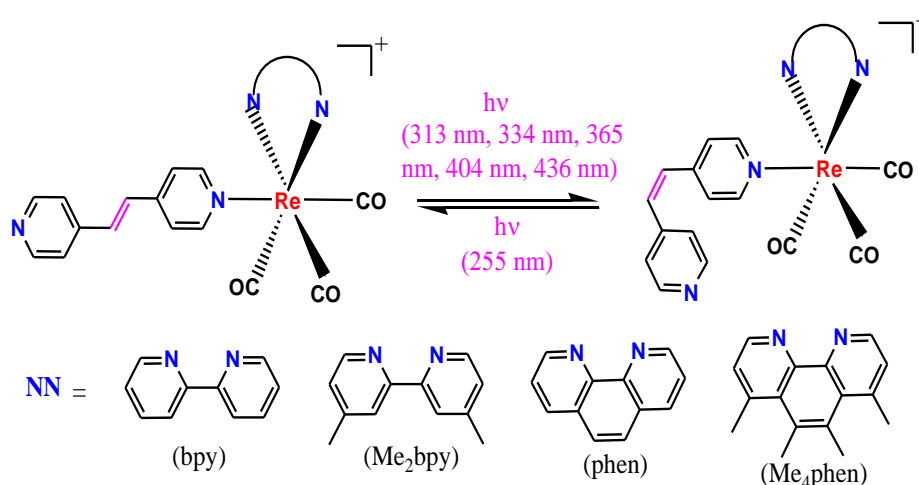


Fig. 1.32

reverse process occurred when the solution was irradiated with 250 nm light. It was observed that the *trans* forms were non-luminescent whereas their *cis* forms exhibited yellow luminescence.

Iha and coworkers designed a wide variety of organometallic Re(I)-carbonyl complexes and thoroughly investigated their photophysical, photochemical and photo-



isomerization behaviors through different spectroscopic techniques, viz. absorption, emission and  $^1\text{H}$  NMR spectroscopy (Fig. 1.33) [123-126]. The complexes exhibited *trans*→*cis* isomerization in various light sources like 313 nm, 334 nm, 365 nm, 404 nm and 436 nm (Fig. 1.33). The quantum yields ( $\Phi = 0.29$ -0.38) were found to be independent on the irradiating wavelength for *fac*-[Re(CO)<sub>3</sub>(Me<sub>4</sub>phen)(*trans*-bpe)]<sup>+</sup> and *fac*-[Re(CO)<sub>3</sub>(ph<sub>2</sub>phen)(*trans*-stpyCN)]<sup>+</sup>. The proposed isomerization pathway was via  $^3\text{IL}_{\text{trans-bpe/trams-stpyCN}}$  state obtained upon internal conversion from  $^3\text{MLCT}_{\text{Re} \rightarrow \text{Me4phen/ph2phen}}$  (Fig. 1.33b,e) [123-124]. The calculated isomerization quantum yields for *fac*-[Re(CO)<sub>3</sub>(Me<sub>4</sub>phen)(stpy)]<sup>+</sup>, *fac*-[Re(CO)<sub>3</sub>(bpy)(stpyCN)]<sup>+</sup> and *fac*-[Re(CO)<sub>3</sub>(dmb)(stpyCN)], were found to be higher with UV light sources (at 315-365 nm,  $\Phi = 0.44$ -0.57) relative to those with visible light (at 404 nm,  $\Phi = 0.35$ -0.39). The results indicate that the  $^1\text{IL}$  state predominantly involved in UV light and the major involvement of  $^3\text{IL}$  state in presence of visible light (Fig. 1.33a, c and d) [123, 126]. The backward photoisomerization for all these systems were feasible upon irradiation with ~255 nm light ( $\Phi=0.15$ -0.26) [123-126]. While the *trans* forms of *fac*-[Re(CO)<sub>3</sub>(Me<sub>4</sub>phen)(L)]<sup>+</sup> are non-luminescent, the *cis* form exhibited dual emission with maxima at 498 nm and 525 nm due to radiative relaxation of  $^3\text{IL}_{\text{Me4phen}}$  and  $^3\text{MLCT}_{\text{Re} \rightarrow \text{Me4phen}}$  excited states, respectively [123].

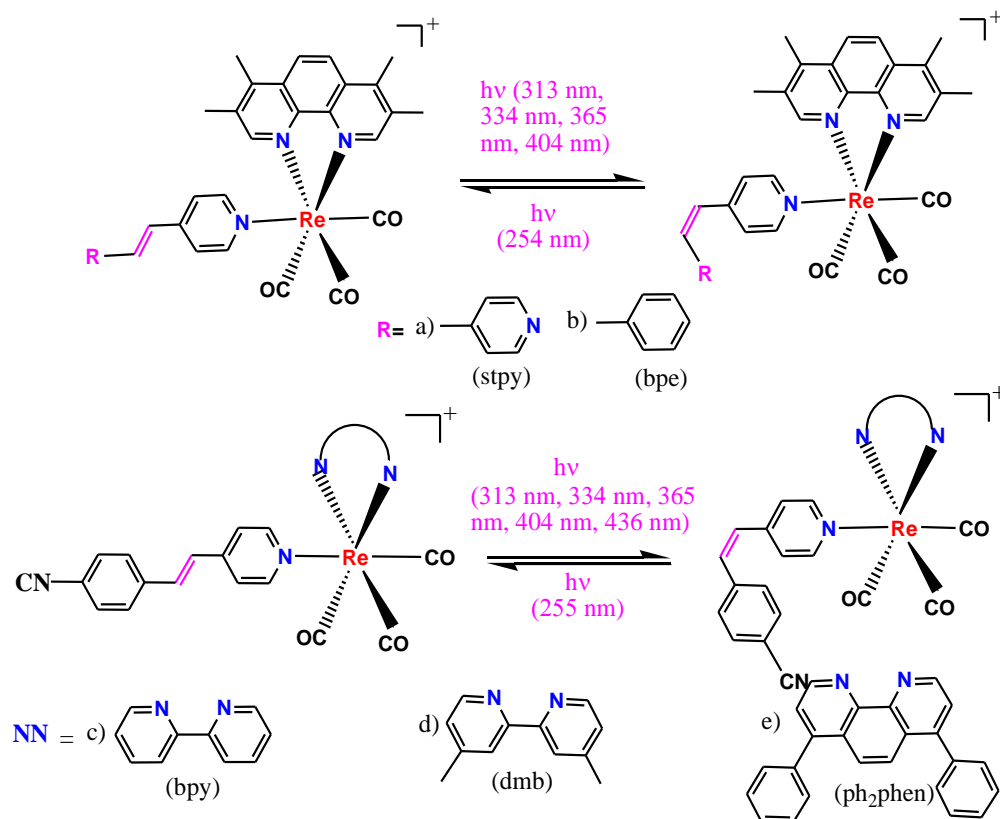


Fig. 1.33

Yam and coworkers designed various types of Re(I)-diimine complexes bearing isomerizable units (azo-, -ethenyl or -ethyl motifs) (Fig. 1.34) [114]. The team meticulously studied the photophysical as well as photoisomerization aspects of the complexes. *Trans-cis* isomerization of the complexes across the double bond was observed in DCM upon irradiation with UV light ( $\lambda > 350$  nm). Upon isomerization, the emission quantum yield increased by ~40 times together with the red-shift of the emission band (~50 nm). The increment of emission intensity and quantum yield is mainly due to the restricted energy transfer from excited  $^3\text{MLCT}$  state(s) to the azo/ethyl unit in the *cis* form.

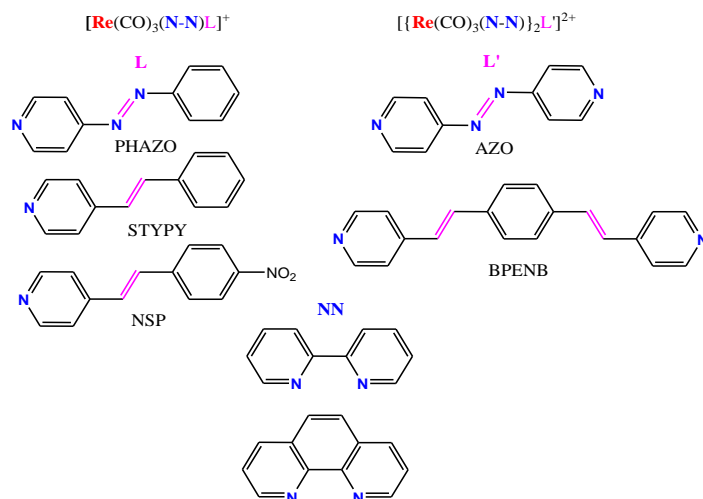


Fig. 1.34

Patrochino and co-workers reported photophysical and photo-isomerization behaviors of *fac*- $[\text{Re}(\text{CO})_3(\text{dcbH}_2)(\text{trans-stpy})]^+$ , ( $\text{dcbH}_2 = 4,4'$ -dicarboxylic acid-2,2'-bipyridine; *trans-stpy* = *trans*-4-styrylpyridine) (Fig. 1.35) [127]. The quantum yield for *trans* to *cis* isomerization ( $\Phi_{t \rightarrow c}$ ) was  $0.81 \pm 0.08$  at 365 nm light irradiation and gradually decreased on changing the irradiation wavelength towards the visible range. Upon 405 nm light irradiation, the  $\Phi_{t \rightarrow c}$  was  $0.010 \pm 0.005$ , which is almost 2 orders of magnitude lower than that of 365 nm light irradiation. Under visible light irradiation, the low lying  $^3\text{MLCT}$  state restricts the triplet mechanism for isomerization, whereas UV irradiation leads to direct population of  $^1\text{IL}$  state and the singlet mechanism became operative which in turn increases the isomerization efficiency.

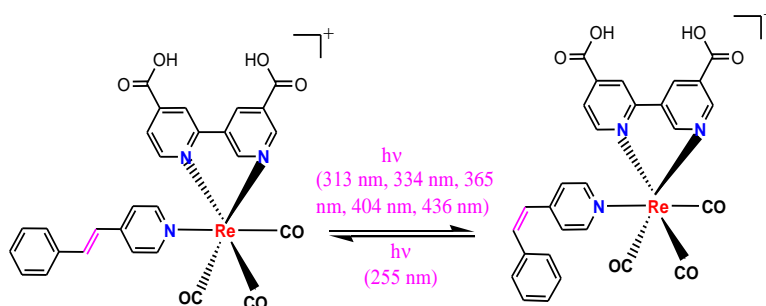
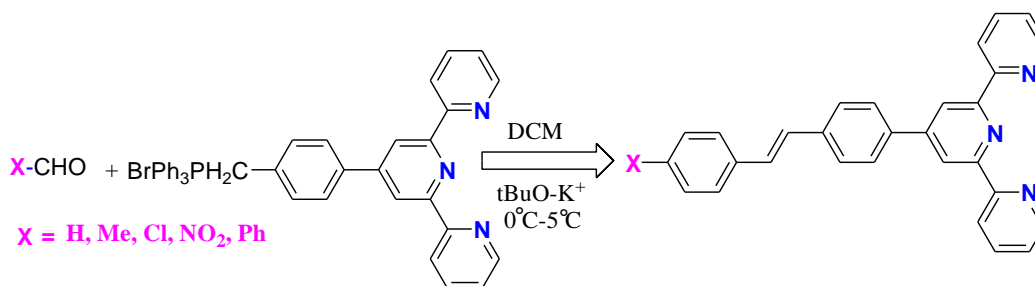


Fig. 1.35

## 1.7 Objective and scope of the present work

A brief survey of literature indicates that the compounds containing stilbene, azobenzene, spiropyran, and diaryethylenes undergo reversible *trans/cis* photoisomerization and lead to the generation of a wide range of photo-responsive materials. Photo-irradiation induces conformational change of the said molecules which in turn gives rise to remarkable alteration of their photophysical behaviors. The reversible alteration of the optical as well as emission spectral response of the compounds upon the action of light of desired wavelength has been utilized for the construction of different photo-switches. Survey of literature also shows that although lots of studies were reported with purely organic stilbene derivatives, but similar studies with their coordination complexes are relatively sparse in the literature. The metal complexes have the ability to offer a wide range of electronic structures with regard to coordination sphere, electronic configuration and photophysical and electrochemical behaviors. Thus, design of photo-switches based on coordination complexes is more advantageous over their organic counterparts. Among the coordination complexes with stilbene moiety, the majority of the reports are based on the noble metals (such as Ru, Re, Ir, and Pt) which are very expensive as well as synthetically challenging [21-31]. The primary objective of the dissertation is to design suitable base-metal complexes which could demonstrate similar behavior and can lead to the design of a new class of low-cost and easily synthesizable photo-switches.

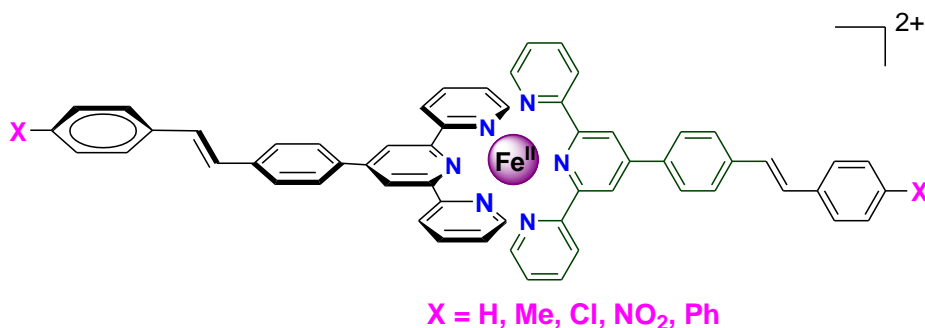
In order to fulfill our objective, a series of terpyridine derivatives {2-(6-(pyridin-2-yl)-4-(4-styrylphenyl)pyridin-2-yl)pyridine} appended with substituted stilbene units (tpy-pvp-X) has been designed. Both electron-donating as well as electron-withdrawing groups were incorporated to the ligand framework to tune their photophysical properties upon adjusting the HOMO-LUMO energy gap (Scheme 1.1).



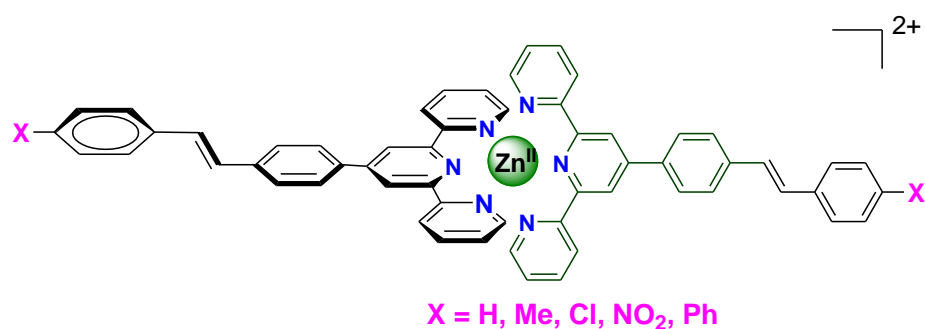
Scheme 1.1

## Chapter 1

The scope of formation of various homoleptic complexes of Fe(II) and Zn(II) based on these tpy-pvp-X ligands are presented in [Scheme 1.2-1.3](#).



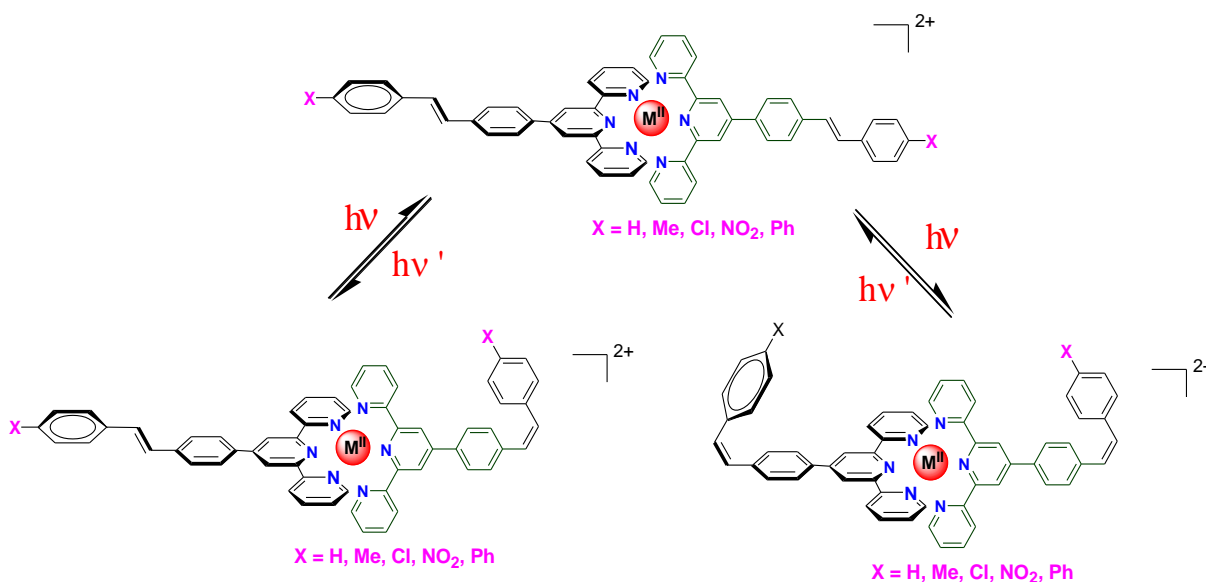
**Scheme 1.2**



**Scheme 1.3**

All the synthesized ligands as well as their Fe(II) and Zn(II) complexes will be thoroughly characterized by standard analytical tools and spectroscopic techniques, viz. elemental analysis, ESI mass spectra, and NMR spectroscopic methods. Detailed investigation of the photophysical behaviors of the ligands as well as their metal complexes will be carried out by using UV-vis absorption and both steady state and time-resolved emission spectroscopic techniques. The redox behaviors of the compounds will be investigated via cyclic voltammetry (CV) and square wave voltammetry (SWV).

All the ligands as well as their metal complexes possess one or more stilbene units in their molecular framework. One of the important objectives of this dissertation is to carry out *trans-cis* isomerization behaviors of the compounds upon the action of light of desired wavelength. The mode of photo-isomerization aspects of the compounds are outlined in [Scheme 1.4](#). The isomerization behavior of the compounds will be monitored through multiple optical channels (such as absorption, emission and lifetime) as well as



Scheme 1.4

by NMR spectroscopy. Absorption and emission titration profiles will be utilized to calculate rate constant and quantum yield of the photo-isomerization processes. We will also use light source of varying wavelength in the UV-vis domain as well as solvents of varying polarity to fine tune the rate and quantum yield of the isomerization processes.

Another important objective of the present dissertation is to develop smart molecular systems capable of processing information at the molecular level. As the terpyridine motif is a versatile coordinating motif, the optical properties of the ligands could be significantly modulated by the presence of incoming cationic guests as well as in presence of acid. The stilbene moiety, on the other hand, can induce switching of the optical properties in both the free ligands as well as their cationic adducts upon interaction with light. Thus, there remains scope to mimic the functions of advanced Boolean logic functions by utilizing the optical spectral response of the ligands upon the action of selected cations as well as light of specific wavelength. Additionally, fuzzy logic approach could also be implemented to construct an infinite-valued system for locating the imprecise values between completely true (1) and completely false (0). Thus, it is expected that the present photo-switchable terpyridine based receptors can act as potential building blocks for information processing and computation at the molecular level.

Finally, the homoleptic complexes of the terpyridine ligands, in particular the Fe(II) complexes could undergo decomplexation in presence of the selective anions (such as  $\text{CN}^-$  and  $\text{F}^-$ ) and again complexation in presence of  $\text{Fe}^{2+}$ . This complexation-decomplexation process is reversible and could be repeated many times. Although the free ligands are colorless, their Fe(II) complexes exhibit deep violet color due to  $\text{Fe(II)} \rightarrow \text{tpy} (\pi^*)$  MLCT transition. Thus, the reversible complexation-decomplexation behaviors of the terpyridine ligands accompanied with the visual color change could be utilized for sensing of selected anions.

The execution of different scopes together with relevant investigations has been reported in chapter 2-6. [Chapter 2](#) deals with the synthesis and characterization of a series of terpyridine ligands,  $\text{tpy-pvp-X}$  (where  $\text{X} = \text{H}, \text{Me}, \text{Cl}, \text{NO}_2, \text{Ph}$ ) covalently coupled with styryl-benzene and thorough investigation of their photophysical and reversible *trans-cis* photo-isomerization behaviors. The photochromic behaviors of the compounds were also explored and modulated in presence of acid. The "on-off" and "off-on" emission switching was made possible upon alternate interaction of the compounds with UV and visible light. Finally, detailed computation work was performed on both the *trans* and *cis* forms of the compounds by employing DFT and TD-DFT methods to acquire deeper insight about their electronic structures as well as proper assignment of the experimentally observed absorption and emission bands.

[Chapter 3](#) deals with synthesis, characterization, photophysics, and reversible *trans-cis* photoisomerization behaviours of three homoleptic Fe(II)-terpyridine complexes,  $[\text{Fe}(\text{tpy-pvp-X})_2]^{2+}$  where  $\text{X} = \text{H}, \text{Me}, \text{and } \text{NO}_2$ ) covalently coupled with photo-active styrylbenzene moiety. The complexes undergo *trans-trans* to *cis-cis* isomerization upon treating with both visible and UV light with substantial alteration of their absorption and emission spectral profiles. The reverse process (*cis-cis* to *trans-trans* isomerization) also proceeds, albeit very slowly, on keeping and can be accelerated upon heating. The isomerization studies were performed in different solvents of varying polarity to tune the thermodynamic and kinetic aspects of the isomerization process. The rate, rate constant and quantum yield of photoisomerization were determined in all the solvents. Computational investigations involving DFT and TD-DFT methods were also

carried out in their *trans-trans*, *trans-cis* and *cis-cis* forms to understand the electronic structures and correctly assign the experimental optical spectral bands.

Anion sensing properties of a bis-terpyridine Fe(II) complex,  $[\text{Fe}(\text{tpy-pvp-Cl})_2]^{2+}$  as reported in chapter 3, is thoroughly investigated in chapter 4 in both acetonitrile and water-acetonitrile (100:1, v/v) media through multiple optical channels and spectroscopic techniques. Interestingly, the complex acts as chromogenic and fluorogenic receptor for cyanide (among the other studied anions such as  $\text{F}^-$ ,  $\text{Cl}^-$ ,  $\text{Br}^-$ ,  $\text{I}^-$ ,  $\text{CN}^-$ ,  $\text{OAc}^-$ ,  $\text{H}_2\text{PO}_4^-$ ,  $\text{SCN}^-$ ,  $\text{BF}_4^-$  and  $\text{ClO}_4^-$ ) in predominantly aqueous medium with very low detection limit.

Synthesis, characterization, photophysics, and photo-isomerization behaviors of three Zn(II)-terpyridine complexes of the type  $[\text{Zn}(\text{tpy-pvp-X})_2]^{2+}$  ( $\text{X} = \text{H}$ ,  $\text{Me}$ , and  $\text{NO}_2$ ) are reported in chapter 5. The Zn(II) complexes show strong absorption bands stretching up to the edge of the visible domain due to ligand→ligand charge transfer (LLCT) transitions and strong emission at room temperature in the visible due to radiative deactivation of  $^3\text{LLCT}$  state having lifetime within 1.0-3.0 ns. The stilbene motifs in the complexes undergo *trans* to *cis* isomerization upon irradiating with UV and visible light accompanied by significant alteration of their absorption, emission, and  $^1\text{H}$  NMR spectral profiles. Apart from the variation of electron donating and electron withdrawing substituent ( $\text{X}$ ), the isomerization studies were also carried out in three different solvents (DCM, MeCN, and DMSO) to further tune their kinetic and thermodynamic parameters. The rate, rate constant and quantum yield of isomerization were estimated in all the solvents. The reverse process (*cis* to *trans*) also occurs very slowly on keeping but could be accelerated upon heating. The emission spectral responses upon successive action of photonic and thermal input were utilized to mimic the function of INHIBIT and IMPLICATION logic gates. DFT and TD-DFT computational investigations were undertaken to visualize their electronic structures, correct assignment of the spectral bands, and mode of isomerization process.

In chapter 6, the terpyridine-stilbene system was utilized to demonstrate multiple advanced logic functions. Upon using the optical response profile of the receptor in presence of selected cations as well as light of specific wavelength, we are able to demonstrate multiple Boolean logic functions such as INHIBIT, IMPLICATION, OR, NOR and NAND as well as various combinations of them. Of particular interest, we



utilized the present system for the construction of security keypad locks and memory devices by maintaining proper sequence of the stimuli and monitoring either absorption or emission spectral response at a specific wavelength as the output signal. In addition to various Boolean logic functions, the present system has also been used to demonstrate fuzzy logic operations for building an infinite-valued logic scheme based the emission spectral responses upon varying the concentration of cationic ( $\text{Fe}^{2+}$  and/or  $\text{Zn}^{2+}$ ) and anionic ( $\text{CN}^-$ ) inputs.

### 1.8 References

- [1] A.J. McConnell, C.S. Wood, P.P. Neelakandan, J.R. Nitschke, Stimuli-responsive metal-ligand assemblies, *Chem. Rev.* 115 (2015) 7729–7793.
- [2] Q. Li (Ed.), *Intelligent Stimuli-Responsive Materials*, John Wiley & Sons, Inc., Hoboken, Nj, 2013.
- [3] R.M. Manez, F. Sancenon, Fluorogenic and chromogenic chemosensors and reagents for anions, *Chem. Rev.* 103 (2003) 4419–4476.
- [4] M. Kurihara, H. Nishihara, Azo- and quinone-conjugated redox complexes-photoand proton-coupled intramolecular reactions based on d- $\pi$  interaction, *Coord. Chem. Rev.* 226 (2002) 125-135.
- [5] C.C. Ko, V.W.W. Yam, Coordination compounds with photochromic ligands: ready tunability and visible light-sensitized photochromism, *Acc. Chem. Res.* 51 (2018) 149-159.
- [6] B. Valeur, *Molecular Fluorescence: Principles and Applications*; Wiley. 2002.
- [7] L. Prodi, F. Bolletta, M. Montalti, Luminescent chemosensors for transition metal ions, *Coord. Chem. Rev.* 205 (2000) 59-83.
- [8] K. Müllen, U. Scherf, *Organic light emitting devices-synthesis, properties and applications*, Wiley, 2006.
- [9] H. N. Kim, W. X. Ren, J. S. Kim, J. Yoon, Fluorescent and colorimetric sensors for detection of lead, cadmium, and mercury ions, *Chem. Soc. Rev.* 41 (2012) 3210-3244.
- [10] M. Irie, Diarylethenes for memories and switches, *Chem. Rev.* 100 (2000) 1685–1716.

- 
- [11] B. L. Feringa, R. A. van Delden, M. K. J. terWiel, Chiroptical molecular switches; Wiley-VCH, 2001.
- [12] H. Tian, S. Yang, Recent progresses on diarylethene based photochromic switches, Chem. Soc. Rev. 33 (2004) 85–97.
- [13] S. Kawata, Y. Kawata, Three-dimensional optical data storage using photochromic materials, Chem. Rev. 100 (2000) 1777–1788.
- [14] H. Rau, H. Dürr, H.B. Laurent (Eds.), Photochromism: Molecules and Systems, Elsevier, Amsterdam, 1990, pp. 165–192.
- [15] K. Ichimura, S. K. Oh, M. Nakagawa, Light-driven motion of liquids on a photoresponsive surface, Science. 288 (2000) 1624–1626.
- [16] R. Sakamoto, S. Kume, H. Nishihara, Visible-light photochromism of triarylamine- or ferrocene-bound diethynylethenes that switches electronic communication between redox sites and luminescence, Chem. Eur. J. 14 (2008) 6978–6986.
- [17] D. H. Waldeck, Photoisomerization dynamics of stilbenes, Chem. Rev. 91 (1991) 415–436.
- [18] J. Bossert, C. Daniel, Trans-cis photoisomerization of the styrylpyridine ligand in  $[\text{Re}(\text{CO})_3(2,2'\text{-bipyridine})(\text{t-4-styrylpyridine})]^+$ : role of the metal-to-ligand charge transfer excited states, Chem. Eur. J. 12 (2006) 4835–4843.
- [19] D.M. Dattelbaum, M.K. Itokazu, N.Y.M. Iha, T.J. Meyer, Mechanism of metal-to-ligand charge transfer sensitization of olefin trans-to-cis isomerization in the *fac*- $[\text{ReI}(\text{phen})(\text{CO})_3(1,2\text{-bpe})]^+$  cation, J. Phys. Chem. A. 107 (2003) 4092–4095.
- [20] S. S. Sun, A. J. Lees, Synthesis, photophysical properties, and photoinduced luminescence switching of trinuclear diimine rhenium(I) tricarbonyl complexes linked by an isomerizable stilbene-like ligand, Organometallics. 21 (2002) 39–49.
- [21] V. W.-W. Yam, Y. Yang, J. Zhang, B. W.-K. Chu, N. Zhu, Synthesis, characterization, and photoisomerization studies of azo- and stilbene-containing surfactant rhenium(I) complexes, Organometallics, 20 (2001) 4911–4918.
- [22] M. Kurihara, H. Nishihara, Azo- and quinone-conjugated redox complexes photo- and proton-coupled intramolecular reactions based on d- $\pi$  interaction, Coord. Chem. Rev. 226 (2002) 125–135.

- [23] H. Nishihara, Multi-mode molecular switching properties and functions of azo-conjugated metal complexes, *Bull. Chem. Soc. Jpn.* 77 (2004) 407–428.
- [24] H. Nishihara, Y.F. Kodansha (Ed.), *Inorganic Photochromism*, Springer, 2007, pp. 239–257.
- [25] S. Kume, H. Nishihara, Metal-based photoswitches derived from photoisomerization, *Struct. bonding (Berlin, Ger.)*. 123 (2006) 79–112.
- [26] C.-C. Ko, V. W.-W. Yam, Transition metal complexes with photochromic ligands—photosensitization and photoswitchable properties, *J. Mater. Chem.* 20 (2010) 2063–2070.
- [27] C.-C. Ko, L.-X. Wu, K. M.-C. Wong, N. Zhu, V. W.-W. Yam, Synthesis, characterization and photochromic studies of spirooxazine- containing 2,2'-bipyridine ligands and their Rhenium(I) tricarbonyl complexes, *Chem.-Eur. J.* 10 (2004) 766-776.
- [28] P. Pal, S. Mukherjee, D. Maity, S. Baitalik, Synthesis, structural characterization, and luminescence switching of diarylethene-conjugated Ru(II)-terpyridine complexes by trans-cis photoisomerization: experimental and DFT/TD-DFT investigation, *Inorg. Chem.* 57 (2018) 5743–5753.
- [29] P. Pal, S. Mukherjee, D. Maity, S. Baitalik, Synthesis, photophysics, and switchable luminescence properties of a new class of ruthenium(II)–terpyridine complexes containing photoisomerizable styrylbenzene units, *ACS Omega.* 3 (2018) 14526–14537.
- [30] P. Pal, T. Ganguly, D. Maity, S. Baitalik, Experimental and theoretical exploration of photophysics and trans-cis photoisomerization of styrylbenzene conjugated terpyridine complexes of Ru(II): strong effect of deprotonation from second coordination sphere, *J. Photochem. Photobiol. A.* 392 (2020) 112409.
- [31] P. Pal, T. Ganguly, A. Sahoo, S. Baitalik, Emission switching in the near-infrared by reversible trans–cis photoisomerization of styrylbenzene-conjugated osmium terpyridine complexes, *Inorganic Chemistry.* 60 (2021) 4869-4882.
- [32] A. P. De Silva, H.Q.N. Gunaratne, C.P. McCoy, A molecular photoionic AND gate based on fluorescent signaling, *Nature.* 364 (1993) 42-44.

- [33] A. P. De Silva, D. P. Fox, A. J. M. Huxley, T. S. Moody, Combining luminescence, coordination and electron transfer for signaling purposes, *Coord. Chem. Rev.* 205 (2000) 41-57.
- [34] E. Katz. Molecular and supramolecular information processing: from molecular switches to logic system, Wiley-VCH Weinheim, Germany, 2012.
- [35] R. Guliyev, S. Ozturk, Z. Kostereli, E. U. Akkaya, From virtual to physical: integration of chemical logic gates, *Angew. Chem Int. Ed.* 50 (2011) 9826-9831.
- [36] S. Karmakar, S. Mardanya, S. Das, S. Baitalik, Efficient deep-blue emitter and molecular-scale memory device based on dipyrindyl-phenylimidazole-terpyridine assembly, *J. Phys. Chem. C.* 119 (2015) 6793-6805.
- [37] E. M. Nolan, S. J. Lippard, Tools and tactics for the optical detection of mercuric ion  
*Chem. Rev.* 108 (2008) 3443-3480.
- [38] F. A. Cotton, G. Wilkinson, *Advanced Inorganic Chemistry*, 5th Ed., Wiley Interscience Publication, John-Wiley & Sons, 1988.
- [39] N. N. Greenwood, A. Earnshaw, *Chemistry of the Elements*: Maxwell Macmillan International Edn, 1989.
- [40] C. Creutz, M. Chou, T.L. Netzel, M. Okumura, N. Sutin, Lifetimes, spectra, and quenching of the excited states of polypyridine complexes of iron(II), ruthenium(II), and osmium(II), *J. Am. Chem. Soc.* 102 (1980) 1309-1319.
- [41] H. Cho, M.L. Strader, K. Hong, L. Jamula, E.M. Gullikson, T.K. Kim, F.M.F. deGroot, J.K. McCusker, R.W. Schoenlein, N. Huse, Ligand-field symmetry effects in Fe(II) polypyridyl compounds probed by transient X-ray absorption spectroscopy, *Faraday Discuss.* 157 (2012) 463–474.
- [42] J.K. McCusker, K.N. Walda, R.C. Dunn, J.D. Simon, D. Magde, D.N. Hendrickson, Subpicosecond 1MLCT  $\rightarrow$  5T2 intersystem crossing of low-spin polypyridyl ferrous complexes, *J. Am. Chem. Soc.* 115 (1993) 298-307.
- [43] A.T. Yeh, C.V. Shank, J.K. McCusker, Ultrafast Electron localization dynamics following photo-induced charge transfer, *Science.* 289 (2000) 935–938.

- [44] S. Baitalik, X. Wang, R.H. Schmehl, A trimetallic mixed Ru(II)/Fe(II) terpyridyl complex with a long-lived excited state in solution at room temperature, *J. Am. Chem. Soc.* 126 (2004) 16304.
- [45] X. Wang, A.D. Guerzo, S. Baitalik, G. Simon, G.B. Shaw, L.X. Chen, R.H. Schmehl, The influence of bridging ligand electronic structure on the photophysical properties of noble metal diimine and triimine light harvesting systems, *Photosynth. Res.* 87 (2006) 83.
- [46] A. Paul, M. Bar, S. Deb, S. Baitalik, Long-lived trimetallic complexes of Fe(II), Ru(II), and Os(II) based on a heteroditopic bipyridine–Terpyridine bridge: synthesis, photophysics, and electronic energy transfer, *Inorg. Chem.* 58 (2019) 10065–10077.
- [47] D. Maity, C. Bhaumik, S. Mardanya, S. Karmakar, S. Baitalik, Light harvesting and directional energy transfer in long-lived Homo- and heterotrimetallic complexes of FeII, RuII, and OsII, *Chem. Eur. J.* 20 (2014) 13242–13252.
- [48] M.S. Wrighton, D.L. Morse, L. Pdungsap, Intraligand lowest excited states in tricarbonylhalobis(styrylpyridine)rhenium(I) complexes, *J. Am. Chem. Soc.* 97 (1975) 2073-2079.
- [49] X. Chen, Q. Zhou, Y. Cheng, Y. Geng, D. Ma, Z. Xie, L. Wang, Synthesis, structure and luminescence properties of zinc (II) complexes with terpyridine derivatives as ligands, *Journal of Luminescence.* 126 (2007) 81-90.
- [50] F. Tessoro, D. Roberto, R. Ugo, M. Pizzotti, Terpyridine Zn(II), Ru(III), and Ir(III) Complexes: The relevant role of the nature of the metal ion and of the ancillary ligands on the second-order nonlinear response of terpyridines carrying electron donor or electron acceptor groups, *Inorg. Chem.* 44 (2005) 8967-8978.
- [51] T. Tsukamoto, K. Takada, R. Sakamoto, R. Matsuoka, R. Toyoda, H. Maeda, T. Yagi, M. Nishikawa, N. Shinjo, S. Amano, T. Iokawa, N. Ishibashi, T. Oi, K. Kanayama, R. Kinugawa, Y. Koda, T. Komura, S. Nakajima, R. Fukuyama, N. Fuse, M. Mizui, M. Miyasaki, Y. Yamashita, K. Yamada, W. Zhang, R. Han, W. Liu, T. Tsubomura, H. Nishihara, Coordination nanosheets based on terpyridine-zinc(II) complexes: as photoactive host materials, *J. Am. Chem. Soc.* 139 (2017) 5359-5366.

- [52] T. Tsukamoto, R. Aoki, R. Sakamoto, R. Toyoda, M. Shimada, Y. Hattori, Y. Kitagawa, E. Nishibori, M. Nakano, H. Nishihara, Mechano-, thermo-, solvato-, and vapochromism in bis(acetato- $k^1O$ )[4'-(4-(diphenylamino)phenyl)]-2,2':6',2''-terpyridine- $k^3N,N',N''$ )zinc(II) and its polymer, *Chem. Commun.* 53 (2017) 9805-9808.
- [53] R. S. H. Liu, Photoisomerization by hula-twist: a fundamental supramolecular photochemical reaction, *Acc. Chem. Res.* 34 (2001) 555-562.
- [54] W. M. Horspool, *Dienes Polydienes*. 2 (2000) 257.
- [55] T. S. Zyubina, V.F. Razumov, A Theoretical Study on the mechanism of iodine-photocatalyzed cis trans isomerization of stilbene, *High Energy Chem.* 35 (2001) 100-106.
- [56] R. S. H. Liu, G. S. Hammond, The case of medium-dependent dual mechanisms for photoisomerization: one-bond-flip and hula-twist, *Proc. Natl. Acad. Sci. U.S.A.* 97 (2000) 11153-11158.
- [57] G.T. Morgan, F.H. Burstall, Dehydrogenation of pyridine by anhydrous ferric chloride, *J. Chem. Soc.* (1932) 20-30.
- [58] E.A. Medlycott, G.S. Hanan, Designing tridentate ligands for ruthenium(II) complexes with prolonged room temperature luminescence lifetimes, *Chem. Soc. Rev.* 34 (2005) 133-142.
- [59] A.K. Pal, G.S. Hanan, Design, synthesis and excited-state properties of mononuclear ru(II) complexes of tridentate heterocyclic ligands, *Chem. Soc. Rev.* 43 (2014) 6184-6197.
- [60] J.A.G. Williams, The coordination chemistry of dipyritylbenzene: N-deficient terpyridine or panacea for brightly luminescent metal complexes, *Chem. Soc. Rev.* 38 (2009) 1783-1801.
- [61] J.A.G. Williams, Photochemistry and photophysics of coordination compounds: platinum. Photochemistry and photophysics of coordination compounds II, *Top. Curr. Chem.* 281 (2007) 205-268.
- [62] E.H. Hofmeier, U.S. Schubert, Recent developments in the supramolecular chemistry of terpyridine-metal complexes, *Chem. Soc. Rev.* 33 (2004) 373-399.

- [63] X.Y. Wang, A. Guerzo, R.H. Schmehl, Preferential solvation of an ILCT excited state in bis (terpyridine-phenylene-vinylene) Zn(II) complexes, *Chem. Commun.* (2002) 2344–2345.
- [64] X.-Y. Wang, A. Del Guerzo, H. Tunuguntla, R.H. Schmehl, Photophysical behavior of Ru(II) and Os(II) terpyridyl phenylene vinylene complexes: perturbation of MLCT state by intra-ligand charge-transfer state, *Res. Chem. Intermed.* 33 (2007) 63–77.
- [65] L.S. Natrajan, A. Toulmin, A. Chew, S.W. Magennis, Two-photon luminescence from polar bis-terpyridyl-stilbene derivatives of Ir(III) and Ru(II), *Dalton Trans.* 39 (2010) 10837–10846.
- [66] A. Sil, D. Giri, S.K. Patra, Arylene–vinylene terpyridine conjugates: highly sensitive, reusable and simple fluorescent probes for the detection of nitroaromatics, *J. Mater. Chem. C Mater. Opt. Electron. Devices* 5 (2017) 11100–11110.
- [67] B. Jędrzejewska, B. Ośmiałowska, R. Zaleśny, Application of spectroscopic and theoretical methods in the studies of photoisomerization and photophysical properties of the push–pull styryl-benzimidazole dyes, *Photochem. Photobiol. Sci.* 15 (2016) 117–128.
- [68] J. Saltiel, D. Papadimitriou, T.S.R. Krishna, Z-N. Huang, G. Krishnamoorthy, S. Laohhasurayotin, R.J. Clark, Photoisomerization of all-cis-1,6-diphenyl-1,3,5-hexatriene in the solid state and in solution: a simultaneous three-bond twist process, *Angew. Chem. Int. Ed.* 48 (2009) 8082–8085.
- [69] Y. Fan, J. Chen, L. Yu, A. Li, G. Zhai, Y. Lei, C. Zhu, Methyl substitution enhanced photoisomerization of trans,trans-1,4-diphenyl-1,3-butadiene: direct Ab initio trajectory surface hopping dynamic simulations, *Phys. Chem. Chem. Phys.* 20 (2018) 2260–2273.
- [70] J.-L. Lin, C.-W. Chen, S.-S. Sun, A.J. Lees, Photoswitching tetranuclear rhenium(I)tricarboxyl diimine complexes with a stilbene-like bridging ligand, *Chem. Commun.* 47 (2011) 6030–6032.
- [71] S.-S. Sun, J.A. Anspach, A.J. Lees, Self-assembly of transition-metal-based macrocycles

- linked by photoisomerizable ligands: examples of photoinduced conversion of tetranuclear-dinuclear squares, *Inorg. Chem.* 41 (2002) 1862–1869.
- [72] K.H. Glusac, I. Ghiviriga, K.A. Abboud, K.S. Schanze, Photophysics and photochemistry of stilbene-containing platinum acetylides, *J. Phys. Chem. B* 108 (2004) 4969–4978.
- [73] J.J. Santos, S.H. Toma, P.M. Lalli, M.F. Riccio, M.N. Eberlin, H.E. Toma, K. Araki, Exploring the coordination chemistry of isomerizable terpyridine derivatives for successful analyses of cis and trans isomers by travelling wave ion mobility mass spectrometry, *Analyst* 137 (2012) 4045–4051.
- [74] Y. Hasegawa, K. Takahashi, S. Kume, H. Nishihara, Complete solid state photoisomerization of bis(dipyrazolylstyrylpyridine)iron(II) to change magnetic properties, *Chem. Commun.* 47 (2011) 6846–6848.
- [75] X.Y. Wang, A. Guerzo, R.H. Schmehl, Preferential solvation of an ILCT excited state in bis (terpyridine-phenylene-vinylene) Zn(II) complexes, *Chem. Commun.* (2002) 2344–2345.
- [76] L.S. Natrajan, A. Toulmin, A. Chew, S.W. Magennis, Two-photon luminescence from polar bis-terpyridyl-stilbene derivatives of Ir(III) and Ru(II), *Dalton Trans.* 39 (2010) 10837–10846.
- [77] J.-P. Lehn, *Supramolecular Chemistry: Concepts and Perspectives*, VCH: Weinheim, 1995.
- [78] J. W. Steed, J. L. Atwood, *Supramolecular Chemistry: a concise introduction*; John Wiley & Sons, Ltd.: Chichester, 2000.
- [79] G. F. Swiegers, T. J. Malefetse, New self-assembled structural motifs in coordination chemistry, *Chem. Rev.* 100 (2000) 3483–3537.
- [80] F. Würthner, C.-C. You, C. Saha-Möller, Metallosupramolecular squares: from structure to function, *Chem. Soc. Rev.* 33 (2004) 133–146.
- [81] G. R. Newkome, T. J. Cho, C. N. Moorefield, P. P. Mohapatra, L. A. Godinez, Towards ordered architectures: self-assembly and stepwise procedures to the hexameric metallomacrocycles  $[\text{Arylbis(terpyridinyl)}_6\text{Fe}^{\text{II}}_{6-n}\text{-Ru}^{\text{II}}_n]$  ( $n=0,2,3,5$ ), *Chem. Eur. J.* 10 (2004) 1493–1500.



- [82] G. R. Newkome, T. J. Cho, C. N. Moorefield, R. Cush, P. S. Russo, L. A. Godinez, M. J. Saunders, P. Mohapatra, Hexagonal terpyridine–ruthenium and –iron macrocyclic complexes by stepwise and self-assembly procedures, *Chem. Eur. J.* 8 (2002) 2946-2954.
- [83] E. C. Constable, A. M. W. C. Thompson, Multinucleating 2,2' : 6',2''-terpyridine ligands as building blocks for the assembly of co-ordination polymers and oligomers, *J. Chem. Soc. Dalton Trans.* (1992) 3467-3475.
- [84] M. Schütte, D. G. Kurth, M. R. Linford, H. Cölfen, H. Möhwald, Metallosupramolecular thin polyelectrolyte films, *Angew. Chem.Int. Ed.* 37 (1998) 2891-2893.
- [85] S. Kelch, M. Rehahn, Synthesis and properties in solution of rodlike, 2,2':6',2''-terpyridine-based ruthenium(II) coordination polymers, *Macromolecules* 32 (1999) 5818-5828.
- [86] G. R. Newkome, E. He, C. N. Moorefield, Suprasupermolecules with novel properties: metallodendrimers, *Chem. Rev.* 99 (1999) 1689-1746.
- [87] U. Ziener, J.-M. Lehn, A. Mourran, M. Möller, Supramolecular assemblies of a bis(terpyridine) ligand and of its [2×2] grid-type Zn<sup>II</sup> and Co<sup>II</sup> complexes on highly ordered pyrolytic graphite, *Chem. Eur. J.* 8 (2002) 951-957.
- [88] C. Piguet, G. Bernardinelli, G. Hopfgartner, Helicates as versatile supramolecular complexes, *Chem. Rev.* 97 (1997) 2005-2062.
- [89] J.-P. Sauvage, J. P. J. Collin, C. Chambron, S. Guillerez, C. Coudret, V. Balzani, F. Barigelletti, L. De Cola, L. Flamigni, Ruthenium(II) and osmium(II) bis(terpyridine) complexes in covalently-linked multi component systems: synthesis, electrochemical behavior, absorption spectra, and photochemical and photophysical properties, *Chem. Rev.* 94 (1994) 993-1019.
- [90] E. Baranoff, J.-P. Collin, L. Flamigni, J.-P. Sauvage, From ruthenium(ii) to iridium(iii): 15 years of triads based on bis-terpyridine complexes, *Chem. Soc. Rev.* 33 (2004) 147-155.
- [91] R. Ziessel, M. Hissler, A. El-Ghayoury, A. Harriman, Multifunctional transition metal complexes: information transfer at the molecular level, *Coord. Chem. Rev.* 178(1998) 1251-1298.

- [92] C. Goze, G. Ulrich, L. Charbonniere, M. Cesario, T. Prange, R. Ziessel, Cation sensors based on terpyridine-functionalized boradiazaindacene, *Chem. Eur.J.* 9 (2003) 3748-3755.
- [93] F. Barigelletti, L. Flamigni, G. Calogero, L. Hammarstrom, J.-P. Sauvage, J.-P. Collin, A functionalized ruthenium(II)-bis-terpyridine complex as a rod-like luminescent sensor of zinc(II), *Chem. Commun.* (1998) 2333-2334.
- [94] H. Aiet-Haddou, S. L. Wiskur, V. M. Lynch, E. V. Anslyn, Achieving large color changes in response to the presence of amino acids: a molecular sensing ensemble with selectivity for aspartate, *J. Am. Chem. Soc.* 123 (2001) 11296-11297.
- [95] W.-L. Wong, K.-H. Huang, P.-F. Teng, D.-S. Lee, H.-L. Kwong, A novel chiral terpyridinemacrocyclic as a fluorescent sensor for enantioselective recognition of amino acid derivatives, *Chem. Commun.* (2004) 384-385.
- [96] M. C. Jimenez-Molero, C. Dietrich-Buchecker, J.-P. Sauvage, Towards artificial muscles at the nanometric level, *Chem. Commun.* (2003) 1613-1616.
- [97] G. Markiewicz, A. Walczak, F. Perlitius, M. Piasecka, J. M. Harrowfield, A. R. Stefankiewicz, Photoswitchable transition metal complexes with azobenzene-functionalized imine-based ligands: structural and kinetic analysis, *Dalton Trans.* 47 (2018) 14254-14262.
- [98] R. H. Holyer, C. D. Hubbard, S. F. A. Kettle, R. G. Wilkiss, The kinetics of replacement reactions of complexes of the transition metals with 2,2',2''-terpyridine, *Inorganic Chemistry*, 5 (1966) 622-625.
- [99] D. N. Bowman, A. Bondarev, S. Mukherjee, E. Jakubikova, Tuning the electronic structure of Fe(II) polypyridines via donor atom and ligand scaffold modifications: a computational study, *Inorg. Chem.* 54 (2015) 8786-8793.
- [100] C. W. Machan, M. Adelhardt, A. A. Sarjeant, C. L. Stern, J. Sutter, K. Meyer, C. A. Mirkin, One-pot synthesis of an Fe(II) bis-terpyridine complex with allosterically regulated electronic properties, *J. Am. Chem. Soc.* 134 (2012) 16921-16924.
- [101] A. K. Sonkar, A. Rai, K. Tripathi, P. Sharma, H. W. Roesky, M. G. B. Drewd, L. Mishra, Abenzimidazolyl terpyridine-Fe<sup>2+</sup> system and its recognition driven molecular model of a traffic light, *Dalton Trans.* 48 (2019) 158-167.

- [102] Y. Liang, D. Strohecker, V. M. Lynch, B. J. Holliday, R. A. Jones, A thiophene-containing conductive metallopolymer using an Fe(II) bis(terpyridine) core for electrochromic materials, *ACS Applied Materials & Interfaces*. 8 (2016) 34568-34580.
- [103] P. C. Mondal, A. K. Manna, Synthesis of heteroleptic terpyridyl complexes of Fe(ii) and Ru(ii): optical and electrochemical studies, *New J. Chem.* 40 (2016) 5775-5781.
- [104] A. K. Pal, B. Laramée-Milette, G. S. Hanan, One- and two-dimensional polymerisation of homoleptic M(II)- complexes of 4'-(3-pyridyl)-2,2';6',2''-terpyridine in the solid state: A combined study by XRD, Cyclic Voltammetry, NMR and UV-vis Spectroscopies, *Inorganica Chimica Acta*. 418(2014) 15-22.
- [105] M. Darari, A. Francés-Monerris, B. Marekha, A. Doudouh, E. Wenger, A. Monari, S. Haacke, P. C. Gros, Towards iron(II) complexes with octahedral geometry: synthesis, structure and photophysical properties, *Molecules*. 25 (2020) 5991.
- [106] B. N. Ghosh, F. Topić, P. K. Sahoo, P. Mal, J. Linnera, E. Kalenius, H. M. Tuononen, K. Rissanen, Synthesis, structure and photophysical properties of a highly luminescent terpyridinediphenylacetylene hybrid fluorophore and its metal complexes, *Dalton Trans.* 44 (2015) 254-267.
- [107] X. Y. Wang, A. DelGuerzo, R. H. Schmehl, Photophysical behavior of transition metal complexes having interacting ligand localized and metal-to-ligand charge transfer states, *J. Photochem. Photobiol. C*. 5 (2004) 55-77.
- [108] Q. Zhang, X. Tian, Z. Hu, C. Brommesson, J. Wu, H. Zhou, S. Li, J. Yang, Z. Sun, Y. Tian, K. Uvdal, A series of Zn(II) terpyridine complexes with enhanced two-photon-excited fluorescence for in vitro and in vivo bioimaging, *J. Mater. Chem. B*. 3 (2015) 7213.
- [109] Y. Tang, M. Kong, X. Tian, J. Wang, Q. Xie, A. Wang, Q. Zhang, H. Zhou, J. Wu, Y. Tian, A series of terpyridine-based zinc(II) complexes assembled for third-order nonlinear optical responses in the near-infrared region and recognizing lipid membranes, *J. Mater. Chem. B*. 5 (2017) 6348-6355.

- [110] X. Bi, Y. Pang, Optical response of terpyridine ligands to zinc binding: a close look at the substitution effect by spectroscopic studies at low temperature, *J. Phys. Chem. B.* 13 (2016) 3311-3317.
- [111] J. Li, R. Liu, J. Jiang, X. Liang, L. Huang, G. Huang, H. Chen, L. Pan, Z. Ma, Zinc(II) terpyridine complexes: substituent effect on photoluminescence, Antiproliferative Activity, and DNA Interaction, *Molecules* 2019, 24, 4519.
- [112] M. Presselt, B. Dietzek, M. Schmitt, J. Popp, A. Winter, M. Chipper, C. Friebe, U.S. Schubert, Zinc(II) bisterpyridine complexes: the influence of the cation on the  $\pi$ -conjugation between terpyridine and the lateral phenyl substituent, *J. Phys. Chem. C.* 112 (2008) 18651-18660.
- [113] H. Wang, F. Cai, D. Feng, L. Zhou, D. Li, Y. Wei, Z. Feng, J. Zhang, J. He, Y. Wu, Synthesis, crystal structure, photophysical property and bioimaging application of a series of Zn(II) terpyridine complexes, *Journal of Molecular Structure*, 1194 (2019) 157-162.
- [114] V. W. W. Yam, V. C. Y. Lau, L. X. Wu, Synthesis, photophysical, photochemical and electrochemical properties of rhenium(I) diimine complexes with photoisomerizable pyridyl-azo, -ethenyl or -ethyl ligands, *J. Chem. Soc. Dalton Trans.* (1998) 1461-1468.
- [115] S. Kume, M. Kurihara, H. Nishihara, Coordination-synchronized trans-cis photoisomerization of bipyridylazobenzene driven by a Cu(II)/Cu(I) redox change, *Inorg. Chem.* 42 (2003) 2194-2196.
- [116] H. Nishihara, Combination of redox- and photochemistry of azo-conjugated metal complexes, *Coord. Chem. Rev.* 249 (2005) 1468-1475.
- [117] T. Yutaka, M. Kurihara, Nishihara, H. Synthesis and physical properties of a  $\pi$ -conjugated ruthenium(II) dinuclear complex involving an azobenzene-bridged bis(terpyridine) ligand, *Mol. Cryst. Liq. Cryst.* 343 (2000) 193-198.
- [118] T. Yutaka, I. Mori, M. Kurihara, J. Mizutani, K. Kubo, S. Furusho, K. Matsumura, N. Tamai, H. Nishihara, Synthesis, characterization, and photochemical properties of azobenzene-conjugated Ru(II) and Rh(III) bis(terpyridine) complexes, *Inorg. Chem.* 40 (2001) 4986-4995.

- [119] T. Yutaka, M. Kurihara, K. Kubo, H. Nishihara, Novel photoisomerization behavior of Rh binuclear complexes involving an azobenzene-bridged bis(terpyridine) ligand. Strong effects of counterion and solvent and the induction of redox potential shift, *Inorg. Chem.* 39 (2000) 3438-3439.
- [120] S. Kume, M. Kurihara, H. Nishihara, Reversible *trans*–*cis* photoisomerization of azobenzene-attached bipyridine ligands coordinated to cobalt using a single UV light source and the Co(III)/Co(II) redox change, *Chem. Commun.* (2001) 1656-1657.
- [121] R. Sakamoto, M. Murata, S. Kume, H. S. ampei, M. Sugimoto, H. Nishihara, Photo-controllable tristability of a dithiolato-bipyridine-Pt(II) complex molecule containing two azobenzene moieties, *Chem. Commun.* (2005) 1215-1217.
- [122] M. E. Moustafa, M. S. McCready, R.J. Puddephatt, Switching by photochemical *trans*–*cis* isomerization of azobenzene substituents in organoplatinum complexes, *Organometallics* 31 (2012) 6262-6269.
- [123] A. O. T. Patrocínio, N. Y. M. Iha, Photoswitches and luminescent ligidity sensors based on fac-[Re(CO)<sub>3</sub>(Me<sub>4</sub>phen)(L)]<sup>+</sup>, *Inorg. Chem.* 47 (2008) 10851-10857.
- [124] K. P. S. Zanoni, N. Y. M. Iha, Reversible *trans* ⇌ *cis* photoisomerizations of [Re(CO)<sub>3</sub>(ph<sub>2</sub>phen)(stpyCN)]<sup>+</sup> towards molecular machines, *Dalton Trans.* 46 (2017) 9951-9958.
- [125] R. C. Amaral, N. Y. M. Iha, Molecular engineered rhenium(I) carbonyl complexes to promote photoisomerization of coordinated stilbene-like ligands in the visible region, *Dalton Trans.* 47 (2018) 13081-13087.
- [126] R. C. Amaral, L. S. Matos, K. P. S. Zanoni, N. Y. M. Iha, Photoreversible molecular motion of stpyCN coordinated to fac-[Re(CO)<sub>3</sub>(NN)]<sup>+</sup> complexes, *J. Phys. Chem. A* 122 (2018) 6071-6080.
- [127] L. A. Faustino, A. E. H. Machado, A. O. T. Patrocínio, Photochemistry of fac-[Re(CO)<sub>3</sub>(dcbH<sub>2</sub>)(*trans*-stpy)]<sup>+</sup>: New insights on the isomerization mechanism of coordinated stilbene-like ligands, *Inorg. Chem.* 57 (2018) 2933-2941.
- [128] O. S. Wenger, L. M. Henling, M. W. Day, J. R. Winkler, H. B. Gray, Photoswitchable luminescence of rhenium(I) tricarbonyl diimines, *Inorg. Chem.* 43 (2004) 2043-2048.

\*\*\*\*\*

## ***Chapter 2***

**Photophysics and luminescence switching  
properties of a series of photochromic  
styrylbenzene-terpyridine conjugate:  
experimental and DFT/TD-DFT  
investigation**

## 2.1 Introduction

There is widespread interest in the design of photochemical molecular devices whose properties could be modulated upon interaction with external stimuli like light, pH, and chemical species [1-5]. Among the different stimuli, light is the most convenient as it is a clean energy source and required wavelength of light can easily be used for excitation of a particular molecular fragment. Photoswitchable molecules have widely been used for optical data storage, optoelectronics, and molecular switching devices [6-12]. Among the photoswitchable materials, photochromic compounds capable of undergoing light-induced reversible transformation between two forms having distinguishable color are well known for their promising application in many areas [13-21]. Some of the most common processes involved in photochromism are pericyclic reactions, *trans-cis* isomerizations, intramolecular hydrogen or other group transfer, dissociation processes and electron transfers (oxidation-reduction). Diarylethenes, azobenzenes and spiropyrans have been found to be representative photochromic molecules that undergo a reversible photoreaction between two states, with discrete conversion and fairly high stability [13-21].

With regard to our recent interest in designing photo-switchable and photochromic molecule [22-28], we designed in this work a series of terpyridine derivatives {2-(6-(pyridin-2-yl)-4-(4styrylphenyl)pyridin-2-yl)pyridine}, wherein a terpyridine moiety is connected to differently substituted stilbene units at its 4'-position [27]. Since the discovery of 2,2':6',2''-terpyridine (tpy) in 1932, a variety of terpyridine derivatives functionalized at different positions have been designed and are found to be useful building blocks in both organic and inorganic supramolecular chemistry [29-38]. In the design strategy, a stilbene moiety has also been covalently coupled to the 4'-position of the terpyridine which is capable of undergoing *trans-cis* isomerization upon interaction with light. Stilbene-like compounds constitute an important class of photoactive molecules and one of the best-known *cis/trans* isomerization model systems [39-46]. Covalent coupling of a stilbene moiety and electron accepting terpyridine moiety through  $\pi$ -linker induces intramolecular charge transfer (ICT) character in tpy-pvp-X. As the donor-acceptor system has been proven to be an effective approach to adjust the optical properties, a variety of electron-donating and electron-accepting groups (X = H, Me, Cl,

NO<sub>2</sub>, and Ph) have been incorporated in tpy-pvp-X to tune their photophysical properties. In the present work, we will thoroughly discuss reversible *trans* → *cis* photoisomerization behaviors of the said ICT-sensitive fluorophoric receptors in different solvents of varying polarity. As the receptors contain free pyridine groups with a lone pair of electrons residing on each of them, we will also be interested to investigate the influence of protons on the photochromic and photo-isomerization behaviors of the compounds. Detailed kinetic and thermodynamic aspects of the photo-isomerization process will also be addressed in the present study. Interestingly, the compounds exhibit photochromic behavior in both of their free form as well as in their different protonated forms. Finally, detailed computation work was also performed on both the *trans* and *cis* forms of the compounds by employing DFT and TD-DFT methods to acquire deeper insight about their electronic structures as well as proper assignment of the experimentally observed absorption and emission bands.

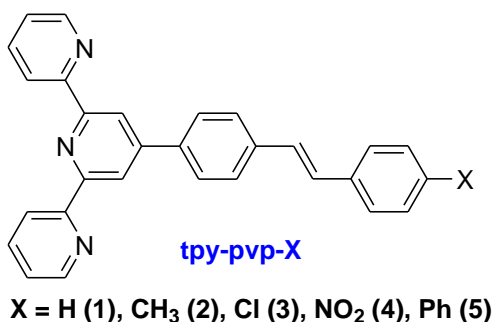


**Chart 2.1.** Chemdraw structures of the compounds under present investigation.

## 2.2 Experimental

### 2.2.1 Materials

The chemicals and solvents were procured either from Sigma or from local vendors.

### 2.2.2 Synthesis of the styrylbenzene-terpyridine conjugates

A general procedure as described below was adopted for the synthesis of the styrylbenzene-terpyridine conjugates.



*Synthesis of 4'-(4-Styryl-phenyl)-[2,2';6',2'']terpyridine (tpy-pvp-H) (1)*

A mixture of 4'-(2,2':6',2''-terpyridyl-4)-benzyltriphenylphosphonium bromide (tpy-PhCH<sub>2</sub>PPh<sub>3</sub>Br) (0.33 g, 0.5 mmol) and benzaldehyde (0.053 g, 0.5 mmol) was thoroughly dissolved in dry dichloromethane and was cooled to 0°-5° C under nitrogen protection. To the mixture, t-BuOK (0.12 g, 1.0 mmol) was added slowly and the resulting mixture was stirred magnetically for ~12 h. The volume of the resulting solution was reduced and dichloromethane was completely removed by the addition of methanol. The crude compound was washed with water, dried in air and purified by silica gel column chromatography using 10:1 (v/v) CHCl<sub>3</sub>-MeOH mixture. The compound was finally purified by recrystallization from CHCl<sub>3</sub>-MeOH (1:2, v/v) mixture. Yield: 114 mg (55%). Elemental anal. Calcd. for C<sub>29</sub>H<sub>21</sub>N<sub>3</sub>: C, 84.64; H, 5.14; N, 10.21. Found: C, 84.60; H, 5.20; N, 10.08. <sup>1</sup>H NMR (300 MHz, CDCl<sub>3</sub>, δ/ppm): 8.77(s, 2H, H3'), 8.76-8.73(m, 2H, H6), 8.68(d, 2H, *J* = 7.9 Hz, H3), 7.95-7.84(m, 4H, 2H8+2H4), 7.66(d, 2H, *J* = 7.4, H7), 7.56(d, 2H, *J* = 8.0, H11), 7.41-7.30(m, 4H, 2H12+2H5), 7.28-7.23(m, 2H, 1H13+1H9), 7.19(d, 1H, *J* = 2.4, H10). <sup>13</sup>C NMR (75 MHz, CDCl<sub>3</sub>, δ /ppm): 156.23, 155.91, 149.62, 149.07, 138.10, 137.36, 137.13, 136.82, 129.51, 128.67, 127.94, 127.77, 127.54, 126.98, 126.58, 123.76, 121.34, 118.49. ESI-MS (positive, CHCl<sub>3</sub>): *m/z* 412.11 (100%) [(tpy-pvp-H+H)]<sup>+</sup>.

*4'-[4-(2-p-Tolyl-vinyl)-phenyl]-[2,2';6',2'']terpyridine (tpy-pvp-Me) (2)*

Yield: 56% (120 mg). Elemental anal. Calcd. for C<sub>30</sub>H<sub>23</sub>N<sub>3</sub>: C, 84.67; H, 5.44; N, 9.87. Found: C, 84.60; H, 5.52; N, 9.91. <sup>1</sup>H NMR (300 MHz, CDCl<sub>3</sub>, δ / ppm): 8.76 (s, 4H, 2H3'+2H6), 8.69-8.66(d, 2H, 2H3, *J* = 7.5), 7.94-7.89 (m, 4H, 2H8+2H4), 7.65-7.62(d, 2H, 2H7, *J* = 7.7), 7.46-7.44(d, 2H, 2H11, *J* = 7.4), 7.38-7.36(t, 2H, 2H5, *J* = 6), 7.20-7.08(m, 4H, 2H12+H9+H10), 2.37 (s, 3H, -CH<sub>3</sub>). <sup>13</sup>C NMR (75 MHz, CDCl<sub>3</sub>, δ / ppm): 156.26, 155.90, 149.65, 149.07, 138.31, 137.72, 137.12, 136.80, 134.35, 129.45, 129.39, 127.50, 126.94, 126.85, 126.50, 123.74, 121.33, 118.46. ESI-MS (positive, CHCl<sub>3</sub>): *m/z* 426.16(100%) [(tpy-pvp-Me+H)]<sup>+</sup>.

*4'-[4-[2-(4-Chloro-phenyl)-vinyl]-phenyl]-[2,2';6',2'']terpyridine (tpy-pvp-Cl) (3)*

Yield: 120 mg (54%). Elemental anal. Calcd. for C<sub>29</sub>H<sub>20</sub>N<sub>3</sub>Cl: C, 78.10; H, 4.52; N, 9.42. Found: C, 78.05; H, 4.57; N, 9.38. <sup>1</sup>H NMR (300 MHz, CDCl<sub>3</sub>, δ / ppm): 8.76(s, 2H, H3'), 8.72(nr, 2H, H6), 8.69-8.65 (m, 2H, H3), 7.94-7.89(m, 2H, H8), 7.88(t, 1H, *J*

= 2.1, H4), 7.85(t, 1H,  $J$  = 2.2, H4), 7.79(d, 1H,  $J$  = 8.3, H7), 7.64(d, 1H,  $J$  = 8.3, H7), 7.47(d, 1H,  $J$  = 8.5, H11), 7.37-7.32(m, 3H, 1H11+2H5), 7.26( nr, 1H, H12), 7.21(nr, 1H, H12), 7.13(nr, 1H, H10), 6.70-6.57(m, 1H, H9). ESI-MS (positive, CHCl<sub>3</sub>):  $m/z$  446.09(100%) [(tpy-pvp-Cl+H)]<sup>+</sup>.

### 4'-[4-[2-(4-Nitro-phenyl)-vinyl]-phenyl]-[2,2';6',2'']terpyridine(tpy-pvp-NO<sub>2</sub>) (**4**)

Yield: 128 mg (56%). Elemental anal. Calcd. for C<sub>29</sub>H<sub>20</sub>N<sub>4</sub>O<sub>2</sub>: C, 76.30; H, 4.41; N, 12.27. Found: C, 76.38; H,4.46; N, 12.11. <sup>1</sup>H NMR (300 MHz, CDCl<sub>3</sub>,  $\delta$  / ppm): 8.76(s, 2H, H3'), 8.71(nr, 2H, H6), 8.68-8.65(m, 2H, H3), 8.22(d, 1H,  $J$  = 8.2, H12), 8.11(d, 1H,  $J$  = 8.1, H12), 7.95(d, 1H,  $J$  = 7.8, H8), 7.91-7.85( m, 2H, H4), 7.80(d, 1H,  $J$  =7.9, H8), 7.68-7.63(m, 2H, 1H7+1H11), 7.42-7.18(m, 4H, 1H11+2H5+ 1H7), 6.86(d, 1H,  $J$  = 12.2, H10), 6.68(d, 1H,  $J$  = 12.3, H9). <sup>13</sup>C NMR (75 MHz, CDCl<sub>3</sub>,  $\delta$ /ppm): 156.06, 155.93, 149.36, 149.24, 149.07, 146.78, 146.60, 143.94, 143.57, 138.54, 137.87, 136.83, 133.13, 132.46, 129.62, 129.36, 128.66, 127.68, 127.50, 127.38, 126.88, 124.07, 123.83, 123.63, 121.29, 118.56, 118.46). ESI-MS (positive, CHCl<sub>3</sub>):  $m/z$  457.09 (100%) [(tpy-pvp-NO<sub>2</sub>+H)]<sup>+</sup>.

### 4'-(4-Styryl-biphenyl)-[2,2';6',2'']terpyridine (tpy-pvp-Ph) (**5**)

Yield: 134 mg (55%). Elemental anal. Calcd. for C<sub>35</sub>H<sub>25</sub>N<sub>3</sub>: C, 86.01; H, 5.16; N, 8.61. Found: C, 86.11; H,4.57; N, 8.55. ESI-MS (positive, CHCl<sub>3</sub>):  $m/z$  488.21 (100%) [(tpy-pvp-Ph+H)]<sup>+</sup>. Due to solubility limitation of the ligand, its concentration level could not be reached to the required level for recording any NMR spectrum.

## 2.2.3 Physical measurements

### 2.2.3.1 Determination of *trans-cis* photoisomerization rate constant and quantum yields

A 1-cm light path length quartz cell was used for the photoisomerization measurements. The concentration of the compounds was maintained in the range of  $1 \times 10^{-5}$  M-  $2 \times 10^{-5}$  M, and the solution was thoroughly degassed with N<sub>2</sub> before photoirradiation and stirred magnetically during *trans*-to-*cis* isomerization. Isomerization studies were carried out in a photocatalytic reactor designed by Lelesil Innovative Systems by using both ultraviolet and visible light source. The rate constant of the isomerization process was evaluated from the absorbance titration data using equation 1 [47-48]

$$\ln\{(A_0 - A_\infty)/(A_t - A_\infty)\} = k_{\text{iso}} t \quad (1)$$

where  $A_0$ ,  $A_t$ , and  $A_\infty$  indicate the absorbance at time  $t = 0$ ,  $t$ , and  $\infty$ , respectively.  $k_{\text{iso}}$  is the rate constant of isomerization and  $t$  is the required time for the completion of the isomerization process. Both  $k_{\text{iso}}$  and  $A_\infty$  were estimated by nonlinear least-square method. The intensity of the light source was  $\sim 0.11$  W. Quantum yields ( $\phi$ ) of the isomerization process were obtained by using the equation 2 [49],

$$\phi = (\phi I_0/V)(1-10^{-\text{Abs}}) \quad (2)$$

where  $I_0$  is the photon flux at the front of the cell,  $V$  is the volume of the solution. and Abs is the initial absorbance.

### 2.2.3.2 Computational methods

All calculations were performed with the Gaussian 09 program [50] employing the DFT method with Becke's three-parameter hybrid functional and Lee-Yang-Parr's gradient corrected correlation functional B3LYP level and of theory [51-52] using 6-31G as well as 6-31g(d) basis set for the compounds. Geometries were fully optimized using the criteria of the respective programs. To compute the UV-vis transitions of the compounds, the time-dependent DFT (TD-DFT) scheme was adopted considering the ground state geometries optimized in solution phase [53-54]. The excitation energies, computed in DCM were simulated by PCM model [55- 56]. The geometries of the lowest energy singlet states of the compounds were also optimized in DCM by using TD-DFT method and employing the PCM models to calculate the emission energies. Orbital and fractional contribution analysis was done with Gauss View [57] and Gauss Sum 2.1 [58].

Actually, we have checked three functional (B3LYP, BPV86, and CAM-B3LYP) and two basis sets (6-31G and 6-31G (d)) in our calculations and we have taken that combination where the calculated data match well with the experimental data. While calculating the *trans*-form of the compounds, B3LYP along with 6-31G (d) yield better results compared with other possible combinations. On the other hand, BPV86 along with 6-31G yield better results for *cis* compared with other combinations.

### 2.3 Results and discussion

#### 2.3.1 Synthesis and characterization

The photo-switchable compounds, tpy-pvp-X (X = H, Me, Cl, NO<sub>2</sub>, and Ph) were synthesized by stoichiometric reaction between 4'-(2,2':6',2''-terpyrididyl-4)-benzyltriphenyl phosphonium bromide (tpyPhCH<sub>2</sub>PPh<sub>3</sub>Br) and different 4-substituted benzaldehyde in dichloromethane in the temperature range of 0-5° C under argon protection and thoroughly characterized by our recent reported procedure [27]. <sup>1</sup>H NMR spectra indicate all the four compounds exist in the *trans* form (Fig. 2.1).

#### 2.3.2 Computational investigations

Geometry optimization of tpy-pvp-X (X = H, Me, Cl, NO<sub>2</sub> and Ph) in both of their *trans* and *cis* forms as well as their mono-protonated forms were done by employing Gaussian 09 program in dichloromethane medium (Fig. 2.2). Three nitrogen atoms of the terpyridine moiety in each compound adopt transoid conformation to minimize inter electronic repulsions among the lone pairs on the nitrogen atoms.

Frontier molecular orbital sketch indicates that with few exceptions, the low energy HOMOs are localized mainly on the styrylbenzene moiety and terminal *p*-substituted phenyl group, while the LUMOs are localized predominantly on the terpyridine and to some extent also on styrylbenzene group in all forms of the compounds (Fig. 2.3-2.5 and Tables 2.1-2.3).

In nitro derivative, the lowest energy LUMO is localized mostly on nitro-benzene moiety because of strong electron withdrawing nature of the nitro group (Figs. 2.3c-2.5c and Table 2.3). In the monoprotonated form, the contributions of terpyridine moiety in the LUMOs are generally increased to a great extent. On going from the *trans* to the *cis* form, the composition of HOMOs and LUMOs varies to a very small extent. The asymmetric charge distribution within the molecular backbone in their *trans* and *cis* form as well as *trans* form of the protonated species can be observed through their electric surface potential plots (ESP) as shown in Fig. 2.6.

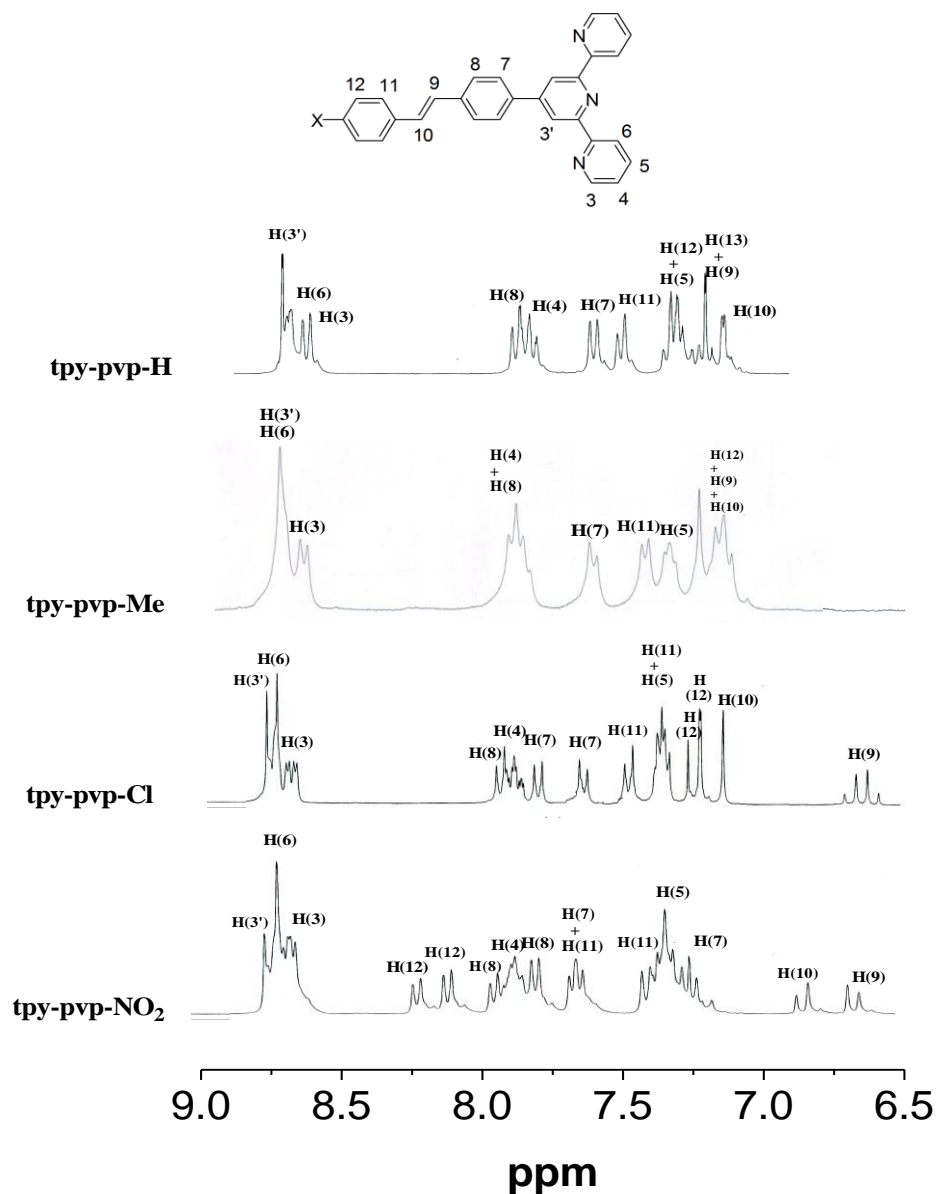


**Fig. 2.1.**  $^1\text{H}$  NMR spectra of **tpy-pvp-X** (X= H, Me, Cl,  $\text{NO}_2$ ) in  $\text{CDCl}_3$ .

TD-DFT calculations were also performed and the calculated absorption spectra together with their experimental spectra are displayed in [Fig. 2.7-2.8](#). For better clarity, we also presented the calculated results in sticks form. Relevant spectral data along with the assignment of different peaks are summarized in [Tables 2.4-2.5](#).

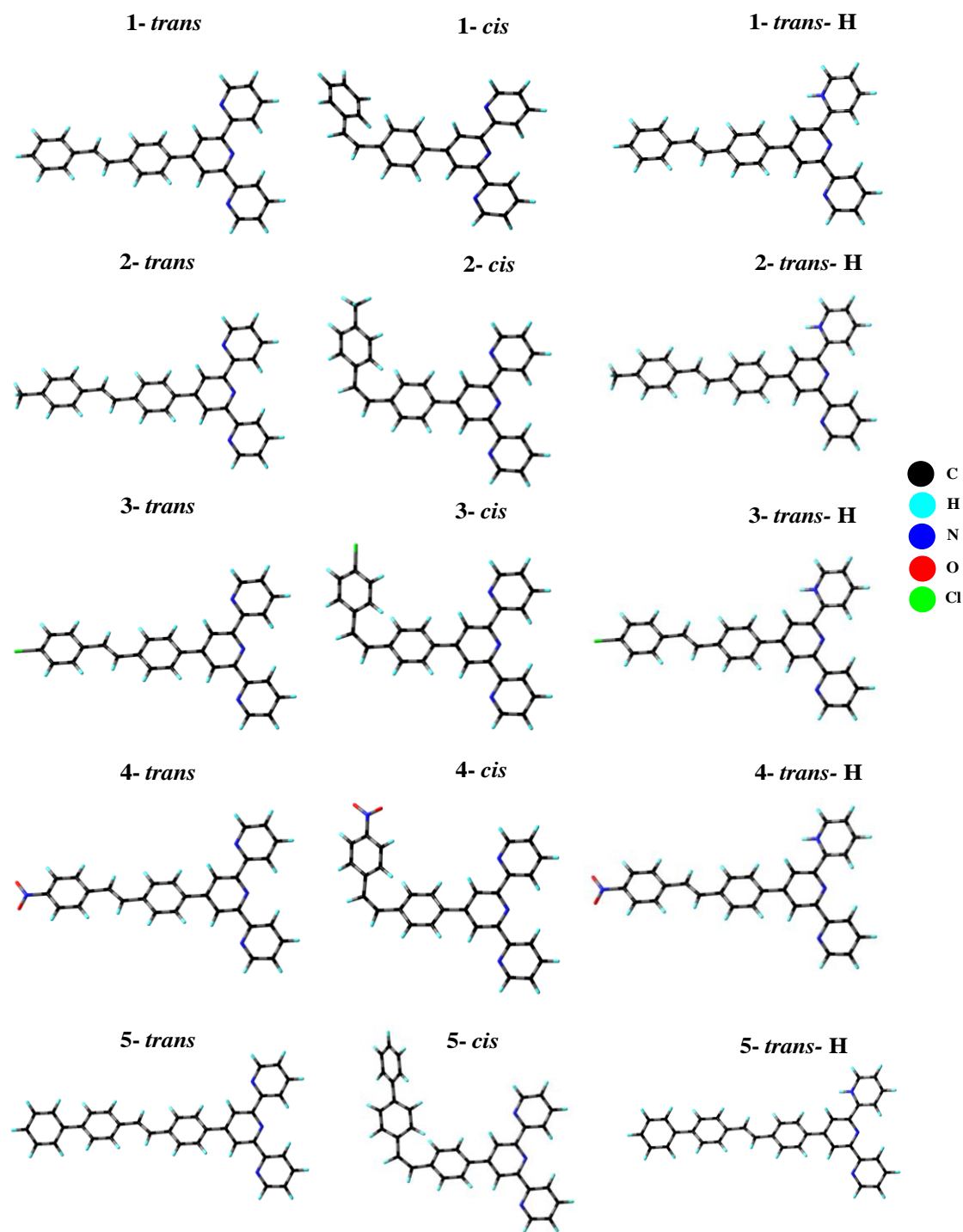


**Fig. 2.2.** Ground state optimized geometries of the *trans*-, *cis*- and mono-protonated *trans* forms of tpy-pvp-X in dichloromethane.

**Table 2.1** Selected MOs along with their energies and compositions in the ground state for tpy-pvp-H (**1**) and its mono-protonated form [(tpy-pvp-H)+H<sup>+</sup>] in dichloromethane.

MO	[(tpy-pvp-H)]							
	Energy/ev		% Compositions					
	<i>trans</i>	<i>cis</i>	<i>trans</i>			<i>cis</i>		
			Terpy	Vinyl-phenyl	benzal	Terpy	Vinyl-phenyl	benzal
LUMO+3	-0.69	-1.52	95.21	2.33	2.46	92.75	3.30	3.94
LUMO+2	-1.26	-1.88	59.38	24.07	16.55	43.87	35.63	20.49
LUMO+1	-1.58	-2.29	99.15	0.84	0.00	99.24	0.75	0.00
LUMO	-1.91	-2.44	42.02	44.45	13.51	61.19	32.89	5.90
HOMO	-5.64	-5.27	6.42	62.78	30.00	6.55	63.13	30.31
HOMO-1	-6.33	-5.73	99.75	0.24	0.00	98.54	1.41	0.04
HOMO-2	-6.85	-5.77	46.45	11.68	41.86	99.59	0.39	0.00
HOMO-3	-6.85	-5.92	78.82	13.00	8.18	99.74	0.13	0.12
MO	[(tpy-pvp-H)]+H <sup>+</sup>							
	% Compositions							
	Energy/ev		<i>trans</i>					
			Terpy	Vinyl-phenyl	benzal	Terpy	Vinyl-phenyl	benzal
LUMO+3				-1.74		50.30	34.47	15.21
LUMO+2				-2.17		89.28	8.49	2.21
LUMO+1				-2.43		73.99	21.43	4.56
LUMO				-3.19		99.44	0.50	0.04
HOMO				-5.88		5.01	64.46	30.51
HOMO-1				-7.05		99.52	0.42	0.04
HOMO-2				-7.07		0.05	0.13	99.80
HOMO-3				-7.33		16.13	59.32	24.53

**Table 2.2** Selected MOs along with their energies and compositions in the ground state of tpy-pvp-Me (**2**) and its mono-protonated form [(tpy-pvp-Me)+H<sup>+</sup>] in dichloromethane.

MO	[(tpy-pvp-Me)]							
	Energy/ev		% Compositions					
	<i>trans</i>	<i>cis</i>	<i>trans</i>			<i>cis</i>		
			Terpy	Vinyl-phenyl	Me-Benz	Terpy	Vinyl-phenyl	Me-Benz
LUMO+3	-0.68	-1.64	2.38	2.38	95.24	93.14	3.41	3.43
LUMO+2	-1.23	-2.07	57.65	25.85	16.49	49.90	31.96	18.13
LUMO+1	-1.57	-2.42	99.15	0.84	0.00	99.15	0.08	0.00
LUMO	-1.88	-2.64	44.71	42.89	12.39	54.21	37.38	8.40
HOMO	-5.54	-5.13	5.61	58.51	35.87	5.65	57.71	36.63
HOMO-1	-6.32	-5.78	99.75	0.24	0.00	99.66	0.32	0.00
HOMO-2	-6.85	-5.87	46.36	26.50	27.14	98.41	1.56	0.02
HOMO-3	-6.89	-6.03	0.12	0.16	99.72	99.49	0.24	0.26
MO	[(tpy-pvp-Me)]+H <sup>+</sup>							
	% Compositions							
	Energy/ev		<i>trans</i>					
			Terpy	Vinyl-phenyl	Me-Benz	Terpy	Vinyl-phenyl	Me-Benz
LUMO+3				-1.71		49.76	35.50	14.72
LUMO+2				-2.16		89.34	8.55	2.10
LUMO+1				-2.42		76.00	19.90	4.09
LUMO				-3.19		99.46	0.49	0.04
HOMO				-5.77		4.46	55.72	39.81
HOMO-1				-7.03		0.00	0.05	99.93
HOMO-2				-7.04		99.36	0.53	0.10
HOMO-3				-7.21		15.44	44.22	40.33



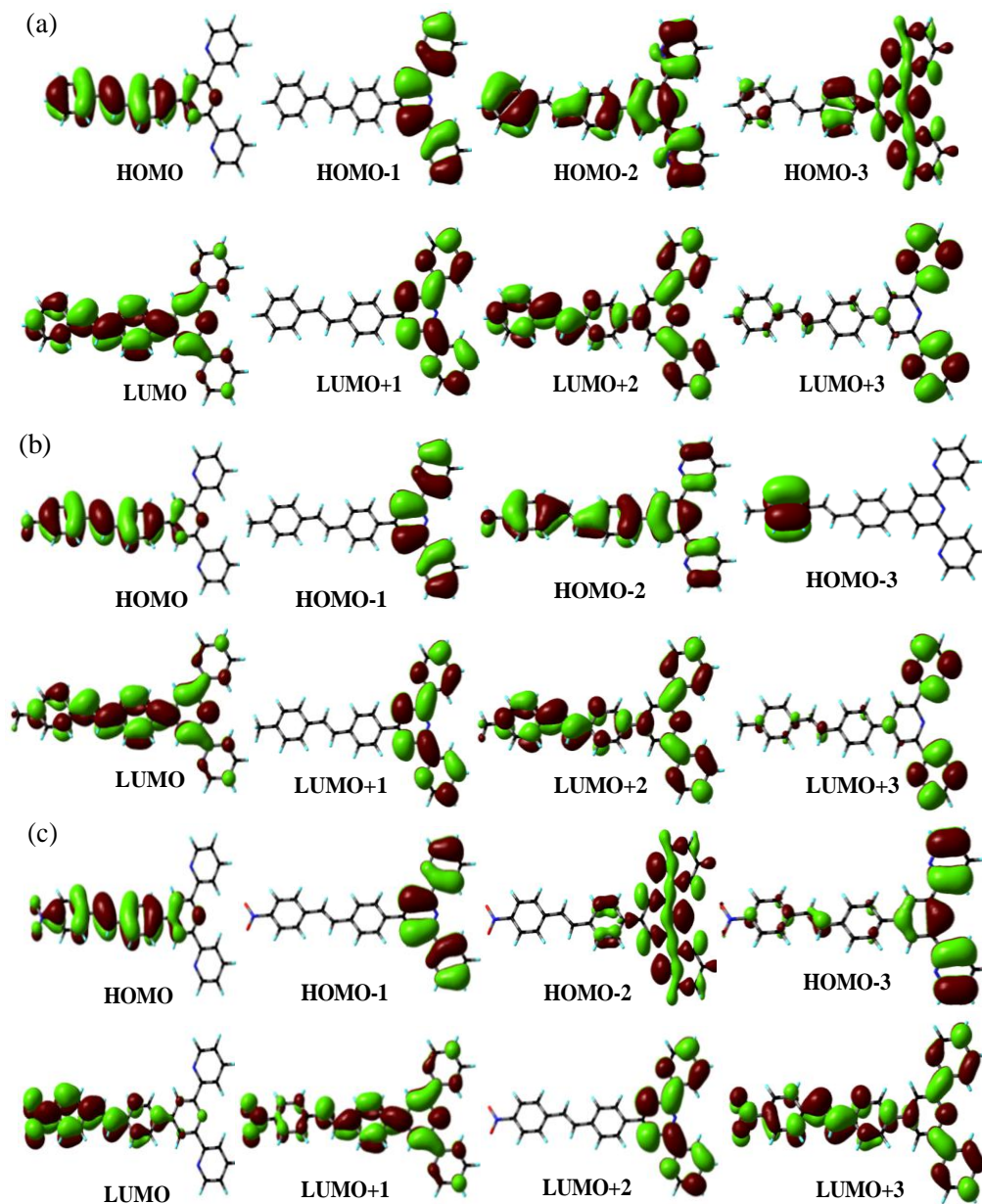


**Fig. 2.3.** Schematic drawings of the selective frontier molecular orbitals of *trans* form of tpy-pvp-H (a), tpy-pvp-CH<sub>3</sub> (b) and tpy-pvp-NO<sub>2</sub> (c) in the ground state in dichloromethane.



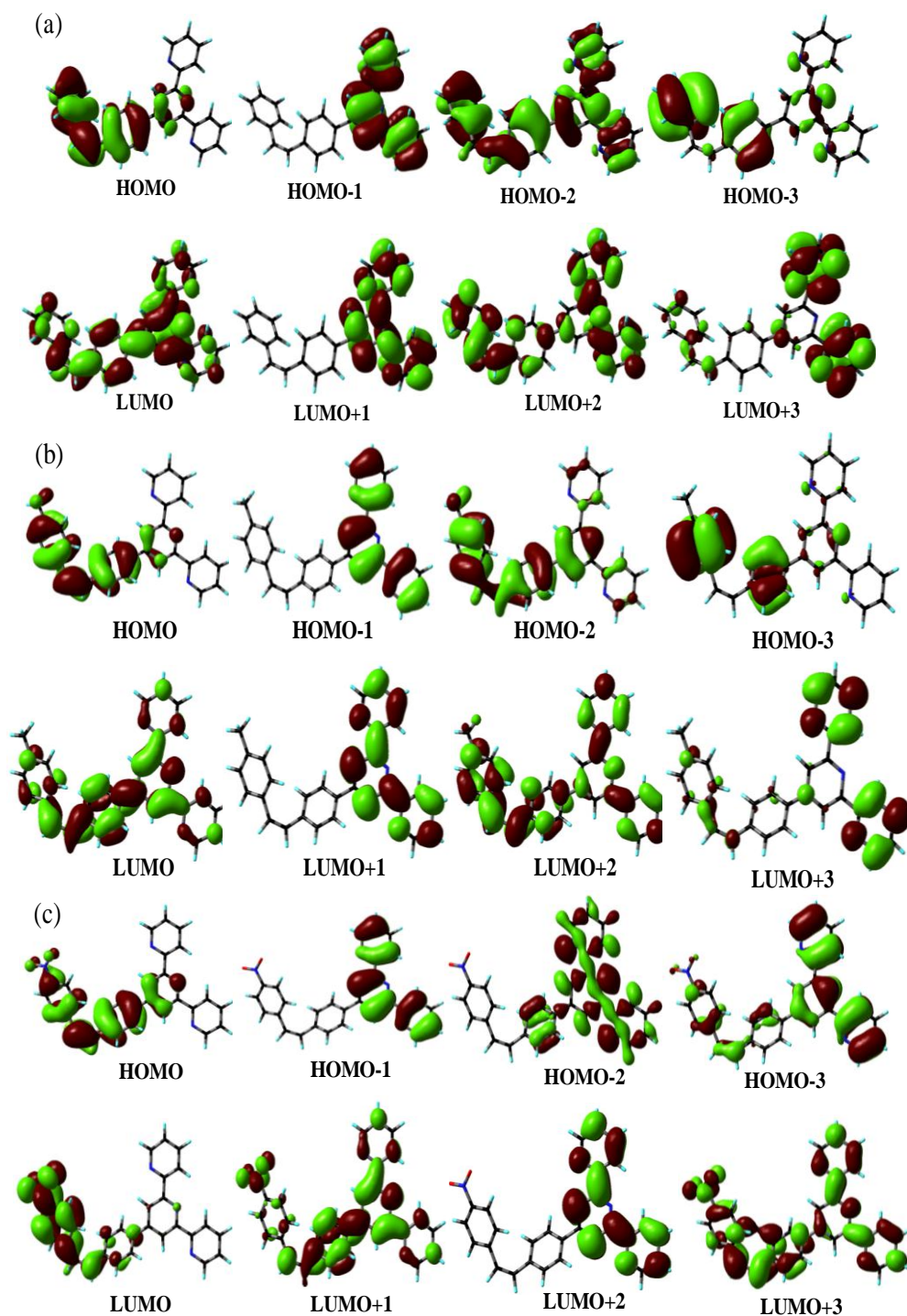


**Fig. 2.4.** Schematic drawings of the selective frontier molecular orbitals of *cis* form of tpy-pvp-H (a), tpy-pvp-CH<sub>3</sub> (b) and tpy-pvp-NO<sub>2</sub> (c) in the ground state in dichloromethane.

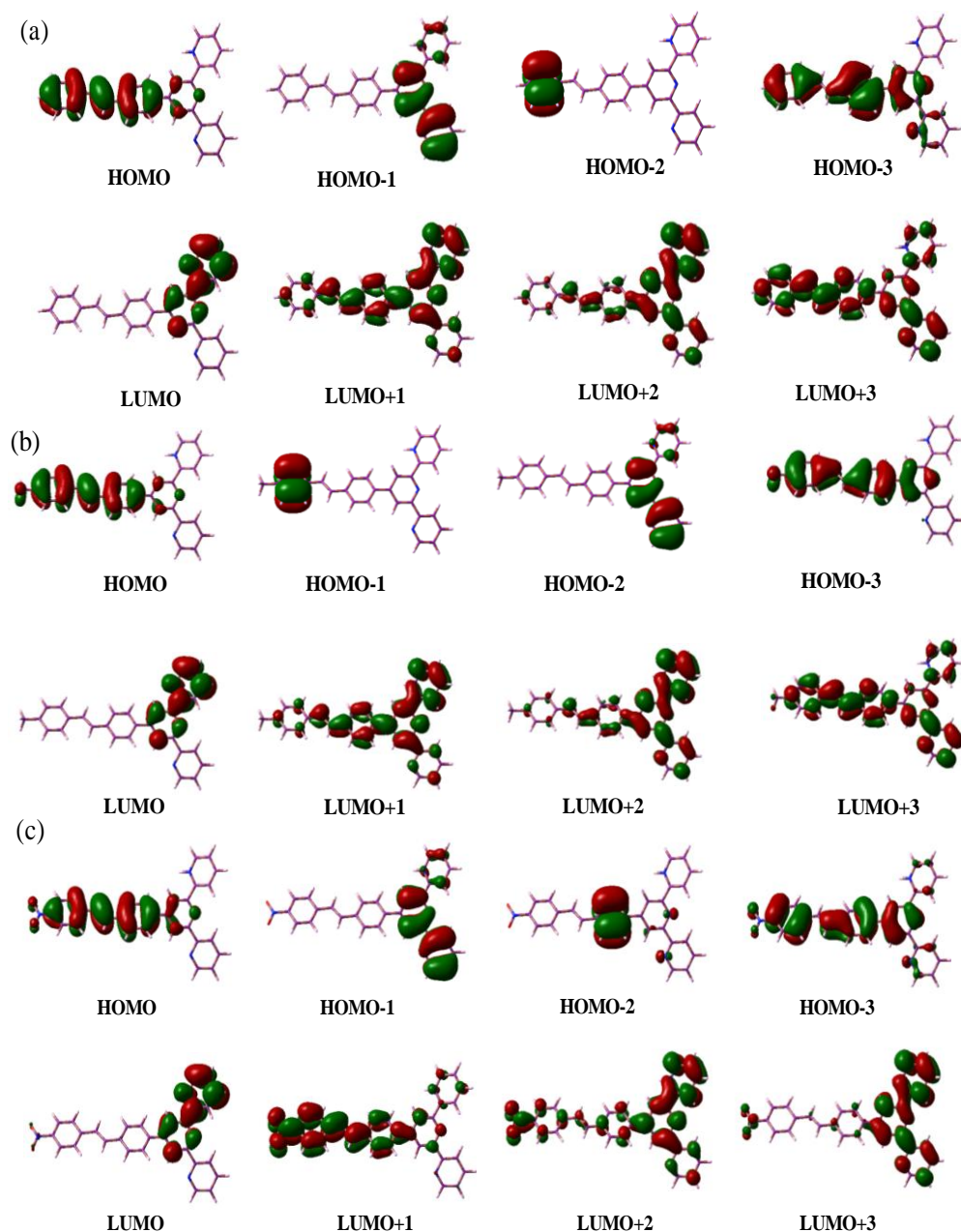


**Fig. 2.5.** Schematic drawings of the selective frontier molecular orbitals of mono-protonated *trans* form of tpy-pvp-H (a), tpy-pvp-CH<sub>3</sub> (b) and tpy-pvp-NO<sub>2</sub> (c) in the ground state in dichloromethane.

**Table 2.3** Selected MOs along with their energies and compositions in the ground state for tpy-pvp-NO<sub>2</sub> (**4**) and its mono-protonated form [(tpy-pvp-NO<sub>2</sub>)+H<sup>+</sup>] in dichloromethane.

MO	[(tpy-pvp-NO <sub>2</sub> )]							
	Energy/ev		% Compositions					
	<i>trans</i>	<i>cis</i>	<i>trans</i>			<i>cis</i>		
			Terpy	Vinyl-phenyl	Nitro-Benz	Terpy	Vinyl-phenyl	Nitro-Benz
LUMO+3	-1.19	-1.13	48.75	28.97	22.28	44.25	34.51	21.24
LUMO+2	-1.60	-1.59	99.13	0.87	0.00	99.10	8.80	0.01
LUMO+1	-1.79	-1.78	52.29	28.20	19.51	59.34	29.60	11.05
LUMO	-2.76	-2.71	2.88	19.56	77.56	1.55	13.08	85.36
HOMO	-5.95	-6.08	8.81	67.54	23.65	10.09	70.46	19.44
HOMO-1	-6.35	-6.34	99.78	0.22	0.00	99.77	0.22	0.00
HOMO-2	-6.96	-6.95	93.67	6.32	0.00	90.13	9.57	0.30
HOMO-3	-7.00	-6.94	3.83	3.35	92.34	87.38	6.91	5.70
MO	[(tpy-pvp-NO <sub>2</sub> )]+H <sup>+</sup>							
	% Compositions							
	Energy/ev		<i>trans</i>					
			Terpy	Vinyl-phenyl	Nitro-Benz			
LUMO+3		-0.86	94.20	2.77	3.01			
LUMO+2		-1.05	74.69	7.42	17.88			
LUMO+1		-1.67	12.08	25.88	62.03			
LUMO		-1.96	97.52	1.45	1.02			
HOMO		-7.51	6.11	68.29	25.59			
HOMO-1		-8.43	99.80	0.18	0.01			
HOMO-2		-8.93	3.41	96.11	0.46			
HOMO-3		-9.09	25.90	32.78	41.31			

The energy level diagrams of HOMOs and LUMOs that are involved in the lowest energy band in all the three forms (free *trans*-, mono-protonated *trans*- and *cis*) of the compounds are displayed in Fig. 2.9. The calculated results indicate that with few exceptions, the two low energy absorption bands arise due to combination of both intra-ligand charge transfer (ICT) and  $\pi-\pi^*$  transitions. But the contribution of ICT is greater than  $\pi-\pi^*$  for the lowest energy band, while the contribution of  $\pi-\pi^*$  transition is greater than ICT for the next higher energy band. It is of interest to note that in case of nitro derivative, both bands possess the higher ICT character and in particular, the bands in the *cis* form are predominantly of ICT character. The calculated lowest energy band in the mono-protonated *trans* form of the compounds (except nitro-derivative) is found to be

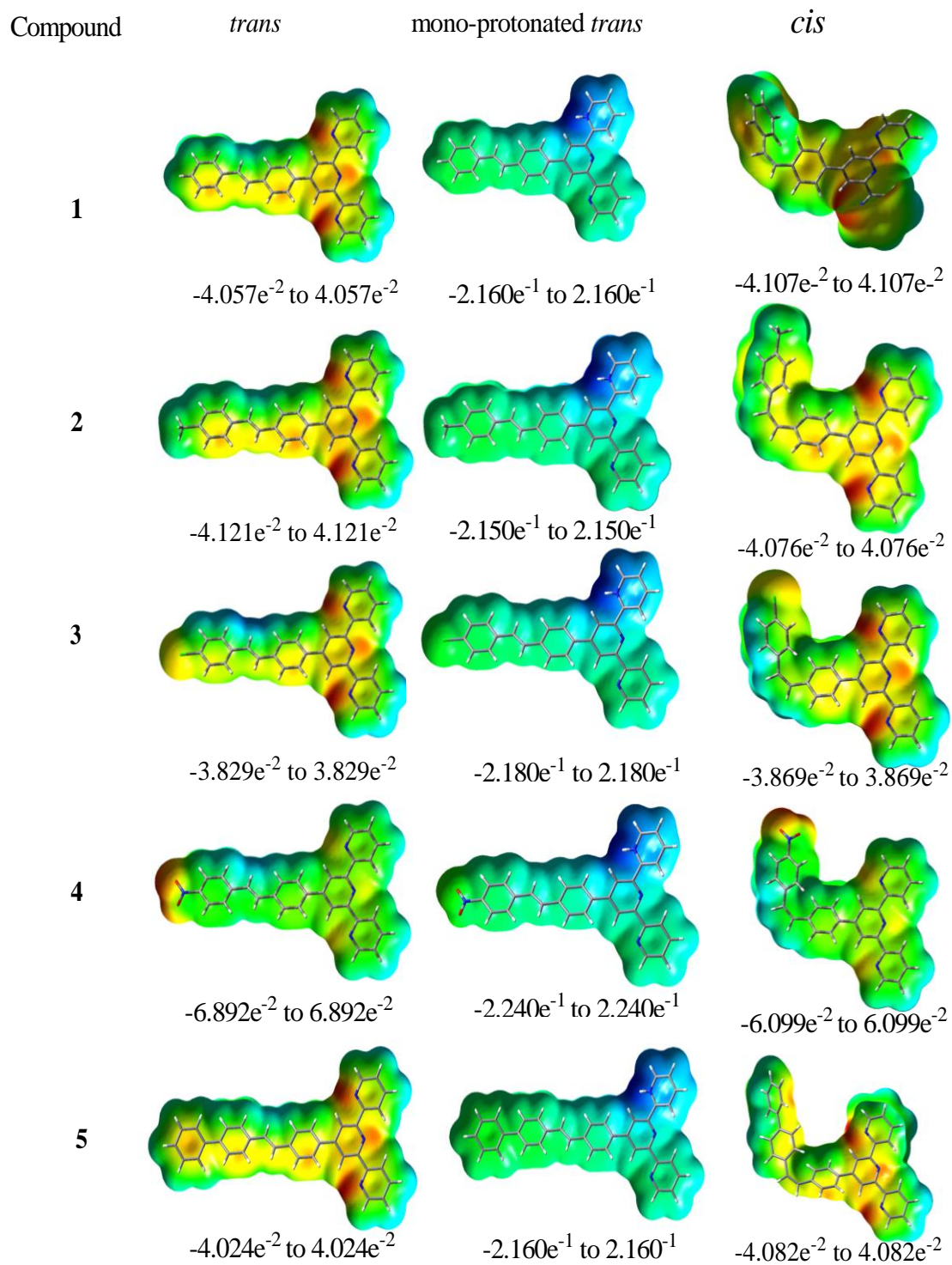


**Fig. 2.6.** ESP plots of *trans*-, mono-protonated *trans*- and *cis* forms of tpy-pvp-X (1-5).



**Table 2.4** Selected low energy calculated and experimental absorption bands of tpy-pvp-H (**1**) and tpy-pvp-Me (**2**) in dichloromethane.

Excited state	$\lambda_{cal}/nm$	Oscillator strength(f)	$\lambda_{expt}/nm$ ( $\epsilon_{expt}/M^{-1}cm^{-1}$ )	Key transitions	Character
<i>trans</i> [(tpy-pvp-H)]					
S <sub>1</sub>	367	1.47	330(38800)	H→L(99%)	ICT, $\pi-\pi^*$
S <sub>4</sub>	307	0.38	289(25800)	H-3→L+2(95%)	ICT
<i>cis</i> [(tpy-pvp-H)]					
S <sub>1</sub>	443	0.38	382(10200)	H→L (88%), H→L+2 (10%)	ICT, $\pi-\pi^*$
S <sub>6</sub>	363	0.41	316(26500)	H→L+2 (73%), H→L+3 (12%)	ICT, $\pi-\pi^*$
S <sub>29</sub>	288	0.36	294(25400)	H-8→L+1(20%), H-7→L+1(15%), H-1→L+3 (17%), H-9→LUMO (6%), H-5→L+1 (7%)	$\pi-\pi^*$
<i>trans</i> [(tpy-pvp-H)+H] <sup>+</sup>					
S <sub>2</sub>	399	0.91	413(10100)	H→L+1 (98%)	ICT
S <sub>3</sub>	369	0.18	327(25600)	H→L+2 (92%), H-1→L (5%)	ICT, $\pi-\pi^*$
S <sub>9</sub>	325	0.63	289(23300)	H→L+3 (96%)	ICT, $\pi-\pi^*$
S <sub>14</sub>	288	0.29	243(12800)	H-6→L (65%), H-1→L+2 (5%), H-4→L+1 (7%)	$\pi-\pi^*$
<i>trans</i> [(tpy-pvp-Me)]					
S <sub>1</sub>	375	1.48	335(48100)	H→L(99%)	ICT, $\pi-\pi^*$
S <sub>4</sub>	311	0.45	286(29100)	H→L+2(96%)	ICT, $\pi-\pi^*$
<i>cis</i> [(tpy-pvp-Me)]					
S <sub>1</sub>	458	0.37	390(15100)	H→L(89%), H→L+2(9%)	
S <sub>5</sub>	372	0.39	321(37100)	H→L+2(72%), H→L+3(17%)	ICT, $\pi-\pi^*$
S <sub>29</sub>	288	0.44	293(31500)	H-7→L+1(47%), H-1→L+2(10%), H-1→L+3 (15%), H-9→L (6%)	ICT, $\pi-\pi^*$
<i>trans</i> [(tpy-pvp-Me)+H] <sup>+</sup>					
S <sub>2</sub>	411	0.89	420(15800)	H→L+1 (98%)	ICT, $\pi-\pi^*$
S <sub>9</sub>	331	0.55	332(47400)	H→L+3 (80%), H-5→L (8%), H-4→L (9%)	ICT, $\pi-\pi^*$
S <sub>14</sub>	288	0.24	290(41600)	H-6→L (53%), H-4→L+1 (19%), H-2→L+2 (98%)	$\pi-\pi^*$

considerably red-shifted compared with their respective free forms (Fig. 2.7). This is due to enhanced styrylbenzene→terpyridine ICT character as the contribution of LUMO increased substantially upon protonation. In case of nitro, the LUMO is primarily localized in nitrobenzene unit in both of their free and protonated form, although the contribution differs. Thus, in nitro-compound, the ICT is primarily due to styrylbenzene→nitrobenzene charge transfer. Interestingly, the calculated lowest energy band in the *cis* form of the compounds is again profoundly red-shifted (with the exception

of nitro) relative to both free *trans* and mono-protonated *trans* form of the compounds (Fig. 2.7-2.8).

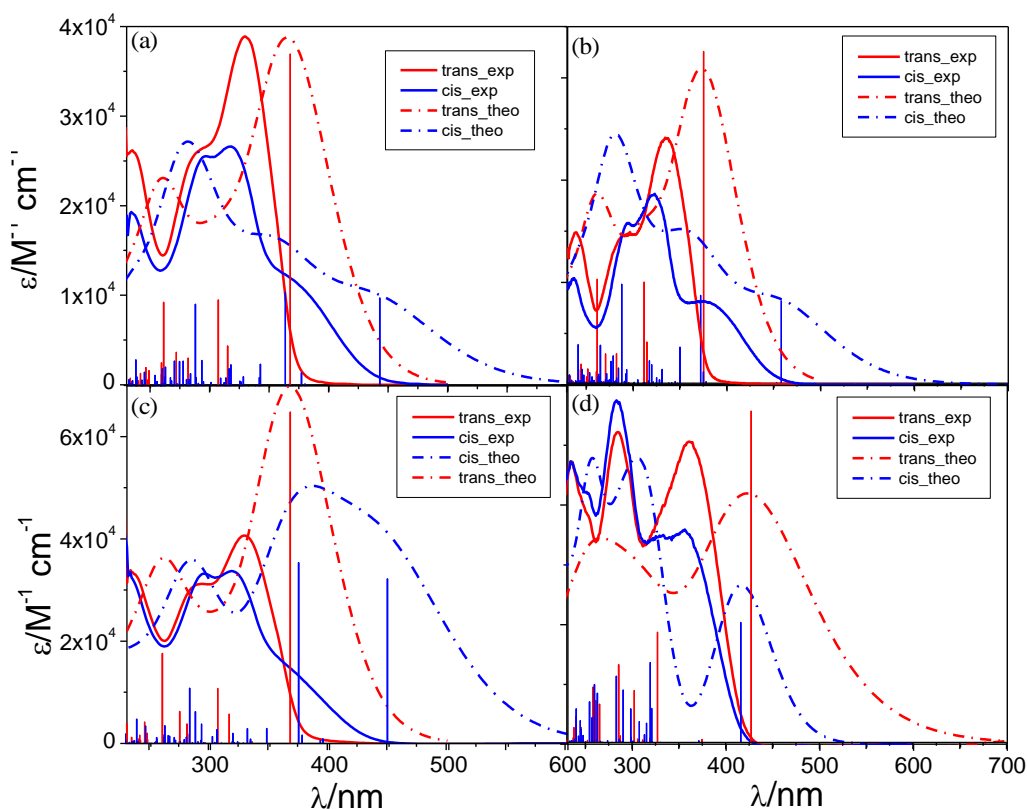


**Fig. 2.7.** Overlay of the calculated (dotted lines) and experimental (solid lines) absorption spectra of *trans* (red) and *cis* (blue) form of **tpy-pvp-X** with X= H (a), Me (b), Cl (c) and NO<sub>2</sub> (d) in dichloromethane. Calculated results are also presented in the sticks form.

We also performed optimization of the geometries of the compounds (both *cis* and *trans* and protonated *trans* forms) in their lowest singlet ( $S_1$ ) excited state by adopting TD-DFT methodology to understand their emission characteristics (Fig. 2.10 and Table 2.6). The calculated emission maximum in all forms is summarized in Table 2.6. It is observed that calculated emission maximum gets red-shifted on going from the *trans* to the *cis* form along with considerable decrease in intensity in each case. By considering the participation of LUMOs and HOMOs, it appears that the emitting excited state of the

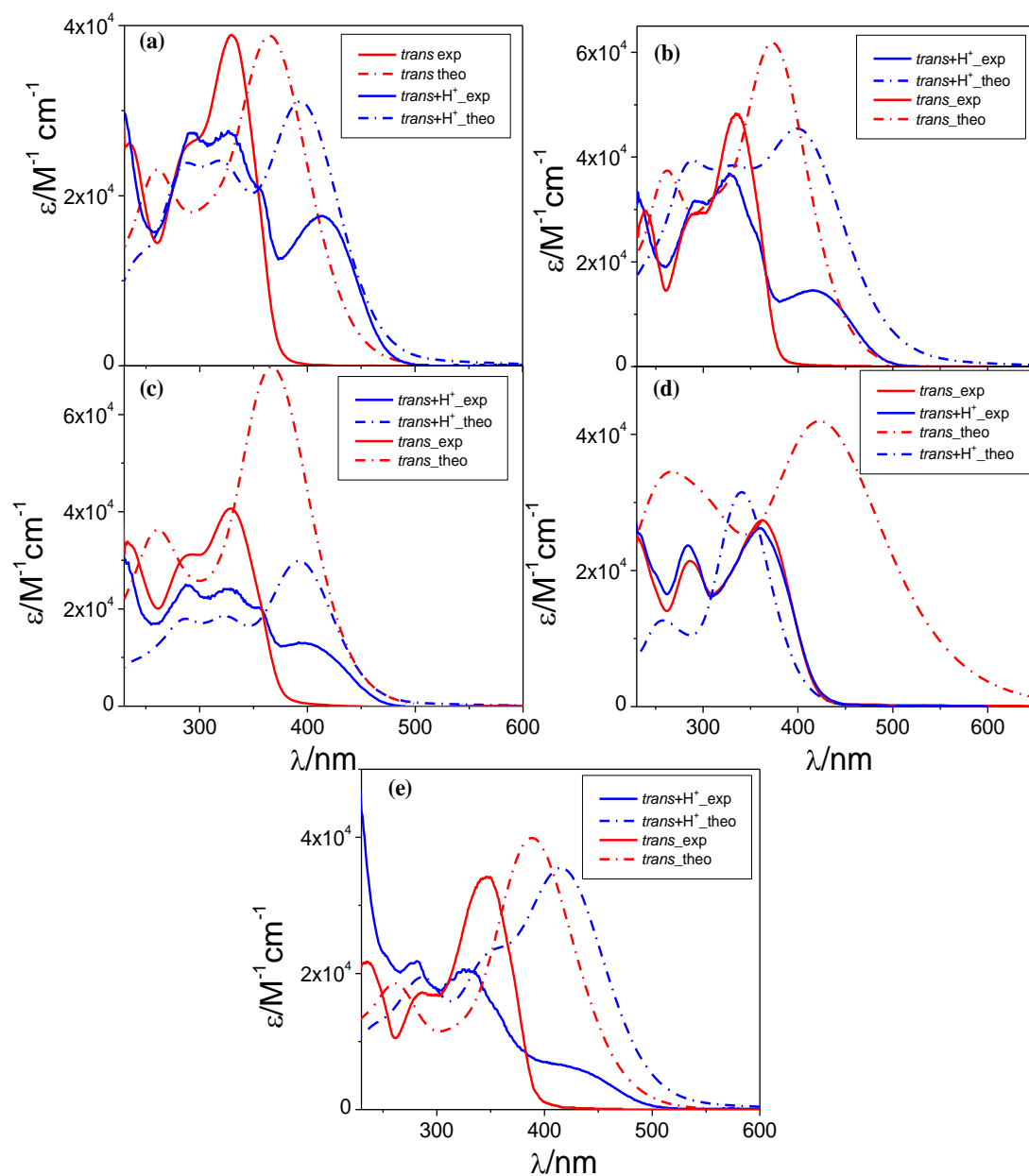


**Fig. 2.8.** Calculated and experimental absorption spectra of free *trans*- and mono-protonated *trans* forms of tpy-pvp-X, with X=H (a), Me (b), Cl (c), NO<sub>2</sub> (d) and Ph(e) in dichloromethane.

## Chapter 2

**Table 2.5** Selected low energy calculated and experimental absorption bands of tpy-pvp-Cl (**3**), tpy-pvp-NO<sub>2</sub> (**4**) and tpy-pvp-Ph (**5**) in dichloromethane.

Excited state	$\lambda_{cal}/nm$	Oscillator strength (f)	$\lambda_{expt}/nm$ ( $\epsilon_{expt}/M^{-1}cm^{-1}$ )	Key transitions	Character
<i>trans</i> [(tpy-pvp-Cl)]					
S <sub>1</sub>	368	1.68	325(42100)	H→L(99%)	ICT, $\pi-\pi^*$
S <sub>4</sub>	307	0.28	287(39100)	H-3→L+2(95%)	$\pi-\pi^*$ , ICT
<i>cis</i> [(tpy-pvp-Cl)]					
S <sub>1</sub>	450	0.83	373(15200)	H→L (79%), H→L+2 (19%)	ICT, $\pi-\pi^*$
S <sub>6</sub>	376	0.91	317(38000)	H→L (16%), H→L+2 (66%), H-4→L (4%), H→L+3 (6%)	ICT, $\pi-\pi^*$
S <sub>32</sub>	284	0.28	294(39400)	H-9→L(56%), H-7→L+1(11%), H-1→L+3 (10%), H-4→L+1 (8%)	$\pi-\pi^*$
<i>trans</i> [(tpy-pvp-Cl)+H] <sup>+</sup>					
S <sub>2</sub>	396	1.10	396(16500)	H→L+1 (98%)	ICT, $\pi-\pi^*$
S <sub>4</sub>	363	0.14	356(29500)	H→L+2 (97%)	ICT
S <sub>8</sub>	325	0.59	326(36100)	H→L+3 (95%)	ICT, $\pi-\pi^*$
S <sub>13</sub>	288	0.31	288(37600)	H-6→L (69%), H-1→L+2 (11%), H-3→L+1 (5%)	$\pi-\pi^*$
<i>trans</i> [(tpy-pvp-NO <sub>2</sub> )]					
S <sub>1</sub>	426	1.36	361(25320)	H→L(99%)	$\pi-\pi^*$ , ICT
S <sub>4</sub>	326	0.45	284(26040)	H→L+1(92%)	ICT, $\pi-\pi^*$
<i>cis</i> [(tpy-pvp-NO <sub>2</sub> )]					
S <sub>1</sub>	416	0.49	320(22700)	H→L (99%)	ICT
S <sub>3</sub>	319	0.33	292(25000)	H-4→L (10%), H-2→L(28%), H→L+1(49%)	ICT, $\pi-\pi^*$
<i>trans</i> [(tpy-pvp-NO <sub>2</sub> )+H] <sup>+</sup>					
S <sub>1</sub>	341	1.87	360(26200)	H→L+1 (82%), H→L (7%)	ICT
S <sub>4</sub>	288	0.33	285(23640)	H-1→L(58%), H→L(19%), H-6→L (8%)	$\pi-\pi^*$
S <sub>12</sub>	247	0.37	235(25060)	H-7→L (10%), H-6→L (20%), H-1→L+3 (14%)	$\pi-\pi^*$
<i>trans</i> [(tpy-pvp-Ph)]					
S <sub>1</sub>	389	1.94	346(35700)	H→L(99%)	ICT, $\pi-\pi^*$
S <sub>3</sub>	322	0.31	280(14700)	H→L+2(97%)	ICT, $\pi-\pi^*$
S <sub>16</sub>	266	0.29	236(18400)	H-2→L+1 (66%), H-6→L+1 (9%), H-1→L+2 (8%)	$\pi-\pi^*$
<i>cis</i> [(tpy-pvp-Ph)]					
S <sub>1</sub>	471	0.46	391(9800)	H→L(89%), H→L+2(8%)	ICT, $\pi-\pi^*$
S <sub>3</sub>	391	0.51	330(22100)	H→L+2(83%), H→L(8%)	ICT, $\pi-\pi^*$
S <sub>32</sub>	296	0.34	292(15700)	H-10→L(42%), H→L+5(18%), H-3→L(7%), H-3→L+2 (8%)	$\pi-\pi^*$
<i>trans</i> [(tpy-pvp-Ph)+H] <sup>+</sup>					
S <sub>2</sub>	421	1.23	425(11380)	H→L+1 (97%)	ICT, $\pi-\pi^*$
S <sub>6</sub>	344	0.66	331(22100)	H→L+3 (96%)	ICT, $\pi-\pi^*$
S <sub>20</sub>	287	0.31	283(15700)	H-8→L (70%), H-3→L+2 (13%), H→L+4 (7%)	$\pi-\pi^*$

compounds are predominantly  $^1\pi-\pi^*$  in character, although some ICT character is also involved therein. In addition to the presence of an intense emission bands within the range of 398-420 nm corresponding to the free *trans* forms, the protonated compounds also exhibit a very weak band in the longer wavelength region (495-591 nm).



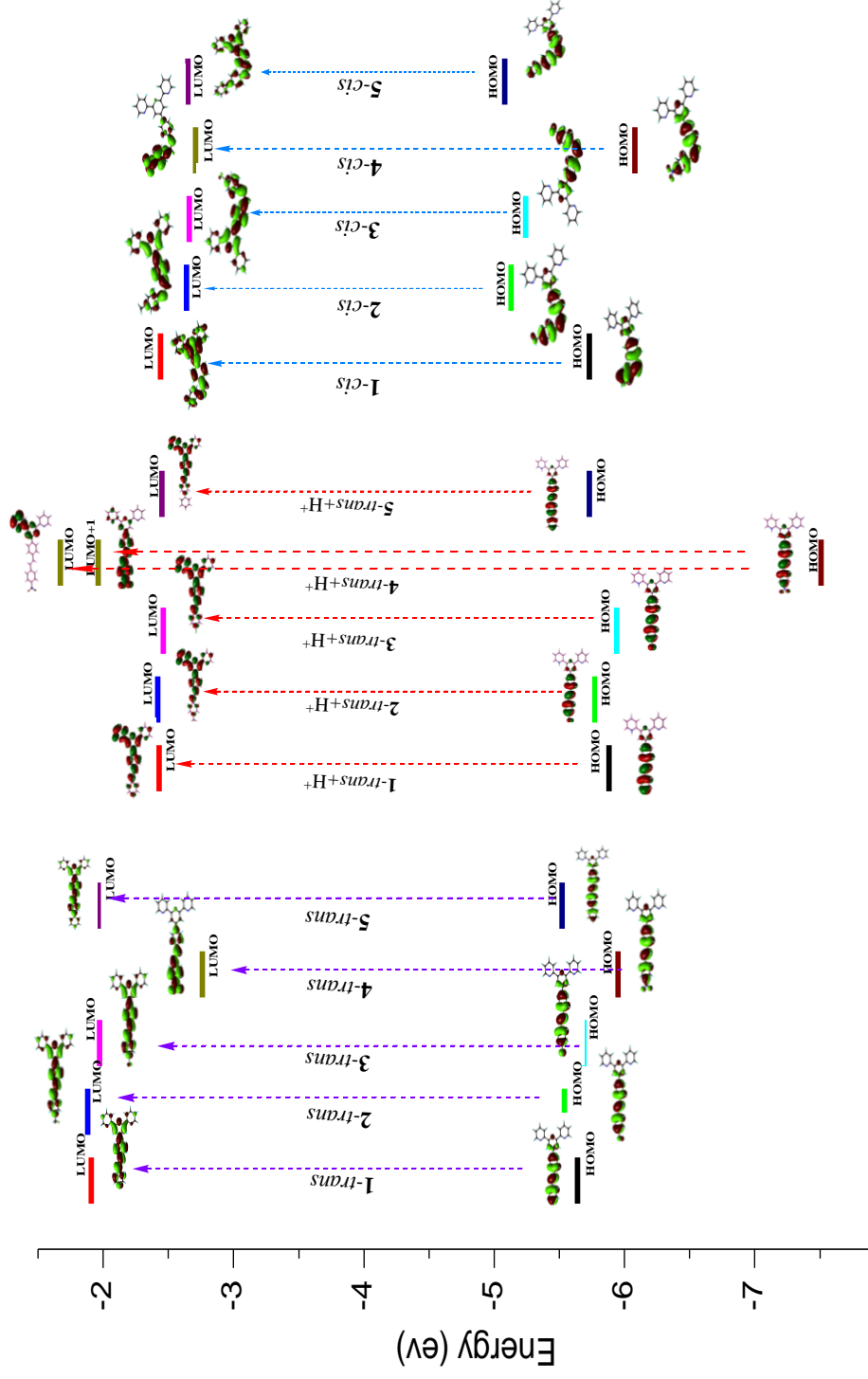


**Fig. 2.9.** Calculated energy level diagram in dichloromethane depicting the dominant transition that comprises the lowest-energy absorption band for *trans*, mono-protonated *trans* and *cis* form of tpy-pvp-X with X= H (1), Me (2), Cl (3), NO<sub>2</sub> (4) and Ph (5).

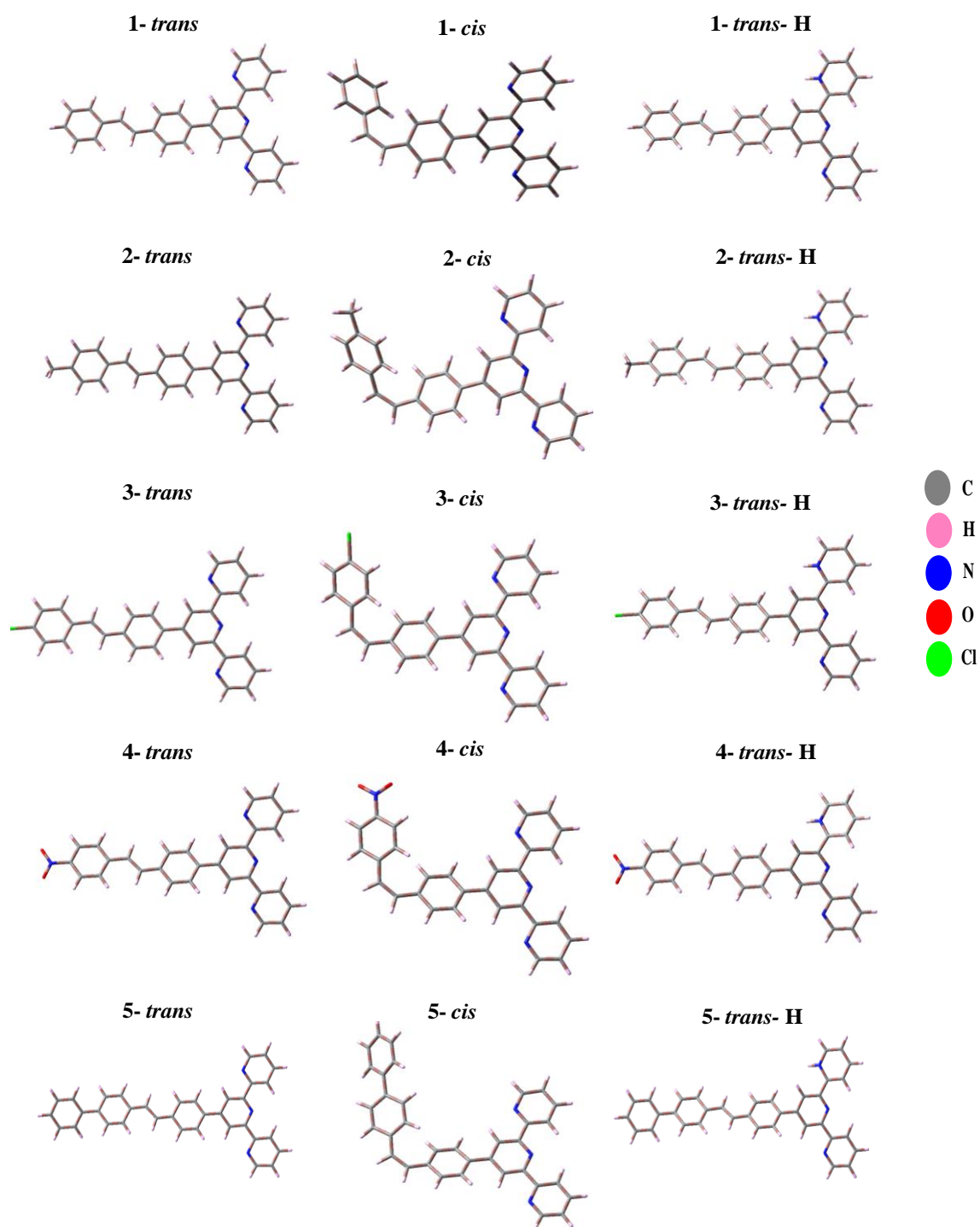


**Fig. 2.10.** Excited state optimized geometries of the *trans*-, *cis*- and mono-protonated *trans* forms of tpy-pvp-X in dichloromethane.

**Table 2.6** Calculated and experimental emission bands of tpy-pvp-X (**1-5**) in dichloromethane.

Excited state	$\lambda_{cal}/nm$	Oscillator strength(f)	$\lambda_{exp}/nm$	Key transitions	Character
<i>trans</i> [(tpy-pvp-H)]					
S <sub>1</sub>	459	1.92	398	L→H(99%)	ICT, $\pi$ - $\pi^*$
<i>cis</i> [(tpy-pvp-H)]					
S <sub>1</sub>	508	1.02	540	L→H (98%)	ICT, $\pi$ - $\pi^*$
<i>trans</i> [(tpy-pvp-H)+H <sup>+</sup> ]					
S <sub>34</sub>	698	0.02	552	L→H(100%)	ICT
S <sub>35</sub>	439	1.27	398	L+I→H(96%)	ICT, $\pi$ - $\pi^*$
<i>trans</i> [(tpy-pvp-Me)]					
S <sub>1</sub>	466	1.97	410	L→H(99%)	$\pi$ - $\pi^*$ , ICT
<i>cis</i> [(tpy-pvp-Me)]					
S <sub>1</sub>	515	1.03	548	L→H (97%)	$\pi$ - $\pi^*$ , ICT
<i>trans</i> [(tpy-pvp-Me)+H <sup>+</sup> ]					
S <sub>34</sub>	740	0.02	575	L→H(100%)	ICT
S <sub>35</sub>	452	1.22	410	L+I→H(97%)	ICT, $\pi$ - $\pi^*$
<i>trans</i> [(tpy-pvp-Cl)]					
S <sub>1</sub>	464	2.05	398	L→H(99%)	$\pi$ - $\pi^*$ , ICT
<i>cis</i> [(tpy-pvp-Cl)]					
S <sub>1</sub>	521	1.01	531	L→H (98%)	$\pi$ - $\pi^*$ , ICT
<i>trans</i> [(tpy-pvp-Cl)+H <sup>+</sup> ]					
S <sub>34</sub>	479	0.02	542	L→H(99%)	ICT
S <sub>35</sub>	439	1.49	398	L+I→H(96%)	ICT, $\pi$ - $\pi^*$
<i>trans</i> [(tpy-pvp-NO <sub>2</sub> )]					
S <sub>1</sub>	510	1.74	420	L→H(98%)	ICT, $\pi$ - $\pi^*$
<i>cis</i> [(tpy-pvp-NO <sub>2</sub> )]					
S <sub>1</sub>	529	0.88	500	L→H (99%)	ICT, $\pi$ - $\pi^*$
<i>trans</i> [(tpy-pvp- NO <sub>2</sub> )+H <sup>+</sup> ]					
S <sub>28</sub>	448	2.03	495	L→H(90%) L+I→H(5%)	ICT
<i>trans</i> [(tpy-pvp-Ph)]					
S <sub>1</sub>	497	2.38	420	L→H (97%)	ICT, $\pi$ - $\pi^*$
<i>cis</i> [(tpy-pvp-Ph)]					
S <sub>1</sub>	543	1.19	487	L→H (99%)	ICT, $\pi$ - $\pi^*$
<i>trans</i> [(tpy-pvp- Ph)+H <sup>+</sup> ]					
S <sub>40</sub>	748	0.02	591	L→H(99%)	ICT
S <sub>41</sub>	469	1.69	420	L+I→H(97%)	ICT, $\pi$ - $\pi^*$

### 2.3.3 Experimental absorption and emission spectra

Absorption and emission spectra of the compounds were acquired in few selected solvents and the necessary photophysical data are summarized in Table 2.7-2.8. The spectra of the compounds in dichloromethane are displayed in Fig. 2.11(a and b), while the spectra in other solvents are presented in Figs. 2.12-2.14. Spectral features are basically similar with small variation of peak position and intensity, depending upon the electronic nature of the substituent X.

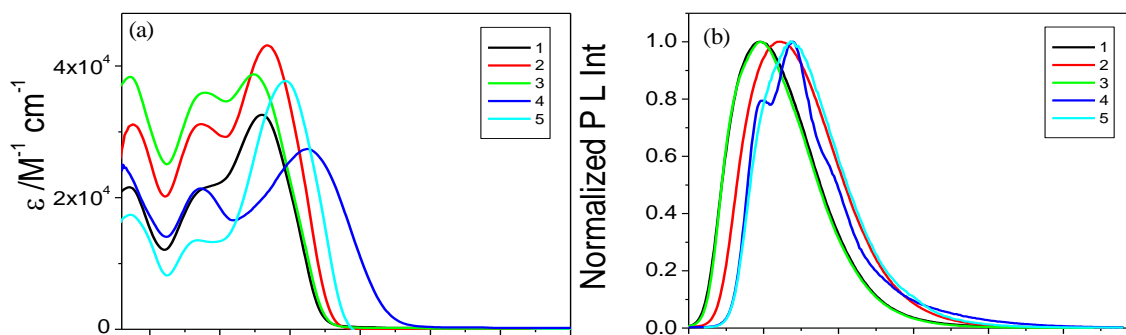
**Table 2.7** Absorption and emission spectral data of tpy-pvp-X (**1-5**) in dichloromethane.

Compounds	Free Condition				After photolysis			
	Absorption $\lambda_{\max}/\text{nm}$ ( $\epsilon/\text{M}^{-1}\text{cm}^{-1}$ )	Luminescence			Absorption $\lambda_{\max}/\text{nm}$ ( $\epsilon/\text{M}^{-1}\text{cm}^{-1}$ )	Luminescence		
		$\lambda_{\max}/\text{nm}$	$\tau/\text{ns}$	$\Phi$		$\lambda_{\max}/\text{nm}$	$\tau/\text{ns}$	$\Phi$
<b>1</b>	330(38800),288(25830)	398	1.05	0.33	382(10200),316(26500), 294(25400)	540	$\tau_1=2.10(88\%)$ , $\tau_2=3.37(12\%)$	0.011
<b>2</b>	335(48100),289(29100)	410	1.06	0.39	390(15100),321(37100), 294(31500)	548	$\tau_1=0.60(56\%)$ , $\tau_2=3.90(44\%)$	0.010
<b>3</b>	325(42100),287(39100)	398	1.00	0.19	373(15200)317(38000), 294(39400)	531	$\tau_1=1.65(76\%)$ , $\tau_2=5.69(24\%)$	0.007
<b>4</b>	361(25320),284(26040)	420	0.86	0.04	355(17850),283(28650)	495	$\tau_1=1.20(72\%)$ , $\tau_2=6.77(28\%)$	0.006
<b>5</b>	346(35700),282(14700)	418	0.98	0.36	391(9800),330(22100), 294(15700)	487	$\tau_1=0.91(57\%)$ , $\tau_2=2.77(43\%)$	0.006
<b>1+H<sup>+</sup></b>	413(10100),327(25600), 289(23300)	398 552	$\tau_1=1.01(78\%)$ , $\tau_2=1.95(22\%)$ 3.24	0.011	382(13300),317(30200), 294(27400)	540	$\tau_1=2.07(85\%)$ , $\tau_2=3.21(15\%)$	0.005
<b>2+H<sup>+</sup></b>	420(15800),332(47400), 290(41600)	410 575	$\tau_1=1.51(77\%)$ , $\tau_2=4.09(23\%)$ 2.90	0.009	390(23800),321(56380), 294(48527)	525	$\tau_1=0.60(41\%)$ , $\tau_2=3.91(59\%)$	0.006
<b>3+H<sup>+</sup></b>	396(16500),356(29500), 326(36100),288(37600)	398 542	1.12 3.50	0.060	374(25300),320(52800), 294(45800)	547	$\tau_1=1.12(86\%)$ , $\tau_2=5.14(14\%)$	0.012
<b>4+H<sup>+</sup></b>	360(26200), 285(23640), 235(25060)	420 495	$\tau_1=0.82(63\%)$ , $\tau_2=1.10(37\%)$ 1.86	0.028	355(18600),287(19900)	495	$\tau_1=0.66(45\%)$ , $\tau_2=1.80(55\%)$	0.004
<b>5+H<sup>+</sup></b>	425(11380),331(22100), 283(15700)	420 591	1.00 2.38	0.007	393(15420),327(33600), 293(20000)	505	$\tau_1=0.92(79\%)$ , $\tau_2=2.80(21\%)$	0.002

Considering the contributions of HOMOs and LUMOs and differences in the ground and excited state dipole moments (Table 2.9) as well as the experimental data of the structurally related systems, the lowest energy absorption band observed between 325 nm (for **3**) and 361 nm (for **4**) can be assigned mainly as intra-ligand CT, although substantial amount of  $\pi-\pi^*$  character is also mixed therein. The next higher energy band located in the range of 282-289 nm is again admixture of ICT and  $\pi-\pi^*$  transitions, although the contribution of  $\pi-\pi^*$  transitions is greater than ICT for this band (Fig. 2.11a). It is found that the correlation between TD-DFT calculated results and experimental spectra are reasonably good (Fig. 2.7).

**Table 2.8** Photophysical data of **tpy-pvp-X** in four different solvents.

Compounds	Solvents	Absorption $\lambda_{\max}/\text{nm}$ , $\varepsilon/\text{M}^{-1}\text{cm}^{-1}$	Luminescence		
			$\lambda_{\max}$ (nm)	$\tau$ , ns	$\Phi$
<b>1</b>	DCM	330(38800), 288(25830)	398	1.05	0.33
	DMSO	332(34270), 295(27550)	419	1.28	0.22
	MeCN	328(34000), 286(21620), 236(20950)	410	1.40	0.15
	MeOH	328(35190), 286(25940), 235(25440)	425	1.47	0.18
<b>2</b>	DCM	335(48100), 289(29100)	410	1.06	0.39
	DMSO	341(47000), 287(33500)	432	1.38	0.16
	MeCN	332(21800), 284(13200)	422	1.25	0.13
	MeOH	334(35500), 287(26000)	440	1.43	0.14
<b>3</b>	DCM	325(42100), 287(39100)	398	1.00	0.19
	DMSO	330(61800), 287(59200)	414	1.20	0.15
	MeCN	321(39000), 286(38300)	411	1.13	0.10
	MeOH	318(58600), 286(73200)	422	1.37	0.12
<b>4</b>	DCM	361(25320), 284(26040)	420	0.86	0.04
	DMSO	371(43200), 287(32300)	431	0.91	0.03
	MeCN	361(32600), 284(24300)	416	0.94	0.02
	MeOH	359(22900), 284(17300)	423	1.09	0.01
<b>5</b>	DCM	346(35700), 282(14700)	418	0.98	0.36
	DMSO	353(43000), 287(20700)	437	1.19	0.15
	MeCN	334(24200), 282(23700)	425	1.12	0.09
	MeOH	338(9100), 281(9600)	442	1.33	0.04

**Fig. 2.11.** UV-vis absorption and normalized emission spectra of **tpy-pvp-X** (a and b, respectively) with X=H (**1**), Me (**2**), Cl (**3**), NO<sub>2</sub> (**4**) and Ph (**5**) in dichloromethane. Excitation wavelength for recording emission spectra of the compounds is 330 nm.

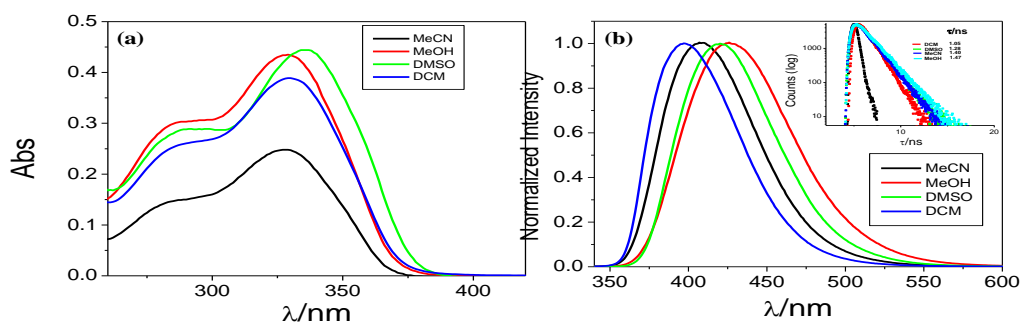


**Fig. 2.12.** UV-vis absorption (a) and normalized emission (b) spectra of [tpy-pvp-H] in different solvents. Inset to figure b shows the decay profiles and lifetimes. Excitation wavelength for recording both steady state emission spectra and excited state lifetime of the compound is 330nm

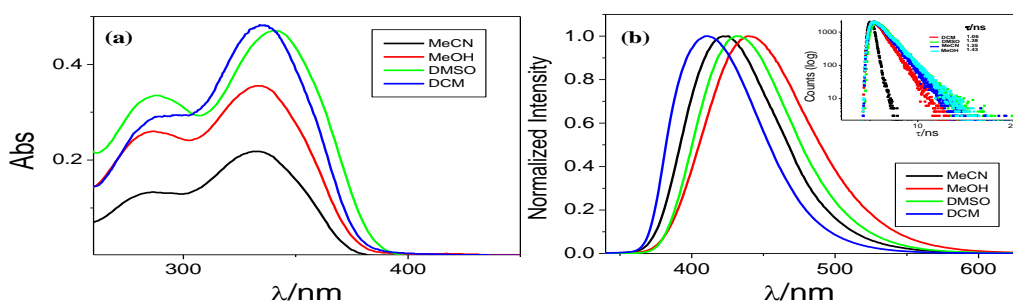


**Fig. 2.13.** UV-vis absorption (a) and normalized emission (b) (inset lifetime) spectra of [tpy-pvp-Me] in four different solvents. Inset to figure b shows the decay profiles and lifetimes. Excitation wavelength for recording steady state emission spectra of the compounds is 330 nm.

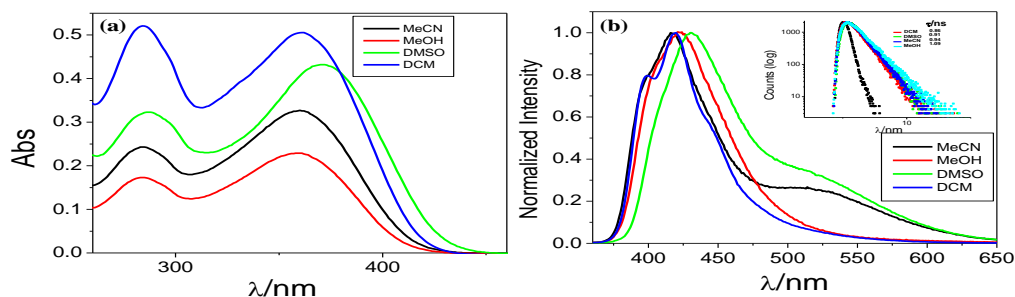


**Fig. 2.14.** UV-vis absorption (a,b) and normalized emission (c,d) spectra of [tpy-pvp-NO<sub>2</sub>] in four different solvents. Inset to figure b shows the decay profiles and lifetimes. Excitation wavelength for recording steady state emission spectra of the compounds is 330 nm.

**Table 2.9** Dipole moment values in both the ground and excited states of the compounds in their *trans*, protonated *trans* and *cis* forms.

Compounds	Dipole Moment/ Debye (Ground State)	Dipole Moment/ Debye (Excited State)
tpy-pvp-H ( <i>trans</i> )	1.6957	0.7015
tpy-pvp-H ( <i>cis</i> )	1.8682	1.7550
tpy-pvp-H+H <sup>+</sup> ( <i>trans</i> )	21.7489	21.3228
tpy-pvp-Me ( <i>trans</i> )	0.9211	0.3632
tpy-pvp-Me ( <i>cis</i> )	2.0083	1.6615
tpy-pvp-Me+H <sup>+</sup> ( <i>trans</i> )	22.6297	22.0688
tpy-pvp-Cl ( <i>trans</i> )	4.4906	3.5540
tpy-pvp-Cl ( <i>cis</i> )	3.1625	2.4614
tpy-pvp-Cl+H <sup>+</sup> ( <i>trans</i> )	27.2495	26.5855
tpy-pvp-NO <sub>2</sub> ( <i>trans</i> )	9.1186	11.0980
tpy-pvp-NO <sub>2</sub> ( <i>cis</i> )	7.0748	8.5236
tpy-pvp-NO <sub>2</sub> +H <sup>+</sup> ( <i>trans</i> )	32.8391	33.3476
tpy-pvp-Ph ( <i>trans</i> )	1.6360	0.6620
tpy-pvp-Ph ( <i>cis</i> )	1.8760	1.4019
tpy-pvp-Ph+H <sup>+</sup> ( <i>trans</i> )	29.6750	29.0502

Upon excitation on either of the two absorption maxima, an intense emission band lying between 398 nm (for **1**, **3**) and 420 nm (for **4**) was observed (Fig. 2.11b). The quantum yield of emission varies between 0.04 and 0.39, depending upon the electronic nature of the compound as well as the nature of solvents. Emission lifetime of the compounds recorded upon exciting with 330 nm Nanoled showed that all the compounds exhibit mono-exponential decay profile with lifetimes very close to 1.0 ns (Table 2.7-2.8

and Figs. 2.12-2.14). Result of the TD-DFT calculation in the previous section suggest that the emitting excited state of the compounds is predominantly  $^1\pi-\pi^*$  in character although some ICT character is also involved therein. In addition, correlation between the calculated and experimental emission energy is observed for all the compounds (Table 2.6).

It is observed that the compounds exhibit small solvatochromic shift (~50 nm) with the increase of solvent polarity indicating some charge transfer characteristics of the emitting excited states (Table 2.8 and Figs. 2.12-2.14). Increase of lifetime, although to a very small extent, in more polar solvents also indicates CT state of the emission processes.

### 2.3.4 Proton binding studies of the compounds

As the receptors contain three nitrogen atoms in the terpyridine moiety with a lone pair of electrons residing on each of them, we are interested to investigate the influence of protons on the photophysical as well as photochromic behaviors of the compounds in different solvents (DCM, MeOH, MeCN, and DMSO). Absorption and emission titrations experiments were performed upon incremental addition of  $H^+$  to obtain quantitative information about the interaction process (Fig. 2.15-2.17). Upon progressive addition of acid, diminution of the intensity of the major peak within the range of 330-361 nm (depending on electronic nature of X) occurs and at its expense a new band in the visible region (396-425 nm) is evolved and gradually intensified up to the addition of 1 equiv of acid. Continued addition of acid leads to small blue-shift of the lowest energy band with concomitant increase of band intensity within 320-340 nm and finally saturated upon addition of 3 equiv of acid. In emission side, gradual quenching of the original emission peak is observed along with emergence of a new broad peak in the longer wavelength region (495-591 nm), with incremental addition of acid in the first step. By contrast, the emission intensity of both the bands gradually decreased and finally almost quenched in the second step (Fig. 2.15d-2.17d). Thus, two-step changes along with requirement of 3 equiv of acid for reaching the saturation point probably indicates the presence of mono-, bi- as well as tri-protonated species of the compounds. Absorption and emission spectra of all the compounds in DCM at the saturation point of the first protonation step are presented in Fig. 2.18(a and b). As the emission band is fully



quenched in the second stage of protonation, we presented only the absorption spectra of all the compounds at the saturation point of the second protonation step in Fig. 2.19.

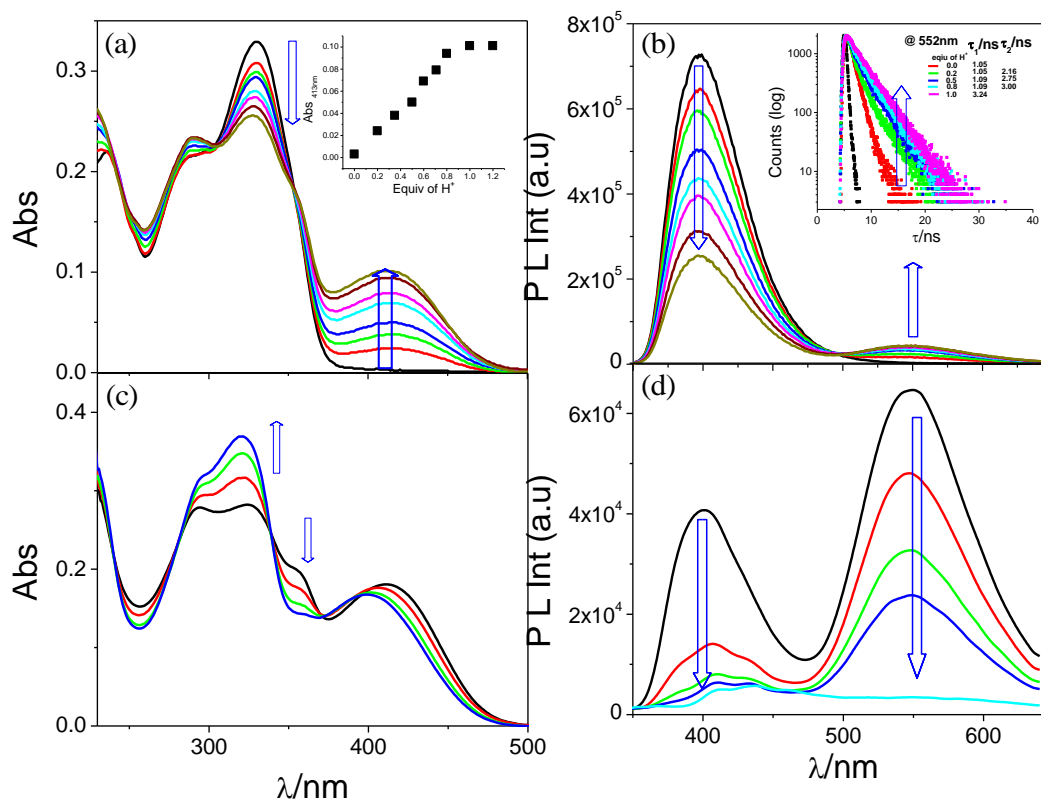


**Fig. 2.15.** UV-vis absorption and emission (a and b, respectively for the first step, while c and d, respectively for the second step) spectral changes of tpy-pvp-H (**1**) in dichloromethane upon incremental addition of  $H^+$ . Inset to figure a and c shows the absorbance *vs.* equivalent of acid plot, while inset to figure b and d shows emission decay profiles and lifetimes of the compound. Excitation wavelength for recording both emission spectra and lifetime are 330 nm.

It is observed that among the studied solvents, the compounds exhibit a strong band in the visible region, assignable to ICT only in DCM with evolution of bright yellow colour in presence of acid (Fig. 2.20). The extent of spectral change is much less in other solvents with requirement of more acid to reach the saturation point which is probably due to competitive hydrogen bonding interaction with MeOH, MeCN and DMSO. With the exception of nitro-derivative, red-shift of both absorption and emission

band is observed upon protonation, albeit in different extent, which is due to enhanced styrylbenzene→protonated tpy CT process as protonated tpy is a better electron acceptor than free tpy in the compounds. In contrast to others, ICT process in the nitro-compound predominantly occurs from styrylbenzene moiety to the nitrobenzene unit. DFT and TD-DFT calculations also support this proposition. Interestingly, the lowest energy absorption and emission energy in the first stage of protonation increases systematically with the increase of electron withdrawing nature of X and a linear correlation is obtained by plotting the energy of the band maxima in DCM and Hammett  $\sigma_p$  parameters (Fig. 2.21a,b).

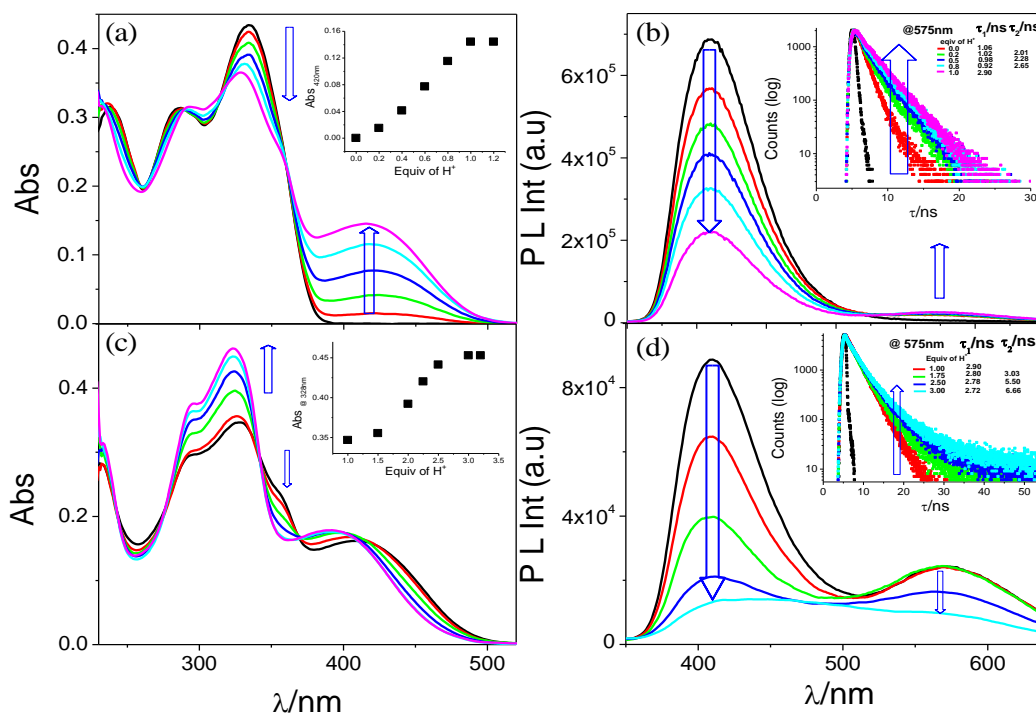


**Fig. 2.16.** UV-vis absorption and emission (a and b, respectively for the first step, while c and d, respectively for the second step) spectral changes of tpy-pvp-Me (2) in dichloromethane upon incremental addition of  $H^+$ . Inset to figure a and c shows the absorbance vs. equivalent of acid plot, while inset to figure b and d shows emission decay profiles and lifetimes of the compound. Excitation wavelength for recording both emission spectra and lifetime are 330 nm.

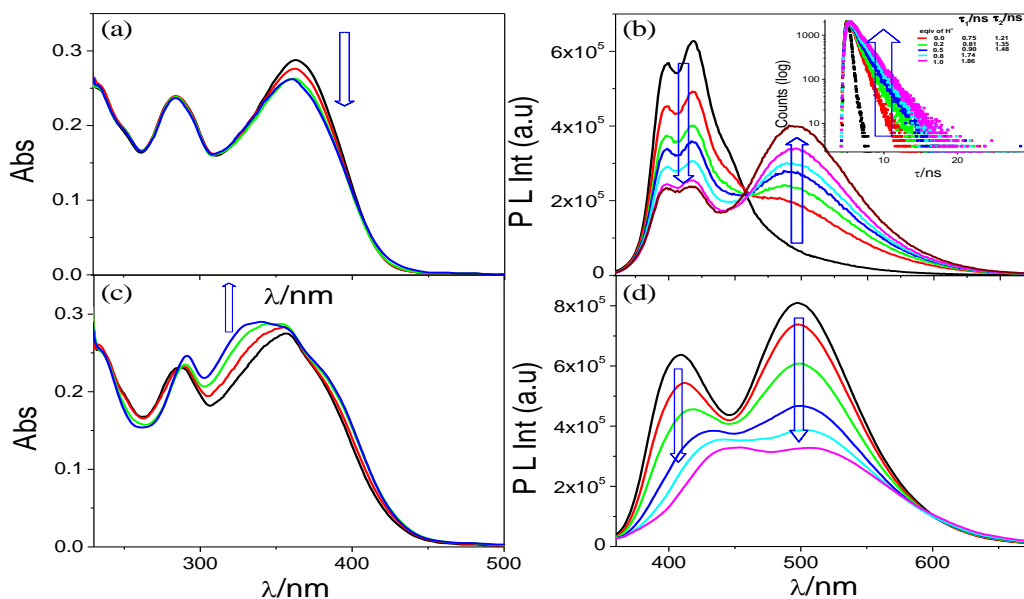


**Fig. 2.17.** UV-vis absorption and emission (a and b, respectively for the first step, while c and d, respectively for the second step) spectral changes of tpy-pvp-NO<sub>2</sub> (**4**) in dichloromethane upon incremental addition of H<sup>+</sup>. Inset to figure a and c shows the absorbance vs. equivalent of acid plot, while inset to figure b and d shows emission decay profiles and lifetimes of the compound. Excitation wavelength for recording both emission spectra and lifetime are 330 nm.

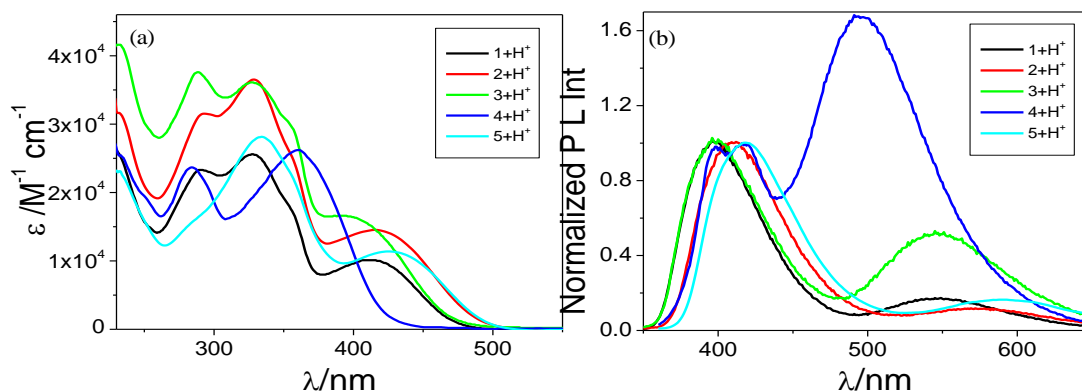


**Fig. 2.18.** UV-vis absorption (a) and normalized emission (b) spectra of tpy-pvp-**X** at the saturation point of first protonation step with X=H (**1**), Me (**2**), Cl (**3**), NO<sub>2</sub> (**4**) and Ph (**5**) in dichloromethane. Excitation wavelength for recording emission spectra of the compounds is 330 nm.

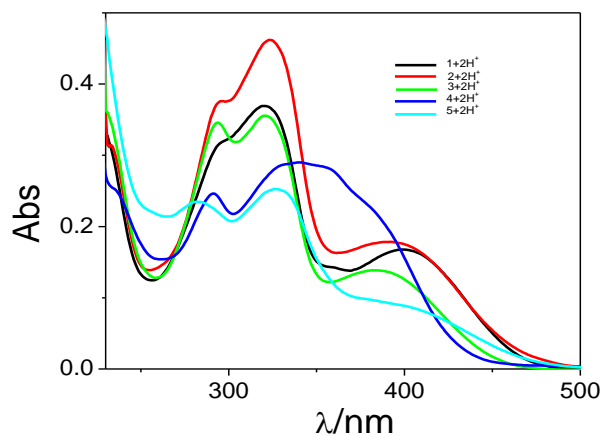


**Fig. 2.19.** UV-vis absorption spectra of **tpy-pvp-X** at the saturation point of second protonation step (3 equiv of acid) with X=H (1), Me (2), Cl (3), NO<sub>2</sub> (4) and Ph (5) in dichloromethane.

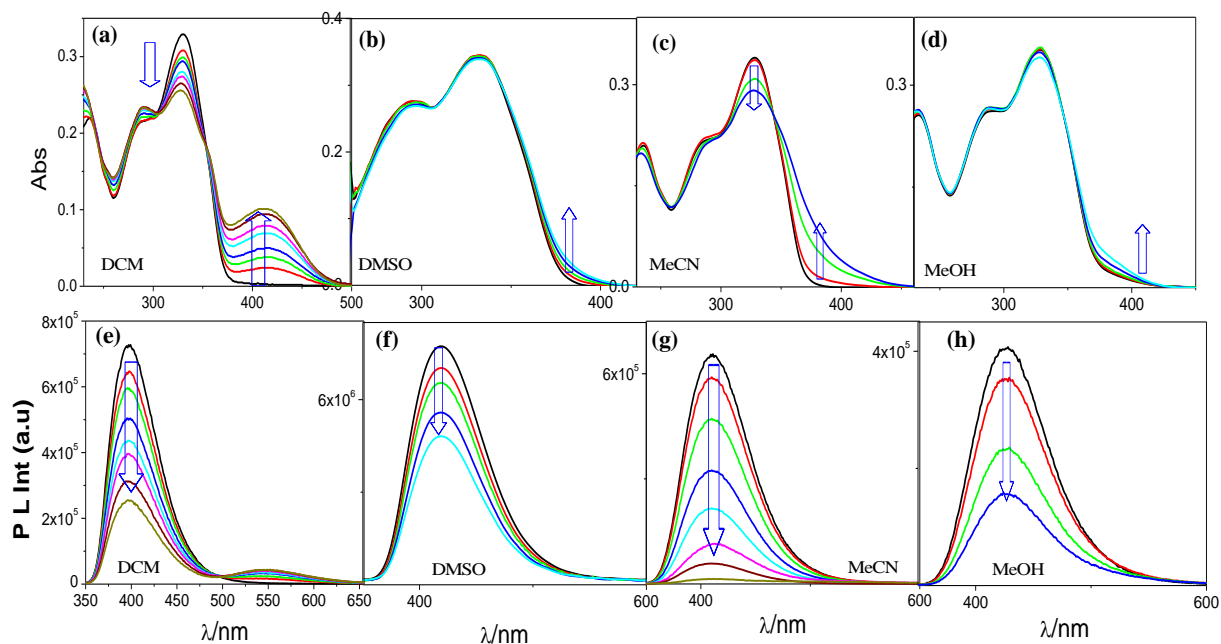


**Fig. 2.20.** Change in UV-vis absorption (a, b, c, d) and emission (e, f, g, h) spectra of [tpy-pvp-H] in various solvents upon incremental addition of H<sup>+</sup>. Excitation wavelength for recording steady state emission spectra of the compound is 330 nm.

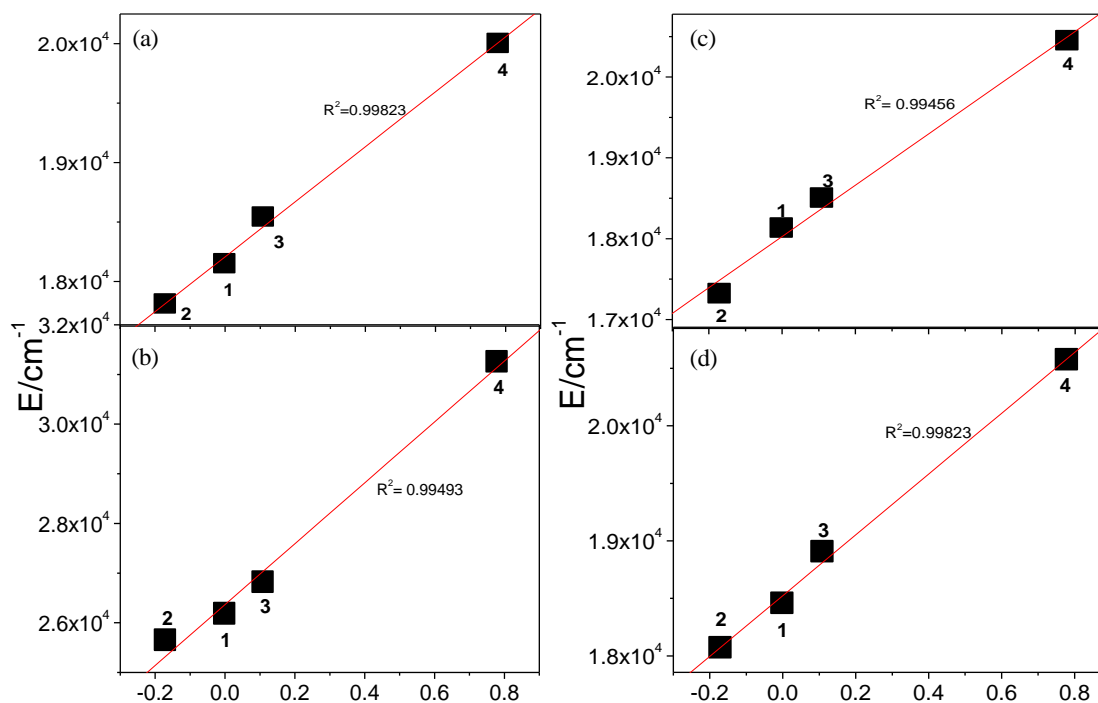


**Fig. 2.21.** Plot of energy of absorption and emission maxima of *trans* form (in their first protonation step) of **tpy-pvp-X** (a and c respectively) and their *cis* forms (b and d, respectively), where  $X = \text{H}$  (1),  $\text{Me}$  (2),  $\text{Cl}$  (3) and  $\text{NO}_2$  (4) vs. Hammett  $\sigma_p$  parameters with linear least-squares fit to the data.

Lifetimes of selected compounds were acquired at two wavelengths [(i) 398-420 nm and (ii) 495-591 nm] upon incremental addition of acid. Although the steady state emission intensity gradually decreases within 398-420 nm corresponding to the emission of the free compounds but the lifetimes remain almost unaltered with  $\text{H}^+$ . On the other hand, in line with the steady state spectra, lifetime also gradually increases when the emission was monitored within 495-591 nm corresponding to that of the protonated species (Inset of Fig. 2.15 b,d -2.17 b,d).

### 2.3.5 Photo-isomerization studies

All the compounds in the present study possess a styrylbenzene unit and are thus expected to undergo *trans-cis* isomerization induced by light. Isomerization studies were performed in dichloromethane and visualized through absorption and both steady state and time-resolved emission spectroscopic techniques. Upon irradiation with UV light, the

intensity of the lowest energy absorption band (except nitro derivative) gradually decreases along with small blue-shift and at its expense, a new broad absorption band arises at the lower energy region (in the range of 373-391 nm) and gradually intensified and finally saturates upon photolysis of ~30 min (Fig. 2.22a, b and Fig. 2.23a). The observed spectral change is due to *trans*→*cis* isomerization process. Presence of well-defined isosbestic points in each case clearly indicates that only two species are exchanging during the photo-isomerization process. The percentage change in abundance of *trans* form of [tpy-pvp-Me] (**2**) and [tpy-pvp-NO<sub>2</sub>] (**4**) during photolysis is shown in Fig. 2.24. In the emission side, almost complete quenching of emission (within 398-420 nm) along with red-shift of the band occurs in all cases upon photolysis (Fig. 2.22c,d and Fig. 2.23b). Although the steady state emission intensity of the complexes decreases substantially, the lifetime of the compounds increases to some extent on going from *trans* to *cis* form

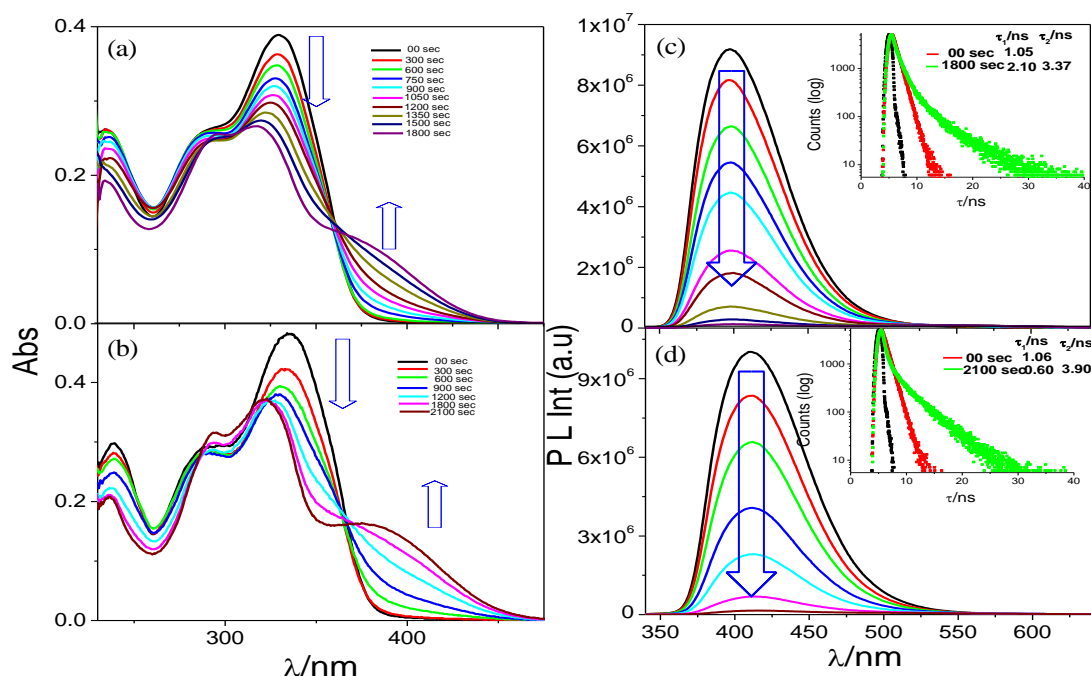


**Fig. 2.22.** Changes in UV-vis absorption and emission spectra of tpy-pvp-H (**1**) (a and c, respectively) and tpy-pvp-CH<sub>3</sub> (**2**) (b and d, respectively) in dichloromethane upon irradiation with UV light. Emission decay profiles along with lifetimes are given in the insets of figures c and d. Excitation wavelength for recording both emission spectra and lifetimes is 330 nm.

and the extent of increase depends upon electronic nature of the substituent, X (Table 2.7). It is of interest to note the enhancement of lifetime is highest with strongly electron withdrawing nitro-compound. The reverse *cis*→*trans* isomerization process proceeds slowly upon irradiating the UV treated solution with visible (at  $\lambda \sim 400$  nm) light and original spectrum reappeared again upon irradiation for about an hour.

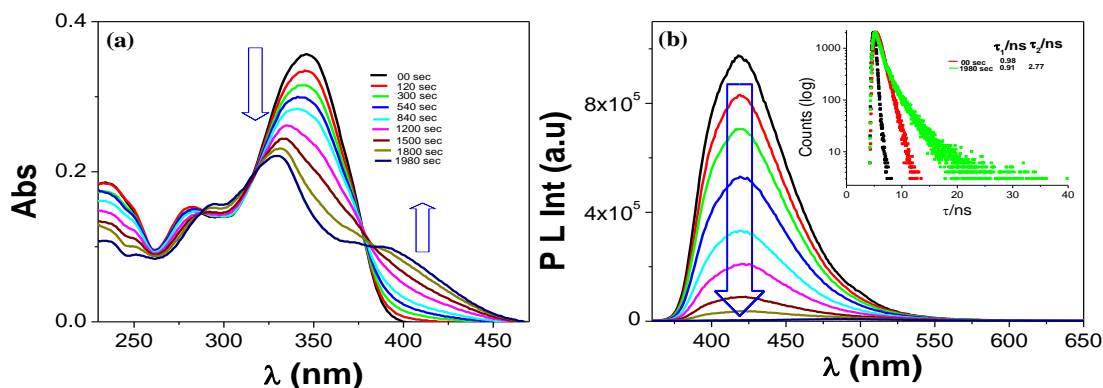


**Fig. 2.23.** Changes in UV-vis absorption (a) and emission (b) spectrum of tpy-pvp-Ph (5) in dichloromethane upon irradiation of UV light. Emission decay profiles along with lifetimes are given in inset of figure b. Excitation wavelength for recording both steady state emission spectra and excited state lifetime of the compounds is 330 nm.

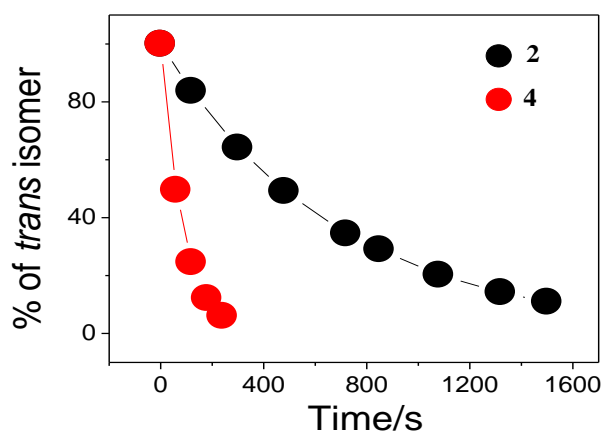


**Fig. 2.24.** Changes in abundance of *trans*→*cis* of [tpy-pvp-Me] (2) and [tpy-pvp-NO<sub>2</sub>] (4) during irradiation with UV light.

The behaviour of the nitro compound is quite different from the rest of the compounds. Upon irradiation with UV light, two-step changes are observed in both absorption and emission spectrum compared with one-step change for the remaining compounds (Fig. 2.25). In the first step, the lowest energy band at 361 nm gradually decreased in intensity and at its expense the intensity of the band at 285 nm increased and during this process successive absorption curves were found to pass through a well defined isosbestic point at 315 nm (Fig. 2.25a). In the second step, the intensity of the broad band in the range of 310-360 nm increased gradually, while the intensity of the band at 285 nm decreased along with small red-shift and the absorption lines in this step also pass through a new isosbestic point at 295 nm (Fig. 2.25b). In the second step, the intensity of the broad band in the range of 310-360 nm increased gradually, while the intensity of the band at 285 nm decreased along with small red-shift and the absorption lines in this step also pass through a new isosbestic point at 295 nm (Fig. 2.25b).

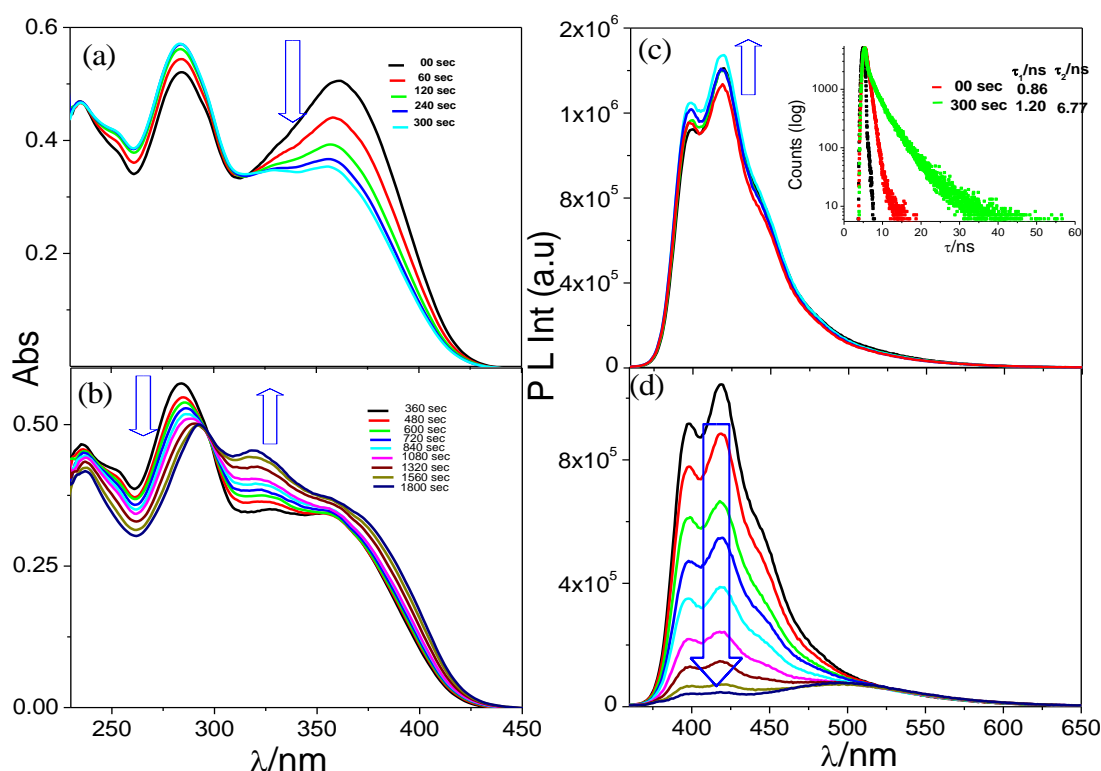


**Fig. 2.25.** Changes in UV-vis absorption (a and b) and emission (c and d) spectra of tpy-tpvp-NO<sub>2</sub> (**4**) in dichloromethane upon irradiation with UV light. Emission decay profiles along with lifetimes are given in inset of figure c. Excitation wavelength for recording both emission spectra and lifetime is 330 nm.



The structured emission band for the nitro compound with its maximum at 420 nm increased to some extent in the first step (Fig. 2.25c), while the intensity of the said band quenched to a significant extent with broadening and red-shifting to 495 nm in the second step (Fig. 2.25d). The exact reason of the two-step changes for the nitro-derivative is not very clear to us. The first step change which completed within 5 min is most likely due to *trans*→*cis* isomerization of the double bond, while the second change is probably associated with transformation of nitro (-NO<sub>2</sub>) to some other form such as nitroso (-NO) along with the generation of aryl-oxo free radical and ultimately to the phenolic form (-OH) in presence of light, although no direct proof of the hypothesis could be given [59].

Except nitro, all the compounds are colorless in their original *trans* forms and became light yellow in color upon photo-isomerization to their respective *cis* forms and thus exhibit photochromic behavior (Fig. 2.26). Distinct emission color changes were also clearly observed under UV illumination (Fig. 2.26). The initial *trans* form of the compounds are strongly fluorescent, while their final *cis* forms after photolysis exhibit very weak emission, which are in line with the usual trend observed in *trans* stilbene→*cis* stilbene

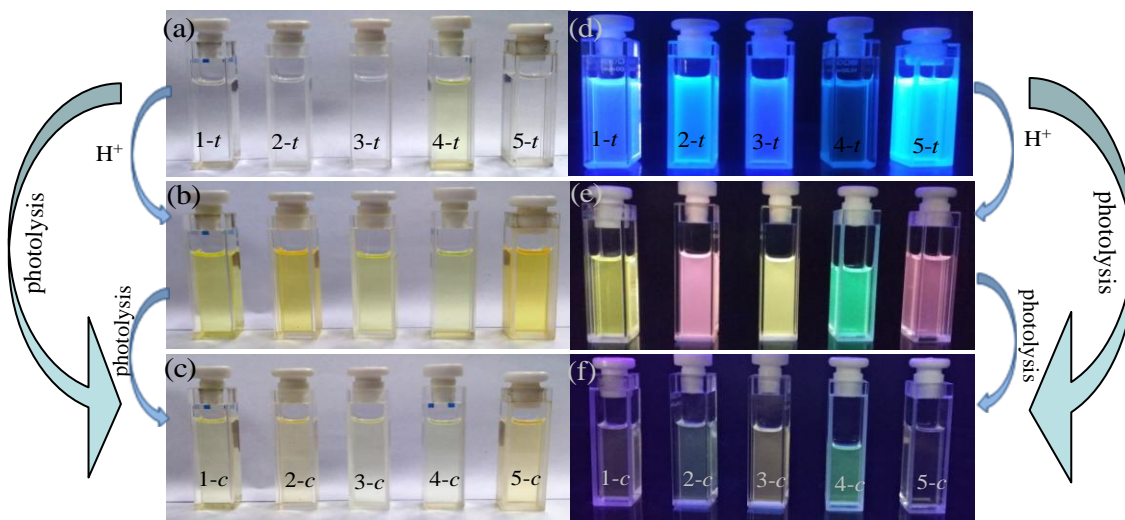


**Fig. 2.26.** Color changes that are observed in naked eye (a,b,c) and under UV illumination (d,e,f) of **tpy-pvp-X** [H (1), Me (2), Cl (3), NO<sub>2</sub> (4) and ph (5)] in their *trans*-, mono-protonated *trans*- and *cis*- forms. *t* and *c* correspond to *trans*- and *cis*- forms of the compounds.

## Chapter 2

---

conversion (Table 2.7) [60-62]. Interestingly, isomerization from *trans* to *cis* leads to emission quenching, while from *cis* to *trans* form gives rise to restoration of the original emission. Thus, the compounds display "on-off" and "off-on" emission switching upon alternate interaction with UV and visible light.

Few important points need to be mentioned here. In contrast to their *trans* form, the lowest energy absorption and emission energy of the *cis* form of the compounds increases systematically with the increase of electron withdrawing nature of X and a linear correlation is obtained between the energy of band maxima and Hammett  $\sigma_p$  parameters (Fig. 2.21b,d). The experimental absorption spectral trend as a function of the substituent at the *para* position of the terminal phenyl group is reproduced by the calculated results (Fig. 2.7). Experimentally observed blue-shift of the lowest energy absorption bands and newly generated band in the longer wavelength region (~373-391 nm) upon photolysis is also in-line with calculated results (Fig. 2.7). In addition, experimentally observed red-shift of the emission band along with substantial quenching upon photolysis is also nicely reproduced by calculations (Table 2.6).

The rate constants of the *trans*→*cis* isomerization processes were estimated from absorption titration data and with the help of equation 1. The rate follows first order kinetics and the estimated values were found to vary between  $1.17 \times 10^{-2} \text{ s}^{-1}$  and  $1.39 \times 10^{-3} \text{ s}^{-1}$ , depending upon the electronic nature of the substituent X (Table 2.10). The quantum yields of *trans*→*cis* photoisomerization process were also measured and the values are in general low and vary between  $1.54 \times 10^{-3}$  and  $2.35 \times 10^{-4}$  (Table 2.10). It appears that the rate constant and quantum yield of photo-isomerization of nitro-compound (**4**) is one order of magnitude higher than the rest of the compounds probably because of its strong withdrawing property of the NO<sub>2</sub> group. We also estimated the free energy of activation ( $\Delta G^\ddagger$ ) of the photo-isomerization processes from the values of the rate constants and utilizing Eyring's theory of absolute reaction rates and the calculated  $\Delta G^\ddagger$  values of the isomerization processes are summarized in Table 2.10.

$$\Delta G^\ddagger_{298\text{K}} = 298R \{ \ln(k_B 298/h.k_{iso}) \} \quad (3)$$

Apart from variation of electron donating and electron withdrawing substituent, we also interested to modulate the kinetics and thermodynamic aspects of the photo-isomerization process by other means. To this end, we carried out the isomerization studies of a representative compound (tpy-pvp-H) in four different solvents (DCM, MeOH, MeCN, and DMSO) to check the influence of solvent polarity as well as viscosity on the rate of isomerization process. The spectral profiles and related parameters are provided in Fig. 2.27 and Table 2.11.

**Table 2.10** Rate constants, quantum yield and free energy of activation of the *trans*→*cis* photo-isomerization process of tpy-pvp-X (**1-5**) and its mono-protonated form in DCM.

comp ds	tpy-pvp-X				tpy-pvp-X +H <sup>+</sup>			
	$\lambda/\text{nm}$	$k_{\text{iso}} \times 10^3 / \text{s}^{-1}$	$\Phi \times 10^4$	$\Delta G^\ddagger / \text{kJmol}^{-1}$	$\lambda/\text{nm}$	$k_{\text{iso}} \times 10^3 / \text{s}^{-1}$	$\Phi \times 10^4$	$\Delta G^\ddagger / \text{kJmol}^{-1}$
<b>1</b>	330	1.61	2.35	88.92	382	2.53	12.9	87.80
<b>2</b>	335	1.65	2.05	88.86	390	1.59	5.18	88.95
<b>3</b>	325	2.07	1.62	88.29	325	2.74	4.52	87.60
<b>4</b>	361	11.7	15.4	84.00	360	10.2	13.7	84.34
<b>5</b>	346	1.39	1.31	89.28	450	1.87	6.39	88.54

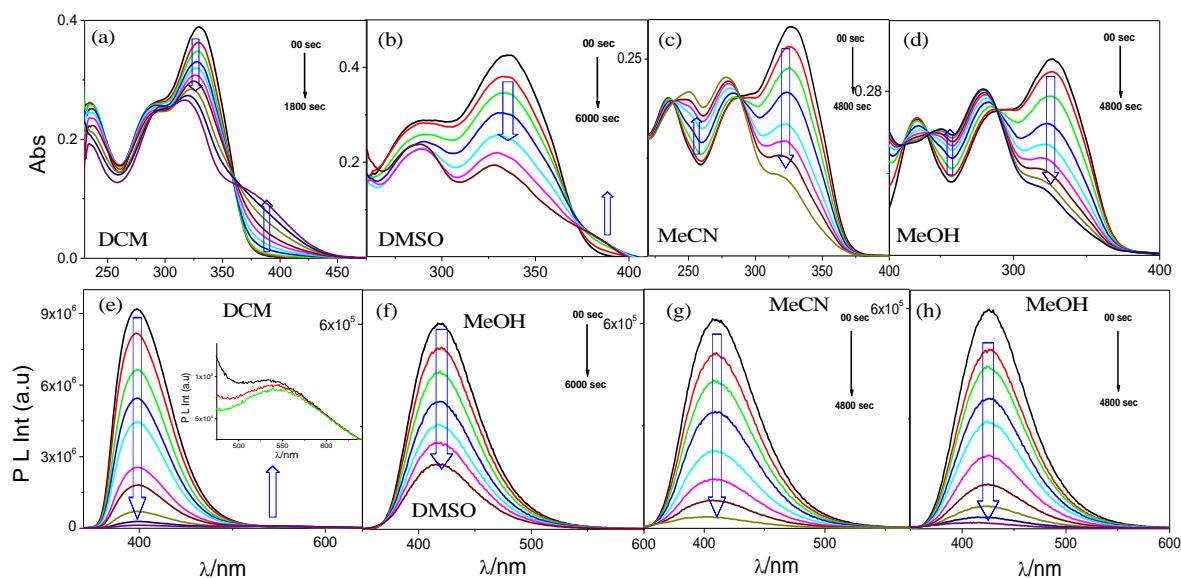


**Fig. 2.27.** Changes of UV-vis absorption (a-d) and emission (e-h) of tpy-pvp-H (**1**) in four different solvents upon irradiation with UV light. Excitation wavelength for recording emission spectra is 330 nm.

## Chapter 2

The rate constants of the isomerization processes were estimated and correlated with polarity and bulk viscosity of the solvents (Table 2.12). The rate of photo-isomerization is found to be highest in dichloromethane and least in dimethylsulfoxide. Among the studied solvents, relative polarity of dichloromethane is least, while DMSO is

**Table 2.11** Photophysical table of tpy-pvp-H (**1**) and its mono-protonated form in four different solvents.

Cmpds	Free Condition					After photolysis			
	Solvent	Absorption $\lambda_{\max}/\text{nm}$ ( $\epsilon/\text{M}^{-1}\text{cm}^{-1}$ )	Luminescence			Absorption $\lambda_{\max}/\text{nm}$ ( $\epsilon/\text{M}^{-1}\text{cm}^{-1}$ )	Luminescence		
			$\lambda_{\max}/\text{nm}$	$\tau$ , ns	$\Phi$		$\lambda_{\max}/\text{nm}$	$\tau$ , ns	$\Phi$
<b>1</b>	DCM	330(38800), 288(25830)	398	1.05	0.330	382(10200), 316(26500), 294(25400)	540	$\tau_1=2.10(88\%)$ , $\tau_2=3.37(12\%)$	0.011
	DMSO	332(34270), 295(27550)	419	1.28	0.220	327(19320), 288(23780),	416	$\tau_1=1.29(89\%)$ , $\tau_2=7.76(11\%)$	0.007
	MeCN	328(34000), 286(21620), 236(20950)	410	1.40	0.150	322(9960), 278(22690), 251(20850)	405	$\tau_1=1.40(68\%)$ , $\tau_2=8.92(32\%)$	0.002
	MeOH	328(35190), 286(25940), 235(25440)	425	1.47	0.180	320(11520), 278(28300), 250(21560)	420	$\tau_1=1.46(42\%)$ , $\tau_2=5.80(58\%)$	0.001
<b>1+H<sup>+</sup></b>	DCM	413(10100),327(25600),289(23300)	398	$\tau_1=1.01(78\%)$ , $\tau_2=1.95(22\%)$	0.011	382(13300), 317(30200), 294(27400)	540	$\tau_1=2.07(85\%)$ , $\tau_2=3.21(15\%)$	0.005
			552	3.24					
	DMSO	332(33890), 294(26790)	419	1.36	0.015	332(20900), 295(19300)	419	$\tau_1=1.27(94\%)$ , $\tau_2=5.18(6\%)$	0.009
	MeCN	327(29140), 290(21450), 234(19800)	418	$\tau_1=1.68(63\%)$ , $\tau_2=3.95(37\%)$	0.009	360(sh)(15300), 318(26200), 293(27100), 234(19400)	418	$\tau_1=1.38(78\%)$ , $\tau_2=3.24(22\%)$	0.001
	MeOH	328(34100), 286(26380), 235(25840)	426	$\tau_1=1.97(82\%)$ , $\tau_2=6.18(18\%)$	0.007	328(26500), 287(24300), 236(22300)	426	$\tau_1=2.21(76\%)$ , $\tau_2=6.83(23\%)$	0.001

**Table 2.12** Rate constants and quantum yields of the *trans*→*cis* photo-isomerization process of tpy-pvp-H (**1**) in four different solvents.

Solvent	Rate constant ( $K_{\text{iso}} \times 10^4/\text{s}^{-1}$ )	Quantum yield ( $\Phi \times 10^4$ )
DCM	16.1	2.35
DMSO	3.45	1.08
MeCN	5.50	1.11
MeOH	5.38	1.00

highly viscous as well as polar aprotic solvent. Thus, the rate constant of the photo-isomerization processes gradually decreases with the increase of polarity as well as the viscosity of the solvents. As the present compounds have significant amount of charge transfer character, slower isomerization rate in more polar solvents like MeOH, MeCN and DMSO is also due to large degree of solvation which in turn lead to increase of the effective rotor volume of the compounds.

We also studied the influence of proton by carrying out photolysis of all the compounds in DCM in presence of acid. Firstly, we carried out the photolysis in presence of one equiv of  $H^+$  (first protonation step). Upon irradiation with UV light, lowest energy absorption band within the range of 360-425 nm gets blue-shifted to ~355-393 nm range (Fig. 2.28-2.30). Spectral lines were passed through several clean isosbestic for each compound. Inspection of the spectrum at the saturation point shows close similarity to that of the spectrum obtained upon photolysis in neat DCM in absence of acid. Irradiation of UV light leads to quenching of both the emission bands of the protonated compounds and finally gives rise to very weak and broad emission band in between 495 and 547 nm, depending on X. In line with absorption spectral behavior, the final emission spectrum in each case after photolysis looks very similar to that *cis* form of the compounds. Thus, photolysis of the acid treated solution leads to both deprotonation as well as isomerization of the compounds to their corresponding *cis* form. In addition, the rate of photolysis of the compounds was found to be much faster in presence of acid than that of their free form (Table 2.10). The reverse process is also achieved upon treating the solution with visible light followed by acidification. It is of interest to note the intense yellow color of the acid treated solution of the compound became very light upon photolysis and thus exhibiting reversible photochromic behavior. In line with their free form, emission color changes were nicely demonstrated for the protonated forms under UV illumination (Fig. 2.26).

We also carried out the photo-isomerization behaviors of two compounds (**1** and **2**) upon addition of 3 equiv of  $H^+$  (second protonation step) in DCM. In line with first step, the lowest energy absorption band at ~396 nm shifted to the blue region (380-390 nm) upon irradiation with UV light (Figs. 2.31-2.32). The weak emission band due to multiply protonated species gets almost fully quenched along with blue-shift in each case.

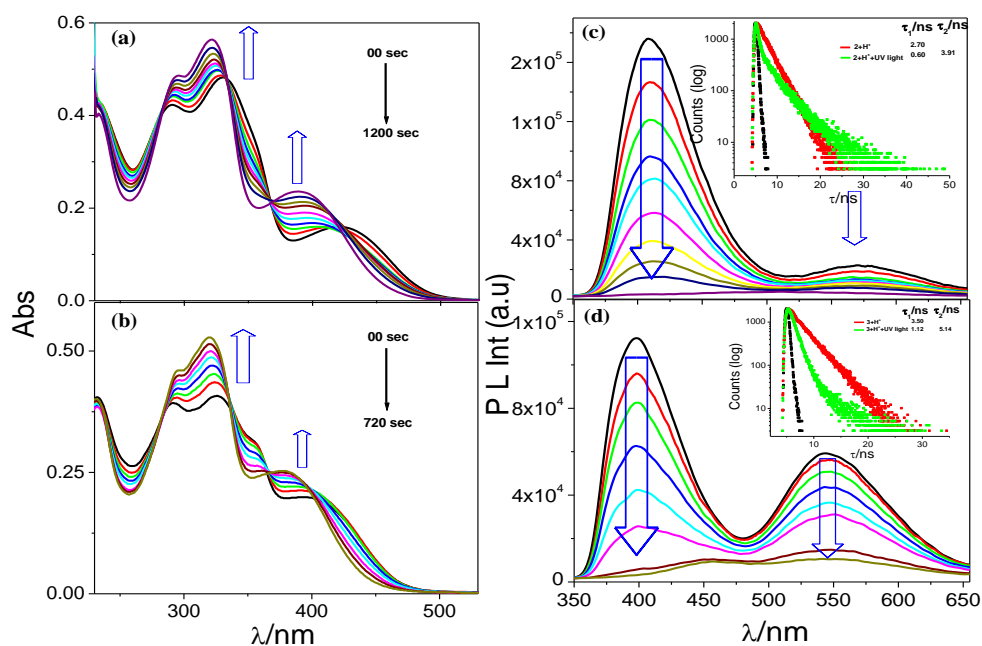


**Fig. 2.28.** Changes in UV-vis absorption and emission spectra of the acid treated solutions of tpy-pvp-Me (**2**) (a and c, respectively) and tpy-pvp-Cl (**3**) (b and d, respectively) in dichloromethane upon irradiation with UV light. Insets to figure b and d show emission decay profiles and lifetimes. Excitation wavelength for recording both emission spectra and lifetime are 330 nm.

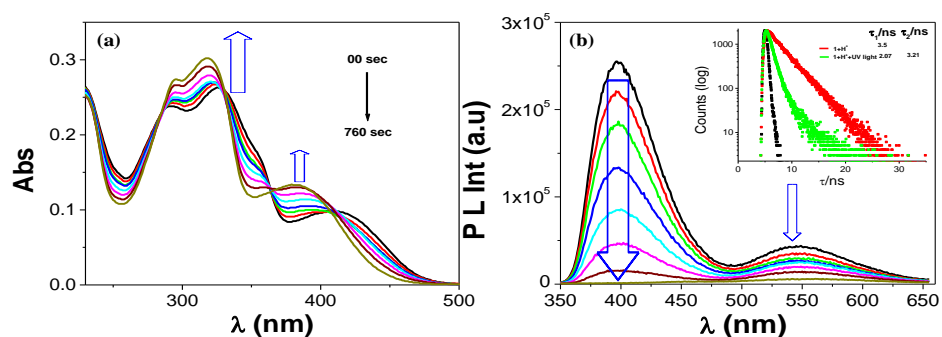


**Fig. 2.29.** Changes in UV-vis absorption (a) and emission (b) spectra of tpy-pvp-H (**1**) in dichloromethane upon irradiation of UV light after incremental addition of one equiv of  $H^+$ . Emission decay profiles and lifetimes are provided in the inset of figure b. Excitation wavelength for recording the emission is 330 nm.

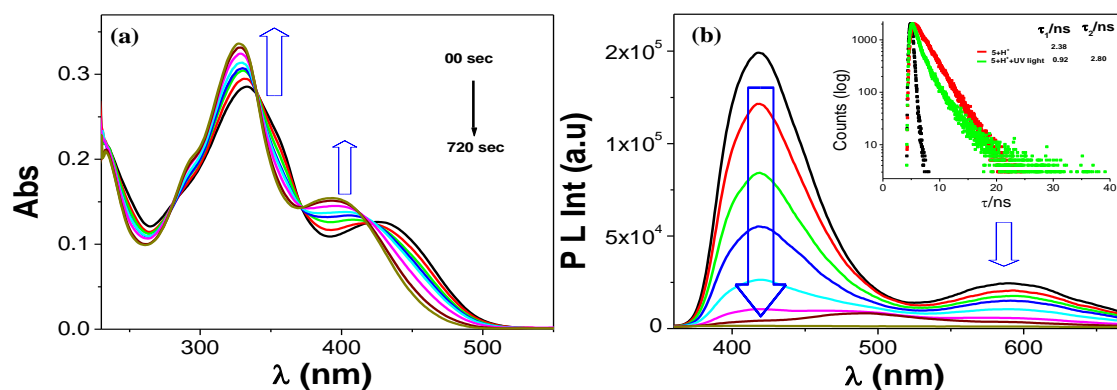


**Fig. 2.30.** Changes in UV-vis absorption (a) and emission (b) spectra of tpy-pvp-Ph (**5**) in dichloromethane upon irradiation of UV light after incremental addition of H<sup>+</sup>. Emission decay profiles and lifetimes are provided in the inset of figure b. Excitation wavelength for recording the emission is 330 nm.

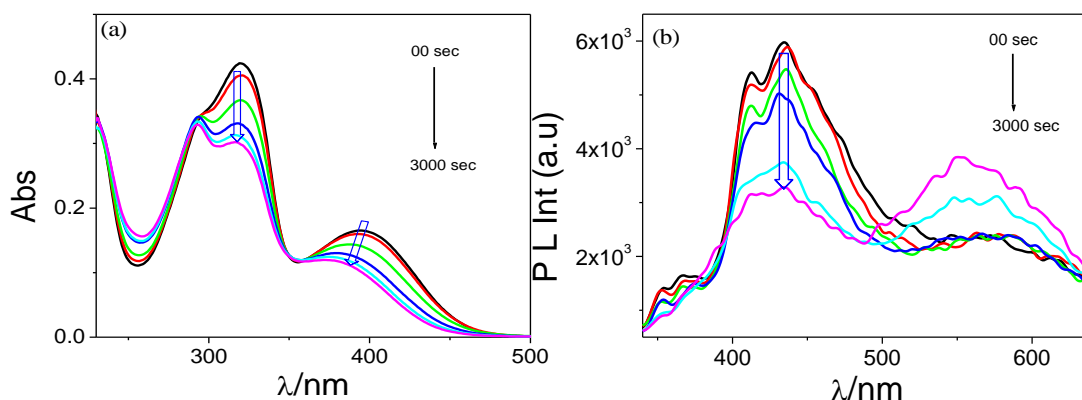


**Fig. 2.31.** UV-vis absorption (a) and emission (b) spectral changes of acid treated (3 equiv) dichloromethane solution of tpy-pvp-H (**1**) upon irradiation with UV light. Excitation wavelength for recording the emission is 330 nm.

It would be appropriate to give some insight here about the isomerization process. Upon excitation with UV-light, stilbene is promoted to the S<sub>1</sub> excited-state with a C=C bond order shorter compared with the ground state species which takes into account for the free rotation around the ethylenic bridge within its short lifetime. Strongly electron withdrawing



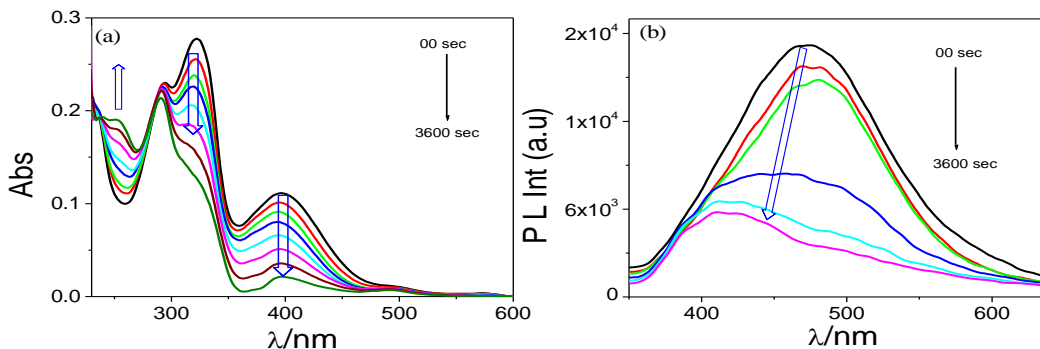


**Fig. 2.32.** UV-vis absorption (a) and emission (b) spectral changes of acid treated (3 equiv) dichloromethane solution of tpy-pvp-Me (**2**) upon irradiation with UV light. Excitation wavelength for recording the emission is 330 nm.

nitro group probably leads to lengthening of the C-C bond more compared with the other derivatives and thus facilitates the isomerization process. One of the most commonly accepted mechanism of the isomerization process involves the so-called phantom state  $p^*$  [60] because of its extremely short lifetime of  $\sim 1$  ps. The phantom state can be reached from both, electronically excited *trans* and *cis* states, as a consequence of a  $90^\circ$  twisting of the C=C bond around its axis. Now, the deactivation of this upper lying excited state gives rise to statistical formation of both *cis* and *trans* isomers. The second mechanism involves the intersystem crossing and isomerization of the molecule in the lowest excited triplet state, at the crossing point with the ground singlet pathway responsible for the *trans* to *cis* conversion. Intersystem crossing from the singlet  $S_1$  excited-state to a triplet excited-state can be neglected at room temperature in fluid solution, such that only the singlet state can be considered. However, the fluorescence decay from this state cannot be neglected. Interestingly, experiments show the *trans* form of the compounds are strongly fluorescent than their *cis* forms. In line with our observation, previously reported *trans*-*n*-pentane was found to much more fluorescent ( $\Phi_f = 0.035$ ) [63] than the corresponding *cis*-isomer ( $\Phi_f = \sim 9 \times 10^{-5}$ ) [64] and exhibits some solvent and temperature dependence.



## 2.4 Conclusions

With regard to our continued effort for developing switchable functional materials, we report in this work, photophysical and photo-isomerization behavior of a series of photochromic terpyridine derivatives covalently coupled with styrylbenzene unit. Covalent coupling of styrylbenzene moiety and terpyridine motif leads to the generation of ICT sensitive species whose photophysical properties are highly sensitive to light as well as other chemical stimuli (proton and solvents). Both electron-donating and electron-accepting groups were incorporated in the compound, tpy-pvp-X (X = H, Me, Cl, NO<sub>2</sub>, and Ph) to tune their photophysical as well photo-isomerization behaviors. All the compounds underwent *trans*→*cis* isomerization upon irradiation with UV light with substantial changes in their absorption and emission spectra. *Cis*→*trans* isomerization were also feasible upon interacting with visible light. *Trans*→*cis* isomerization leads quenching of emission, while backward *cis*→*trans* isomerization gives rise to restoration of the original emission. Thus, "on-off" and "off-on" emission switching was made possible upon alternate interaction of the compounds with UV and visible light. Interestingly, the photochromic and photo-isomerization behaviors of the compounds are strongly influenced by acid. Detailed kinetic and thermodynamic aspects of the photo-isomerization process were also addressed in this study. Finally, detailed computation work was also performed on both the *trans* and *cis* forms of the compounds by employing DFT and TD-DFT methods to acquire deeper insight about their electronic structures as well as proper assignment of the experimentally observed absorption and emission bands.

## 2.5 References

- [1] A. J. McConnell, C. S. Wood, P. P. Neelakandan, J. R. Nitschke, Stimuli-responsive metal-ligand assemblies, *Chem. Rev.* 115 (2015) 7729-7793.
- [2] Intelligent stimuli-responsive materials; Li, Q., Ed.; John Wiley & Sons, Inc.: Hoboken, Nj, 2013.
- [3] R. M. Manez, F. Sancenon, Fluorogenic and chromogenic chemosensors and reagents for anions, *Chem. Rev.* 103 (2003) 4419-4476.

- [4] M. Kurihara, H. Nishihara, Azo- and quinone-conjugated redox complexes-photo- and proton-coupled intramolecular reactions based on d- $\pi$  interaction, *Coord. Chem. Rev.* 226 (2002) 125-135.
- [5] C. C. Ko, V. W. W. Yam, Coordination compounds with photochromic ligands: ready tunability and visible light-sensitized photochromism, *Acc. Chem. Res.* 51 (2018) 149-159.
- [6] K. Matsuda, M. Irie, Diarylethene as a photoswitching unit, *J. Photochem. Photobiol. C* 5 (2004) 169-182.
- [7] T. Ikeda, O. Tsutsumi, Optical switching and image storage by means of azobenzene liquid-crystal films, *Science*. 268 (1995) 1873-1875.
- [8] S. Kawata, Y. Kawata, Three-dimensional optical data storage using photochromic materials, *Chem. Rev.* 100 (2000) 1777-1788.
- [9] K. Ichimura, S. K. Oh, M. Nakagawa, Light-driven motion of liquids on a photoresponsive surface. *Science*. 288 (2000) 1624-1626.
- [10] M. Irie, Diarylethenes for memories and switches. *Chem. Rev.* 100 (2000) 1685-1716.
- [11] B. L. Feringa, R. A. van Delden, M. K. ter Wiel, J. Chiroptical molecular switches. Wiley-VCH, 2001.
- [12] S. Kume, H. Nishihara, Metal-based photoswitches derived from photoisomerization, *Struct. Bond.* 123 (2007) 79-112.
- [13] Organic photochromic and thermochromic compounds, Vol 1: Main photochromic families, J.C.; Crano, R. Guglielmetti, Ed.; Plenum Press: New York, 1999.
- [14] Organic photochromic and thermochromic compounds, Vol 2: physicochemical studies, biological applications and thermochromism, J. C. Crano, R. Guglielmetti, Ed.; Plenum Press: New York, 1999.
- [15] Photochromic materials: preparation, properties and applications, H. Tian, J. Zhang, Ed.; Wiley-VCH: Weinheim, Germany, 2016.

- [16] N. M-W. Wu, M. Ng, W. H. Lam, H-L. Wong, V.W.W. Yam, Photochromic heterocycle-fused thieno[3,2-*b*]phosphole oxides as visible light switches without sacrificing photoswitching efficiency, *J. Am. Chem. Soc.* 139 (2017) 15142–15150.
- [17] S. Kume, H. Nishihara, Photochrome-coupled metal complexes: molecular processing of photon stimuli, *Dalton Trans.* (2008) 3260-3271.
- [18] H. Tian, S. Yang, Recent progresses on diarylethene based photochromic switches, *Chem. Soc. Rev.* 33 (2004) 85-97.
- [19] H. Rau, in *Photochromism: molecules and systems*, Ed. H. Dürr, H. B. Laurent, Elsevier, Amsterdam, 1990, 165-192.
- [20] H. Nishihara, *Inorganic photochromism*, ed. Y. F. Kodansha, Springer, 2007, 239-257.
- [21] H. M. D. Bandara, S.C. Burdette, Photoisomerization in different classes of azobenzene, *Chem. Soc. Rev.* 41 (2012) 1809–1825.
- [22] C. Bhaumik, S. Das, D. Maity, S. Baitalik, A terpyridyl-imidazole (tpy-HImzPh3) based bifunctional receptor for multichannel detection of  $\text{Fe}^{2+}$  and  $\text{F}^-$  ions, *Dalton Trans.* 40 (2011) 11795–11808.
- [23] D. Maity, C. Bhaumik, S. Karmakar, S. Baitalik, Photoinduced electron and energy transfer and pH-induced modulation of the photophysical properties in homo- and heterobimetallic complexes of ruthenium(II) and rhodium(III) based on a heteroditopic phenanthroline-terpyridine bridge, *Inorg. Chem.* 52 (2013) 7933–7946.
- [24] S. Karmakar, D. Maity, S. Mardanya, S. Baitalik, Demonstration of multiple logic operations in a heteroditopic pyrene–phenylimidazole–terpyridine conjugate based on optical responses by selective anions and cations: an experimental and theoretical investigation, *J. Phys. Chem. A.* 118 (2014) 9397–9410.
- [25] S. Karmakar, S. Mardanya, S. Das, S. Baitalik, Efficient deep-blue emitter and molecular-scale memory device based on dipyrityl-phenylimidazole-terpyridine assembly, *J. Phys. Chem. C.* 119 (2015) 6793–6805.

- [26] D. Mondal, M. Bar, D. Maity, S. Baitalik, Anthraimidazoledione-terpyridine-based optical chemosensor for anions and cations that works as molecular half-subtractor, key-pad lock, and memory device, *J. Phys. Chem. C*. 119(2015) 25429–25441.
- [27] P. Pal, S. Mukherjee, D. Maity, S. Baitalik, Synthesis, structural characterization, and luminescence switching of diarylethene-conjugated ru(II)-terpyridine complexes by trans-cis photoisomerization: experimental and DFT/TD-DFT investigation, *Inorg. Chem.* 57 (2018) 5743–5753.
- [28] M. Bar, S. Deb, A. Paul, S. Baitalik, Stimuli-responsive luminescent bis-tridentate Ru(II) complexes toward the design of functional materials, *Inorg. Chem.* 57 (2018) 12010–12024.
- [29] G. T. Morgan, F. H. Burstall, Dehydrogenation of pyridine by anhydrous ferric chloride, *J. Chem. Soc.* 1932, 20-30.
- [30] E. A. Medlycott, G. S. Hanan, Designing tridentate ligands for ruthenium(II) complexes with prolonged room temperature luminescence lifetimes, *Chem. Soc. Rev.* 34 (2005) 133-142.
- [31] A. K. Pal, G. S. Hanan, Design, synthesis and excited-state properties of mononuclear ru(II) complexes of tridentate heterocyclic ligands, *Chem. Soc. Rev.* 43 (2014) 6184-6197.
- [32] J. A. G. Williams, The coordination chemistry of dipyritylbenzene: N-deficient terpyridine or panacea for brightly luminescent metal complexes, *Chem. Soc. Rev.* 38 (2009) 1783-1801.
- [33] J. A. G. Williams, Photochemistry and photophysics of coordination compounds: platinum. photochemistry and photophysics of coordination compounds II, *Topics in Current Chemistry*, 281(2007) 205-268.
- [34] E. H. Hofmeier, U. S. Schubert, Recent developments in the supramolecular chemistry of terpyridine–metal complexes, *Chem. Soc. Rev.* 33 (2004) 373-399.
- [35] X. Y. Wang, A. Guerzo, R. H. Schmehl, Preferential solvation of an ILCT excited state in bis(terpyridine-phenylene-vinylene) Zn(II) complexes, *Chem. Commun.* (2002) 2344-2345.

- [36] X-Y. Wang, A. Del Guerzo, H. Tunuguntla, R. H. Schmehl, Photophysical behavior of ru(II) and Os(II) terpyridyl phenylene vinylene complexes: perturbation of MLCT state by intra-ligand charge-transfer state, *Res. Chem. Intermed.* 33 (2007) 63-77.
- [37] L. S. Natrajan, A. Toulmin, A. Chew, S. W. Magennis, Two-photon luminescence from polar bis-terpyridyl-stilbene derivatives of Ir(III) and Ru(II), *Dalton Trans.* 39 (2010) 10837-10846.
- [38] A. Sil, D. Giri, S. K. Patra, Arylene–vinylene terpyridine conjugates: highly sensitive, reusable and simple fluorescent probes for the detection of nitroaromatics, *J. Mater. Chem. C* 5 (2017) 11100-11110.
- [39] Y. Fan, J. Chen, L. Yu, A. Li, G. Zhai, Y. Lei, C. Zhu, Methyl substitution enhanced photoisomerization of *trans,trans*-1,4-diphenyl-1,3-butadiene: direct *Ab initio* trajectory surface hopping dynamic simulations, *Phys.Chem.Chem.Phys.* 20 (2018) 2260-2273.
- [40] B. Jędrzejewska, B. Ośmiałowska, R. Zaleśny, Application of spectroscopic and theoretical methods in the studies of photoisomerization and photophysical properties of the push–pull styryl-benzimidazole dyes, *Photochem. Photobiol. Sci.* 15 (2016) 117-128.
- [41] J. Saltiel, D. Papadimitriou, T.S.R. Krishna, Z-N. Huang, G. Krishnamoorthy, S. Laohhasurayotin, R.J. Clark, Photoisomerization of all-cis-1,6-diphenyl-1,3,5-hexatriene in the solid state and in solution: a simultaneous three-bond twist process, *Angew. Chem. Int. Ed.* 48 (2009) 8082 –8085.
- [42] J.-L. Lin, C.-W. Chen, S.-S. Sun, A. J. Lees, Photoswitching tetranuclear rhenium(I) tricarbonyl diimine complexes with a stilbene-like bridging ligand, *Chem. Commun.* 47 (2011) 6030-6032.
- [43] S.-S. Sun, J. A. Anspach, A. J. Lees, Self-assembly of transition-metal-based macrocycles linked by photoisomerizable ligands: examples of photoinduced conversion of tetranuclear-dinuclear squares, *Inorg. Chem.* 41 (2002) 1862-1869.

- [44] K. H. Glusac, I. Ghiviriga, K. A. Abboud, K. S. Schanze, Photophysics and photochemistry of stilbene-containing platinum acetylides, *J. Phys. Chem. B.* 108 (2004) 4969-4978.
- [45] J. J. Santos, S. H. Toma, P. M. Lalli, M. F. Riccio, M. N. Eberlin, H. E. Toma, K. Araki, Exploring the coordination chemistry of isomerizable terpyridine derivatives for successful analyses of cis and trans isomers by travelling wave ion mobility mass spectrometry, *Analyst.* 137 (2012) 4045-4051.
- [46] Y. Hasegawa, K. Takahashi, S. Kume, H. Nishihara, Complete solid state photoisomerization of bis(dipyrazolylstyrylpyridine)iron(II) to change magnetic properties, *Chem. Commun.* 47 (2011) 6846-6848.
- [47] K. Gille, H. Knoll, K. Quitzsch, Rate constants of the thermal cis-trans isomerization of azobenzene dyes in solvents, acetone/water mixtures, and in microheterogeneous surfactant solutions, *Int. J. Chem. Kinet.* 31(1999) 337-350.
- [48] T. Yutaka, I. Mori, M. Kurihara, J. Mizutani, K. Kubo, S. Furusho, K. Matsumura, N. Tamai, H. Nishihara, Synthesis, characterization, and photochemical properties of azobenzene-conjugated Ru(II) and Rh(III) bis(terpyridine) complexes, *Inorg. Chem.* 40 (2001), 4986-4995.
- [49] J. Otsuki, K. Suwa, K. Narutaki, C. Sinha, I. Yoshikawa, K. Araki, Photochromism of 2-(phenylazo)imidazoles, *J. Phys. Chem A.* 109 (2005) 8064-8069.
- [50] M. J. Frisch, G. W. Trucks, H. B. Schlegel, G. E. Scuseria, M. A. Robb, J. R. Cheeseman, G. Scalmani, V. Barone, B. Mennucci, G. A. Petersson, H. Nakatsuji, M. Caricato, X. Li, H. P. Hratchian, A. F. Izmaylov, J. Bloino, G. Zheng, J. L. Sonnenberg, M. Hada, M. Ehara, K. Toyota, R. Fukuda, J. Hasegawa, M. Ishida, T. Nakajima, Y. Honda, O. Kitao, H. Nakai, T. Vreven, J. A. Jr. Montgomery, J. E. Peralta, F. Ogliaro, M. Bearpark, J. J. Heyd, E. Brothers, K. N. Kudin, V. N. Staroverov, R. Kobayashi, J. Normand, K. A. Raghavachari, Rendell, J. C. Burant, S. S. Iyengar, J. Tomasi, M. Cossi, N. Rega, J. M. Millam, M. Klene, J. E. Knox, J. B. Cross, V. Bakken, C. Adamo, J. Jaramillo, R. Gomperts, R. E. Stratmann, O. Yazyev, A. J. Austin, R. Cammi, C. Pomelli, J. W. Ochterski, R. L. Martin, K. Morokuma, V. G. Zakrzewski, G. A. Voth, P. Salvador, J. J. Dannenberg,

- S. Dapprich, A. D. Daniels, Ö. Farkas, J. B. Foresman, J. V. Ortiz, J. Cioslowski, D. J. Fox, Gaussian 09, revision A.02; Gaussian Inc.: Wallingford, CT, 2009.
- [51] A. D. Becke, Density functional thermochemistry. III. the role of exact exchange, *J. Chem. Phys.* 98(1993) 5648-5652.
- [52] C. T. Lee, W. T.; Yang, R. G. Parr, Development of the colle-salvetti correlation-energy formula into a functional of the electron density, *Phys. Rev. B.* 37(1988) 785-789.
- [53] M. E. Casida, C. Jamorski, K. C. Casida, D. R. Salahub, Molecular excitation energy to high-lying bound state from time-dependent density functional response theory: characterization and correction of the time dependent local density approximation ionization threshold, *J. Chem. Phys.* 108(1998) 4439-4449.
- [54] R. E. Stratmann, G. E. Scuseria, M. J. Frisch, An efficient implementation of time-dependent density-functional theory for the calculation of excitation energies of large molecules, *J. Chem. Phys.* 109(1998) 8218-8224.
- [55] M. Caricato, B. Mennucci, J. Tomasi, F. Ingrosso, R. Cammi, S. Corni, G. Scalmani, Formation and relaxation of excited states in solution: A new time dependent polarizable continuum model based on time dependent density functional theory, *J. Chem. Phys.* 124 (2006) 124520-124530.
- [56] B. Mennucci, C. Cappelli, C. A. Guido, R. Cammi, J. Tomasi, Structures and properties of electronically excited chromophores in solution from the polarizable continuum model coupled to the time-dependent density functional theory, *J. Phys. Chem. A.* 113(2009) 3009.
- [57] R. Dennington, II. T. Keith, J. Millam, Gauss View 3; Semichem, Inc.: Shawnee Mission, KS, 2007.
- [58] N. M. O Boyle, A. L. Tenderholt, K. M. Langner, cclib: A Library for package independent computational chemistry algorithms, *J. Comput. Chem.* 29 (2008) 839.

- [59] Y. Li, J. Sun, K. Han, G. He, Z. Li, The dynamics of NO radical formation in the UV 266 nm photodissociation of nitroethane, *Chemical Physics Letters*, 421 (2006) 232-236.
- [60] D. H. Waldeck, Photoisomerization dynamics of stilbenes, *Chem. Rev.* 91(1991) 415-436.
- [61] F. D. Lewis, Formation and reactions of stilbene exciplexes, *Acc. Chem. Res.* 12 (1979) 152-158.
- [62] A. Momotake, T. Arai, Photochemistry and photophysics of stilbene dendrimers and related compounds, *J. Photochem. Photobiol. C* 5 (2004) 1-25.
- [63] J. L. Charlton, J. Saltiel, An analysis of trans-stilbene fluorescence quantum yields and lifetimes, *J. Phys. Chem.* 81 (1977) 1940-1944.
- [64] J. Saltiel, A. S. Waller, D. F. S. Jr, Dynamics of cis-stilbene photoisomerization: the adiabatic pathway to excited trans-stilbene, *J. Photochem. Photobiol. A* 65(1992) 29-40.

\*\*\*\*



## ***Chapter 3***

**Photo-switchable iron-terpyridine complexes  
functionalized with styrylbenzene Unit**

### 3.1 Introduction

Functional molecules with switchable spectral properties induced by light have received great attention due to their crucial roles in the design of optical materials, photoswitches and memory devices [1-6]. To this end, photoisomerization behaviours of a wide variety of compounds such as azobenzenes, stilbenes, diarylethenes, spiropyrans, and spirooxazines were thoroughly studied [7-12]. Transition metal-based compounds are very attractive in this regard over their organic counterparts as the complexes possess additional features in the context of better tunability of their electronic properties by varying both inorganic and organic components [13-24]. For coordination complexes, modulation of their properties by inducing conformational changes on the photo-responsive component appended on ligands has received most of the attentions. Majority of studies in this regard are mainly centered on noble metals which are very expensive and their synthetic procedures often required very drastic conditions [13-24]. Our aim in this work is to design suitable base-metal complexes which could exhibit similar behavior and can lead to the development of a new class of low-cost and easily synthesizable photo-switches.

In order to fulfill our objective, we report herein the synthesis, characterization, photophysics, and reversible *trans-cis* photoisomerization behaviours of three homoleptic Fe(II)-terpyridine complexes ( $[\text{Fe}(\text{tpy-pvp-X})_2]^{2+}$ , where X = H, Me, and  $\text{NO}_2$ ) covalently coupled with photo-active styrylbenzene moiety (**Chart 1**). Iron is the most abundant low-cost element in Earth's crust and also plays crucial role in transport and storage of oxygen and in electron transport in diverse metalloenzymes of living organisms [25-27]. Compared to their low spin  $d^6$  analogues (such as  $\text{Ru}^{2+}$  and  $\text{Os}^{2+}$ ), Fe(II)-polypyridine complexes usually don't function as effective sensitizers because of low lying  $^3/5\text{MC}$  states localized on Fe(II) induces very fast non-radiative deactivation leading to remarkable lowering of excited state lifetime [28-35]. Although the Fe(II)-terpyridine complexes don't exhibit Fe(II)-centred emission but they exhibit strong  $^1\text{MLCT}$  absorption at longer wavelength region ( $\sim 575$  nm) compared with both Ru(II)- and Os(II)-terpyridine motif [36,32-34]. Photoinduced isomerization studies of styrylbenzene appended heavier transition metal complexes (particularly Re, Ru, Ir and Pt) have been performed by several research groups in recent times [37-43]. These studies contribute

significantly for designing of photochemical molecular devices [44-52]. On the other hand, related studies incorporating styrylbenzene appended terpyridine ligands and 3d metals are relatively sparse in literature. Photo-isomerization behaviours of selected Fe(II) complexes based on terpyridine-azobene conjugate were reported by Nishihara and co-workers [53-54]. Prior to this work, only a single report on photo-isomerization behaviour of one Fe(II)-terpyridine complex covalently coupled with styrylbenzene moiety was reported by Araki and co-workers [55]. But to our knowledge, no detailed discussions on optical switching behaviours of Fe(II)-terpyridine complexes covalently coupled with photo-active styrylbenzene moiety were reported in the literature. In the present work, we thoroughly studied the effect of solvents and influence of both electron donating and electron withdrawing substituent (X) on the photophysics as well as thermodynamic and kinetic aspects of isomerization process of complexes. Effect of excitation wavelength on thermodynamic and kinetic aspects of photoisomerization process were also addressed in this work. Recently, we reported photophysics and photoisomerization behaviours of a homoleptic ( $[\text{Ru}(\text{tpy-pvp-X})_2]^{2+}$ ) as well as a heteroleptic series ( $[(\text{tpy-PhCH}_3)\text{Ru}(\text{tpy-pvp-X})]^{2+}$ ) of Ru-terpyridine complexes with same styrylbenzene-terpyridine ligands [56-57]. In this study, we will also be interested to compare the photo-isomerization behaviours of present Fe(II) complexes with previously reported analogous complexes of Ru(II). Finally, DFT and TD-DFT calculations were also performed on various forms of the complexes (*trans-trans*, *trans-cis* and *cis-cis*) to get insight about the electronic structures as well as for appropriate assignment of their optical spectral band.

## 3.2 Experimental

### 3.2.1 Materials

Chemicals and solvents were procured either from Sigma or from local vendors. Synthesis and characterisation of tpy-pvp-X (X = H, Me, and NO<sub>2</sub>) has been provided in chapter 2 [58]. Detailed procedure for synthesis, purification and characterization of Fe(II) complexes are provided in the next section.

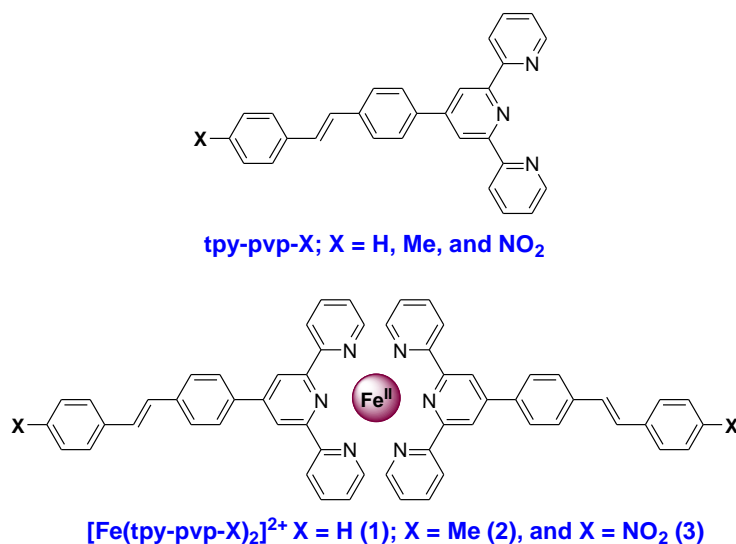


**Chart 3.1.** Chemical structures of the complexes under present investigation.

### 3.2.2 Synthesis of the metal complexes

A general procedure that was adopted for the complexes is described below.

#### *[Fe(tpy-pvp-H)<sub>2</sub>](ClO<sub>4</sub>)<sub>2</sub> (1)*

To a stirred CHCl<sub>3</sub>-MeOH (1:2, v/v) solution (25 mL) of tpy-pvp-H (206 mg, 0.5 mmol), a MeOH solution of Fe(ClO<sub>4</sub>)<sub>2</sub>·6H<sub>2</sub>O (91 mg 0.25 mmol) was added. The color of the solution immediately changed into blue-violet and during stirring for ~1h, a microcrystalline compound deposited. The compound was filtered, washed with water, and dried in a vacuum. Crude compound was washed with chloroform and then purified by alumina column chromatography using 1:10 (v/v) PhCH<sub>3</sub>-MeCN mixture. The compound was finally recrystallized from MeCN-MeOH (1:2, v/v) mixture resulting in violet microcrystalline compound: yield 169 mg (64%). Elemental anal. Calcd. for C<sub>58</sub>H<sub>42</sub>N<sub>6</sub>Cl<sub>2</sub>O<sub>8</sub>Fe: C, 64.63; H, 3.927; N, 7.797. Found: C, 64.64; H, 3.920; N, 7.795. <sup>1</sup>H NMR (400 MHz, CD<sub>3</sub>CN, δ/ppm) : 9.24 (s, 4H, H<sub>3'</sub>), 8.66 (d, 4H, *J*=8.0, H<sub>6</sub>), 8.39 (d, 4H, *J*=8.0, H<sub>8</sub>), 8.03 (d, 4H, *J*=8.4, H<sub>7</sub>), 7.97-7.93 (m, 4H, H<sub>4</sub>), 7.73(d, 4H, *J*=7.20, H<sub>11</sub>), 7.52-7.48 (m, 10H, H<sub>3</sub>+H<sub>10</sub>+H<sub>12</sub>), 7.44-7.38 (m, 2H, H<sub>13</sub>), 7.23 (d, 2H, *J*=5.6, H<sub>9</sub>), 7.14-7.10 (m, 4H, H<sub>5</sub>). ESI-MS (positive, CH<sub>3</sub>CN): *m/z* = 439.08 (100%) [Fe(tpy-pvp-H)<sub>2</sub>]<sup>2+</sup>.

#### *[Fe(tpy-pvp-Me)<sub>2</sub>](ClO<sub>4</sub>)<sub>2</sub> (2)*

Yield 156 mg (62%). Elemental anal. Calcd. for  $C_{60}H_{46}N_6Cl_2O_8Fe$ : C, 65.17; H, 4.19; N, 7.60. Found: C, 65.18; H, 4.18; N, 7.61.  $^1H$  NMR (400 MHz,  $CD_3CN$ ,  $\delta/ppm$ ): 9.17 (s, 4H,  $H_{3'}$ ), 8.58 (d, 4H,  $J=8.0$ ,  $H_6$ ), 8.31 (d, 4H,  $J=7.6$ ,  $H_8$ ), 7.94 (d, 4H,  $J=8.0$ ,  $H_7$ ), 7.89-7.85 (m, 4H,  $H_4$ ), 7.55 (d, 4H,  $J=8.0$ ,  $H_{11}$ ), 7.43 (d, 2H,  $J=16.4$ ,  $H_{10}$ ), 7.33 (d, 2H,  $J=16.0$ ,  $H_9$ ), 7.24 (d, 4H,  $J=7.6$ ,  $H_{12}$ ), 7.16 (d, 4H,  $J=5.6$ ,  $H_3$ ), 7.06-7.03 (m, 4H,  $H_5$ ). ESI-MS (positive,  $CH_3CN$ ):  $m/z = 453.08$  (100%)  $[Fe(tpy-pvp-Me)_2]^{2+}$ .

### *$[Fe(tpy-pvp-NO_2)_2](ClO_4)_2$ (3)*

Yield 162 mg (63%). Elemental anal. Calcd. for  $C_{58}H_{40}N_8Cl_2O_{12}Fe$ : C, 59.65; H, 3.45; N, 9.59. Found: C, 59.64; H, 3.46; N, 9.58.  $^1H$  NMR (400 MHz,  $CD_3CN$ ,  $\delta/ppm$ ): 9.18 (s, 4H,  $H_{3'}$ ), 8.59 (d, 4H,  $J=8.0$ ,  $H_6$ ), 8.34 (d, 4H,  $J=8.0$ ,  $H_8$ ), 8.26 (d, 4H,  $J=8.0$ ,  $H_7$ ), 8.01 (d, 4H,  $J = 7.6$ ,  $H_{11}$ ), 7.90-7.84 (m, 8H,  $H_4+H_{10}+H_{12}$ ), 7.62-7.52 (m, 4H,  $H_3+H_{12}$ ), 7.17-7.16 (nr, 4H,  $H_9+H_3$ ), 7.07-7.04 (m, 4H,  $H_5$ ). ESI-MS (positive,  $CH_3CN$ ):  $m/z = 484.04$  (100%)  $[Fe(tpy-pvp-NO_2)_2]^{2+}$ .

### 3.2.3 Physical measurements

The details of instruments and procedures of physicochemical measurements have already been discussed in [chapter 2](#). The detailed description about the computation methods is also provided in [chapter 2](#).

## 3.3 Results and discussions

### 3.3.1 Synthesis and characterization

The synthesis and characterization of the ligands have already been described in [chapter 2](#). The complexes were synthesized by reacting tpy-pvp-X ( $X = H, Me$  and  $NO_2$ ) with  $Fe(ClO_4)_2$  (1:2 ratio) in  $CHCl_3$ -MeOH (1:1, v/v) mixture at room temperature. Purification of the complexes were carried out by alumina column chromatography {1:10 (v/v)  $PhCH_3$ -MeCN mixture} followed by recrystallization from  $CHCl_3$ -MeOH (1:2, v/v) mixture. All complexes were characterized by elemental (C, H and N) analyses, high resolution mass and NMR spectral measurements and characterization data were presented in [Fig. 3.1-3.3](#).

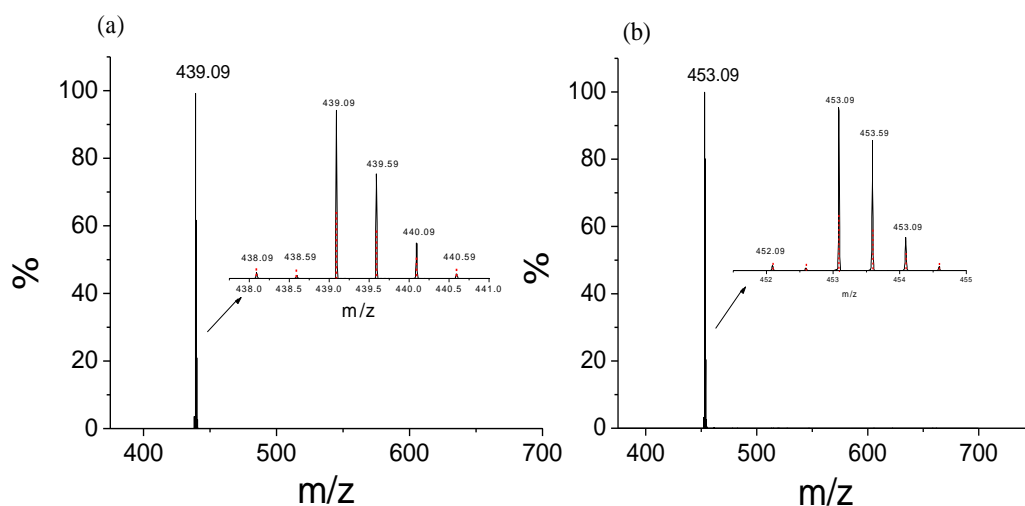


**Fig. 3.1.** ESI-MS (positive) for the complex cation of  $[\text{Fe}(\text{tpy-pvp-H})_2]^{2+}$  with  $m/z = 439.09$  (a) and  $[\text{Fe}(\text{tpy-pvp-CH}_3)_2]^{2+}$  with  $m/z = 453.09$  (b) in acetonitrile showing experimental and simulated isotopic distribution patterns.

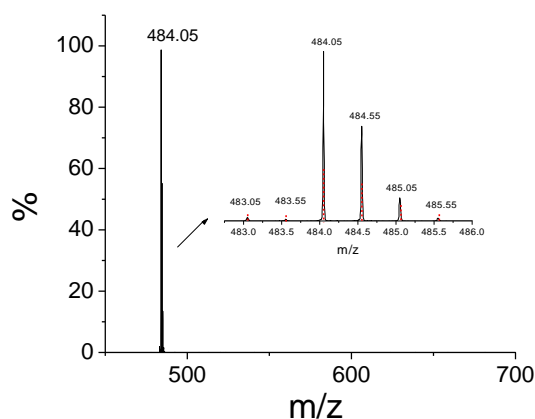


**Fig. 3.2.** ESI-MS (positive) for the complex cations of  $[\text{Fe}(\text{tpy-pvp-NO}_2)_2]^{2+}$  with  $m/z = 484.05$  in acetonitrile showing experimental and simulated isotopic distribution patterns.

### 3.3.1.1 NMR spectra

$^1\text{H}$  NMR spectra of **1-3** were acquired in  $\text{CD}_3\text{CN}$  and displayed in Fig. 3.3. Tentative assignments of all peaks were done with the help of their COSY NMR spectra together with by comparing the spectra of structurally similar complexes. The singlet at  $\sim 2.31$  ppm (not shown in Fig. 3.3) counting three protons for **2** is clearly due to  $-\text{CH}_3$  group of coordinated tpy- $\text{PhCH}_3$  moiety. Another singlet which appears within 9.17-9.24

ppm corresponds to  $H_3'$  proton. A pair of doublets within 7.16-7.90 ppm is assignable as the protons of ethylenic double bond ( $H_9$  and  $H_{10}$ ) and corresponds to *trans-trans* conformation. In some cases, they appeared within the broad multiplet because of the coincidence of other protons.

### 3.3.2 Computational investigations

Geometry optimization of the complexes was carried out with the aid of Gaussian 09 program in acetonitrile medium (Fig. 3.4). Selected bond distances and angles are given in Tables 3.1-3.4. In all complexes, Fe(II) is coordinated in bis-tridentate manner with distorted octahedral geometry. Frontier molecular orbital sketch are presented in Figs. 3.5-3.7. Among four HOMOs, the first two (HOMO and HOMO-1) are mainly composed of vinyl phenyl and *p*-substituted phenyl group, while the other two HOMOs (HOMO-2 and HOMO-3) are mainly localized on Fe(II) center on all of their *trans-trans*, *trans-cis* and *cis-cis* forms. On the other hand, all four LUMOs are composed predominantly of tpy moiety with small contribution of vinyl phenyl group with the exception of  $[\text{Fe}(\text{tpy-pvp-NO}_2)_2]^{2+}$ , where LUMOs are mainly localized either on nitrobenzyl group or on tpy moiety (Table 3.5 and Fig. 3.7). TD-DFT calculated results of the complexes in their *trans-trans*, *trans-cis* and *cis-cis* forms are summarized in Table 3.6-3.8 and the involvement of FMOs in their lowest energy band are displayed in Fig. 3.8. The lowest energy band for Fe(II) complexes is an admixture of  $\text{Fe}^{\text{II}}(\text{d}\pi) \rightarrow \pi^*(\text{tpy-pvp-X})$  metal-to-ligand charge transfer (MLCT) and phenyl-vinyl  $\rightarrow$  terpyridine charge transfer (LLCT) transitions in the visible region. The next higher energy band is found to be an admixture of both LLCT and  $\pi\text{-}\pi^*$  transitions.

### 3.3.3 Absorption and emission spectra

Comparison between the calculated and experimental absorption spectra of the complexes in acetonitrile is presented in Fig. 3.9. All complexes show a very intense band at ~575 nm due to  $\text{Fe}^{\text{II}}(\text{d}\pi) \rightarrow \pi^*(\text{tpy-pvp-X})$  MLCT transition. TD-DFT calculations also indicate finite contribution of phenyl-vinyl  $\rightarrow$  terpyridine charge transfer (LLCT) character to the said MLCT band. The band is shifted to lower energy region compared with the parent  $[\text{Fe}(\text{tpy})_2]^{2+}$  (551 nm) complex probably because of charge delocalization induced by additional phenyl-vinyl group at 4'-position of the terpyridine moiety [53-55].

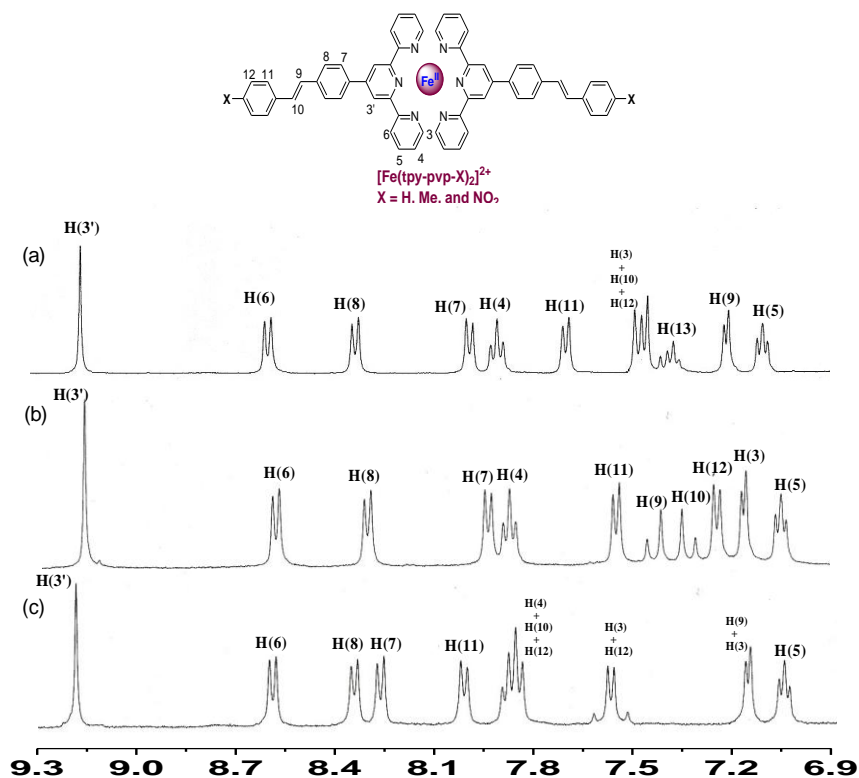


**Fig. 3.3.**  $^1\text{H}$  NMR (400 MHz) spectra of  $[\text{Fe}(\text{tpy-pvp-H})_2]^{2+}$  (a),  $[\text{Fe}(\text{tpy-pvp-Me})_2]^{2+}$  (b) and  $[\text{Fe}(\text{tpy-pvp-NO}_2)_2]^{2+}$  (c) in  $\text{CD}_3\text{CN}$ .

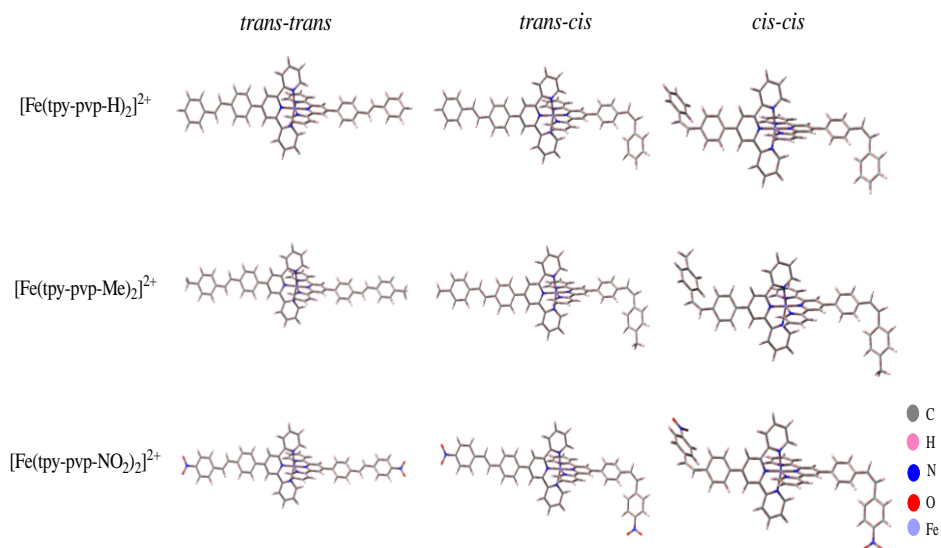


**Fig. 3.4.** Ground state optimized geometries of *trans-trans*, *trans-cis* and *cis-cis* forms of the complexes of composition  $[\text{Fe}(\text{tpy-pvp-X})_2]^{2+}$  ( $\text{X} = \text{H}, \text{Me}, \text{and NO}_2$ ) in acetonitrile.



## Chapter 3

**Table 3.1** Selected calculated bond distances (Å) of *trans-trans*, *trans-cis* and *cis-cis* form of  $[\text{Fe}(\text{tpy-pvp-X})_2]^{2+}$  where X= H, Me, NO<sub>2</sub>.

<i>trans-trans</i>		<i>trans-cis</i>		<i>cis-cis</i>	
$[\text{Fe}(\text{tpy-pvp-H})_2]^{2+}$		$[\text{Fe}(\text{tpy-pvp-H})_2]^{2+}$		$[\text{Fe}(\text{tpy-pvp-H})_2]^{2+}$	
Fe1-N1	2.011	Fe1-N1	2.011	Fe1-N1	2.011
Fe1-N2	1.906	Fe1-N2	1.907	Fe1-N2	1.907
Fe1-N3	2.011	Fe1-N3	2.012	Fe1-N3	2.011
Fe1-N4	2.011	Fe1-N4	2.012	Fe1-N4	2.011
Fe1-N5	1.906	Fe1-N5	1.906	Fe1-N5	1.907
Fe1-N6	2.011	Fe1-N6	2.011	Fe1-N6	2.011
$[\text{Fe}(\text{tpy-pvp-Me})_2]^{2+}$		$[\text{Fe}(\text{tpy-pvp-Me})_2]^{2+}$		$[\text{Fe}(\text{tpy-pvp-Me})_2]^{2+}$	
Fe1-N1	2.011	Fe1-N1	2.011	Fe1-N1	2.011
Fe1-N2	1.906	Fe1-N2	1.907	Fe1-N2	1.907
Fe1-N3	2.011	Fe1-N3	2.012	Fe1-N3	2.011
Fe1-N4	2.011	Fe1-N4	2.012	Fe1-N4	2.011
Fe1-N5	1.906	Fe1-N5	1.906	Fe1-N5	1.907
Fe1-N6	2.011	Fe1-N6	2.010	Fe1-N6	2.011
$[\text{Fe}(\text{tpy-pvp-NO}_2)_2]^{2+}$		$[\text{Fe}(\text{tpy-pvp-NO}_2)_2]^{2+}$		$[\text{Fe}(\text{tpy-pvp-NO}_2)_2]^{2+}$	
Fe1-N1	2.010	Fe1-N1	2.011	Fe1-N1	2.011
Fe1-N2	1.906	Fe1-N2	1.906	Fe1-N2	1.906
Fe1-N3	2.011	Fe1-N3	2.011	Fe1-N3	2.011
Fe1-N4	2.011	Fe1-N4	2.010	Fe1-N4	2.011
Fe1-N5	1.906	Fe1-N5	1.906	Fe1-N5	1.906
Fe1-N6	2.010	Fe1-N6	2.012	Fe1-N6	2.010

**Table 3.2** Selected calculated bond angles (deg) of *trans-trans*, *trans-cis* and *cis-cis* form of  $[\text{Fe}(\text{tpy-pvp-H})_2]^{2+}$ .

<i>trans-trans</i>		<i>trans-cis</i>		<i>cis-cis</i>	
N6Fe1N2	98.97	N6Fe1N2	98.71	N6Fe1N2	98.91
N6Fe1N3	91.39	N6Fe1N3	91.42	N6Fe1N3	91.38
N6Fe1N4	162.02	N6Fe1N4	162.01	N6Fe1N4	162.02
N6Fe1N5	81.00	N6Fe1N5	81.04	N6Fe1N5	81.02
N6Fe1N1	91.45	N6Fe1N1	91.33	N6Fe1N1	91.37
N2Fe1N3	81.02	N2Fe1N3	81.00	N2Fe1N3	81.00
N2Fe1N4	98.99	N2Fe1N4	99.26	N2Fe1N4	99.05
N2Fe1N1	81.00	N2Fe1N1	80.97	N2Fe1N1	81.02
N4Fe1N5	81.02	N4Fe1N5	80.97	N4Fe1N5	81.00
N4Fe1N1	91.39	N4Fe1N1	91.48	N4Fe1N1	91.38
N4Fe1N3	91.35	N4Fe1N3	91.36	N4Fe1N3	91.43
N5Fe1N1	98.97	N5Fe1N1	98.87	N5Fe1N1	98.92
N5Fe1N3	98.99	N5Fe1N3	99.14	N5Fe1N3	99.05
N1Fe1N3	162.02	N1Fe1N3	161.98	N1Fe1N3	162.02
N2Fe1N5	179.97	N2Fe1N5	179.71	N2Fe1N5	179.92

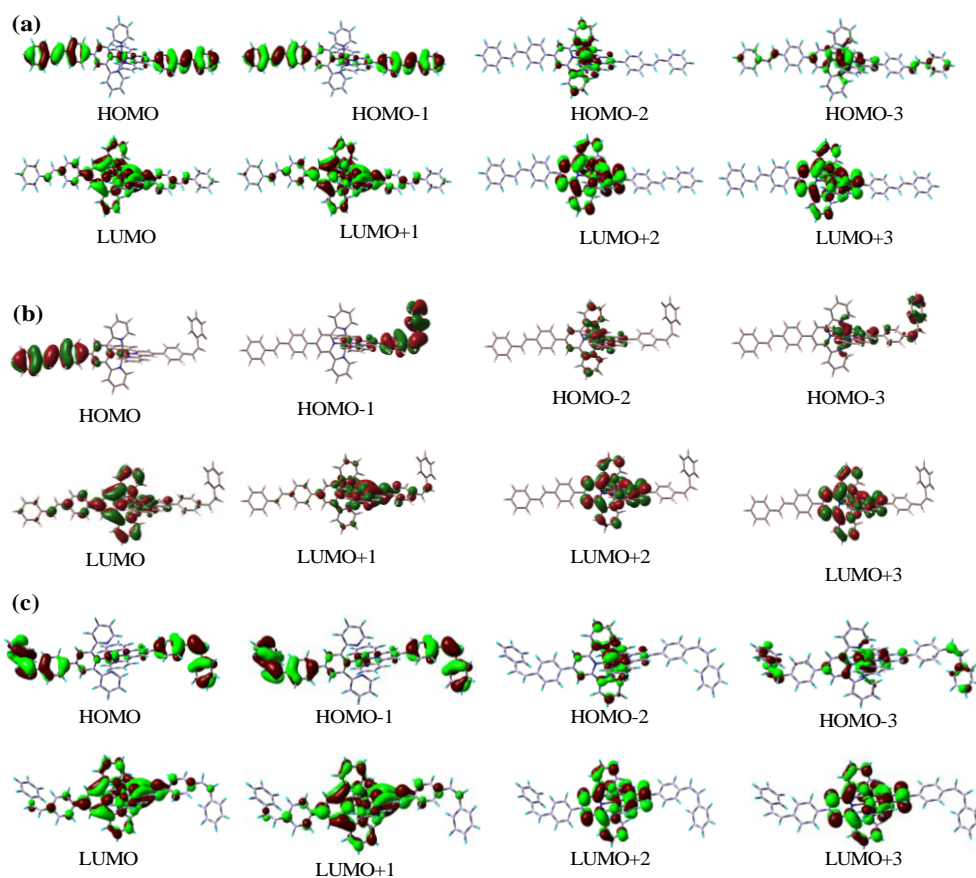


**Fig. 3.5.** Schematic drawings of the selective frontier molecular orbitals of *trans-trans* (a) *trans-cis* (b) and *cis-cis* (c) forms of  $[\text{Fe}(\text{tpy-pvp-H})_2]^{2+}$  (**1**) in acetonitrile.

**Table 3.3** Selected calculated bond angles (deg) of *trans-trans*, *trans-cis* and *cis-cis* form of  $[\text{Fe}(\text{tpy-pvp-Me})_2]^{2+}$ .

<i>trans-trans</i>		<i>trans-cis</i>		<i>cis-cis</i>	
N6Fe1N2	98.97	N6Fe1N2	98.86	N6Fe1N2	98.89
N6Fe1N3	91.38	N6Fe1N3	91.71	N6Fe1N3	91.44
N6Fe1N4	162.02	N6Fe1N4	161.04	N6Fe1N4	162.01
N6Fe1N5	81.00	N6Fe1N5	80.55	N6Fe1N5	81.01
N6Fe1N1	91.45	N6Fe1N1	91.46	N6Fe1N1	91.36
N2Fe1N3	81.01	N2Fe1N3	80.47	N2Fe1N3	80.99
N2Fe1N4	99.00	N2Fe1N4	100.09	N2Fe1N4	99.09
N2Fe1N1	81.00	N2Fe1N1	80.52	N2Fe1N1	81.01
N4Fe1N5	81.01	N4Fe1N5	80.48	N4Fe1N5	80.99
N4Fe1N1	91.38	N4Fe1N1	91.50	N4Fe1N1	91.44
N4Fe1N3	91.36	N4Fe1N3	91.54	N4Fe1N3	91.34
N5Fe1N1	98.97	N5Fe1N1	99.36	N5Fe1N1	98.89
N5Fe1N3	99.00	N5Fe1N3	99.63	N5Fe1N3	99.09
N1Fe1N3	162.02	N1Fe1N3	160.99	N1Fe1N3	162.01
N2Fe1N5	179.97	N2Fe1N5	179.40	N2Fe1N5	179.86

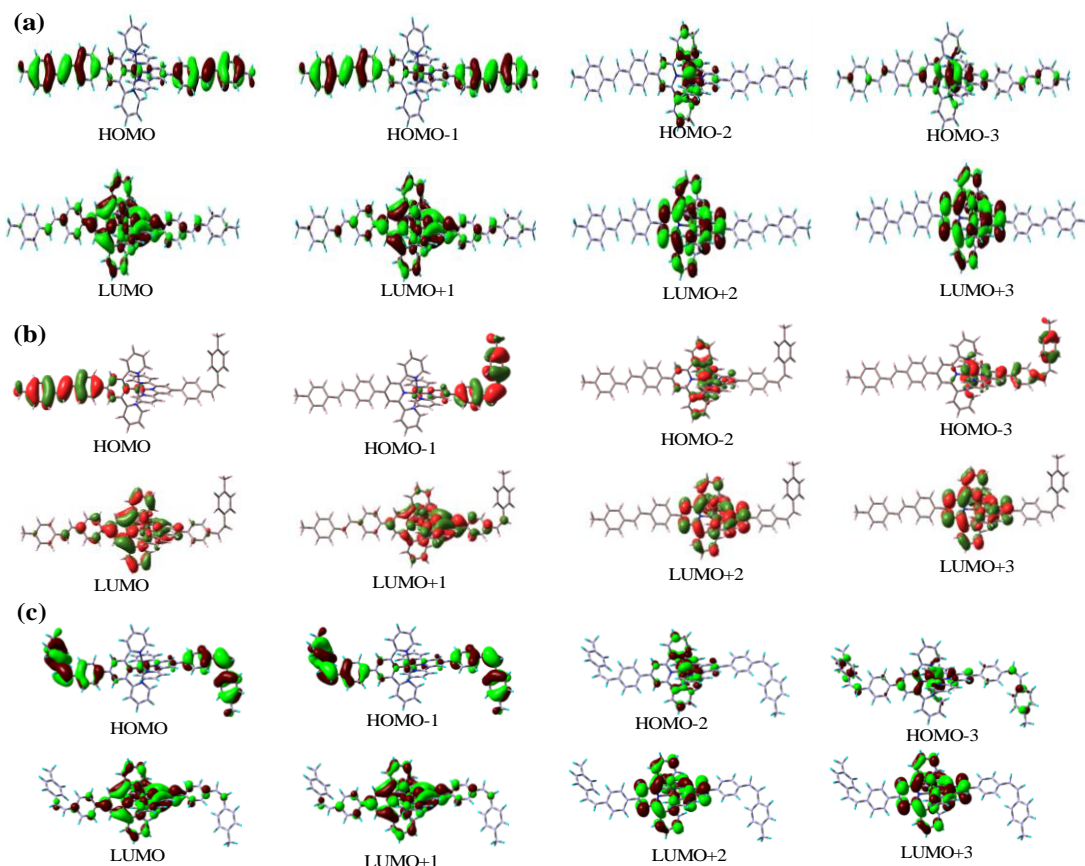


**Fig. 3.6.** Schematic drawings of the selective frontier molecular orbitals of *trans-trans* (a) *trans-cis* (b) and *cis-cis* (c) forms of  $[\text{Fe}(\text{tpy-pvp-Me})_2]^{2+}$  (**2**) in acetonitrile.

**Table 3.4** Selected calculated bond angles (deg) of *trans-trans*, *trans-cis* and *cis-cis* form of  $[\text{Fe}(\text{tpy-pvp-NO}_2)_2]^{2+}$ .

<i>trans-trans</i>		<i>trans-cis</i>		<i>cis-cis</i>	
N6Fe1N2	98.98	N6Fe1N2	99.18	N6Fe1N2	98.94
N6Fe1N3	91.38	N6Fe1N3	91.24	N6Fe1N3	91.29
N6Fe1N4	162.06	N6Fe1N4	162.07	N6Fe1N4	162.06
N6Fe1N5	81.02	N6Fe1N5	81.01	N6Fe1N5	81.03
N6Fe1N1	91.44	N6Fe1N1	91.51	N6Fe1N1	91.45
N2Fe1N3	81.04	N2Fe1N3	81.02	N2Fe1N3	81.02
N2Fe1N4	98.94	N2Fe1N4	98.73	N2Fe1N4	98.99
N2Fe1N1	81.02	N2Fe1N1	81.02	N2Fe1N1	81.03
N4Fe1N5	81.04	N4Fe1N5	81.05	N4Fe1N5	81.02
N4Fe1N1	91.38	N4Fe1N1	91.23	N4Fe1N1	91.29
N4Fe1N3	91.34	N4Fe1N3	91.58	N4Fe1N3	91.52
N5Fe1N1	98.98	N5Fe1N1	98.90	N5Fe1N1	98.94
N5Fe1N3	98.94	N5Fe1N3	99.03	N5Fe1N3	98.99
N1Fe1N3	162.06	N1Fe1N3	162.05	N1Fe1N3	162.06
N2Fe1N5	179.98	N2Fe1N5	179.77	N2Fe1N5	179.97

**Table 3.5** Selected MOs along with their energies and compositions in the ground state for  $[\text{Fe}(\text{tpy-pvp-H})_2]^{2+}$  (**1**) and  $[\text{Fe}(\text{tpy-pvp-Me})_2]^{2+}$  (**2**) and  $[\text{Fe}(\text{tpy-pvp-NO}_2)_2]^{2+}$  (**3**) in acetonitrile.

MO	$[\text{Fe}(\text{tpy-pvp-H})_2]^{2+}$ ( <b>1</b> )											
	Energy/ev			% Compositions								
	Trans-trans	Trans-cis	Cis-cis	Trans-trans			Trans-cis			Cis-cis		
				Fe	Typy	Styryl-benz	Benzal	Benzal	Fe	Typy	Styryl-benz	Benzal
LUMO+3	-2.65	-3.06	-2.66	2.67	96.82	0.50	0.00	0.00	2.64	96.87	0.47	0.00
LUMO+2	-2.68	-3.08	-2.69	0.00	99.50	0.49	0.00	0.00	0.01	99.52	0.45	0.00
LUMO+1	-2.93	-3.31	-2.92	4.23	79.88	13.53	2.37	1.09	4.24	83.87	10.79	1.16
LUMO	-2.94	-3.32	-2.93	4.11	79.94	13.60	2.36	1.66	4.17	82.65	11.50	1.16
HOMO	-5.99	-6.21	-6.12	6.01	6.09	57.64	30.25	33.57	3.60	5.23	57.58	28.48
HOMO-1	-5.99	-6.36	-6.12	5.81	5.94	57.82	30.41	32.03	4.83	5.24	57.89	28.70
HOMO-2	-6.49	-6.89	-6.50	78.10	21.86	0.02	0.00	0.00	78.12	21.83	0.03	0.00
HOMO-3	-6.61	-6.98	-6.61	71.46	16.39	5.68	6.45	8.05	70.11	16.33	5.49	8.87
	$[\text{Fe}(\text{tpy-pvp-Me})_2]^{2+}$ ( <b>2</b> )											
	Trans-trans	Trans-cis	Cis-cis	Fe	Typy	Styryl-benz	Me-Benz	Me-Benz	Fe	Typy	Styryl-benz	Me-Benz
LUMO+3	-2.65	-2.83	-2.66	2.67	96.81	0.50	0.00	0.00	2.21	97.15	0.63	0.00
LUMO+2	-2.68	-2.85	-2.68	0.00	99.49	0.49	0.00	0.00	0.03	99.31	0.64	0.00
LUMO+1	-2.92	-3.09	-2.92	4.24	80.66	12.92	2.16	0.98	4.37	84.40	10.24	0.98
LUMO	-2.93	-3.09	-2.92	4.11	80.71	13.00	2.16	1.54	4.57	83.32	10.88	1.54
HOMO	-5.87	-5.92	-6.00	4.07	5.15	54.04	36.72	40.53	1.85	4.29	53.22	40.53
HOMO-1	-5.87	-6.08	-6.00	3.94	5.03	54.15	36.86	41.89	2.19	3.81	52.18	41.89
HOMO-2	-6.48	-6.84	-6.49	78.11	21.85	0.02	0.00	0.56	76.79	22.20	0.44	0.56
HOMO-3	-6.58	-6.87	-6.58	72.07	16.88	4.45	6.57	9.22	66.80	17.33	6.64	9.22
	$[\text{Fe}(\text{tpy-pvp-NO}_2)_2]^{2+}$ ( <b>3</b> )											
	Trans-trans	Trans-cis	Cis-cis	Fe	Typy	Styryl-benz	Nitro-Benz	Nitro-Benz	Fe	Typy	Styryl-benz	Nitro-Benz
LUMO+3	-2.93	-2.90	-2.93	4.01	78.44	9.61	7.92	64.30	0.68	27.92	7.09	81.83
LUMO+2	-2.94	-2.90	-2.94	3.87	78.39	9.65	8.06	7.73	0.07	90.71	1.47	81.80
LUMO+1	-3.57	-3.19	-3.55	0.33	3.88	12.95	82.82	14.35	3.67	67.96	14.01	1.90
LUMO	-3.57	-3.24	-3.55	0.33	3.98	12.99	82.69	21.70	3.19	56.33	18.77	1.96
HOMO	-6.31	-6.39	-6.39	19.67	9.94	51.99	18.38	25.71	6.08	6.53	61.68	12.25
HOMO-1	-6.31	-6.54	-6.40	19.31	9.63	52.46	18.58	20.46	10.45	7.78	61.31	11.82
HOMO-2	-6.53	-6.90	-6.52	78.03	21.63	0.00	0.00	0.01	77.41	22.51	0.05	0.00
HOMO-3	-6.72	-7.00	-6.75	60.30	13.51	16.57	9.59	5.34	71.88	16.54	6.23	26.72

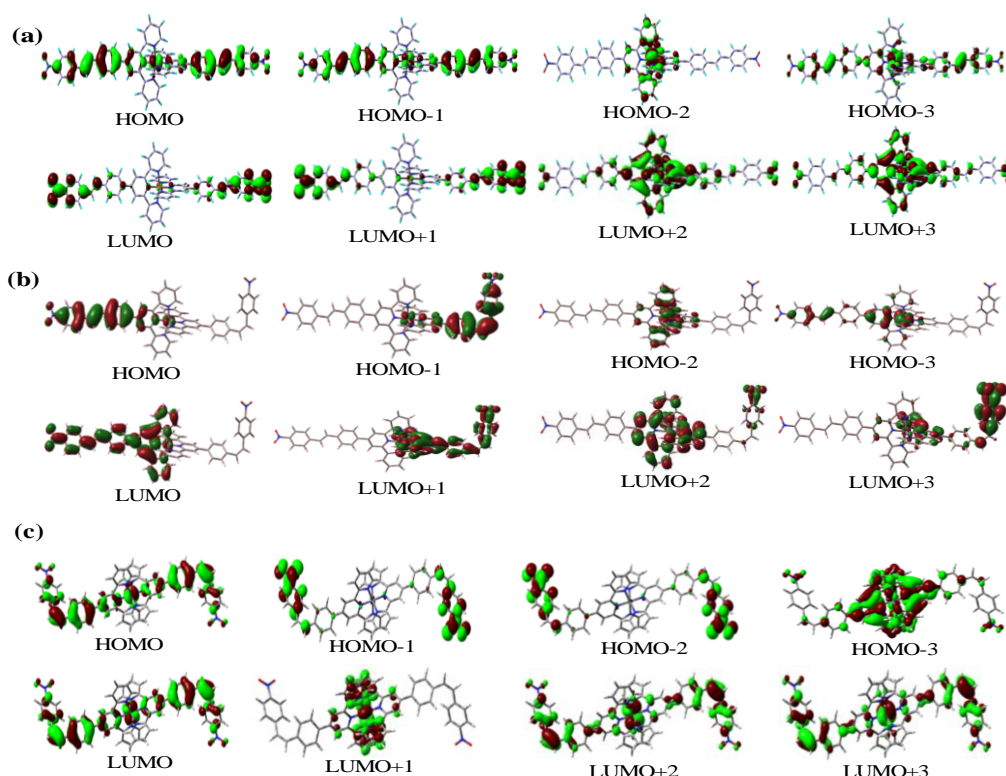


**Fig. 3.7.** Schematic drawings of the selective frontier molecular orbitals of *trans-trans* (a) *trans-cis* (b) and *cis-cis* (c) forms of  $[\text{Fe}(\text{tpy-pvp-NO}_2)_2]^{2+}$  (**3**) in acetonitrile.

**Table 3.6** Selected UV-vis energy transitions at the TD-DFT/B3LYP level for  $[\text{Fe}(\text{tpy-pvp-H})_2]^{2+}$  in acetonitrile.

Excited state	$\lambda_{\text{cal}}/\text{nm}$	Oscillator strength(f)	$\lambda_{\text{expt}}/\text{nm}$	Key transitions	Character
<i>Trans-trans</i> $[\text{Fe}(\text{tpy-pvp-H})_2]^{2+}$					
S <sub>6</sub>	483	1.46	576	H-4→L+1 (18%), H-1→L+1(49%), H→L (26%),	MLCT, LLCT
S <sub>15</sub>	420	0.29	372	H-3→L (43%), H-4→L+1(25%), H→L (16%)	LLCT
S <sub>24</sub>	349	2.09	323	H-1→L +4(47%), H→L+5 (4%)	LLCT, $\pi$ - $\pi^*$
<i>Trans-cis</i> $[\text{Fe}(\text{tpy-pvp-H})_2]^{2+}$					
S <sub>2</sub>	496	0.91	576	H→L(67%), H-4→L (13%)	MLCT, LLCT
S <sub>24</sub>	354	1.16	374	H→L+4 (95%)	LLCT
S <sub>27</sub>	341	0.45	321	H-1→L+5 (94%)	LLCT, $\pi$ - $\pi^*$
<i>Cis-cis</i> $[\text{Fe}(\text{tpy-pvp-H})_2]^{2+}$					
S <sub>6</sub>	471	0.91	576	H-4→L (13%), H-3→L+1 (18%), H-1→L+1 (36%), H→L (32%)	MLCT, LLCT
S <sub>15</sub>	414	0.27	374	H-4→L (28%), H-3→L+1 (26%), H-2→L+2 (16%), H-1→L+1 (14%), H→L (14%)	LLCT
S <sub>26</sub>	336	1.08	321	H-1→L+4 (46%), H→L+5 (47%)	LLCT, $\pi$ - $\pi^*$

**Table 3.7** Selected UV-vis energy transitions at the TD-DFT/B3LYP level for  $[\text{Fe}(\text{tpy-pvp-Me})_2]^{2+}$  in acetonitrile.

Excited state	$\lambda_{\text{cal}}/\text{nm}$	Oscillator strength(f)	$\lambda_{\text{expt}}/\text{nm}$	Key transitions	Character
<i>Trans-trans</i> $[\text{Fe}(\text{tpy-pvp-Me})_2]^{2+}$					
S <sub>2</sub>	494	1.57	575	H→L (57%), H-3→L(15%), H-1→L+1 (24%)	MLCT, LLCT
S <sub>17</sub>	427	0.12	375	H-4→L+1 (39%), H-3→L(37%), H-1→L+1 (9%)	LLCT
S <sub>24</sub>	355	2.19	323	H-1→L+4 (47%), H→L+5 (48%)	LLCT, $\pi$ - $\pi^*$
S <sub>57</sub>	301	0.12	290	H-9→L (46%), H-8→L+1(39%)	$\pi$ - $\pi^*$ , LLCT
<i>Trans-cis</i> $[\text{Fe}(\text{tpy-pvp-Me})_2]^{2+}$					
S <sub>2</sub>	512	1.24	575	H→L(50%), H→L+1 (27%), H-4→L(4%)	MLCT, LLCT
S <sub>24</sub>	362	1.16	374	H→L+4 (96%)	LLCT
S <sub>33</sub>	331	0.15	321	H→L+8 (93%), H-4→L+8 (4%)	LLCT, $\pi$ - $\pi^*$
S <sub>90</sub>	278	0.42	290	H-12→L+3(12%), H-11→L+3(28%), H-12→L+3(12%)	
<i>Cis-cis</i> $[\text{Fe}(\text{tpy-pvp-Me})_2]^{2+}$					
S <sub>6</sub>	479	1.01	575	H-1→L+1 (43%), H→L (31%), H-3→L+1 (17%), H-4→L (8%)	MLCT, LLCT
S <sub>26</sub>	343	1.10	374	H-1→L+4 (47%), H→L+5 (48%)	LLCT
S <sub>39</sub>	314	0.21	321	H-8→L (11%), H-7→L+1 (10%), H-2→L+6 (31%), H→L+8(16%)	LLCT, $\pi$ - $\pi^*$
S <sub>86</sub>	279	0.51	290	H-12→L+2 (27%), H-10→L+2 (24%), H-9→L+3 (30%)	

The next higher energy band(s) spanning with 368-376 nm is due to phenyl-vinyl→terpyridine charge transfer transitions. Multiple very intense peaks within UV region arise from ligand centred  $\pi$ - $\pi^*$  transitions. It is observed that maximum of MLCT and LLCT band in the complexes varies to a small extent depending upon electronic nature of the substituent, X. A large disagreement between experimental and theoretical absorption spectra is noticed in Fig. 3.9. In particular, the presence of a large band within the spectral domain of 400-600 nm in the computed spectra is not reflected in the experimental spectra. This disagreement gives an indication of an inappropriate level of calculations for 1<sup>st</sup> row transition metal complexes. Our method is based on very limited basis sets leading to very localized Kohn-Sham orbitals that do not necessary reflect the real electronic densities in play.

## Chapter 3

**Table 3.8** Selected UV-vis energy transitions at the TD-DFT/B3LYP level for  $[\text{Fe}(\text{tpy-pvp-NO}_2)_2]^{2+}$  in acetonitrile.

Excited state	$\lambda_{\text{cal}}/\text{nm}$	Oscillator strength(f)	$\lambda_{\text{expt}}/\text{nm}$	Key transitions	Character
<i>Trans-trans</i> $[\text{Fe}(\text{tpy-pvp-NO}_2)_2]^{2+}$					
S <sub>2</sub>	510	2.61	575	H-1→L+1 (40%), H→L(46%),	MLCT
S <sub>17</sub>	423	0.57	371	H-4→L (40%), H-3→L+1(37%), H-1→L+3 (10%)	LLCT
S <sub>48</sub>	326	0.94	322	H-1→L +6(41%), H→L+7 (44%)	LLCT, $\pi$ - $\pi^*$
S <sub>80</sub>	292	0.17	285	H-5→L+2 (12%), H-4→L+7(30%), H-3→L+6 (32%)	$\pi$ - $\pi^*$ , LLCT
<i>Trans-cis</i> $[\text{Fe}(\text{tpy-pvp-NO}_2)_2]^{2+}$					
S <sub>2</sub>	493	1.97	576	H-1→L+1(11%), H→L(39%), H→L+1 (19%),	MLCT
S <sub>20</sub>	405	0.14	376	H-4→L (11%), H-4→L+1 (19%), H-2→L+4 (37%), H-1→L+2 (23%)	LLCT
S <sub>44</sub>	325	0.42	322	H→L+6 (56%)	LLCT, $\pi$ - $\pi^*$
S <sub>68</sub>	300	0.27	285	H-1→L+1 (44%), H-4→L+11 (10%), H-1→L+7 (12%)	
<i>Cis-cis</i> $[\text{Fe}(\text{tpy-pvp-NO}_2)_2]^{2+}$					
S <sub>2</sub>	500	0.92	576	H-1→L+1 (40%), H→L (47%)	MLCT
S <sub>12</sub>	449	0.21	376	H-4→L+2 (10%), H-3→L+3 (12%) H-1→L+3 (31%), H→L+2 (28%)	LLCT
S <sub>50</sub>	321	0.40	322	H-10→L (10%), H-9→L+1(10%), H-1→L+6 (27%), H→L+7 (29%)	LLCT, $\pi$ - $\pi^*$
S <sub>83</sub>	288	0.16	285	H-6→L+4 (18%), H-4→L+7(23%), H-3→L+6 (25%)	

On excitation at the lowest energy absorption band (~575 nm), complexes do not exhibit any luminescence. The photophysics of Fe(II)-polypyridine complexes gets complicated by the presence of low-lying metal-centered ( $^3/5\text{MC}$ ) excited states which get populated upon surface crossing from MLCT state within ultrafast time domain [28-35]. This phenomenon is frequently happened in Fe(II)-polypyridine complexes which is responsible for their non-emitting characteristics [28-35]. Upon excitation at the LLCT or  $\pi$ - $\pi^*$  band, the complexes display an intense emission band in spectral domain of 463-503 nm, probably due to LLCT transition (Fig. 3.10). It is to be mentioned here that the free ligands, upon excitation at their LLCT band (spanning within the range of 325-361 nm), display intense emission band in the wavelength range of 398-420 nm. Thus,



coordinating influence of  $\text{Fe}^{2+}$  leads to red-shift of ligand-centered emission in the Fe(II)-terpyridine complexes.

In-situ formation of Fe(II) complexes were also monitored through absorption and emission spectroscopy (Fig. 3.11-3.13). It is observed that a new band is evolved at ~575 nm and intensity of the band increases linearly with  $\text{Fe}^{2+}$  addition till the  $[\text{Fe}^{2+}]/[\text{tpy-pvp-X}]$  ratio reaches to 0.5. Addition of  $\text{Fe}^{2+}$  beyond 0.5 equiv does not produce any further change (Fig. 3.11a-3.13a). The titration profile based on absorbance at 575 nm and several clean isosbestic points imply single conversion of free tpy-pvp-X to  $[\text{Fe}(\text{tpy-pvp-X})_2]^{2+}$ . The composition of the complexes were also confirmed by high resolution mass spectra. The change of emission intensity of the LLCT band on gradual addition of  $\text{Fe}^{2+}$  is delineated in Fig. 3.11b-3.13b and the insets show that complete quenching of emission occurs upon addition of 0.5 equiv of  $\text{Fe}^{2+}$  ion.

#### 3.3.4 Photo-isomerization behaviours

All three complexes possess two isomerizable styrylbenzene units. We are thus interested to investigate their spectral behaviours upon action of light. We carried out photoisomerization studies of the complexes in few selected solvents, viz. dichloromethane, acetonitrile, methanol and dimethylsulfoxide at room temperature (25 °C). In addition, both UV (334 nm) and visible (436 nm) light source were used for irradiating the solutions of the complexes. At first, isomerization studies are carried out in dichloromethane in presence of UV light. The intensity of both MLCT band at ~575 nm and LLCT at ~375 nm was found to decrease to a small extent for **1** and **2**, whereas increase for the nitro-derivative (**3**) (Fig. 3.14a-c). In the emission side, photo-irradiation induces remarkable decrease of ligand-centred emission band intensity at ~500 nm with the exception of nitro-derivative (**3**) where small enhancement is noticed (Fig. 3.14d-f).

It is observed that prolonged irradiation leads to gradual decrease of both MLCT and LLCT bands in all three complexes with concomitant increase of  $\pi$ - $\pi^*$  band intensities in the UV region and eventually the MLCT band is completely removed which is indicative of de-coordination of  $\text{Fe}^{2+}$  centre from the complex backbone (Fig. 3.15-3.17). The final spectrum in each case looks very similar to that of the photolyzed



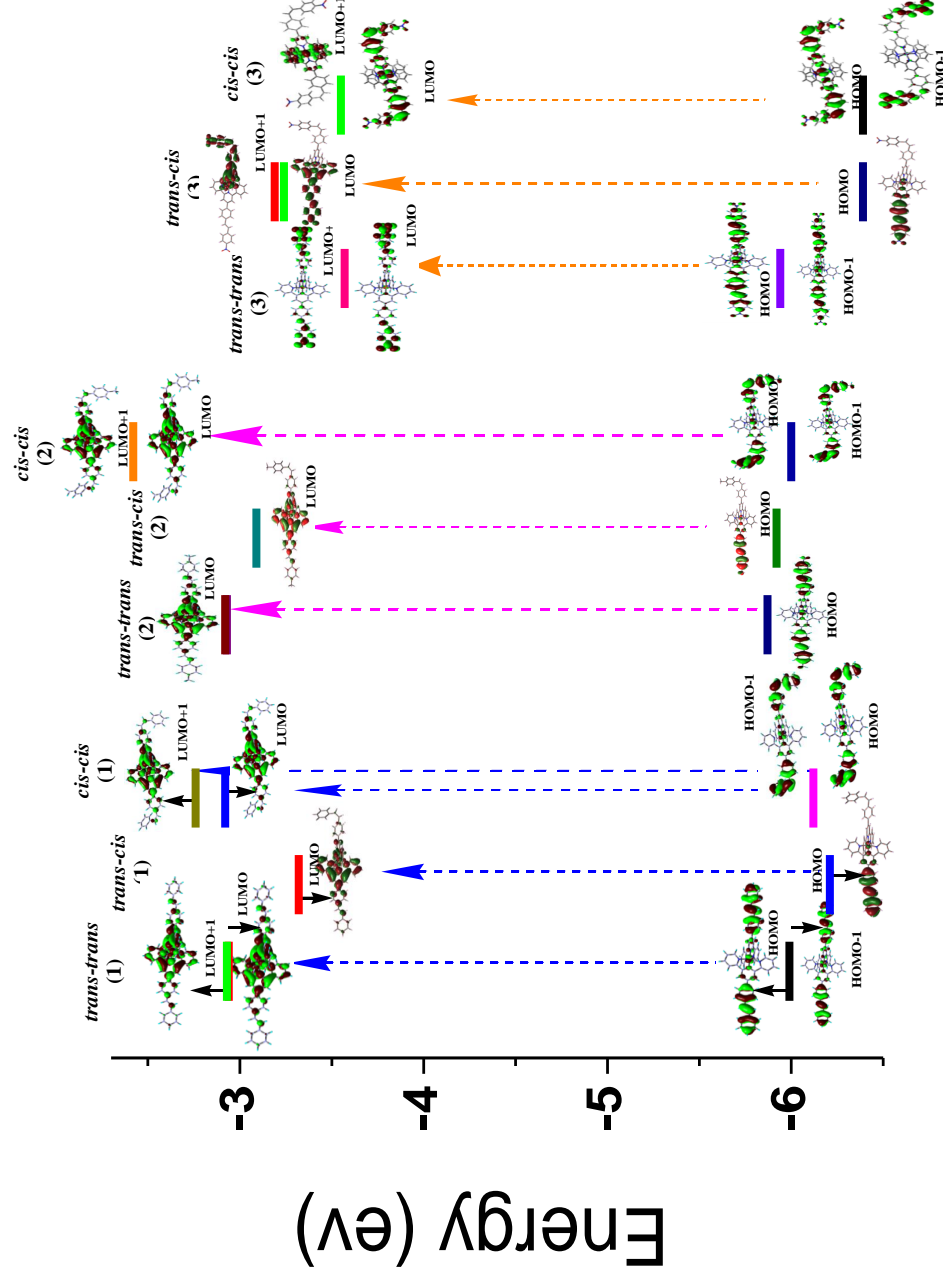


**Fig. 3.8.** Calculated energy level diagram in acetonitrile depicting the dominant transition that comprises the lowest-energy absorption band for *trans-trans*, *trans-cis* and *cis-cis* form of  $[(\text{tpy-pvp-X})_2\text{Fe}]^{2+}$  with X= H (**1**), Me (**2**), and NO<sub>2</sub> (**3**).

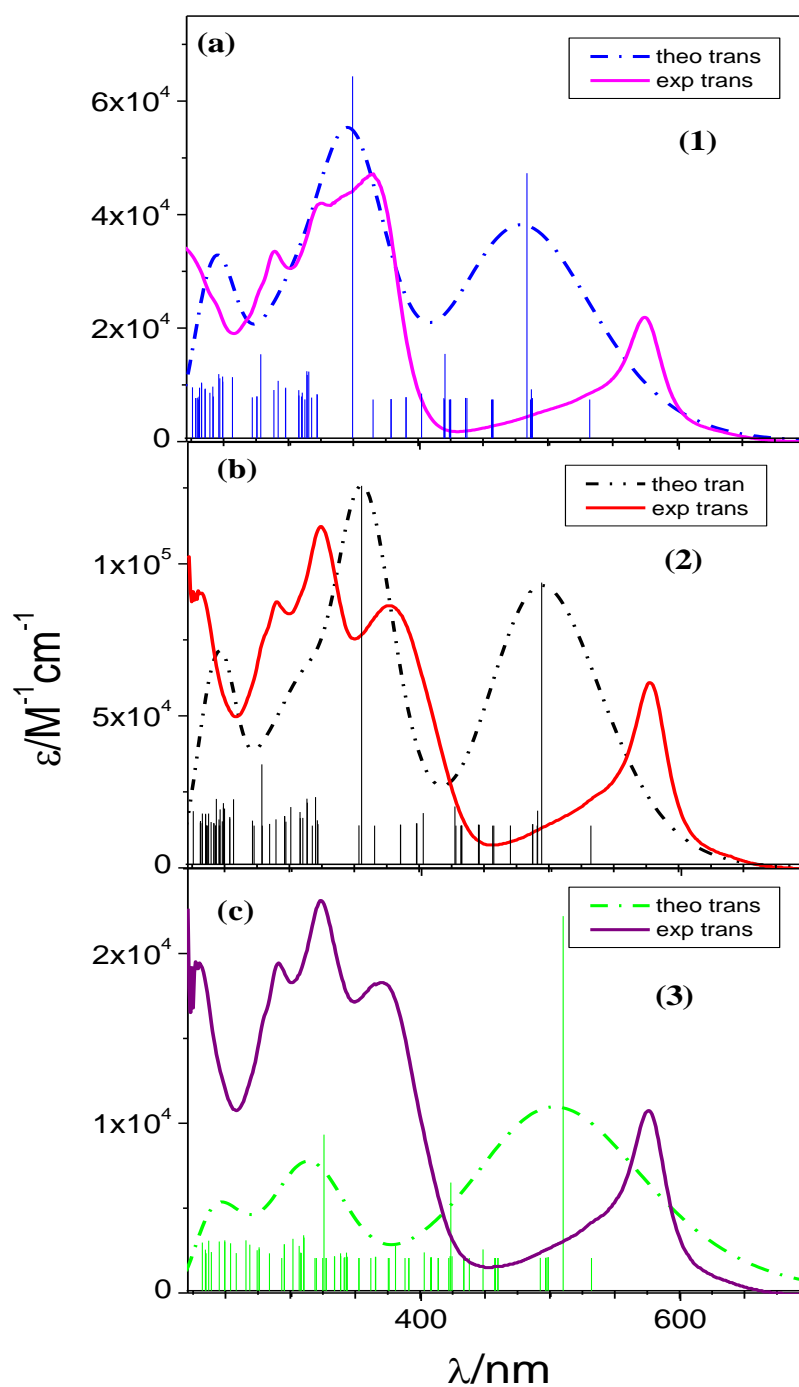


**Fig. 3.9.** Overlay of the calculated (dotted lines) and experimental (solid lines) UV-vis absorption spectra of *trans*-[Fe(tpy-pvp-X)<sub>2</sub>]<sup>2+</sup> with X= H (1), Me (2), and NO<sub>2</sub> (3) in acetonitrile. Calculated results are also presented in the sticks form.

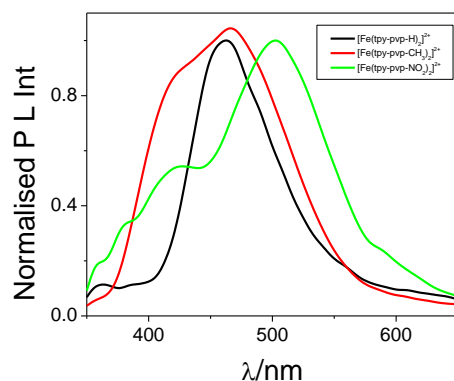


**Fig. 3.10.** Emission spectra of the complexes in dichloromethane upon excitation at 330 nm.

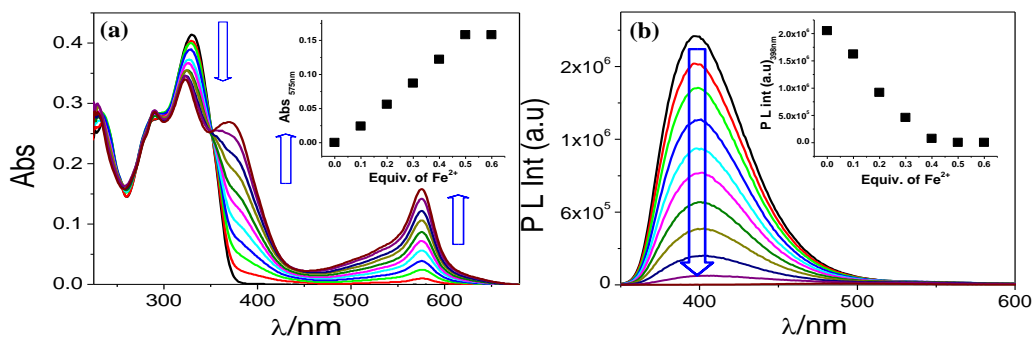


**Fig. 3.11.** UV-vis absorption (a) and emission ( $\lambda_{\text{ex}} = 330$  nm) (b) spectral changes of tpy-pvp-H in dichloromethane upon incremental addition of  $\text{Fe}^{2+}$ . Inset to figure (a) shows the change of absorbance at 575 nm, while inset to figure b indicates the change in emission intensity at 398 nm vs. equivalent of  $\text{Fe}^{2+}$ .

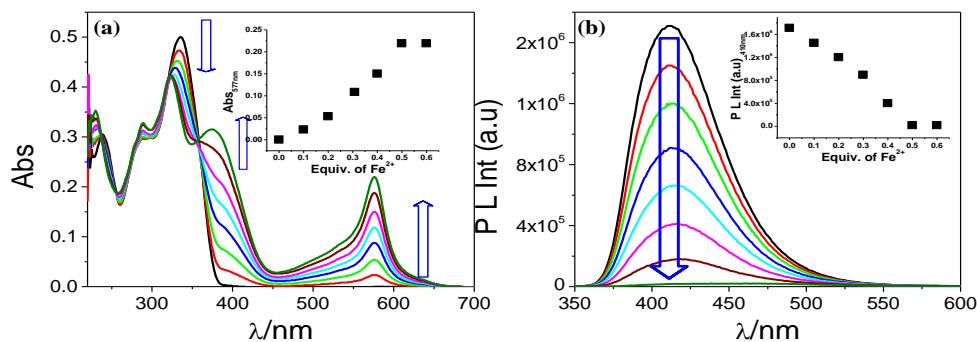


**Fig. 3.12.** UV-vis absorption (a) and emission ( $\lambda_{\text{ex}} = 330$  nm) (b) spectral changes of tpy-pvp-Me in dichloromethane upon incremental addition of  $\text{Fe}^{2+}$ . Inset to figure a shows the change of absorbance at 577 nm, while inset to figure b indicates the change in emission intensity at 410 nm vs. equivalent of  $\text{Fe}^{2+}$ .

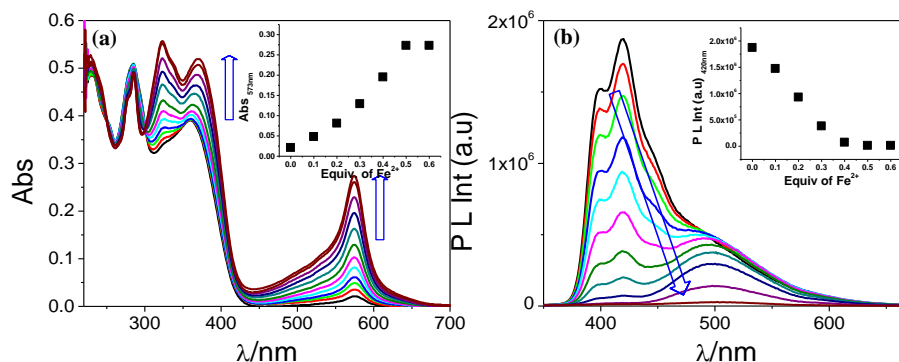


**Fig. 3.13.** UV-vis absorption (a) and emission ( $\lambda_{\text{ex}} = 330 \text{ nm}$ ) (b) spectral changes of tpy-pvp-NO<sub>2</sub> in dichloromethane upon incremental addition of Fe<sup>2+</sup>. Inset to figure a shows the change of absorbance at 573nm, while inset to figure b indicates the change in emission intensity at 420 nm vs. equivalent of Fe<sup>2+</sup>.

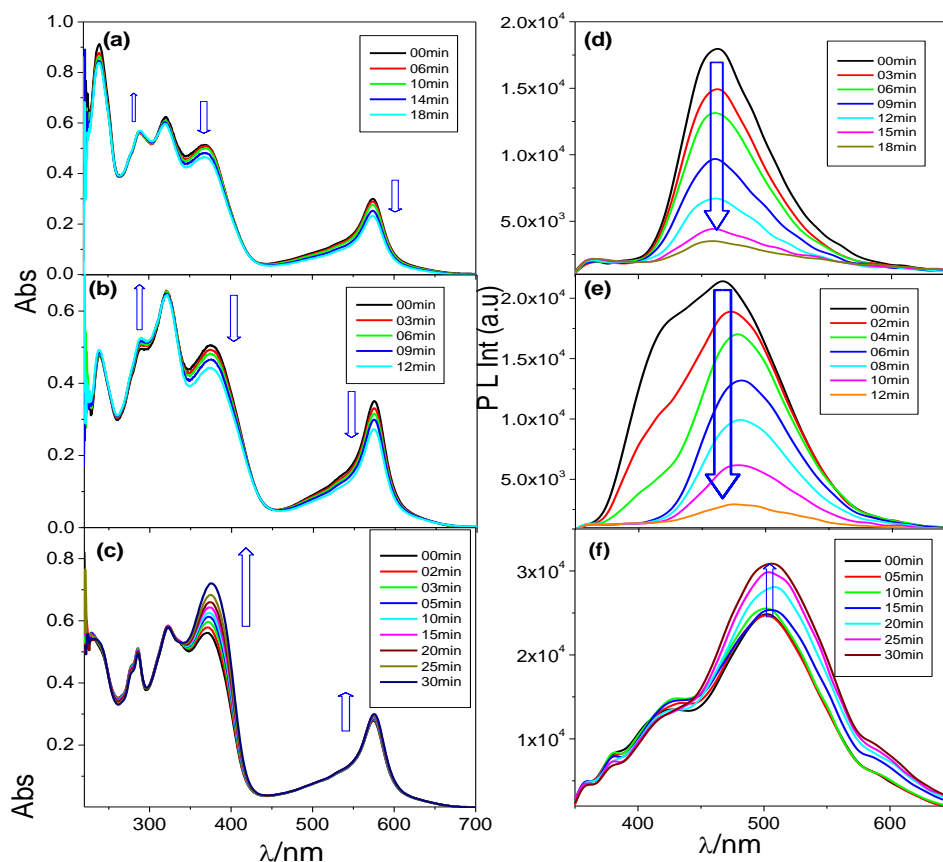


**Fig. 3.14.** Absorption and emission ( $\lambda_{\text{ex}} = 330 \text{ nm}$ ) spectral change of [Fe(tpy-pvp-H)<sub>2</sub>]<sup>2+</sup> (a and d, respectively), [Fe(tpy-pvp-Me)<sub>2</sub>]<sup>2+</sup> (b and e, respectively) and [Fe(tpy-pvp-NO<sub>2</sub>)<sub>2</sub>]<sup>2+</sup> (c and f, respectively) in dichloromethane upon irradiation with UV light. Insets to the figures a-f indicate the irradiation time.

product (*cis*-form) of free ligand [58]. Continued photo-irradiation, also leads to gradual increase of emission intensity in the second step and finally reaches at saturation at the end of photolysis (Fig. 3.15b-3.17b). Enhancement of emission intensity in the second step is again indicative of de-coordination of  $\text{Fe}^{2+}$  from complex architecture. In presence of visible light source, we observed almost similar trend (with small variation of spectral profile) but the rate is much faster than with UV light (Fig. 3.18-3.19). Thus, in dichloromethane, the first-step change is due to *trans*→*cis* isomerization while the second-step change corresponds to de-coordination  $\text{Fe}^{2+}$  from complex architecture.

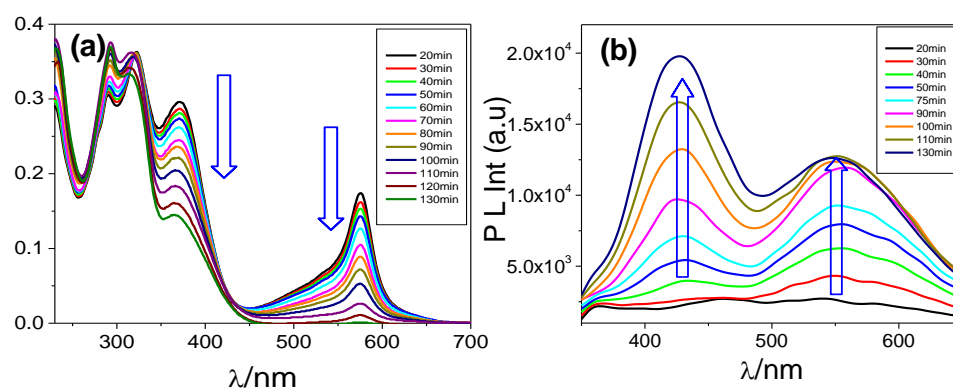


**Fig. 3.15.** Second step change in absorption and emission ( $\lambda_{\text{ex}} = 330 \text{ nm}$ ) (c) spectrum of  $[\text{Fe}(\text{tpy-pvp-H})_2]^{2+}$  (1) (a and b, respectively) in dichloromethane upon irradiation with UV light indicating the de-coordination of the complex. Insets to figure a and indicate the irradiation time.

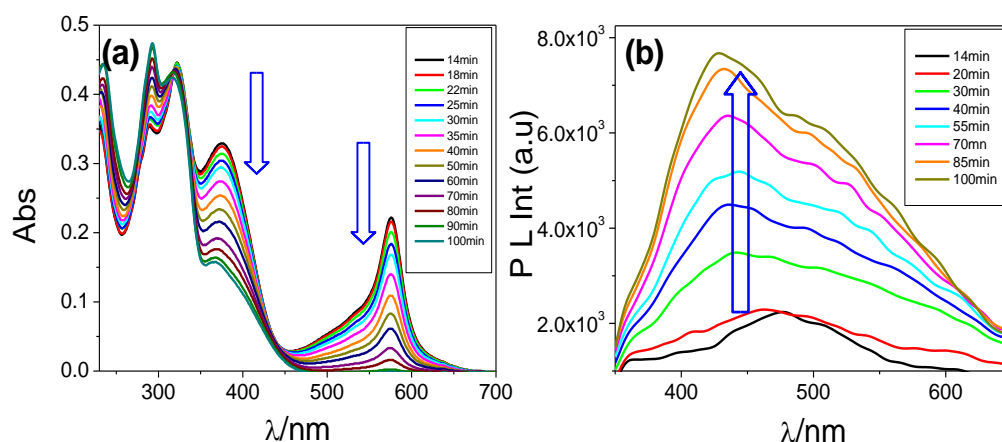


**Fig. 3.16.** Second step change in absorption and emission ( $\lambda_{\text{ex}} = 330 \text{ nm}$ ) (c) spectrum of  $[\text{Fe}(\text{tpy-pvp-Me})_2]^{2+}$  (2) (a and b, respectively) in dichloromethane upon irradiation with UV light indicating the de-coordination of the complex. Insets to figure a and indicate the irradiation time.

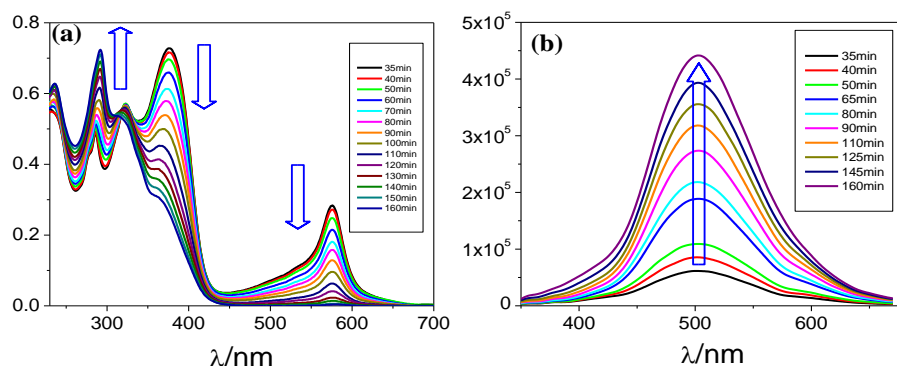


**Fig. 3.17.** Second step change in absorption and emission ( $\lambda_{\text{ex}} = 330 \text{ nm}$ ) (c) spectrum of  $[\text{Fe}(\text{tpy-pvp-NO}_2)_2]^{2+}$  (**3**) (a and b, respectively) in dichloromethane upon irradiation with UV light indicating the de-coordination of the complex. Insets to figure a and indicate the irradiation time.

As photo-irradiation, irrespective of irradiation wavelength, of DCM solution of the complexes leads to de-coordination, we are interested to see the behaviours of the complexes in other solvents. To this end, we have taken a representative complex,  $[\text{Fe}(\text{tpy-pvp-H})_2]^{2+}$  and carried out isomerization experiments in three additional solvents, *viz.* acetonitrile, methanol and dimethylsulfoxide. Absorption and emission spectral changes of  $[\text{Fe}(\text{tpy-pvp-H})_2]^{2+}$  upon action of visible light are presented in Fig. 3.20-3.22, while in presence of UV light are displayed in Fig. 3.23-3.25.

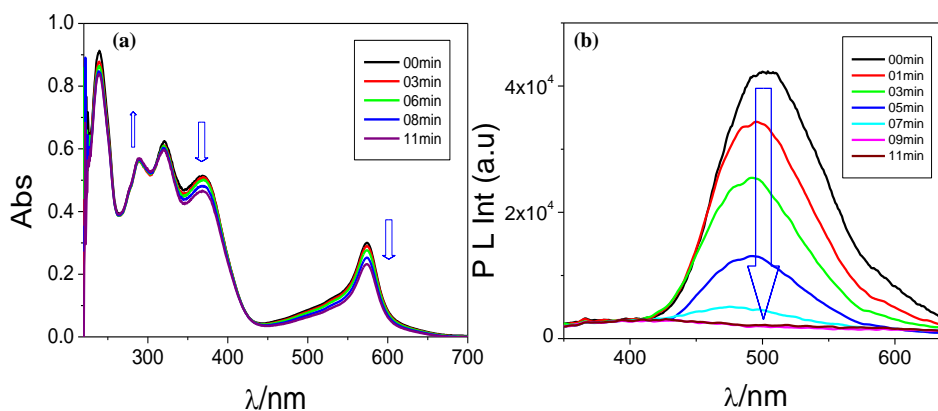


**Fig. 3.18.** First step change in absorption and emission ( $\lambda_{\text{ex}} = 330 \text{ nm}$ ) (c) spectrum of  $[\text{Fe}(\text{tpy-pvp-H})_2]^{2+}$  (**1**) (a and b, respectively) in dichloromethane upon irradiation with visible light indicating the *trans-cis* photoisomerization. Insets to figure a and b indicate the irradiation time.

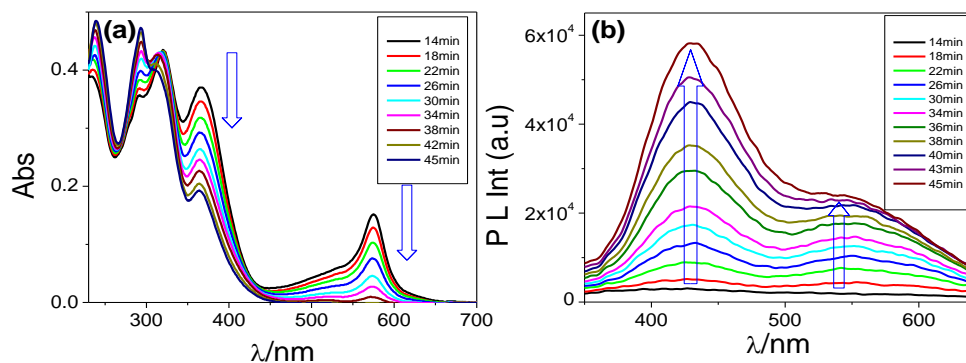


**Fig. 3.19.** Second step change in absorption and emission ( $\lambda_{\text{ex}} = 330 \text{ nm}$ ) (c) spectrum of  $[\text{Fe}(\text{tpy-pvp-H})_2]^{2+}$  (**1**) (a and b, respectively) in dichloromethane upon irradiation with visible light indicating the de-coordination of the complex. Insets to figure a and indicate the irradiation time.

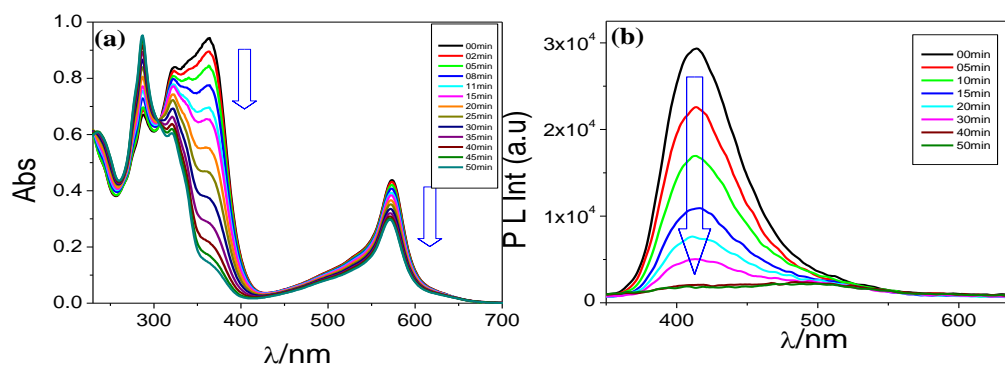


**Fig. 3.20.** UV-vis absorption (a) and emission ( $\lambda_{\text{ex}} = 330 \text{ nm}$ ) (b) spectral changes of  $[\text{Fe}(\text{tpy-pvp-H})_2]^{2+}$  (**1**) in acetonitrile upon irradiation with visible light. Inset to figure (a) indicates the irradiation time.

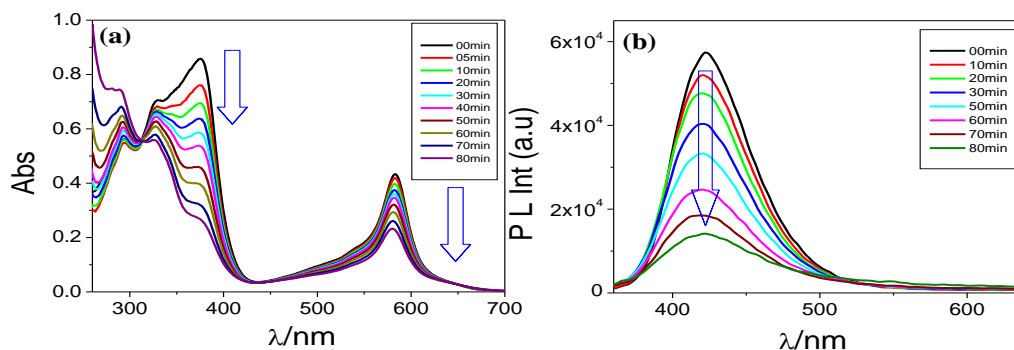


**Fig. 3.21.** UV-vis absorption (a) and emission ( $\lambda_{\text{ex}} = 330 \text{ nm}$ ) (b) spectral changes of  $[\text{Fe}(\text{tpy-pvp-H})_2]^{2+}$  (**1**) in dimethylsulfoxide upon irradiation with visible light. Inset to figure (a) indicates the irradiation time.

In contrast to the behaviours in DCM, all the three complexes exhibit a distinct one-step spectral change in presence of both UV and visible light source and no signature of  $\text{Fe}^{2+}$  de-coordination is observed even after photolysis of more than three hours. One-step spectral change is observed in all three solvents, although the pattern and extent of change differ slightly from each other. Furthermore, the extent of change is much greater with visible light than that of UV light. The spectral change in MeCN and DMSO is very neat and well defined compared with MeOH in presence of visible light. Gradual decrease in intensities for MLCT and LLCT band occurred and at their expense concomitant increase of  $\pi\text{-}\pi^*$  band intensities are observed in both solvents. Well defined isosbestic points are observed in each case.

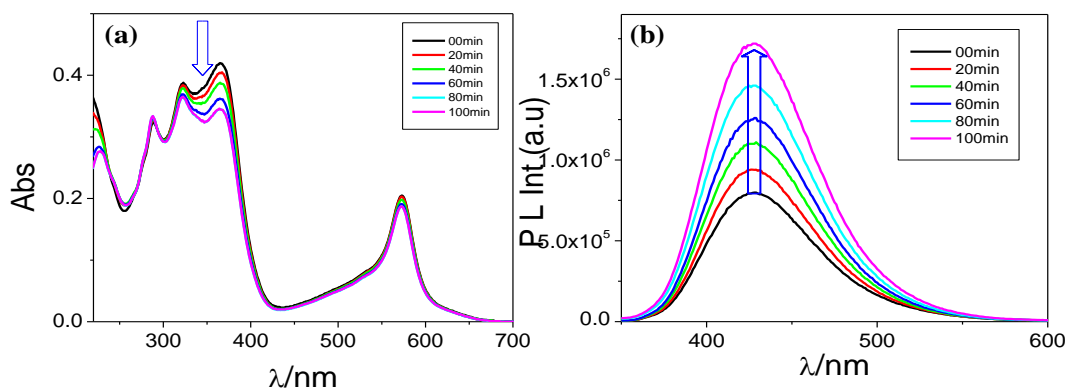


**Fig. 3.22.** UV-vis absorption (a) and emission ( $\lambda_{\text{ex}} = 330 \text{ nm}$ ) (b) spectral changes of  $[\text{Fe}(\text{tpy-pvp-H})_2]^{2+}$  (**1**) in methanol upon irradiation with visible light. Inset to figure (a) indicates the irradiation time.

By contrast, the extent of change in MeOH is much less. The intensity of the ligand-centred emission band at  $\sim 400 \text{ nm}$  for  $[\text{Fe}(\text{tpy-pvp-H})_2]^{2+}$  in MeCN gradually quenched and at the end of photolysis, the band is substantially red-shifted to  $\sim 500 \text{ nm}$ . In DMSO, similar quenching of emission takes place but no red-shift of the band is noticed. The emission spectrum in MeOH is different from both MeCN and DMSO. Instead of quenching, substantial emission enhancement is observed in MeOH in presence of both UV and visible light source.



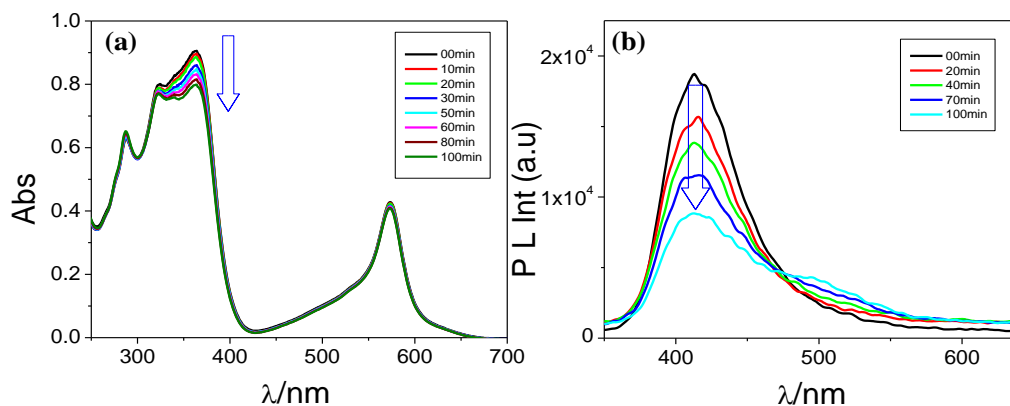


**Fig. 3.23.** UV-vis absorption (a) and emission ( $\lambda_{\text{ex}} = 330 \text{ nm}$ ) (b) spectral changes of  $[\text{Fe}(\text{tpy-pvp-H})_2]^{2+}$  (**1**) in acetonitrile upon irradiation with UV light. Inset to figure a indicates the irradiation time.

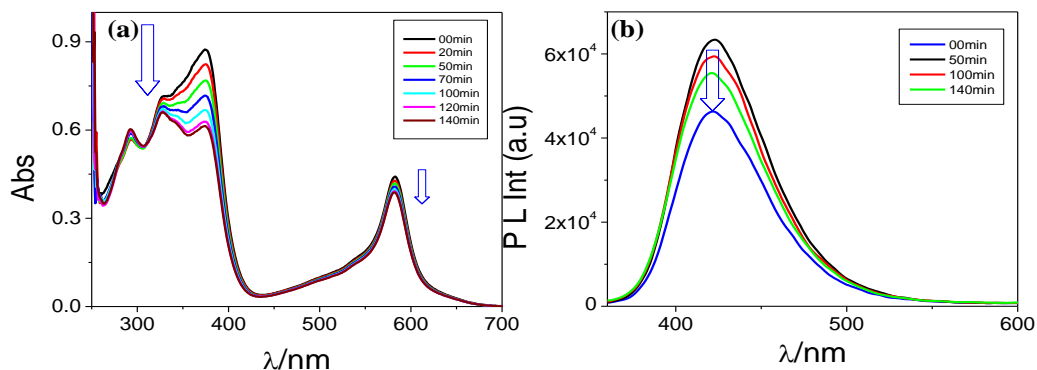


**Fig. 3.24.** UV-vis absorption (a) and emission ( $\lambda_{\text{ex}} = 330 \text{ nm}$ ) (b) spectral changes of  $[\text{Fe}(\text{tpy-pvp-H})_2]^{2+}$  (**1**) in dimethylsulfoxide upon irradiation with UV light. Inset to figure a indicates the irradiation time.

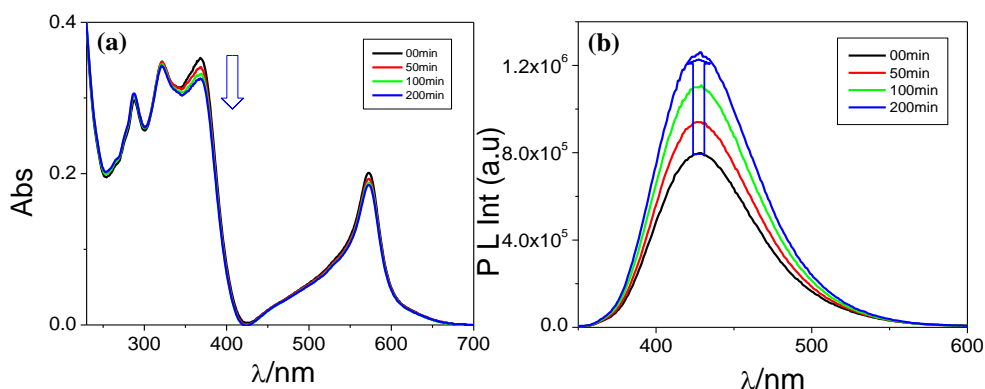


**Fig. 3.25.** UV-vis absorption (a) and emission ( $\lambda_{\text{ex}} = 330 \text{ nm}$ ) (b) spectral changes of  $[\text{Fe}(\text{tpy-pvp-H})_2]^{2+}$  (**1**) in methanol upon irradiation with UV light. Inset to figure a indicates the irradiation time.

Well-defined spectral changes (both absorption and emission) clearly indicate the occurrence of isomerization across the double bond. But we are not very sure whether isomerization taking place from *trans-trans* to *trans-cis* or to *cis-cis* form. In spite of our low level of calculations, TD-DFT results indicate that the MLCT band of *trans-cis* form is red-shifted compared with their *trans-trans* form, while blue-shifted in case of *cis-cis* forms. In the final form of our experimental absorption spectra, the MLCT band also gets blue shifted Fig. 3.26-3.27. That's why we speculate that *trans-trans* to *cis-cis* conversion are occurring for these complexes upon photo-irradiation.

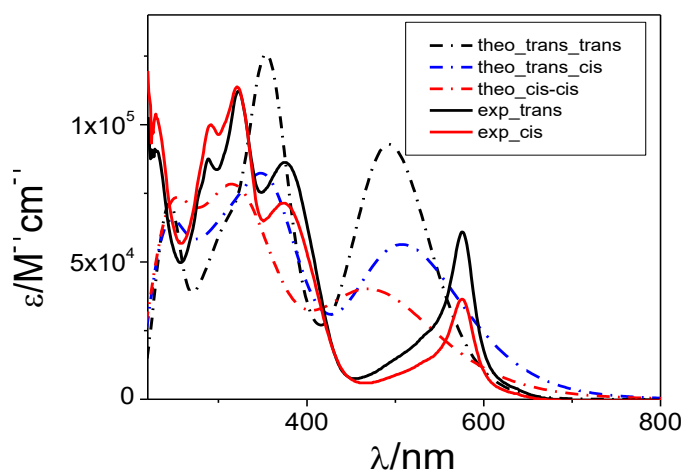


**Fig. 3.26.** Overlay of the calculated (dotted lines) and experimental (solid lines) absorption spectra of *trans-trans* (black), *trans-cis* (blue) and *cis-cis* (red) form of  $[\text{Fe}(\text{tpy-pvp-CH}_3)_2]^{2+}$  in acetonitrile.

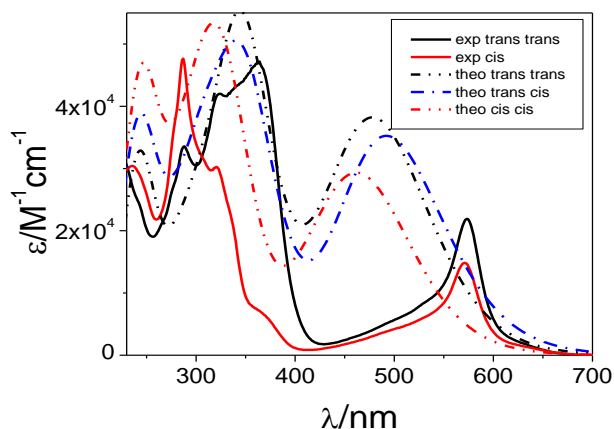


**Fig. 3.27.** Overlay of the calculated (dotted lines) and experimental (solid lines) absorption spectra of *trans-trans* (black), *trans-cis* (blue) and *cis-cis* (red) forms of  $[\text{Fe}(\text{tpy-pvp-H})_2]^{2+}$  in acetonitrile.

While going from *trans-trans* to *cis-cis* form of the complexes, obviously there is an intermediate *trans-cis* state. But we are unable to locate *trans-cis* form during the course of isomerization. The reverse process that is isomerization from *cis-cis* to *trans-trans* form also proceeds very slowly on keeping and accelerated upon heating the solution of the complexes. The complexes are heated around 40 °C in each of three solvents. The reversible changes are very prominent and we got *cis-cis* to *trans-trans* form of the complexes (Fig. 3.28-3.31).

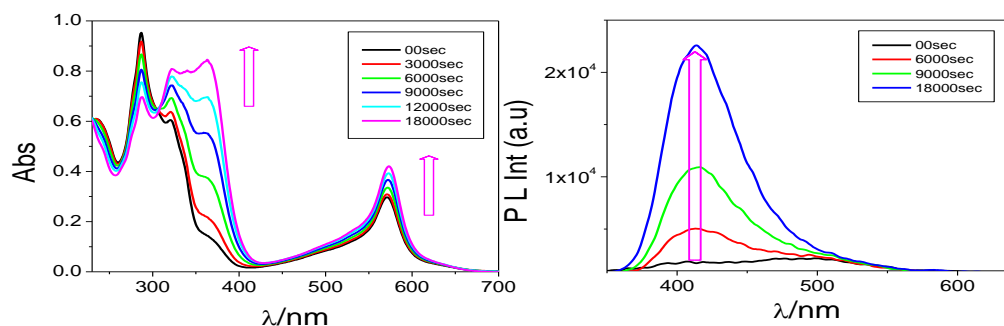


**Fig. 3.28.** The UV-vis absorption (a) and emission ( $\lambda_{\text{ex}}=330$  nm) (b) spectral changes upon heating the photolyzed acetonitrile solution of  $[\text{Fe}(\text{tpy-pvp-H})_2]^{2+}$  (**1**) at 40°C. Insets show the heating time.

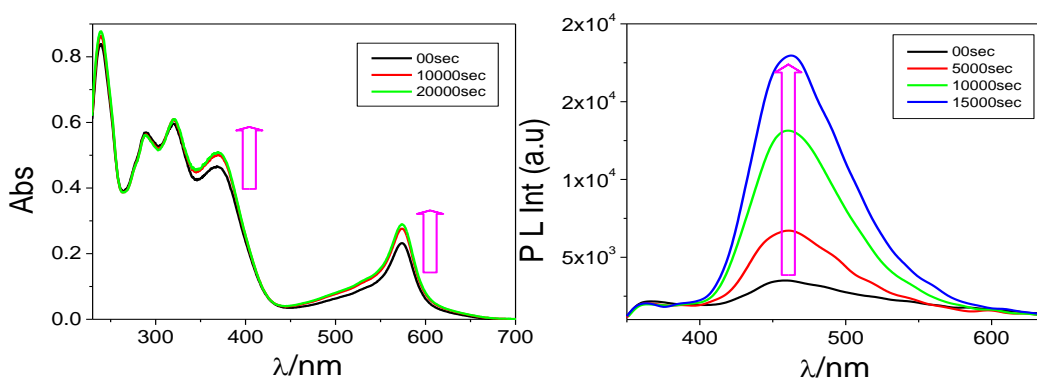


**Fig. 3.29.** The UV-vis absorption (a) and emission ( $\lambda_{\text{ex}}=330$  nm) (b) spectral changes upon heating the photolyzed dichloromethane solution of  $[\text{Fe}(\text{tpy-pvp-H})_2]^{2+}$  (**1**) at 40°C. Insets show the heating time.

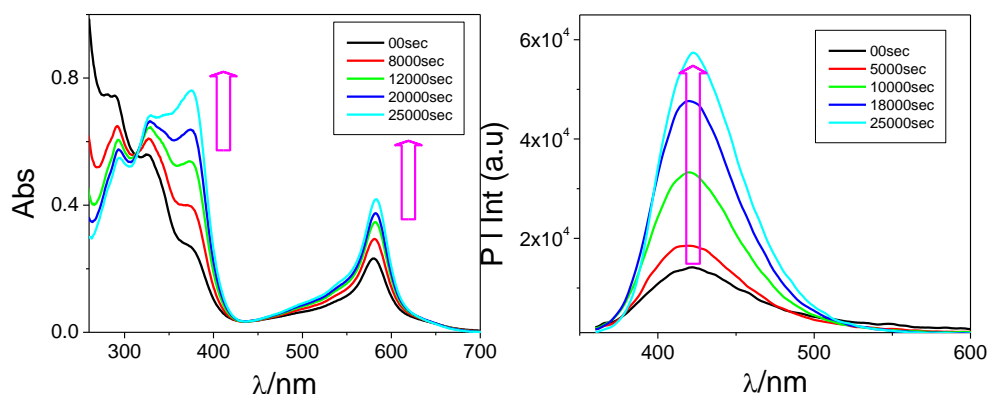


**Fig. 3.30.** The UV-vis absorption (a) and emission ( $\lambda_{\text{ex}}=330$  nm) (b) spectral changes upon heating the photolyzed dimethylsulfoxide solution of  $[\text{Fe}(\text{tpy-pvp-H})_2]^{2+}$  (**1**) at 40°C. Insets show the heating time.

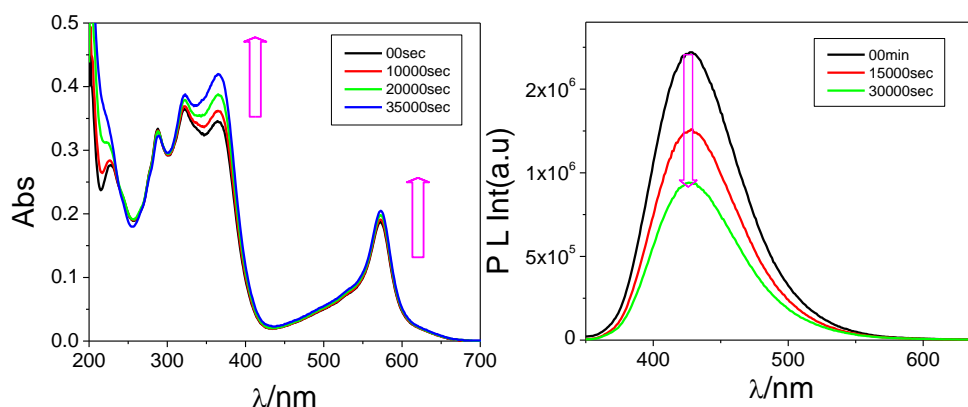


**Fig. 3.31.** The UV-vis absorption (a) and emission ( $\lambda_{\text{ex}}=330$  nm) (b) spectral changes upon heating the photolyzed methanoic solution of  $[\text{Fe}(\text{tpy-pvp-H})_2]^{2+}$  (**1**) at 40°C. Insets show the heating time.

It would be better if we could also monitor the isomerization process through NMR spectroscopy. To this end, we attempted isomerization studies in the said solvents. Unfortunately, the rate of isomerization process is extremely slow and we are unable to see any observable change even after photolysis for about 12h. Concentration of the complexes for NMR experiments were  $10^{-3}$  M compared with  $10^{-5}$  M used for absorption and emission spectral studies.

The rate constant ( $k_{\text{iso}}$ ) and quantum yield ( $\Phi$ ) of isomerization were calculated for both forward and backward process (thermal) in all solvents (Table 3.9). It is noticed that  $k_{\text{iso}}$  as well as  $\Phi$  are dependent upon irradiation wavelength as well as nature of the

solvents. First of all, both  $k_{\text{iso}}$  and  $\Phi$  was found to be much higher in presence of visible light source in all solvents than that of UV light (Table 3.9).  $k_{\text{iso}}$  is also dependent on polarity as well as bulk viscosity of the solvents; found to be highest in DCM and least in MeOH. The dependence of  $k_{\text{iso}}$  and  $\Phi$  with different solvent parameters (viz. polarity index, dielectric constant, and dipole moment) is displayed in Fig. 3.32-3.34. The correlation is reasonably well with the exception of MeOH. Lesser value of  $k_{\text{iso}}$  in more polar solvents is probably because of greater degree of solvation leading to increase of effective rotor volume of the complex cations. Free energy of activation ( $\Delta G^\ddagger$ ) of the isomerization processes (both forward and backward) were also calculated from  $k_{\text{iso}}$  values and by the use of Eying's theory. Calculated  $\Delta G^\ddagger$  values are presented in Table 3.9.

$$\Delta G^\ddagger_{298\text{K}} = 298R \{ \ln(k_B 298/h \cdot k_{\text{iso}}) \} \quad (3)$$

**Table 3.9** Rate constants, quantum yield and free energy of activation of  $\text{trans} \rightarrow \text{cis}$  and  $\text{cis} \rightarrow \text{trans}$  in isomerization process of  $[\text{Fe}(\text{tpy-pvp-H})_2]^{2+}$  in different solvents.

Solvents	Monitoring $\lambda/\text{nm}$	$\text{trans} \rightarrow \text{cis}$ (visible light)			$\text{cis} \rightarrow \text{trans}$ (thermal)		$\text{trans} \rightarrow \text{cis}$ (UV light)			$\text{cis} \rightarrow \text{trans}$ (thermal)	
		$k_{\text{iso}} \times 10^4 / \text{s}^{-1}$	$\Phi \times 10^2$	$\Delta G^\ddagger / \text{kJM}^{-1}$	$k_{\text{iso}} \times 10^5 / \text{s}^{-1}$	$\Delta G^\ddagger / \text{kJM}^{-1}$	$k_{\text{iso}} \times 10^4 / \text{s}^{-1}$	$\Phi \times 10^2$	$\Delta G^\ddagger / \text{kJM}^{-1}$	$k_{\text{iso}} \times 10^5 / \text{s}^{-1}$	$\Delta G^\ddagger / \text{kJM}^{-1}$
DCM	365	32.4	11.9	87.2	12.9	95.2	14.1	5.2	89.2	9.2	96.0
MeCN	361	9.1	3.8	90.9	8.4	96.2	2.6	1.1	100.2	1.7	100.3
DMSO	375	5.3	2.3	91.7	5.5	103.0	2.8	1.2	98.9	3.1	98.7
MeOH	365	4.3	1.3	92.2	2.5	99.2	0.8	0.5	96.2	0.5	103.2

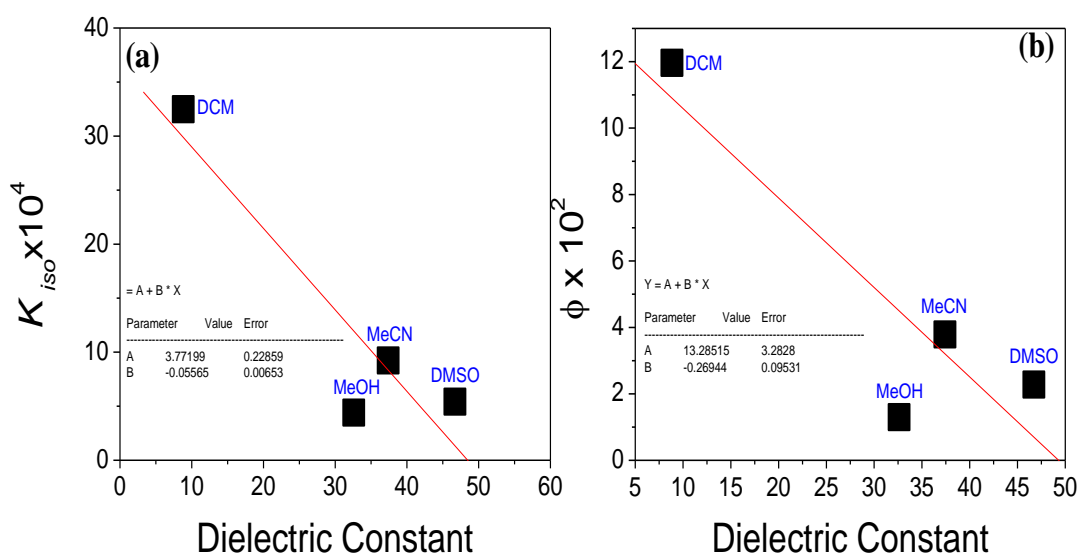


**Fig. 3.32.** Plot of rate constant ( $k_{\text{iso}}$ ) and quantum yield ( $\Phi$ ) vs. dielectric constant of solvents (a and b respectively) with linear least-squares fit to the data.

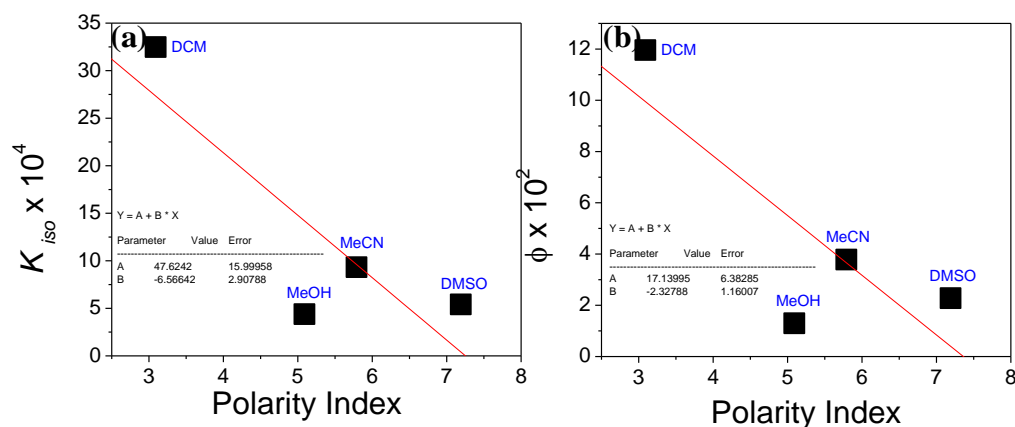


**Fig. 3.33.** Plot of Rate constant ( $k_{iso}$ ) and Quantum Yield( $\phi$ ) vs. Polarity Index of solvents (a and b respectively) with linear least–squares fit to the data.

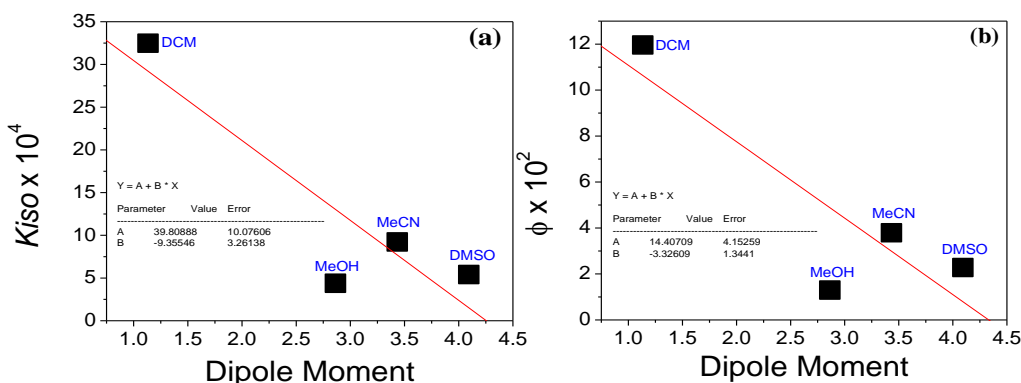


**Fig. 3.34.** Plot of Rate constant ( $k_{iso}$ ) and Quantum Yield ( $\Phi$ ) vs. Dipole Moment of solvents (a and b, respectively) with linear least–squares fit to the data.

We have previously reported photoisomerization behaviours of free tpy-pvp-X ligands in presence of UV light [58]. We found that the lowest energy LLCT absorption band within the spectral domain of 330-361 nm gradually decreases with concomitant increase of a band ~355-390 nm upon irradiation. Free ligands exhibit strong emission band within 389-420 nm which quenched substantially upon isomerization. The rate constant of *trans*→*cis* isomerization was found to vary between  $1.61$  and  $11.7 \times 10^{-3} \text{ s}^{-1}$ . In the present study, we observed that photophysics and photo-isomerization of tpy-pvp-X unit gets dramatically affected upon coordination with  $\text{Fe}^{2+}$ . Coordination of  $\text{Fe}^{2+}$  leads to evolution of a strong band in the visible (~575 nm due to  $\text{Fe(II)} \rightarrow \text{tpy}$  MLCT

transition) and induces significant quenching of ligand-centered emission in  $[\text{Fe}(\text{tpy-pvp-X})_2]$ . Photo-isomerization rate constants of Fe(II) complexes retarded dramatically (varying between  $0.8$  and  $32.4 \times 10^{-4} \text{ s}^{-1}$ , depending upon irradiating wavelength and nature of solvents). This is a consequence of the presence of a low lying MLCT electronic excited state that efficiently quenches the higher energy phantom  $p^*$  state. In addition, presences of several low energy vibrational states that are created upon complexation, restrict the molecule from reaching the crossing point for isomerization.

It would be appropriate to give some insight about the isomerization process. Light-induced ligand substitution of otherwise photochemically inert complexes is not very unusual in DCM. Although  $[\text{Ru}(\text{bpy})_3]^{2+}$  is photochemically inert, there is evidence that it undergoes photo-substitution in chlorinated solvent (such as DCM). While  $[\text{Ru}(\text{bpy})_3]^{2+}$  as the  $\text{PF}_6^-$  salt is photo-inert in water but in DCM, the photochemistry of  $[\text{Ru}(\text{bpy})_3]\text{X}_2$ , ( $\text{X}=\text{Cl}^-$ ,  $\text{Br}^-$ ,  $\text{NCS}^-$ ) is well behaved [59-60], giving rise to  $\text{Ru}(\text{bpy})_2\text{X}_2$  with  $\phi$  lying between  $10^{-1}$  and  $10^{-2}$ . A crucial difference between water and DCM solutions is that salts of  $[\text{Ru}(\text{bpy})_3]^{2+}$  are fully ion-paired in the latter medium. The probable reason for photo-substitution is thermally activated formation of a  $^3\text{MC}$  excited state which induces a large metal-ligand displacement in the excited state leading to the cleavage of Ru-N bond.

Proper understanding of photo-reactivity and photophysics of first-row transition metal complexes is still a challenge for both experimentalists and theoreticians. Indeed the high density of excited states of mixed characters with important contribution of metal-centered (MC) states lead to a rich and extremely complicated photochemistry with various competing channels of deactivation such as luminescence, non-radiative processes, dissociation and isomerization. Due to lack of our expertise, we are unable to calculate appropriately the low-lying triplet and quintet MC states which is crucial for understanding the photophysics of Fe(II)-polypyridine complexes. Usually, the pure triplet IL state localized on the isomerizable ligand plays a central role in the photoisomerization processes. It should be accessible via  $^1\text{MLCT}/^1\text{LLCT}$  to  $^3\text{MLCT}/^3\text{LLCT}$  ISC and/or  $^3\text{MLCT}/^3\text{LLCT}$ - $^3\text{IL}$  vibronic coupling. This could help at deciphering the competition between luminescence /isomerization/dissociation and at understanding why solvent effects are very important. The present data are not at

maturity for pushing too far for mechanistic interpretation for the isomerization process of present Fe(II)-terpyridine complexes. We are still working on this and several fundamental issues which we are unable to address presently are open for further investigation for understanding the complete picture.

### 3.4 Conclusions

With regard to our aim for designing suitable base-metal complexes for the development of new class of low-cost easily synthesizable photo-switches, we designed in this work a new class of homoleptic Fe(II)-terpyridine complexes by incorporating styrylbenzene moiety as the photo-switchable unit and thoroughly investigated their photoisomerization behaviours through absorption and emission spectroscopic techniques. The complexes underwent *trans-trans* to *cis-cis* isomerization upon the action of both visible and UV light with remarkable change in their absorption and emission spectral profiles. The isomerization studies were performed in four different solvents, viz. DCM, MeCN, MeOH and DMSO with both UV and visible light sources. Apart from DCM, where de-coordination of  $\text{Fe}^{2+}$  takes place from the complex backbone upon prolonged light exposure, isomerization process proceeds smoothly in all the other solvents. The reversal from *cis-cis* to *trans-trans* isomerization also proceeds, albeit very slowly, on keeping and can be accelerated upon heating. The rate, rate constant and quantum yield of isomerization were determined in all the solvents in presence of both UV and visible light source. The  $k_{\text{iso}}$  as well as  $\Phi$  is found to be much higher in presence of visible light source in all solvents than that of UV light.  $k_{\text{iso}}$  and  $\Phi$  is also dependent on polarity as well as bulk viscosity of the solvents and a linear correlation is found between either  $k_{\text{iso}}$  or  $\Phi$  and different solvent parameters (viz. polarity index, dielectric constant, and dipole moment). The present data are not sufficient for complete understanding of the mechanistic aspects for isomerization process of Fe(II)-terpyridine complexes. Close proximity of several excited states with mixed characters together with sizeable contribution of metal-centered (MC) states complicate the photochemistry with various competitive process of relaxation, viz. emission, non-radiative processes, dissociation and isomerization. We are still working on this and several fundamental issues which we are unable to address presently are open for further investigation for understanding the



complete picture. Although we are unable to present proper mechanistic details for photoisomerization process, present Fe(II)-terpyridine complexes could be useful for the construction low-cost molecular photo-switches which in turn could be potential building blocks for information processing and at the molecular level.

### 3.5 References

- [1] M. Irie, Diarylethenes for memories and switches, *Chem. Rev.* 100 (2000) 1685–1716.
- [2] B. L. Feringa, R. A. van Delden, M. K. J, ter Wiel, *Chiroptical Molecular Switches*, Wiley-VCH, 2001.
- [3] H. Tian, S. Yang, Recent progresses on diarylethene based photochromic switches, *Chem. Soc. Rev.* 33 (2004) 85–97.
- [4] S. Kawata, Y. Kawata, Three-dimensional optical data storage using photochromic materials, *Chem. Rev.* 100 (2000) 1777–1788.
- [5] H. Rau, Dürr, H, H. B. Eds Laurent, *Photochromism: Molecules and Systems* Elsevier: Amsterdam, The Netherlands. 1990, pp 165–192.
- [6] K. Ichimura, S. K. Oh, M. Nakagawa, Light-driven motion of liquids on a photoresponsive surface, *Science*. 288 (2000) 1624–1626.
- [7] H. Tian, J. Eds. Zhang, *Photochromic Materials: Preparation, Properties and Applications*, Wiley-VCH: Weinheim, Germany, 2016.
- [8] J. C. Crano, R. Eds. Guglielmetti, *Organic Photochromic and Thermochromic Compounds, Vol 1: Main Photochromic Families*, Plenum Press: New York, 1999.
- [9] J. C. Crano, R. Eds. Guglielmetti, *Organic Photochromic and Thermochromic Compounds, Vol 2: Physicochemical Studies, Biological Applications and Thermochromism*, Plenum Press: New York, 1999.
- [10] D. H. Waldeck, Photoisomerization dynamics of stilbenes, *Chem. Rev.* 91 (1991) 415-436.
- [11] T. Ikeda, O. Tsutsumi, Optical switching and image storage by means of azobenzene liquid-crystal films, *Science*. 268 (1995) 1873-1875.

- 
- [12] K. Matsuda, M. Irie, Diarylethene as a photoswitching unit, *J. Photochem. Photobiol. C* 5 (2004) 169-182.
- [13] S. Kume, H. Nishihara, Photochrome-coupled metal complexes: molecular processing of photon stimuli, *Dalton Trans.* (2008) 3260- 3271.
- [14] C.-C. Ko, V.W.-W. Yam, Coordination compounds with photochromic ligands: ready tunability and visible light-sensitized photochromism, *Acc. Chem. Res.* 51 (2018) 149-159.
- [15] M. Kurihara, H. Nishihara, Azo-and quinone-conjugated redox complexes photo- and proton-coupled intramolecular reactions based on d- $\pi$  interaction, *Coord. Chem. Rev.* 226 (2002) 125-135.
- [16] H. Nishihara, Multi-mode molecular switching properties and functions of azo conjugated metal complexes, *Bull. Chem. Soc. Jpn.* 77 (2004) 407-428.
- [17] H. Nishihara, in: Y. F. Kodansha (Ed), *Inorganic photochromism*, Springer, 2007 pp 239-257.
- [18] S. Kume, H. Nishihara, Metal-based photoswitches derived from photoisomerization, *Struct. Bonding*, (Berlin, Ger.) 123 (2006) 79-112.
- [19] C.-C. Ko, V. W.-W. Yam, Transition metal complexes with photochromic ligands- photosensitization and photoswitchable properties, *J. Mater. Chem.* 20 (2010) 2063-2070.
- [20] C.-C. Ko, L.-X. Wu, K. M.-C. Wong, N. Zhu, V. W.-W. Yam, Synthesis, characterization and photochromic studies of spirooxazine-containing 2,2'-bipyridine ligands and their rhenium(I) tricarbonyl complexes, *Chem.-Eur. J.* 10 (2004) 766-776.
- [21] Y. Li, A. Y.-Y Tam, K. M.-C. Wong, W. Li, L. Wu, V. W.-W. Yam, Synthesis, characterization, and the photochromic, luminescence, metallogelation and liquid-crystalline properties of multifunctional platinum (II) bipyridine complexes, *Chem.-Eur. J.* 17 (2011) 8048-8059.
- [22] C.-C. Ko, W.-M. Kwok, V. W.-W. Yam, D. L. Phillips, Triplet MLCT photosensitization of the ring-closing reaction of diarylethenes by design and

- synthesis of a photochromic rhenium(I) complex of a diarylethene-containing 1,10-phenanthroline ligand, *Chem.-Eur. J.* 12 (2006) 5840-5848.
- [23] P. H.-M. Lee, C.-C. Ko, N. Zhu, V. W.-W. Yam, Metal coordination- assisted near-infrared photochromic behavior: a large perturbation on absorption wavelength properties of n,n-donor ligands containing diarylethene derivatives by coordination to the rhenium(I) metal center, *J. Am. Chem. Soc.* 129 (2007) 6058-6059.
- [24] J. C.-H. Chan, W. H. Lam, H.-L. Wong, N. Zhu, W.- T. Wong, V. W.-W. Yam, Diarylethene-containing cyclometalated platinum-(II) complexes: tunable photochromism via metal coordination and rational ligand design, *J. Am. Chem. Soc.* 133 (2011) 12690-12705.
- [25] E. M. Nolan, S. J. Lippard, Tools and tactics for the optical detection of mercuric ion, *Chem. Rev.* 108 (2008) 3443-3480.
- [26] F. A. Cotton, G. Wilkinson, *Advanced Inorganic Chemistry*, 5th Ed. Wiley Interscience Publication, John-Wiley & Sons, 1988.
- [27] N. N. Greenwood, A. Earnshaw, *Chemistry of the Elements*: Maxwell Macmillan International Edn, 1989.
- [28] C. Creutz, M. Chou, T. L. Netzel, M. Okumura, N. Sutin, Lifetimes, spectra, and quenching of the excited states of polypyridine complexes of iron(II), ruthenium(II), and osmium(II), *J. Am. Chem. Soc.* 102 (1980) 1309-1319.
- [29] H. Cho, M. L. Strader, K. Hong, L. Jamula, E. M. Gullikson, T. K. Kim, F. M. F. deGroot, J. K. McCusker, R. W. Schoenlein, N. Huse, Ligand-field symmetry effects in fe(II) polypyridyl compounds probed by transient x-ray absorption spectroscopy, *Faraday Discuss.* 157 (2012) 463-474.
- [30] J. K. McCusker, K. N. Walda, R. C. Dunn, J. D. Simon, D. Magde, D. N. Hendrickson, Subpicosecond  $^1\text{MLCT} \rightarrow ^5\text{T}_2$  intersystem crossing of low-spin polypyridyl ferrous complexes, *J. Am. Chem. Soc.* 115 (1993) 298-307.
- [31] A. T. Yeh, C. V. Shank, J. K. McCusker, Ultrafast electron localization dynamics following photo-induced charge transfer, *Science*. 289 (2000) 935-938.

- [32] S. Baitalik, X. Wang, R. H. Schmehl, A trimetallic mixed ru(II)/fe(II) terpyridyl complex with a long-lived excited state in solution at room temperature, *J. Am. Chem. Soc.* 126 (2004) 16304.
- [33] X. Wang, A. D. Guerzo, S. Baitalik, G. Simon, G. B. Shaw, L. X. Chen, R. H. Schmehl, The influence of bridging ligand electronic structure on the photophysical properties of noble metal diimine and triimine light harvesting systems, *Photosynth. Res.* 87 (2006) 83.
- [34] A. Paul, M. Bar, S. Deb, S. Baitalik, Long-lived trimetallic complexes of fe(II), ru(II), and os(II) based on a heteroditopic bipyridine-terpyridine bridge: synthesis, photophysics, and electronic energy transfer, *Inorg. Chem.* 58 (2019) 10065-10077.
- [35] D. Maity, C. Bhaumik, S. Mardanya, S. Karmakar, S. Baitalik, Light harvesting and directional energy transfer in long-lived homo- and heterotrimetallic complexes of feII, ruII, and osII, *Chem. Eur. J.* 20 (2014) 13242-13252.
- [36] M.S. Wrighton, D.L. Morse, L. Pdungsap, intraligand lowest excited states in tricarbonylhalobis(styrylpyridine)rhenium(I) complexes, *J. Am. Chem. Soc.* 97 (1975) 2073-2079.
- [37] V.W.-W. Yam, Y. Yang, J. Zhang, B.W.-K. Chu, N. Zhu, Synthesis, characterization, and photoisomerization studies of azo- and stilbene- containing surfactant rhenium (I) complexes, *Organometallics.* 20 (2001) 4911- 4918.
- [38] V.W.W. Yam, V.C.Y. Lau, L.X. Wu, Synthesis, photophysical, photochemical and electrochemical properties of rhenium(I) diimine complexes with photoisomerizable pyridyl-azo, -ethenyl or -ethyl ligands, *J. Chem. Soc. Dalton Trans.* (1998), 1461–1468.
- [39] S.S. Sun, A.J. Lees, Synthesis, photophysical properties, and photoinduced luminescence switching of trinuclear diimine rhenium(I) tricarbonyl complexes linked by an isomerizable stilbene-like ligand, *Organometallics.* 21 (2002) 39-49.
- [40] A.S. Polo, M.K. Itokazu, K.M. Frin, A.O.T. Patrocínio, N.Y.M. Iha, Light driven *trans*-to- *cis* isomerization of stilbene-like ligands in *fac*- [Re(CO)<sub>3</sub>(NN)(*trans*-L)]<sup>+</sup> and luminescence of their photoproducts, *Coord. Chem. Rev.* 250 (2006) 1669-1680.

- [41] L.S. Matos, R.C. Amaral, N.Y.M. Iha, Visible photosensitization of trans-styrylpyridine coordinated to  $fac-[Re(CO)_3(dcbH_2)]^+$ : new insights, *Inorg. Chem.* 57 (2018) 9316-9326.
- [42] K.P.S. Zanoni, N.Y.M. Iha, Reversible  $trans \rightleftharpoons cis$  photoisomerizations of  $[Re(CO)_3(ph_2phen)(stpyCN)]^+$  towards molecular machines, *Dalton Trans.* 46 (2017) 9951-9958.
- [43] M. Busby, F. Hartl, P. Matousek, M. Towrie, A.J. Vlcek, Ultrafast excited state dynamics controlling photochemical isomerization of n-methyl-4-[trans-2-(4-pyridyl) ethenyl]pyridinium coordinated to a  $\{ReI(CO)_3(2,2'-bipyridine)\}$  chromophores, *Chem. Eur. J.* 14 (2008) 6912-6923.
- [44] A.J. Vlcek, M. Busby, Ultrafast ligand-to-ligand electron and energy transfer in the complexes  $fac-[ReI(L)(CO)_3(bpy)]^{n+}$ , *Coord. Chem. Rev.* 250(2006) 1755-1762.
- [45] V.W.W. Yam, V.C.Y. Lau, K.K. Cheung, Photophysics and photochemistry of novel luminescent rhenium(I) photoswitchable materials, *J. Chem. Soc. Chem. Commun.* (1995) 259-261.
- [46] R.C. Amaral, L.S. Matos, K.P.S. Zanoni, N.Y.M. Iha, Photoreversible molecular motion of stpyCN coordinated to  $fac-[Re(CO)_3(NN)]^+$  complexes, *J. Phys. Chem. A.* 122 (2018) 6071-6080.
- [47] J. Bossert, C. Daniel, Trans-cis photoisomerization of the styrylpyridine ligand in  $[Re(CO)_3(2,2'-bipyridine)(t-4-styrylpyridine)]^+$ : role of the metal-to-ligand charge transfer excited states, *Chem. Eur. J.* 12 (2006) 4835-4843.
- [48] O.S. Wenger, L.M. Henling, M.W. Day, J.R. Winkler, H.B. Gray, Photoswitchable luminescence of rhenium(I) tricarbonyl diimines, *Inorg. Chem.* 43 (2004) 2043-2048.
- [49] J.D. Lewis, R.N. Perutz, J.N. Moore, Proton-controlled photoisomerization: rhenium (I) tricarbonyl bipyridine linked to amine or azacrown ether groups by a styryl pyridine bridging ligand, *Chem. Commun.* (2000) 1865-1866.
- [50] H. Zhang, C.S. Rajesh, P. K. Dutta, Visible-light-driven photoreactions of  $[(bpy)_2Ru(II)L]Cl_2$  in aqueous solutions ( $bpy$  = bipyridine,  $L$ = 1,2-bis(4-(4'-methyl)-2,2'-bipyridyl)ethene), *J. Phys. Chem. A.* 112 (2008) 808-817.

- [51] D.M. Dattelbaum, M.K. Itokazu, N.Y.M. Iha, T.J. Meyer, Mechanism of metal-to ligand charge transfer sensitization of olefin trans-to-cis isomerization in the *fac*-[ReI(phen)(CO)<sub>3</sub>(1,2-bpe)]<sup>+</sup> cation, *J. Phys. Chem. A*. 107 (2003) 4092-4095.
- [52] P. Pal, T. Ganguly, D. Maity, S. Baitalik, Experimental and theoretical exploration of photophysics and trans-cis photoisomerization of styrylbenzene conjugated terpyridine complexes of Ru(II): strong effect of deprotonation from second coordination sphere, *J. Photochem. Photobiol. A*. 392 (2020) 112409.
- [53] T. Yutaka, I. Mori, M. Kurihara, N. Tamai, H. Nishihara, Photochemical behavior of azobenzene-conjugated Co<sup>II</sup>, Co<sup>III</sup>, and Fe<sup>II</sup> bis(terpyridine) complexes, *Inorg. Chem.* 42 (2003) 6306-6313.
- [54] Y. Hasegawa, K. Takahashi, S. Kume, H. Nishihara, Complete solid state photoisomerization of bis(dipyrazolylstyrylpyridine)iron(II) to change magnetic properties, *Chem. Commun.* 47 (2011) 6846-6848.
- [55] J.J. Santos, S.H. Toma, P. M. Lalli, M.F. Riccio, M. N. Eberlin, H.E. Tomaa, K. Araki, Exploring the coordination chemistry of isomerizable terpyridine derivatives for successful analyses of cis and trans isomers by travelling wave ion mobility mass spectrometry, *Analyst*. 137 (2012) 4045.
- [56] P. Pal, S. Mukherjee, D. Maity, S. Baitalik, Synthesis, structural characterization, and luminescence switching of diarylethene-conjugated Ru(II)-terpyridine complexes by trans-cis photoisomerization: experimental and DFT/TD-DFT investigation, *Inorg. Chem.* 57 (2018) 5743-5753.
- [57] P. Pal, S. Mukherjee, D. Maity, S. Baitalik, Synthesis, photophysics, and switchable luminescence properties of a new class of ruthenium(II)-terpyridine complexes containing photoisomerizable styrylbenzene units, *ACS Omega*. 3 (2018) 14526-14537.
- [58] S. Mukherjee, P. Pal, D. Maity, S. Baitalik, Photophysics and luminescence switching properties of a series of photochromic styrylbenzene-terpyridine conjugate: experimental and dft/ td-dft investigation, *J. Photochem. Photobiol. A*. 378 (2019) 94-104.

## Chapter 3

---

- [59] A. Juris, V. Balzani, F. Barigelletti, S. Campagna, P. Belser, V. A. Zelewsky, Ru(II) polypyridine complexes: photophysics, photochemistry, eletrochemistry, and chemiluminescence, *Coord. Chem. Rev.* 84 (1988) 85-277.
- [60] B. Durham, J.V. Casper, J.K. Nagle, T.J. Meyer, Photochemistry of tris(2,2'-bipyridine)ruthenium(2+) ion, *J. Am. Chem. Soc.* 104 (1982) 4803-4810.

\*\*\*\*\*

## ***Chapter 4***

**Chromogenic and fluorogenic detection  
of selected anions by bis-terpyridine  
Fe(II) complex through displacement  
approach**



## 4.1 Introduction

Supramolecular chemistry of anion recognition and sensing is continued to be a vibrant area of research as few of them play crucial roles in biological, aquatic, environmental and industrial processes [1-4]. Among the anions, detection of cyanide ion as well as its quantification is a crucial task for the scientist because it is extremely toxic to the environment and also for human health and other living organisms [5,6]. Sincere efforts have been devoted for designing effective sensors for cyanide ion [7-11] and most of the chemosensors usually recognize cyanide based on three well known strategies: (i) the "binding site-signaling subunit" approach where the binding sites and the optical signaling moieties are covalently connected in such a manner that the interaction of  $\text{CN}^-$  with the binding site(s) induces electronic reorganization of the signaling subunit resulting in change of their optical spectral behaviours [12-15], (ii) the "chemodosimeter" approach whereby anion-induced chemical reactions usually occur resulting in changes in fluorescence or color [7,8,16-19] and (iii) the "displacement" strategy wherein the binding sites and signaling subunits are not usually covalently connected but form a molecular adduct and upon coordination of  $\text{CN}^-$  to the binding site leads to the displacement of the signaling subunit, which is usually accompanied with optical spectral changes [20-26]. Each strategy has its own merits as well as demerits. In the first strategy, the chemosensors usually detect  $\text{CN}^-$  by means of hydrogen bonding interaction and most of the reported sensors suffer from the lack of selectivity. Both "displacement" and "chemodosimeter" strategies have also some drawbacks such as lack of reversibility, and requirement of energy (heat or light) to overcome the activation barrier for the addition of cyanide to the active site of the chemosensors and usually irreversible in nature. In addition, majority of the small molecule chemosensors for  $\text{CN}^-$  are based on organic molecules and show their sensing abilities mainly in organic media which in turn are major deterrent for their use in practical application.

Compared with pure organic hosts, the receptors based on coordination compounds of transition metals having wide variety of geometries and very rich photophysical and electrochemical properties are relatively less in the literature [27-30]. Metal fragment in the complex usually acts as the reporter unit by modulating optical

and/or electrochemical signal as a result of host–guest interaction [27-30]. Few low spin  $d^6$  transition metal complexes (such as Ru(II), Os(II), Rh(III) and Ir(III)) derived from polyheterocyclic ligands were designed as anion sensors by virtue of their outstanding photo-redox behaviors and in majority of cases the incoming anionic guest interacts with suitable binding group located in the secondary coordination sphere in the complex [31-40]. Although the platinum metals are very efficient in detecting selected anions because of their unique combination of photophysical and electrochemical properties, but the main disadvantage is their high cost which is a major problem for their practical applications. To this end, we designed in this work, an Fe(II) complex derived from a terpyridine ligand functionalized with a diarylethylene moiety at the 4'-position of the terpyridine ring (**Chart 1**). Owing to the lower energy metal-to-ligand charge transfer band in the visible region, the complex offers both chromogenic and fluorogenic detection of selected anions. In this work, we will thoroughly investigate the anion sensing behaviors of the bis-terpyridine Fe(II) complex in both organic as well as mixed aqueous-organic media through multiple optical channels and spectroscopic techniques.

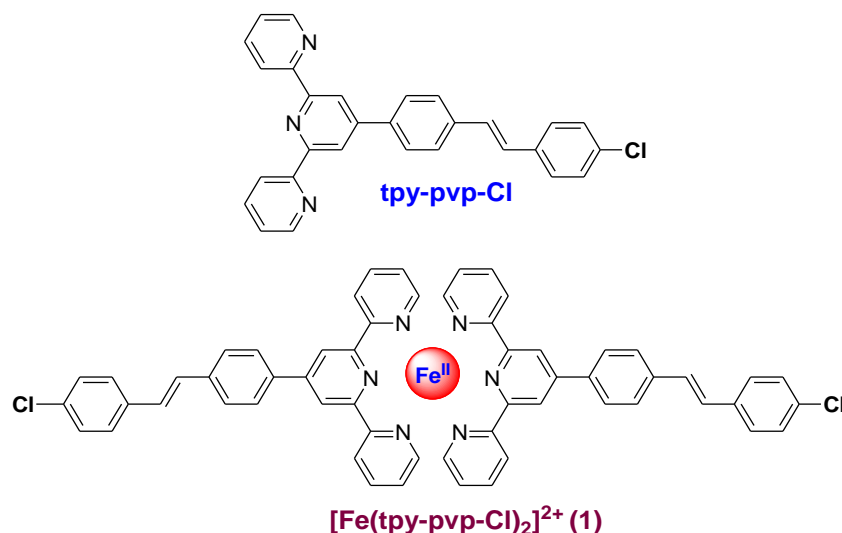


**Chart 4.1.** Molecular structure of the terpyridine ligand (tpy-pvp-Cl) and its Fe(II) complex of composition  $[\text{Fe}(\text{tpy-pvp-Cl})]^{2+}$  (**1**).

## 4.2 Experimental

### 4.2.1 Materials

Tetrabutylammonium (TBA) salt of the anions were purchased from Sigma-Aldrich.

### 4.2.2 Synthesis of the Fe(II) complex, $[Fe(tpy-pvp-Cl)_2](ClO_4)_2$ (**1**)

To a stirred  $CHCl_3$ -MeOH (1:2, v/v) solution (25 mL) of tpy-pvp-Cl (110 mg, 0.25 mmol), a MeOH solution of  $Fe(ClO_4)_2 \cdot 6H_2O$  (44 mg 0.12 mmol) was added. The colorless solution immediately changed into blue-violet and during stirring at room temperature for ~1h microcrystalline compound deposited. The compound was filtered, washed with water, and dried in a vacuum. The crude compound was washed with chloroform and then purified by alumina column chromatography using 1:10 (v/v) toluene-MeCN mixture. The compound was finally recrystallized from MeCN-MeOH (1:2, v/v) mixture when a violet microcrystalline compound was obtained: yield 100 mg (76%). Elemental anal. Calcd. for  $C_{58}H_{40}N_6Cl_4O_8Fe$ : C, 60.75; H, 3.51; N, 7.329. Found: C, 60.71; H, 3.53; N, 7.34.  $^1H$  NMR (300 MHz,  $CD_3CN$ ,  $\delta$  / ppm) : 9.22( s, 2H, H3'), 9.17(s, 2H, H3'), 8.64-8.6028( nr, 4H, H6), 8.36 ( d, 2H, H8,  $J$  = 7.5), 8.23 (d, 2H, H7,  $J$  = 7.92), 7.99(d, 2H, H4,  $J$  = 9.0), 7.90( m, 4H, H4+H8), 7.69-7.62( m, 4H, H11), 7.48-7.46( nr, 2H,  $J$  = 6.0, H7), 7.36( s, 6H, H3+H10), 7.19( d, 4H, H12), 7.08( nr, 4H, H5), 6.86( d, 2H, H9,  $J$  = 6.0). ESI-MS (positive,  $CH_3CN$ ):  $m/z$  = 473.03(100%)  $[Fe(tpy-pvp-Cl)_2]^{2+}$ .

**Caution!** *Perchlorate salt of the Fe(II) complex used in this study is potentially explosive and therefore should be handled in small quantities with care.*

### 4.2.3 Physical measurements

Anion sensing studies of the receptor were carried out in acetonitrile as well as in MeCN- $H_2O$  (1:100 v/v). For a typical titration experiment, 2  $\mu$ L aliquots of a given anion ( $2.0 \times 10^{-2}$  M) were added to a 2.5 mL solution of the Fe(II) receptor ( $1.0 \times 10^{-5}$  M). Either TBA or sodium salts of different anions were used for titration experiments.

### 4.3 Results and discussions

#### 4.3.1 Synthesis and characterization

The synthesis and characterization of the ligand (tpy-pvp-Cl) is reported in [chapter 2](#). The Fe(II) complex is synthesized upon treating tpy-pvp-Cl with  $[\text{Fe}(\text{ClO}_4)_2]$  in 2:1 molar ratio in  $\text{CHCl}_3$ -MeOH (1:2, v/v) mixture at RT and purified through column chromatography followed by recrystallization from  $\text{CHCl}_3$ -MeOH (1:2, v/v) mixture. The complexes are characterized by elemental (C, H and N) analyses as well as ESI mass and NMR spectroscopy.

The  $^1\text{H}$  NMR spectrum of tpy-pvp-Cl as well as its Fe(II) complex,  $[\text{Fe}(\text{tpy-pvp-Cl})_2]^{2+}$  are presented in [Fig. 4.1](#). Both compounds exhibit a number of resonances in the aromatic region and tentative assignment of the proton resonances were done by taking advantage of their ( $^1\text{H}$ - $^1\text{H}$ ) COSY NMR spectra. The terpyridine (H3-H6) protons as well as the protons associated with styrylbenzene unit (H9-H12) lying in the region between 7.32 and 8.72 ppm have been assigned by taking into consideration the multiplicities of the peak, values of the coupling constants as well chemical shifts values.

Upon coordination with  $\text{Fe}^{2+}$ , the chemical shifts of the tpy-pvp-Cl protons are presented in [Fig. 4.1b](#). H3' proton of tpy moiety gets significantly down-field shifted while the other tpy protons (H7-H11) get moderately down-field shifted due to the drift of electron density from the heteroaromatic moieties to the  $\text{Fe}^{2+}$  center. The chemical shift of H9 and H10 protons associated with ethylenic double bond is also shifted towards down-field region. H3 proton resonance, on the other hand, shifted remarkably towards up-field region probably because of ring current anisotropic effect induced by the adjacent terminal pyridine ring of the tpy moiety.

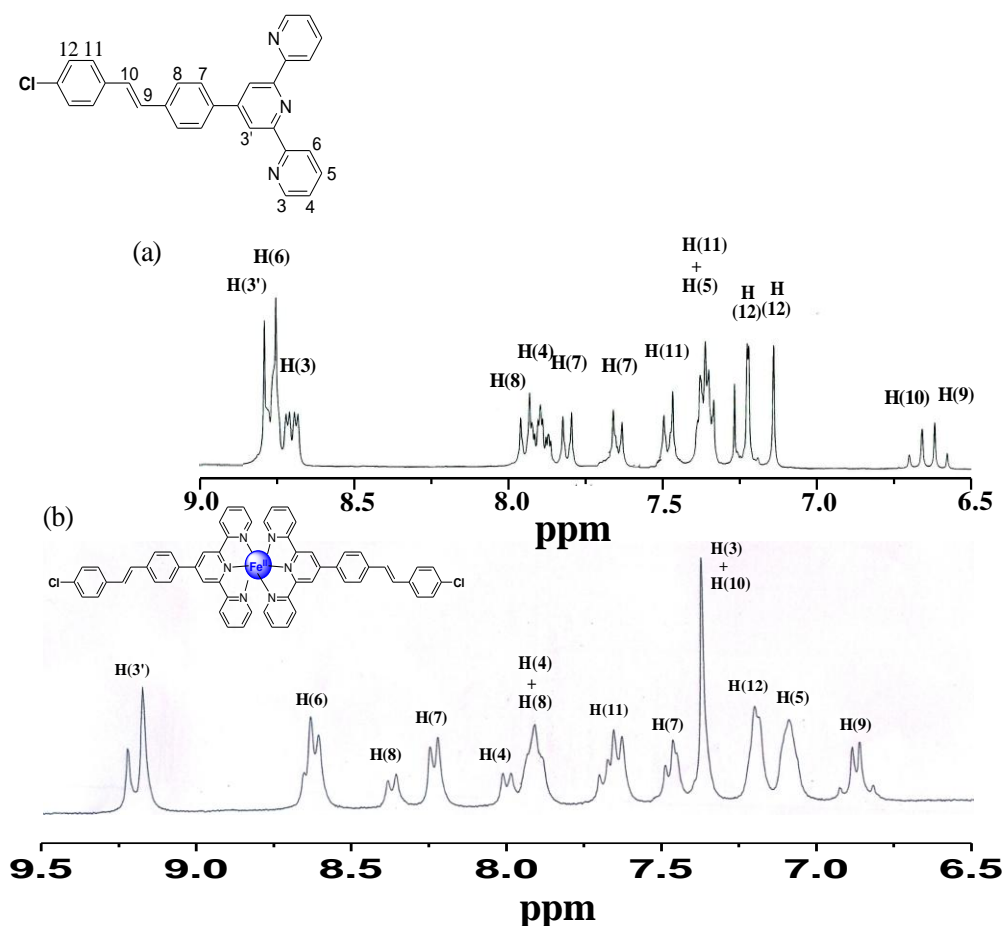


**Fig. 4.1.**  $^1\text{H}$  NMR (300 MHz) spectra of **tpy-pvp-Cl** (a) in  $\text{CDCl}_3$  and  $[\text{Fe}(\text{tpy-pvp-Cl})_2]^{2+}$  (b) in  $\text{CD}_3\text{CN}$ .

#### 4.3.2 Absorption and emission spectral properties

Absorption spectrum of free ligand (tpy-pvp-Cl) in acetonitrile consists of a band at 318 nm which arises mainly due to intra-ligand charge transfer transition (ILCT) and the next higher energy band at 284 nm, assignable predominantly due to  $\pi-\pi^*$  transitions within the aromatic moieties of the ligand. Upon excitation on either of the two absorption maxima, an intense emission band was observed at 407 nm whose quantum yield ( $\Phi$ ) is 0.030 and lifetime ( $\tau = 1.0$  ns). The absorption spectrum of acetonitrile solution of  $[\text{Fe}(\text{tpy-pvp-Cl})_2]^{2+}$  shows an intense band at 572 nm which is due to  $\text{Fe}^{\text{II}}(\text{d}\pi)-\pi^*(\text{tpy})$  MLCT transition. The spectrum of the complex also exhibits a series of

higher energy absorptions arising from ligand centered  $\pi\text{-}\pi^*$  and  $n\text{-}\pi^*$  transitions. Upon excitation at any of the absorption band, the complex does not exhibit any emission at room temperature. Literature reports suggest that the photophysics of the polypyridine Fe(II) complex is complicated by the presence of low lying ligand field (LF) excited states [43-45]. These states arise from population of the empty metal  $d\sigma^*$  orbitals. Although optical transitions to yield the LF excited states are not dipole-allowed and are therefore of low probability, the LF states can become populated by crossing from the MLCT states. This occurs readily in polypyridine Fe(II) complexes where the LF state lies below the MLCT state [43-45].

### *4.3.3 Anion sensing studies of the metalloreceptor through different optical channels and spectroscopic techniques*

The sensing ability of the metalloreceptor was initially investigated on a qualitative basis by visual inspection of its anion-induced color changes in both acetonitrile and water. Tetrabutylammonium salts of  $\text{F}^-$ ,  $\text{Cl}^-$ ,  $\text{Br}^-$ ,  $\text{I}^-$ ,  $\text{CN}^-$ ,  $\text{OAc}^-$ ,  $\text{H}_2\text{PO}_4^-$ ,  $\text{SCN}^-$ ,  $\text{BF}_4^-$  and  $\text{ClO}_4^-$  were used for the sensing studies. It was observed that upon addition of 12 equiv of various anions in acetonitrile, the bright violet colored solution of the Fe(II) complex became colorless in presence of  $\text{F}^-$  and  $\text{OAc}^-$  ions, while the color changes to light green in presence of  $\text{CN}^-$  (Fig. 4.2).

In contrast to acetonitrile, the deep violet color of the metalloreceptor became faint in mixed aqueous-acetonitrile only in presence of  $\text{CN}^-$  among the other studied anions (Fig. 4.3). Upon irradiation with UV light of wavelength 365 nm, bright bluish-green fluorescence color was observed in the presence of  $\text{F}^-$ ,  $\text{OAc}^-$  and  $\text{CN}^-$  ions in acetonitrile (Fig. 4.2), while the similar fluorescence color was observed in presence of only  $\text{CN}^-$  in mixed aqueous-acetonitrile medium (Fig. 4.3). Thus, visual color change of the metalloreceptor can be useful for the “naked-eye” detection of said anions in both organic as well as aqueous medium. In addition, selectivity is increased significantly in water where the metalloreceptor exclusively sense  $\text{CN}^-$  in presence of the other studied anions. This prompts us to investigate the anion sensing behaviors of the metalloreceptor through various spectroscopic techniques.

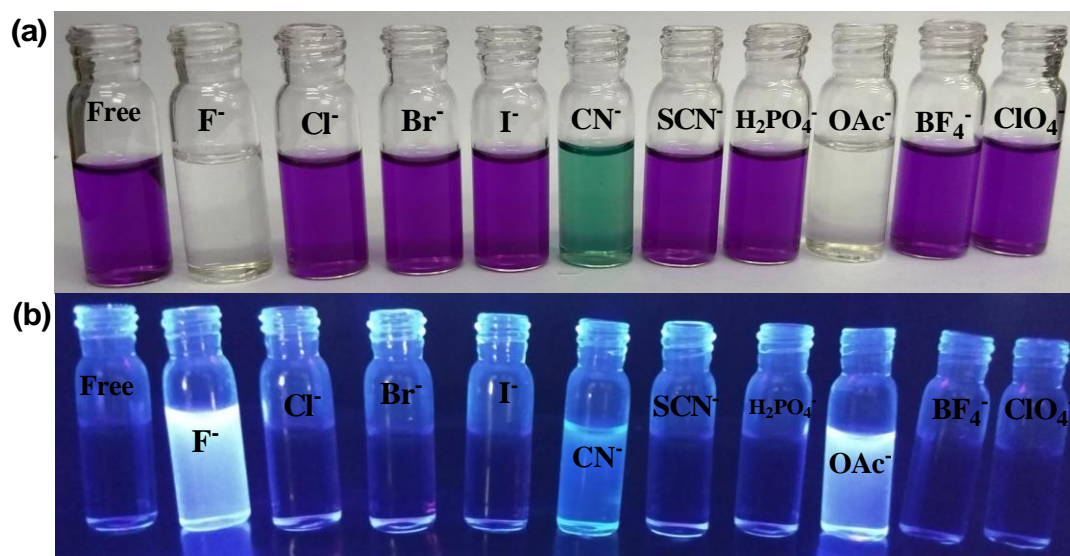


**Fig. 4.2.** Color changes that are observed in naked eye (a) and in presence of UV light (b) when the acetonitrile solutions of the metalloreceptor ( $5 \times 10^{-5}$  M) are treated with various anions ( $5.0 \times 10^{-3}$  M).

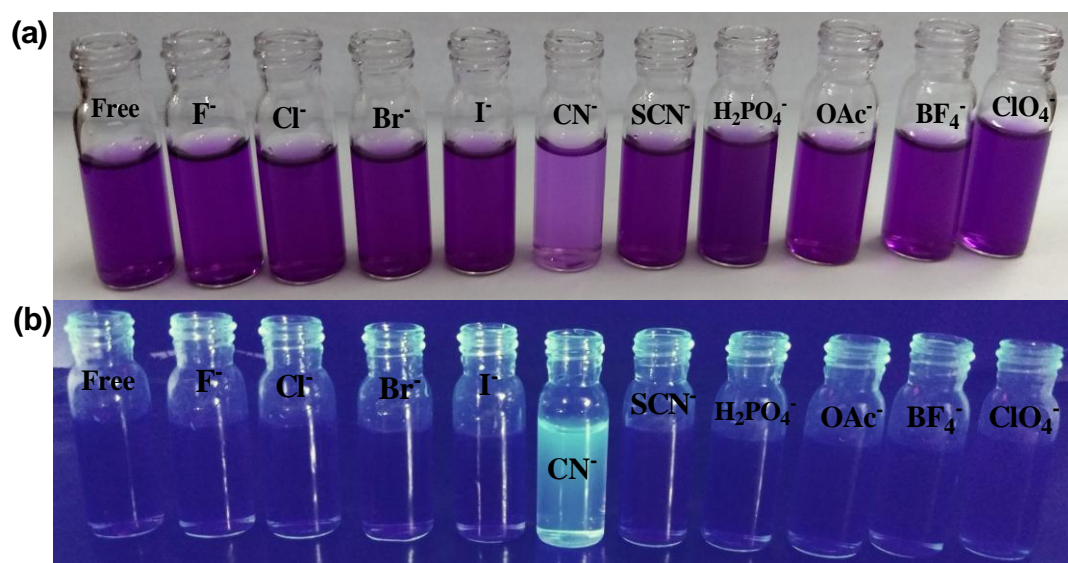


**Fig. 4.3.** Color changes that are observed in naked eye (a) and in presence of UV light (b) when the H<sub>2</sub>O-MeCN (100:1, v/v) solutions of the metalloreceptor ( $5 \times 10^{-5}$  M) are treated with various anions ( $5.0 \times 10^{-3}$  M).



UV-vis absorption and emission spectra of the metalloreceptor in presence of various anions are presented in Fig. 4.4. The MLCT band at 572 nm gets significantly affected compared with the other bands in the UV region in both media. In acetonitrile, upon addition of 12 equiv of the anions, the MLCT band is completely disappeared in presence of  $F^-$ , while substantial diminution of the MLCT band along with evolution of weak and broad band in the longer wavelength region are observed for  $OAc^-$  and  $CN^-$  (Fig. 4.4a). In contrast to neat acetonitrile, the diminution of the MLCT band occurs only with  $CN^-$  in mixed-aqueous medium (Fig. 4.4b). Free metalloreceptor is non-luminescent at room temperature but addition of the various anions, substantial emission enhancement at ~407 nm was observed for each of  $F^-$ ,  $OAc^-$  and  $CN^-$ , albeit in different extent (Fig. 4.4c). In line with absorption spectra, the enhancement of emission occurs only with  $CN^-$  in mixed-aqueous medium (Fig. 4.4d).

To have quantitative information about the receptor-anion interaction process, absorption and emission titration of the metalloreceptor was carried out with incremental addition of the anions. It was observed that the MLCT band at 572 nm in acetonitrile medium gradually decreased in intensity and finally completely disappeared upon addition of 12 equiv of either  $F^-$  or  $OAc^-$  with concomitant disappearance of the violet color of the solution (Fig. 4.5a-4.6a) and the final spectrum at saturation looks very similar to that of the free ligand. In contrast to  $F^-$  or  $OAc^-$ , saturation occurs upon addition of 6 equiv of  $CN^-$  and color of the resultant solution became light green with weak and broad band spanning in the range between 540 nm and 620 nm (Figure 4.7a). In each case, successive absorption curves pass through several well-defined isosbestic points. We are not very sure about the actual species that formed at saturation but to the best of our expectation, the composition of the final product may be  $[Fe(tpy-pvp-Cl)(CN)_3]^{2+}$ . The result of the blank experiment involving titration of  $Fe(ClO_4)_2$  with incremental addition of  $CN^-$  does not impart any green color in the final solution which can rule out the probable formation of  $[Fe(CN)_6]^{2+}$  as in the case of  $F^-$  or  $OAc^-$ .



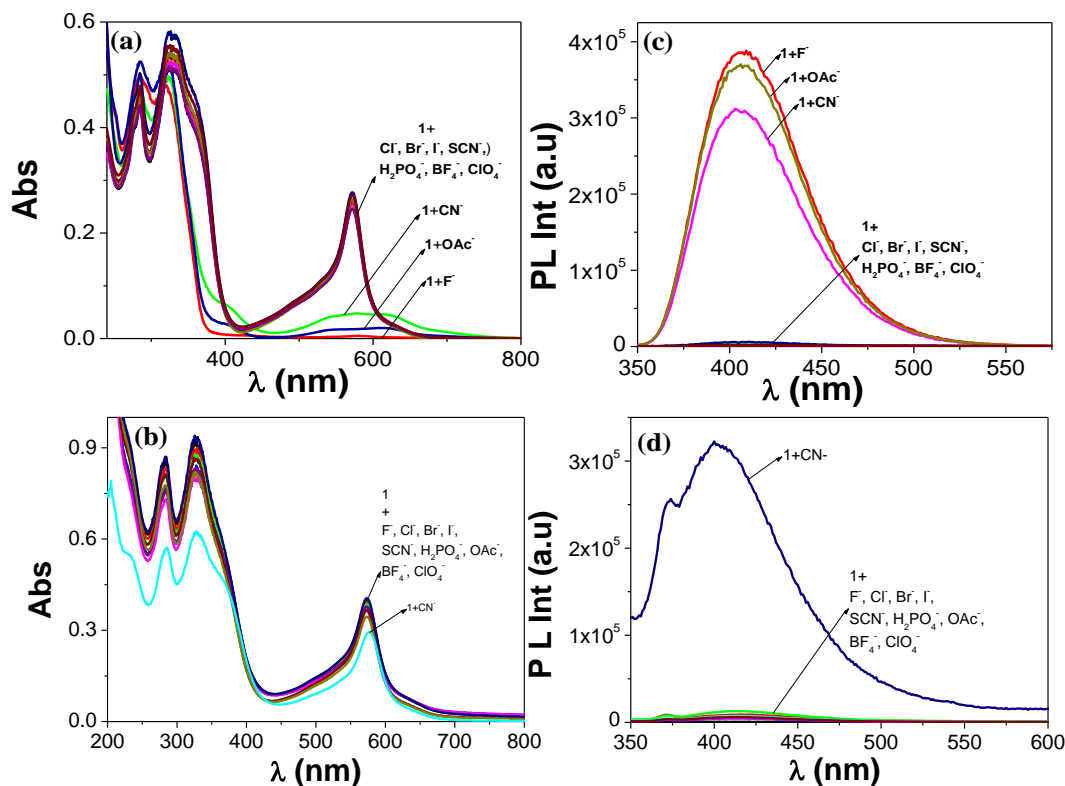


**Fig. 4.4.** UV-vis absorption (a and b, respectively) and photoluminescence (c and d, respectively) spectral changes of  $1.0 \times 10^{-5}$  M solutions of the metalloreceptor in acetonitrile and water-acetonitrile (100:1, v/v) mixture upon addition of different anions (100  $\mu\text{L}$ ) as their TBA and sodium salts ( $5.0 \times 10^{-3}$  M). Excitation wavelength for recording emission is 330 nm.

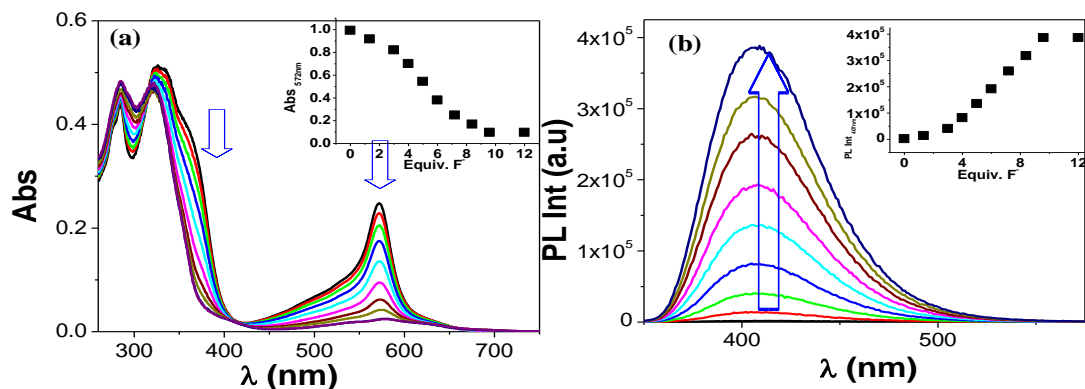


**Fig. 4.5.** UV-vis absorption (a) and photoluminescence ( $\lambda_{\text{ex}}$ : 330 nm) (b) spectral changes of the metalloreceptor ( $1.0 \times 10^{-5}$  M) in acetonitrile upon incremental addition of F<sup>-</sup> ( $5.0 \times 10^{-3}$  M). The insets show the equivalent plot of the experimental absorbance and luminescence data.

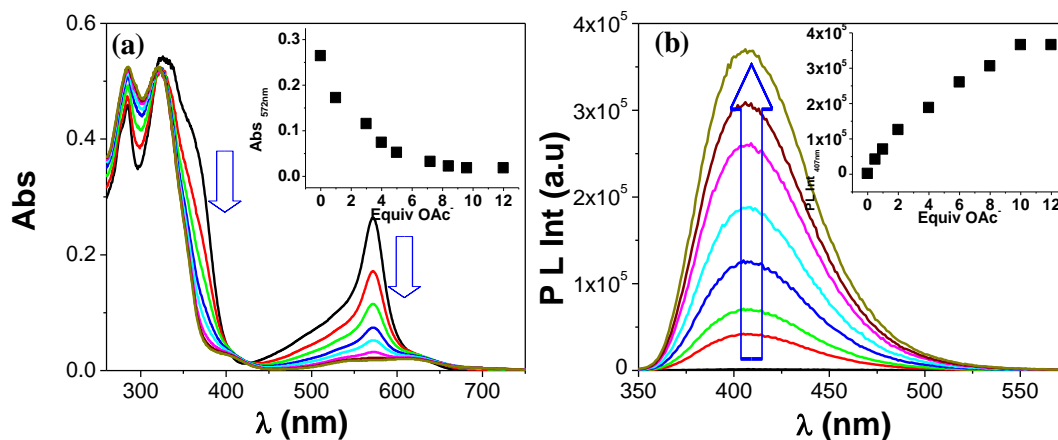


**Fig. 4.6.** UV-vis absorption (a) and photoluminescence ( $\lambda_{\text{ex}}$ : 330 nm) (b) spectral changes of the metalloreceptor ( $1.0 \times 10^{-5}$  M) in acetonitrile upon incremental addition of  $\text{OAc}^-$  ( $5.0 \times 10^{-3}$  M). The insets show the equivalent plot of the experimental absorbance and luminescence data.

The emission titration of  $[\text{Fe}(\text{tpy-pvp-Cl})_2]^{2+}$  as a function of the said anions was also carried out. Incremental addition of the said ions gives rise to gradual emission enhancement at 407 nm and finally saturated upon addition of 12 equiv of  $\text{F}^-$  or  $\text{OAc}^-$  (Fig. 4.5b - 4.6b). It is of interest to note that the extent of emission enhancement is little less in case of  $\text{CN}^-$  compared with  $\text{F}^-$  or  $\text{OAc}^-$  (Fig. 4.4c). Thus both absorption and emission titration data clearly indicate that addition of the said anions lead to sequester  $\text{Fe}^{2+}$  from the

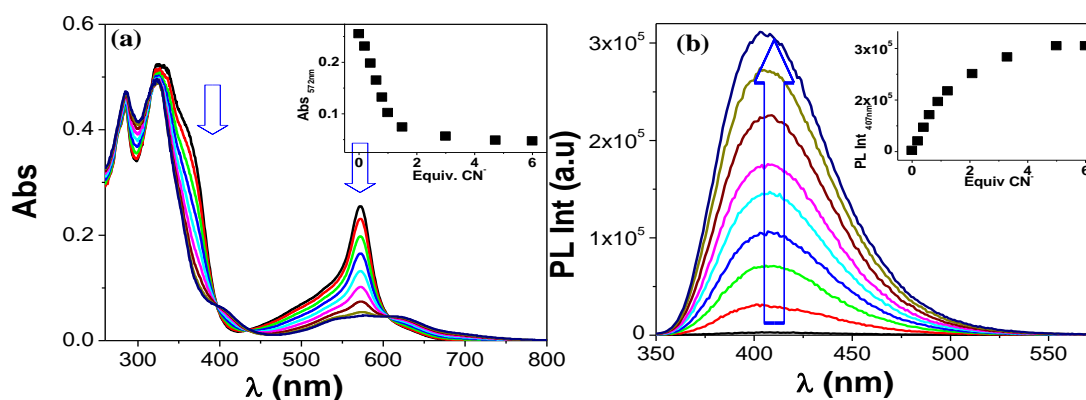


**Fig. 4.7.** UV-vis absorption (a) and photoluminescence ( $\lambda_{\text{ex}}$ : 330 nm) (b) spectral changes of the metalloreceptor ( $1.0 \times 10^{-5}$  M) in acetonitrile upon incremental addition of  $\text{CN}^-$  ( $5.0 \times 10^{-3}$  M). The insets show the equivalent plot of the experimental absorbance and luminescence data.

complex to form a more stable ion-pair or complex cation (such as  $[\text{FeF}_6]^{4-}$ ) and excess anions (except  $\text{CN}^-$ ) lead to regenerate the free terpyridine ligand.

In aqueous-acetonitrile medium, the titration profiles in presence of  $\text{CN}^-$  differ from those in neat acetonitrile (Fig. 4.8). It may be mentioned here that absorption and emission spectral titrations of the metalloreceptor were conducted in HEPES buffer solution at pH 7.2 to exclude the disturbance from hydroxide ion which may be produced from the hydrolysis of cyanide in water. Gradual reduction of absorbance along with small red-shift of the MLCT band and enhancement of emission intensity at 410 nm was also observed upon incremental addition of 12.0 equiv of  $\text{CN}^-$  but the extent of change is much less compared with neat acetonitrile (Fig. 4.7). Further addition of  $\text{CN}^-$  gives rise to gradual precipitation of the resulting complex.

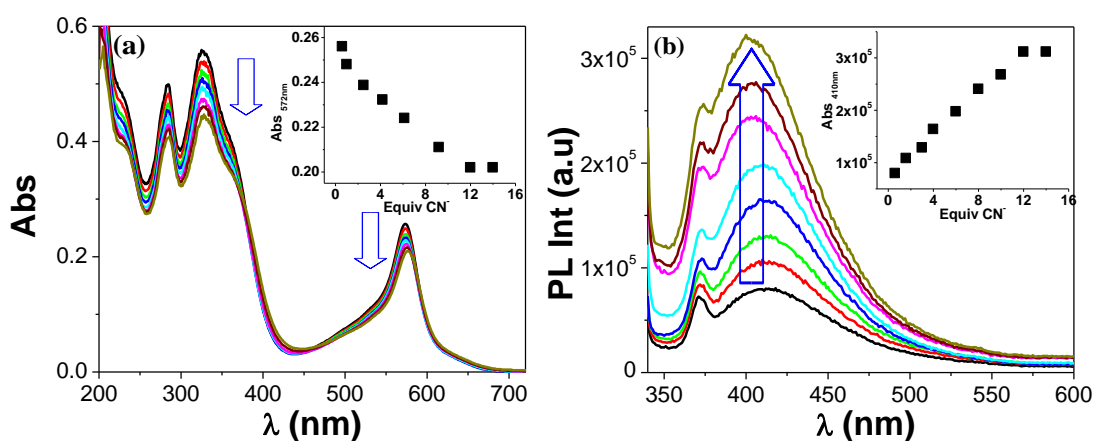


**Fig. 4.8.** UV-vis absorption (a) and photoluminescence ( $\lambda_{\text{ex}}$ : 330 nm) (b) spectral changes of the metalloreceptor ( $2.0 \times 10^{-5}$  M) in water-acetonitrile (100:1, v/v) mixture upon incremental addition of  $\text{CN}^-$  ( $5.0 \times 10^{-3}$  M). The insets show the equivalent plot of the experimental absorbance and luminescence data.

To prove the interaction of metalloreceptor with various anions,  $^1\text{H}$  NMR titration experiments were conducted upon incremental addition of  $\text{F}^-$  and  $\text{OAc}^-$  in  $\text{DMSO}-d_6$  as well as with  $\text{CN}^-$  in  $\text{CD}_3\text{CN}$  (Fig. 4.9-4.10).  $5.0 \times 10^{-3}$  M solution of complex was employed in the titration experiment. Upon addition of both  $\text{F}^-$  and  $\text{OAc}^-$ , the chemical shifts of H3' and H6 are found to be remarkably up-field shifted, H7-H10 protons moderately up-field shifted, while H5 and H11 protons shifted to small down-field

region. Assignments of the different protons in the final spectrum indicate that the spectrum is of that of the free ligand, although small variation of spectral pattern is observed between the spectrum recorded in  $\text{CDCl}_3$  and  $\text{DMSO}-d_6$ . Thus, both  $\text{F}^-$  and  $\text{OAc}^-$  induce complete decooordination of  $\text{Fe(II)}$  center from the complex yielding the free ligand. The spectral profile in presence of  $\text{CN}^-$  is quite different from both  $\text{F}^-$  and  $\text{OAc}^-$  (Fig. 4.10). It is observed that complete displacement of  $\text{Fe(II)}$  ion from the complex does not occur. Instead, one terpyridine ligand is still coordinated with  $\text{Fe(II)}$ , while the second one is probably displaced by three incoming  $\text{CN}^-$  ligands. In addition, some small but

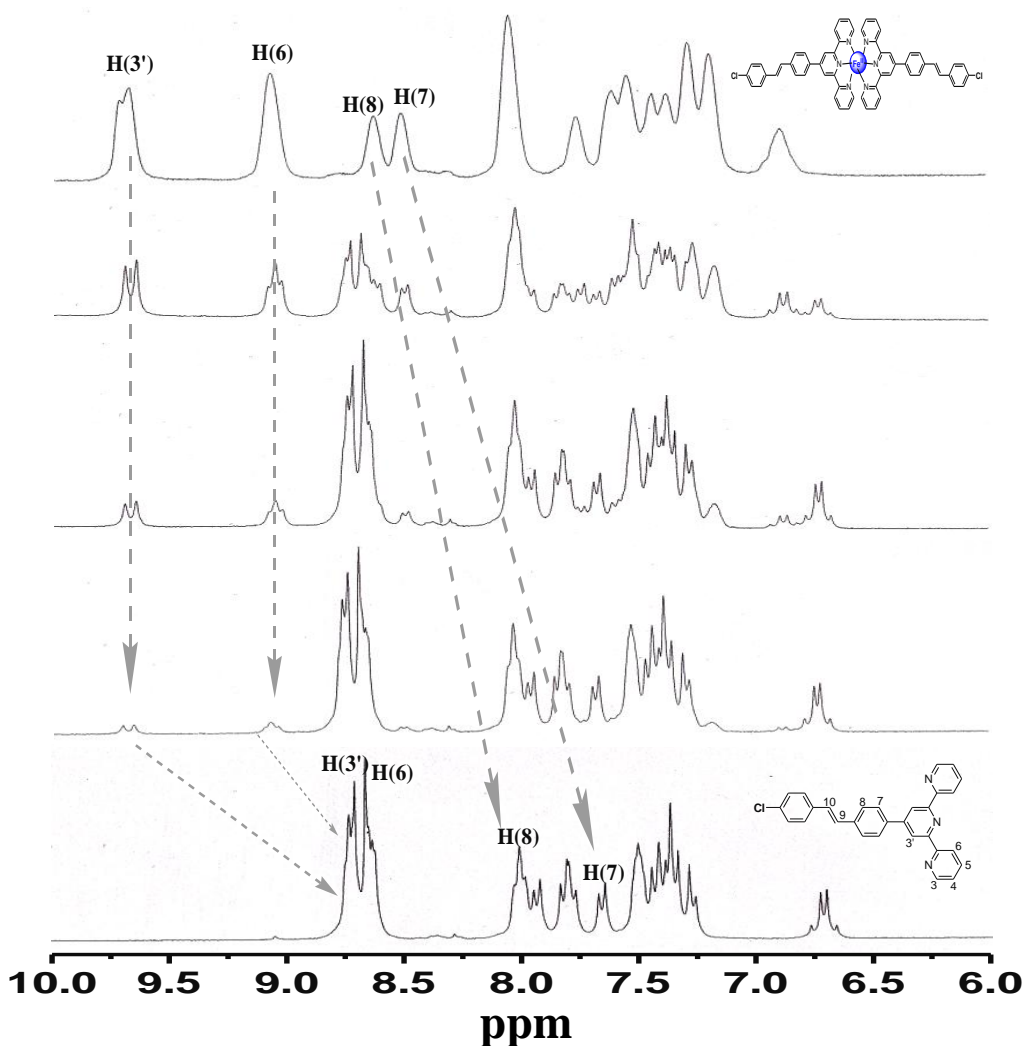


**Fig. 4.9.**  $^1\text{H}$  NMR (300 MHz) spectral titration of the metalloreceptor in  $\text{DMSO}-d_6$  ( $2.5 \times 10^{-3}$  M) upon gradual addition of  $\text{F}^-$  ion (0-12 equiv).

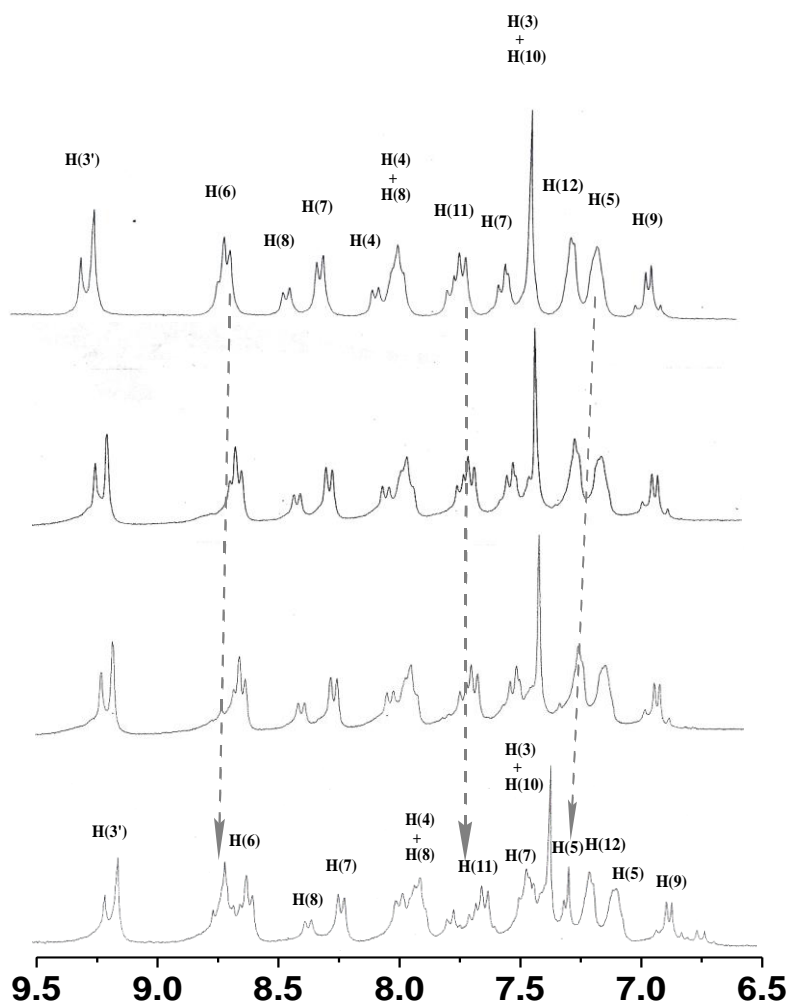


**Fig.4.10.**  $^1\text{H}$  NMR (300 MHz) spectral titration of the metalloreceptor in  $\text{CD}_3\text{CN}$  ( $2.5 \times 10^{-3}$  M) upon gradual addition of  $\text{CN}^-$  ion (0-6 equiv).

finite change in spectral pattern and/or chemical shift of selected terpyridine protons (H6, H5, and H4) occurs upon displacement of one ligand moiety from the  $\text{Fe(II)}$  center. UV-vis absorption spectral titrations also indicate the same conclusion. Even after addition of excess  $\text{CN}^-$  to the acetonitrile solution of the complex, clear broad (most probably MLCT) bands in the visible range (between 540 nm and 620 nm) are observed indicating the coexistence of both the ligand as well as  $\text{Fe(II)}$ .

For practical applicability, the limit of detection and selectivity of the metalloreceptor are very important parameters. To this end, we have determined the detection limit of the metalloreceptor by utilizing the absorption and emission titration data in both media and

the values are provided in Table 4.1. The calculated values (lying in the range between  $(1.18 \pm 0.03) \times 10^{-9}$  M -  $(1.19 \pm 0.04) \times 10^{-9}$  M for  $F^-$  and between  $(1.18 \pm 0.06) \times 10^{-9}$  M and  $(2.20 \pm 0.02) \times 10^{-8}$  M for  $CN^-$ ) indicate that the complex provides extremely low limit detection of  $CN^-$ , even in mixed aqueous-organic medium (Fig. 4.11-4.16). The selectivity of the metalloreceptor towards a particular ion such as  $F^-$  or  $CN^-$  in presence

**Table 4.1** Spectrophotometric and fluorimetric detection limits of  $[Fe(tpy-pvp-Cl)_2]^{2+}$  in acetonitrile and water-acetonitrile (100:1, v/v) mixture.

Compound	Detection Limit (M) in acetonitrile		Detection Limit (M) in acetonitrile		Detection Limit (M) in water-acetonitrile (100:1, v/v) mixture	
$[Fe(tpy-pvp-Cl)_2]^{2+}$	$F^-$		$CN^-$		$CN^-$	
	Abs	Emission	Abs	Emission	Abs	Emission
	$(1.18 \pm 0.03) \times 10^{-9}$	$(1.19 \pm 0.04) \times 10^{-9}$	$(2.00 \pm 0.04) \times 10^{-9}$	$(1.18 \pm 0.06) \times 10^{-9}$	$(2.20 \pm 0.02) \times 10^{-8}$	$(1.90 \pm 0.06) \times 10^{-8}$

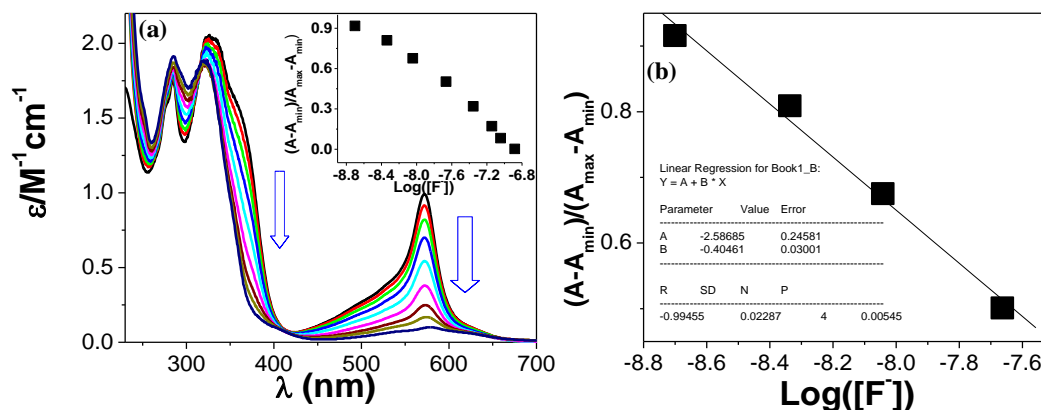


**Fig. 4.11.** (a) Absorption spectral changes during the titration of the  $[Fe(tpy-pvp-Cl)_2]^{2+}$  with  $F^-$  in acetonitrile. Inset to (a) shows normalized absorbance between the minimum absorbance and the maximum absorbance. (b) A plot of  $(A-A_{min})/(A_{max}-A_{min})$  vs  $\text{Log}([F^-])$ ; the calculated detection limit of receptor is  $1.186 \times 10^{-9}$ .

of other studied anions was also investigated. UV-vis absorption and emission measurements were performed by treating the aqueous solution of the complex ( $c \sim 2 \times 10^{-5}$  M) with any of the two anions ( $F^-$  or  $CN^-$ ) in the presence of each of the other studied

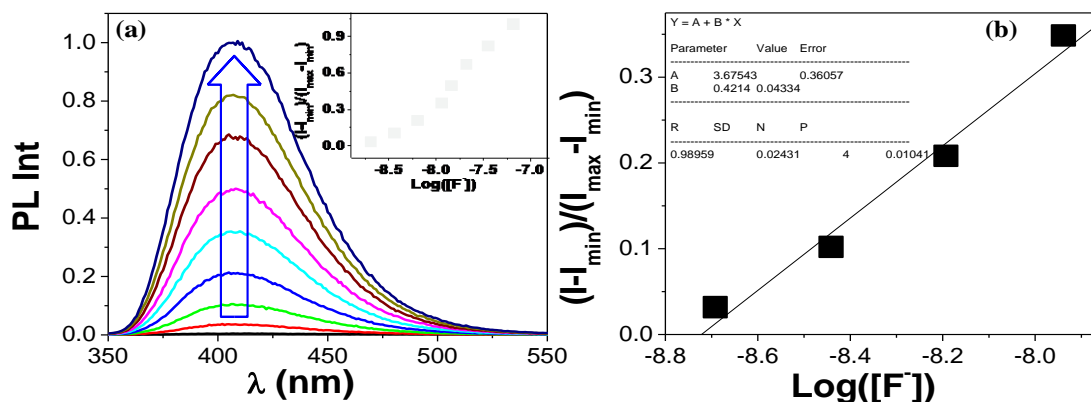


**Fig. 4.12.** (a) Fluorescence spectral changes during the titration of the  $[\text{Fe}(\text{tpy-pvp-Cl})_2]^{2+}$  with  $\text{F}^-$  in acetonitrile. Inset to (a) shows normalized intensity between the minimum intensity and the maximum intensity. (b) A plot of  $(I-I_{\min})/(I_{\max}-I_{\min})$  vs  $\text{Log}([\text{F}^-])$ ; the calculated detection limit of receptor is  $1.19 \times 10^{-9}$ .

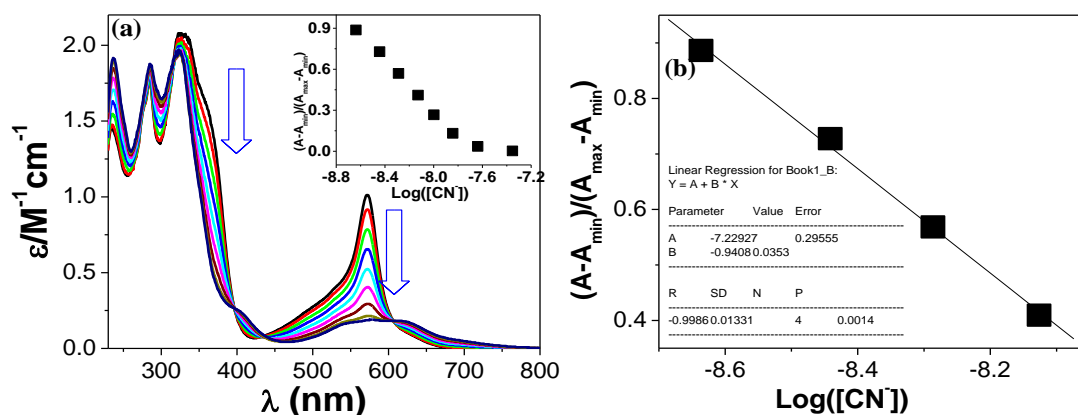


**Fig. 4.13.** (a) Absorption spectral changes during the titration of the  $[\text{Fe}(\text{tpy-pvp-Cl})_2]^{2+}$  with  $\text{CN}^-$  in acetonitrile. Inset to (a) shows normalized absorbance between the minimum absorbance and the maximum absorbance. (b) A plot of  $(A-A_{\min})/(A_{\max}-A_{\min})$  vs  $\text{Log}([\text{CN}^-])$ ; the calculated detection limit of receptor is  $2.0 \times 10^{-9}$ .

anions. In the competition experiments, we are still able to observe color as well as spectral changes in presence of each of  $\text{F}^-$ ,  $\text{CN}^-$  and  $\text{OAc}^-$  in acetonitrile while the color and spectral change occurs only with  $\text{CN}^-$  in water. Likewise, enhancement of emission also occur with  $\text{F}^-$  or  $\text{CN}^-$  in acetonitrile whereas only in presence of  $\text{CN}^-$  in water. Once a particular ion among the two ( $\text{F}^-$  or  $\text{CN}^-$ ) is added, the other anion was unable to make any further change. The inability of the complex to sense  $\text{F}^-$  and  $\text{OAc}^-$  in aqueous medium

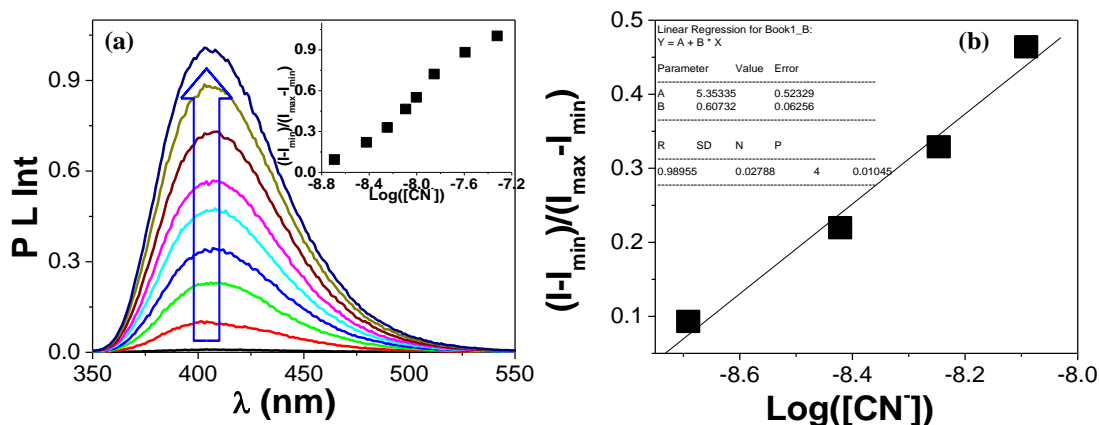


**Fig. 4.14.** (a) Fluorescence spectral changes during the titration of the  $[\text{Fe}(\text{tpy-pvp-Cl})_2]^{2+}$  with  $\text{CN}^-$  in acetonitrile. Inset to (a) shows normalized intensity between the minimum intensity and the maximum intensity. (b) A plot of  $(I-I_{\min})/(I_{\max}-I_{\min})$  vs  $\text{Log}([\text{CN}^-])$ ; the calculated detection limit of receptor is  $1.18 \times 10^{-9}$ .

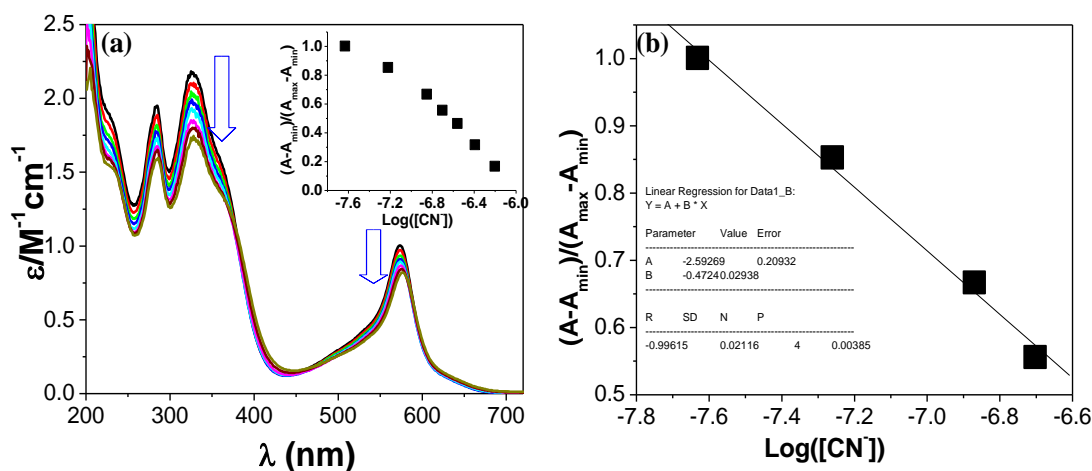


**Fig. 4.15.** (a) Absorption spectral changes during the titration of the  $[\text{Fe}(\text{tpy-pvp-Cl})_2]^{2+}$  with  $\text{CN}^-$  in  $\text{H}_2\text{O-MeCN-}$  (100:1, v/v) mixture. Inset: to (a) shows normalized absorbance between the minimum absorbance and the maximum absorbance. (b) A plot of  $(A-A_{\min})/(A_{\max}-A_{\min})$  vs  $\text{Log}([\text{CN}^-])$ ; the calculated detection limit of receptor is  $2.20 \times 10^{-8}$ .

is due to the higher hydration energy of  $\text{F}^-$  ( $\Delta G_{\text{h}}^\circ = -465 \text{ kJ/mol}$ ) and  $\text{OAc}^-$  ( $\Delta G_{\text{h}}^\circ = -465 \text{ kJ/mol}$ ) compared with  $\text{CN}^-$  ( $\Delta G_{\text{h}}^\circ = -295 \text{ kJ/mol}$ ). In addition, higher  $\text{pK}_{\text{a}}$  value for HCN in water ( $\text{pK}_{\text{a}} = 9.0$ ) compared with HF ( $\text{pK}_{\text{a}} = 3.17$ ) and HOAc ( $\text{pK}_{\text{a}} = 4.75$ ) shows more basic character of  $\text{CN}^-$  compared with  $\text{F}^-$  and  $\text{OAc}^-$  in water.<sup>34</sup> The results clearly



indicate that the metalloreceptor possesses very high selectivity towards  $\text{CN}^-$  over the other anions in predominantly aqueous medium.

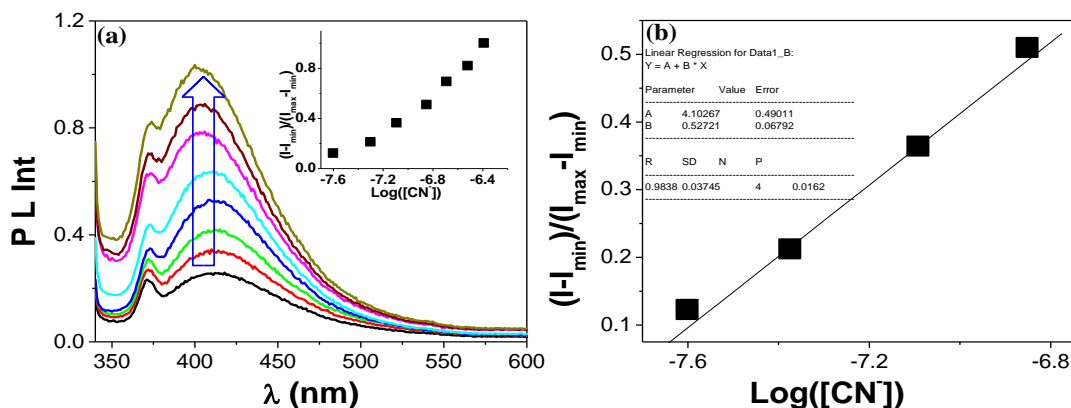


**Fig. 4.16.** (a) Fluorescence spectral changes during the titration of the  $[\text{Fe}(\text{tpy-pvp-Cl})_2]^{2+}$  with  $\text{CN}^-$  in  $\text{H}_2\text{O-MeCN}$  (100:1, v/v) mixture water. Inset to (a) shows normalized intensity between the minimum intensity and the maximum intensity. (b) A plot of  $(I - I_{\min})/(I_{\max} - I_{\min})$  vs  $\text{Log}([\text{CN}^-])$ ; the calculated detection limit of receptor is  $1.90 \times 10^{-8}$ .

## 4.4 Conclusions

In this work, we report an unprecedented homoleptic bis-terpyridine  $\text{Fe}(\text{II})$  complex for multichannel sensing of selective anions in both organic and aqueous medium by taking profit of metal-ligand interaction via displacement approach. In acetonitrile medium the metalloreceptor functions as sensor for  $\text{F}^-$ ,  $\text{OAc}^-$  and  $\text{CN}^-$  without selectivity, but in water it acts as chromogenic and fluorogenic sensor for only  $\text{CN}^-$  ion. One of the most important observations of this work is that the  $\text{Fe}(\text{II})$  complex exhibits very high selectivity and sensitivity towards  $\text{CN}^-$  in water with very low detection limit up to  $10^{-8}$  M and thus may be useful for real practical application.

## 4.5 References

- [1] J L. Sessler, P A. Gale, W S. Cho, Anion receptor chemistry, Royal society of chemistry: Cambridge, U.K, (2006).
- [2] A. Bianchi, K. Bowman-James, E. Garcia-España, Supramolecular Chemistry of Anions (Eds:) Wiley-VCH; New York, (1997).

- [3] K. Bowman-James, Alfred Werner Revisited: The coordination chemistry of anions, *Acc. Chem. Res.* 38 (2005) 671-678.
- [4] P D. Beer, Anion selective recognition and optical/electrochemical sensing by novel transition-metal receptor systems, *Chem. Commun.* (1996) 689-696.
- [5] K W. Kulig, Cyanide toxicity, U.S. department of health and human services, Atlanta, (1991).
- [6] J. Taylor, N. Roney, M. E. Fransen, S. Swarts, Toxicological profile for cyanide, DIANE publishing, Atlanta, (2006).
- [7] Z. Xu, X. Chen, H. N. Kim, J. Yoon, Sensors for the optical detection of cyanide ion, *Chem. Soc. Rev.* 39 (2010) 127-137.
- [8] K. Kaur, R. Saini, A. Kumar, V. Luxami, N. Kaur, P. Singh, S. Kumar, Chemodosimeters: an approach for detection and estimation of biologically and medically relevant metal ions, anions and thiols, *Coord. Chem. Rev.* 256 (2012) 1992-2028.
- [9] F. Wang, L. Wang, X. Chen, J. Yoon, Recent progress in the development of fluorometric and colorimetric chemosensors for detection of cyanide ions, *Chem. Soc. Rev.* 43 (2014) 4312-4324.
- [10] S. Kubik, Anion recognition in water, *Chem. Soc. Rev.* 39 (2010) 3648-3663.
- [11] W. Sun, S. Guo, C. Hu, J. Fan, X. Peng, Recent development of chemosensors based on cyanine platforms, *Chem. Rev.* 116 (2016) 7768-7817.
- [12] T. Gunnlaugsson, M. Glynn, G. M. Tocci, P. E. Kruger, F. M. Pfeffer, Anion recognition and sensing in organic and aqueous media using luminescent and colorimetric sensors, *Coord. Chem. Rev.* 250 (2005) 3094-3117.
- [13] S-S .Sun, A. J. Lees, Advanced concepts in fluorescence sensing: part A: small molecule sensing, *Chem. Commun.* (2000) 1687 -1688.
- [14] S. Saha, A. Ghosh, P. Mahato, S. Mishra, S K. Mishra, E. Suresh, S. Das, A. Das, Specific recognition and sensing of  $\text{CN}^-$  in sodium cyanide solution, *Org. Lett.* 12 (2010) 3406-3409.
- [15] K-S. Lee, H-J. Kim, G-H. Kim, I. Shin, J-I. Hong, Fluorescent chemodosimeter for selective detection of cyanide in water, *Org. Lett.* 10 (2008) 49-51.

- [16] L. E. Santos-Figueroa, M. E. Moragues, E. Climent, A. Agostini, R. Martínez-Máñez, F. Sancenón, Chromogenic and fluorogenic chemosensors and reagents for anions. A comprehensive review of the years 2010-2011, *Chem. Soc. Rev.* 42 (2013) 3489-3613.
- [17] S-Y. Chung, S-W. Nam, J. Lim, S. Park, J. Yoon, A highly selective cyanide sensing in water via fluorescence change and its application to in vivo imaging, *Chem. Commun.* (2009) 2866-2868.
- [18] V. Bhalla, H. Singh, M. Kumar, Triphenylene based copper ensemble for the detection of cyanide ions, *Dalton Trans.* 41 (2012) 11413-11418
- [19] X. Lou, L. Zhang, J. Qin, Z. Li, An alternative approach to develop a highly sensitive and selective chemosensor for the colorimetric sensing of cyanide in water, *Chem. Commun.* (2008) 5848-5850.
- [20] B. T. Nguyen, E. V. Anslyn, Indicator-displacement assays, *Coord. Chem. Rev.* 250 (2006) 3118-3127.
- [21] X. Lou, D. Ou, Q. Li, Z. Li, An indirect approach for anion detection: the displacement strategy and its application, *Chem. Commun.* 48 (2012) 8462-8477.
- [22] K. P. Divya, S. Sreejith, B. Balakrishna, P. Jayamurthy, P. Anees, A. Ajayaghosh, A  $\text{Zn}^{2+}$  specific fluorescent molecular probe for the selective detection of endogenous cyanide in biorelevant samples, *Chem. Commun.* (2010) 6069-6071.
- [23] A. K. Shaily, N. Ahmed, Indirect approach for  $\text{CN}^-$  detection: development of "Naked-Eye"  $\text{Hg}^{2+}$ -induced turn-off fluorescence and turn-on cyanide sensing by the  $\text{Hg}^{2+}$  displacement approach, *Ind. Eng. Chem. Res.* 56 (2017) 6358-6368.
- [24] M. La, Y. Hao, Z. Wang, G-C. Han, L. Qu, Selective and sensitive detection of cyanide based on the displacement strategy using a water-soluble fluorescent probe, *J. Anal. Methods Chem.* (2016) 1-6.
- [25] C-F. Chow, P-Y. Ho, W-L. Wong, C-B. Gong, A multifunctional bimetallic molecular device for ultrasensitive detection, naked-eye recognition, and elimination of cyanide ions *Chem. Eur. J.* 21 (2015) 12984-12990.

- [26] N. Maurya, S. Bhardwaj, A K. Singh, Selective colorimetric and fluorescence ‘turn-on’ sensor for  $\text{Ag}^+$  and in-situ sensing of  $\text{CN}^-$  (off-on-off) via displacement approach, *Mater. Sci Eng. C* 74 (2017) 55-61.
- [27] R. Martínez-Máñez, F. Sancenón, Fluorogenic and chromogenic chemosensors and reagents for anions, *Chem. Rev.* 103 (2003) 4419-4476.
- [28] P D. Beer, S R. Bayly, Transition-metal receptor systems for the selective recognition and sensing of anionic guest species, *Acc. Chem. Res.* 31 (1998) 71-80.
- [29] J. Pérez, L. Riera, Stable metal-organic complexes as anion hosts, *Chem. Soc. Rev.* 37 (2008) 2658-2667.
- [30] V. Amendola, L. Fabbrizzi, Anion receptors that contain metals as structural units, *Chem. Commun.* (2009) 513-531.
- [31] B D. Paul, F. Szemes, V. Balzani, C. M. Salà, M G B. Drew, S W. Dent, M. Maestri, Anion selective recognition and sensing by novel macrocyclic transition metal receptor systems.  $^1\text{H}$  NMR, electrochemical, and photophysical investigations, *J. Am. Chem. Soc.* 119 (1997) 11864–11875.
- [32] Y. Cui, Y-L. Niu, M L. Cao, K. Wang, H-J. Mo, Y-R. Zhong, B-H. Ye, Ruthenium(II) 2,2'-bibenzimidazole complex as a second-sphere receptor for anions interaction and colorimeter, *Inorg. Chem.* 47 (2008) 5616-5624.
- [33] H-J. Mo, Y. Shen, B-H. Ye, Selective recognition of cyanide anion via formation of multipoint NH and phenyl CH hydrogen bonding with acyclic ruthenium bipyridine imidazole receptors in water, *Inorg. Chem.* 51 (2012) 7174-84.
- [34] M. Bar, D. Maity, K. Das, S. Baitalik, Asymmetric bimetallic ruthenium(II) complexes selectively sense cyanide in water through significant modulation of their ground and excited state properties, *Sensors and Actuators B* 251 (2017) 208–223.
- [35] S. Mardanya, S. Karmakar, M. Bar, S. Baitalik, Pyrene-biimidazole based Ru(II) and Os(II) complexes as highly efficient probes for the visible and near infrared detection of cyanide in aqueous media, *Dalton Trans.* 44 (2015) 21053-21072.
- [36] D. Maity, S. Das, S. Mardanya, S. Baitalik, Synthesis, structural characterization, and photophysical, spectroelectrochemical, and anion-sensing studies of heteroleptic ruthenium(II) complexes derived from 4'-polyaromatic-substituted

- terpyridine derivatives and 2,6-bis(benzimidazol-2-yl)pyridine, *Inorg. Chem.* 52 (2013) 6820-6838.
- [37] D. Maity, C. Bhaumik, D. Mondal, S. Baitalik, Photoinduced intramolecular energy transfer and anion sensing studies of isomeric Ru<sup>II</sup>Os<sup>II</sup> complexes derived from an asymmetric phenanthroline–terpyridine bridge, *Dalton Trans.* 43 (2014) 1829-1845.
- [38] S. Mardanya, S. Karmakar, D. Maity, S. Baitalik, Ruthenium(II) and Osmium(II) mixed chelates based on pyrenyl–pyridylimidazole and 2,2'-bipyridine ligands as efficient DNA intercalators and anion sensors, *Inorg. Chem.* 54 (2015) 513-526.
- [39] B. Chowdhury, S. Sinha, P. Ghosh, Selective sensing of phosphates by a new bis-heteroleptic Ru<sup>II</sup> complex through halogen bonding: A superior sensor over its hydrogen-bonding analogue, *Chem. Eur. J.* 22 (2016) 18051-18059.
- [40] B. Chowdhury, R. Dutta, S. Khatua, P. Ghosh, A cyanuric acid platform based tripodal bis-heteroleptic Ru(II) complex of click generated ligand for selective sensing of phosphates via C-H anion interaction, *Inorg. Chem.* 55 (2016) 259-271.
- [41] K T. Pott, D A. Usifer, H D. Abruna, 4-Vinyl-, 6-Vinyl-, and 4'-Vinyl-2,2':6',2'' terpyridinyl ligands: their synthesis and the electrochemistry of their transition-metal coordination complexes, *J. Am. Chem. Soc.* 109 (1987) 3961-3967.
- [42] W. Spahni, G. Calzaferri, Synthese von para -substituierten phenyl-terpyridin liganden *Helv. Chim. Acta.* 67 (1984) 450-454.
- [43] J R. Winker, N. Sutin, Lifetimes and spectra of the excited states of cis dicyanobis(2,2'-bipyridine)iron(II) and -ruthenium(II) in solution, *Inorg. Chem.* 26 (1987) 220-221.
- [44] C. Creutz, M. Chou, T L. Netzel, M. Okumura, N. Sutin, Lifetimes, spectra, and quenching of the excited states of polypyridine complexes of iron(II), ruthenium(II), and osmium(II), *J. Am. Chem. Soc.* 102 (1980) 1309-1319.
- [45] M A. Bergkamp, P. Guetlich, T L. Netzel, N. Sutin, Lifetimes of the ligand-to-metal charge-transfer excited states of iron(III) and osmium(III) polypyridine complexes. Effects of isotopic substitution and temperature, *J. Phys. Chem.* 87 (1983) 3877.

\*\*\*\*\*

## ***Chapter 5***

**Low cost photo-switches based on  
stilbene-appended Zn(II)-terpyridine  
complexes**

## 5.1 Introduction

There is increasing interest in the fabrication of task-specific materials as a response to external stimuli such as light, heat, mechanical effects or chemical species [1-6]. Among the different external stimuli, light is one of the most convenient source and the substances can be excited at desired wavelength of choice spanning within a wide domain (UV to IR). The interaction event can often lead to different performances, such as emission of light, electron or energy transfer, conformational changes, sensitization or chemical transformation which can lay the foundations for many applications [7-16]. An optical stimulation is also very loyal to user, and switching off the source creates an instant turn off of the optical signal. Moreover, the light sources can be remote controlled over a long distance which is beneficial for the design of optical information storage, high density optical memory, and optical switches [11-14,17].

Stilbene and its derivatives undergo optically stimulated reversible *trans-cis* isomerization and constitute an important class of photo-responsive materials [18-22]. The conformational change is coupled with a significant alteration of their photophysical behaviors which in turn is useful for practical applications. Even though lots of studies were performed with purely organic stilbene derivatives, but analogous studies with their coordination complexes are comparatively limited in the literature [18-22]. Compared to organic compounds, metal complexes offer a greater variety of electronic structures, in relation to the coordination sphere, electronic configuration and oxidation state of the metal [23-33]. To mimic the function of photochemical molecular devices (such as photo switches) in metal complexes, one of the most effective strategies is to reversibly alter their properties by inducing conformational changes on the photo-responsive component appended on the ligands. Majority of the studies to this end are primarily focused on noble metals which are very expensive and the synthetic procedures often demand very drastic conditions [23-33]. Our primary objective in this work is to design suitable base-metal complexes which could show off similar behavior and can lead to the construction of a new class of low-cost and easily synthesizable photo-switches.

For achieving our goal, we report in this work synthesis, characterization, photophysics, and reversible *trans-cis* photoisomerization properties of a new class of homoleptic Zn(II)-terpyridine complexes of composition  $[\text{Zn}(\text{tpy-pvp-X})_2]^{2+}$  ( $\text{X} = \text{H}, \text{Me}$ ,

and NO<sub>2</sub>) covalently attached with photo-responsive stilbene moiety (Chart 1). Among the polypyridines, 2,2':6',2''-terpyridine affords an excellent building motif for the construction of molecular systems around the photoactive metal centers [34-41]. The superiority of terpyridine over bipyridines is because of its effortless functionalization, particularly at 4'-position and competence to build up linear achiral structures [34,35].

Low-cost zinc metal is playing progressively important role for the design of a wide variety of coordination complexes with interesting photophysical properties which in turn can be useful in nonlinear optical properties as well as multi-photon fluorescent probes [42-45]. Because of d<sup>10</sup> electronic configuration, Zn(II) complexes do not display stereochemistry preference arising from ligand field stabilization effects and they can acquire a wide variety of geometries and coordination numbers, depending upon the electronic nature and stereochemistry of ligands. The important characteristics of zinc also allows the preparation of complexes with intense intra-ligand charge transfer (LLCT) absorption and emission at low energy [42-45]. In addition, the absence of low-energy metal-to-ligand (MLCT) or metal d-d electronic transitions makes these zinc complexes generally more optically transparent than other metal d<sup>n</sup> congeners.

Optically stimulated reversible *trans-cis* isomerization of stilbene appended heavier transition metal complexes (particularly Re, Ru, Ir and Pt) were thoroughly investigated by different research groups [46-56]. The results of these investigations laid the foundation for the construction of effective photo molecular switches. In contrast to noble metal analogues, similar investigations with low cost 3d metals are much less in literature [57-59]. Although, Zn(II)-terpyridine complexes appended with one or more stilbene moiety are reported with regard to the design of efficient two-photon probes for bioimaging [60] and improvement of second-order nonlinear optical (NLO) responses [61], no report dealing with their photo-isomerization aspects are available in the literature. Herein, we address the influence of solvents and the effect of electron donating/withdrawing substituent (X) on their optical properties as well as thermodynamic and kinetic features of photoisomerization procedure. The influence of excitation wavelength on thermodynamic and kinetic features of isomerization procedure will also be maneuvered. In essence, substantial alteration of the optical properties along with switching of emission spectral characteristics of the complexes is made possible



upon isomerization. Moreover, the emission spectral output as a function of photonic and thermal inputs is utilized for the fabrication of INHIBIT and IMPLICATION logic gates. The processing of information at the molecular level is now a very active area of research and proper utilization of sequential logic functions exhibited by molecular and supramolecular species is a huge challenge in research filed of information technology [62-66]. In conjunction with experiment, theoretical studies employing DFT and TD-DFT methods are also carried out to acquire insight about the electronic structures of the complexes, correct assignment of the spectral bands, and to understand the actual mode of isomerization process.

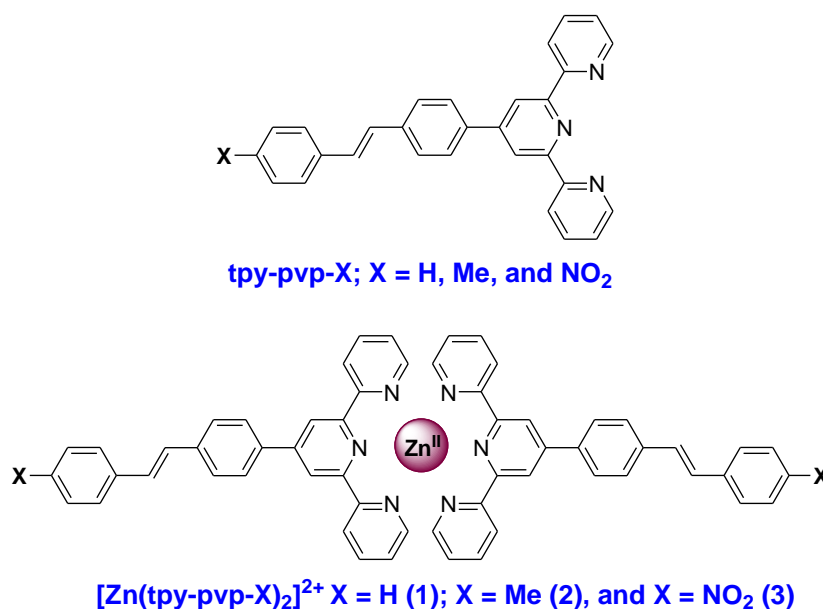


**Chart 5.1.** Chemdraw structures of the complexes under present investigation.

## 5.2 Experimental

### 5.2.1 Materials

Chemicals and solvents are procured either from Sigma or from the local vendors. The synthesis and characterization of the ligands, tpy-pvp-X (X = H, Me, and NO<sub>2</sub>) have already been reported in [chapter 2](#).

## Chapter 5

### 5.2.2 Synthesis of the metal complexes

A general procedure for the synthesis of the Zn(II) complexes is give below.

#### $[Zn(tpy-pvp-H)_2](ClO_4)_2$ (**1**)

To a stirred  $CHCl_3$ -MeOH (1:2, v/v) solution (25 mL) of tpy-pvp-H (222 mg, 0.5 mmol), a MeOH solution of  $Zn(ClO_4)_2 \cdot 6H_2O$  (93 mg 0.25 mmol) was added. The color of the solution immediately changed into yellow and during stirring for ~1h, a microcrystalline compound deposited. The compound was filtered, washed with water, and dried in a vacuum. Crude compound was washed with chloroform and then purified by alumina column chromatography using 1:10 (v/v) DCM-MeCN mixture. The compound was finally recrystallized from MeCN-MeOH (1:2, v/v) mixture resulting in pale yellow microcrystalline compound: yield 380 mg (70%). Elemental anal. Calcd. for  $C_{58}H_{42}N_6Cl_2O_8Zn$ : C, 64.07; H, 3.89; N, 7.72. Found: C, 64.08; H, 3.90; N, 7.72.  $^1H$  NMR (400 MHz,  $CD_3CN$ ,  $\delta/ppm$ ) : 9.16 (s, 4H,  $H_{3'}$ ), 8.89 (d, 4H,  $J=7.6$ ,  $H_6$ ), 8.50-8.42 (m, 8H,  $H_{4+H_7}$ ), 8.33 (d, 4H,  $J=8.0$ ,  $H_8$ ), 7.95-7.90 (m, 8H,  $H_{11+H_3}$ ), 7.69 (d, 4H,  $J=7.6$ ,  $H_{12}$ ), 7.58 (d, 2H,  $J=16.0$ ,  $2H_9$ ), 7.51(d, 2H,  $J=15.8$ ,  $2H_{10}$ ) 7.42 (t, 4H,  $H_5$ ). ESI-MS (positive,  $CH_3CN$ ):  $m/z = 443.15$  (100%)  $[Zn(tpy-pvp-H)_2]^{2+}$ .

#### $[Zn(tpy-pvp-Me)_2](ClO_4)_2$ (**2**)

Yield 362 mg (65%). Elemental anal. Calcd. for  $C_{60}H_{46}N_6Cl_2O_8Zn$ : C, 64.61; H, 4.15; N, 7.53. Found: C, 64.14; H, 4.12; N, 7.33.  $^1H$  NMR (400 MHz,  $CD_3CN$ ,  $\delta/ppm$ ) : 8.86 (s, 4H,  $H_{3'}$ ), 8.66 (d, 4H,  $J=8.0$ ,  $H_6$ ), 8.34-8.31 (m, 8H,  $H_{4+H_7}$ ), 8.07 (d, 4H,  $J=7.2$ ,  $H_8$ ), 7.81 (d, 4H,  $J=9.2$ ,  $H_{11}$ ), 7.52-7.49 (m, 8H,  $H_{12+H_3}$ ), 7.33 (d, 2H,  $J=16.2$ ,  $2H_9$ ), 7.25(d, 2H,  $J=16.0$ ,  $2H_{10}$ ) 7.18 (t, 4H,  $H_5$ ). ESI-MS (positive,  $CH_3CN$ ):  $m/z = 457.13$  (100%)  $[Zn(tpy-pvp-Me)_2]^{2+}$ .

#### $[Zn(tpy-pvp-NO_2)_2](ClO_4)_2$ (**3**)

Yield 424 mg (72%). Elemental anal. Calcd. for  $C_{58}H_{40}N_8Cl_2O_{12}Zn$ : C, 59.17; H, 3.42; N, 9.51. Found: C, 59.10; H, 3.40; N, 9.52.  $^1H$  NMR (400 MHz,  $CD_3CN$ ,  $\delta/ppm$ ) : 9.33 (s, 4H,  $H_{3'}$ ), 9.11 (d, 4H,  $J=8.0$ ,  $H_6$ ), 8.98 (d, 4H,  $J=7.6$ ,  $H_7$ ), 8.87 (d, 4H,  $J=7.4$ ,  $H_8$ ), 8.43-8.39 (t, 8H,  $H_4$ ), 8.26 (d, 4H,  $J=7.8$ ,  $H_{11}$ ), 7.98-7.92 (m, 8H,  $H_{12+H_3}$ ), 7.84(d, 2H,  $J=15.6$ ,  $2H_9$ ), 7.77(d, 2H,  $J=15.8$ ,  $2H_{10}$ ), 7.65 (t, 4H,  $H_5$ ). ESI-MS (positive,  $CH_3CN$ ):  $m/z = 489.18$  (100%)  $[Zn(tpy-pvp-NO_2)_2]^{2+}$ .

### 5.2.3 Physical measurements

Detailed descriptions of the instruments and the methods for carrying out different physicochemical measurements as well as computational works have already been provided in [chapter 2](#) and [chapter 3](#).

## 5.3 Results and discussion

### 5.3.1 Synthesis and characterization

The Zn(II) complexes are synthesized upon treating *tpy-pvp-X* with  $[\text{Zn}(\text{ClO}_4)_2]$  in 2:1 molar ratio in chloroform-methanol (1:1, v/v) mixture at RT and purified through column chromatography followed by recrystallization from chloroform-methanol (1:2, v/v) mixture. The complexes are characterized by elemental (C, H and N) analyses as well as ESI mass and NMR spectroscopy.

### 5.3.2 NMR spectra

$^1\text{H}$  NMR spectra of the complexes **1-3** in  $\text{CD}_3\text{CN}$  are presented in [Fig. 5.1](#). The entire proton resonances are tentatively assigned by comparing with the  $^1\text{H}$  NMR spectra of the related complexes [43]. The overall spectral pattern suggests that the two *tpy-pvp-X* units around the  $\text{Zn}^{2+}$  center are oriented symmetrically. The singlet at  $\sim 2.31$  ppm (not displayed in [Fig. 5.1](#)) which integrates three protons is assignable as methyl protons of *tpy-PhCH<sub>3</sub>* motif in **2**. A second singlet which appears within 9.33-8.86 ppm region and integrates four protons is due to  $\text{H}_3$ . A pair of doublets that appear within 7.25-7.84 ppm is due to ethylenic protons ( $\text{H}_9$  and  $\text{H}_{10}$ ). The spectral pattern and the values of coupling constants of  $\text{H}_9$  and  $\text{H}_{10}$  protons suggest the *trans-trans* conformation of the complexes.

### 5.3.3 Mass spectra

Electrospray ionization mass spectra of the complexes along with their isotopic distribution are presented in [Fig. 5.2](#). A strong peak is observed at  $m/z = 443.15$  for **1** and 457.13 for **2**. The agreement between the experimental and calculated pattern is quite good. The peak corresponds to the bi-positive ion of the type  $[\text{Zn}(\text{tpy-pvp-X})_2]^{2+}$  in the complexes.

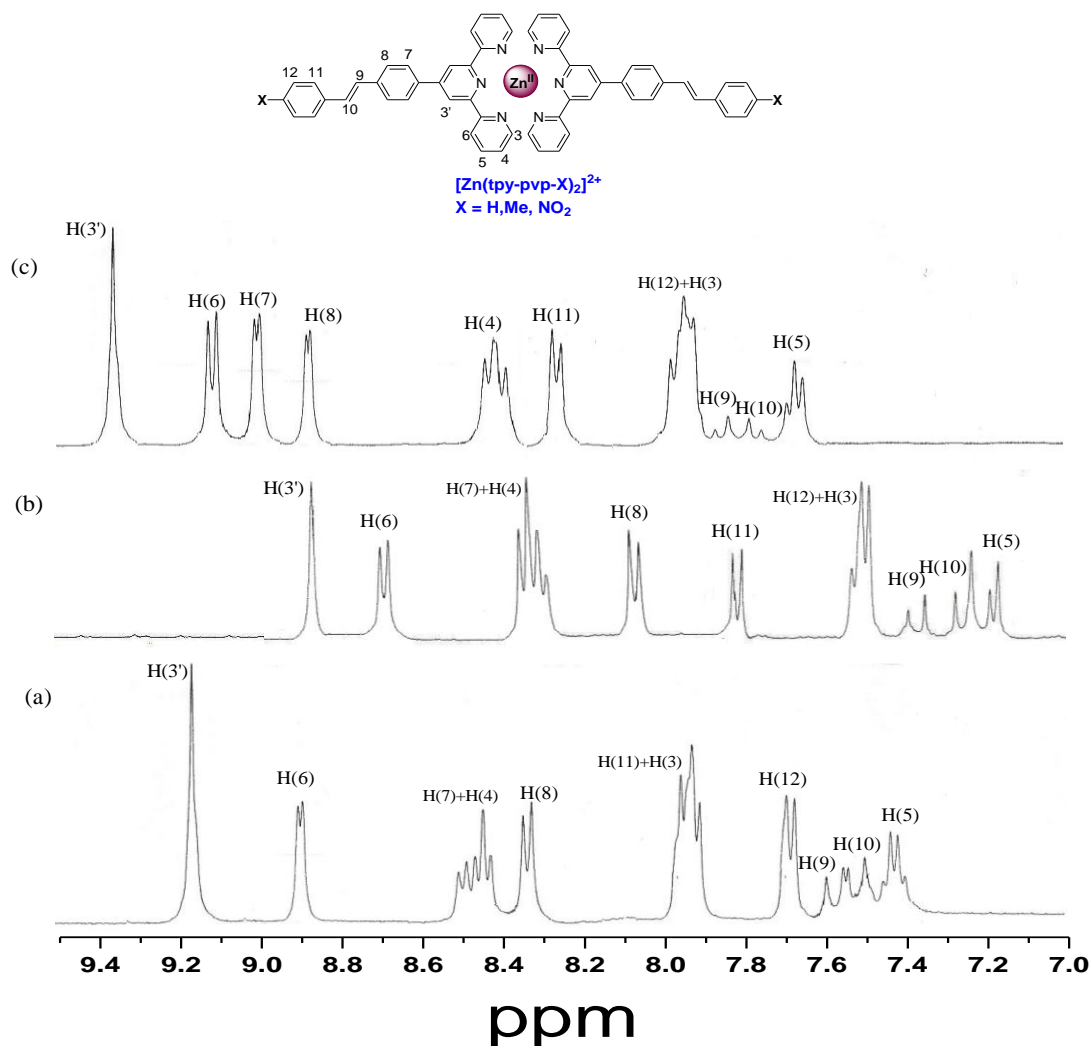


**Fig. 5.1.**  $^1\text{H}$  NMR spectra of **1** (a), **2** (b) and **3** (c) in  $\text{CD}_3\text{CN}$ .

#### 5.3.4 Computational investigations

Geometry optimization of the Zn(II)-terpyridine complexes in their *trans-trans* forms were performed in acetonitrile by using Gaussian 09 program [81] and employing the DFT method with B3LYP/level and CAM- B3LYP level of theory [82-83]. 6-31G\* basis sets were employed for the C, H, N, and O while LanL2DZ basis set was employed for the Zn atom [83]. The optimized structures are presented in Fig. 5.3. Representative bond distances and angles are provided in Tables 5.1-5.2.  $\text{Zn}^{2+}$  is coordinated in bis-

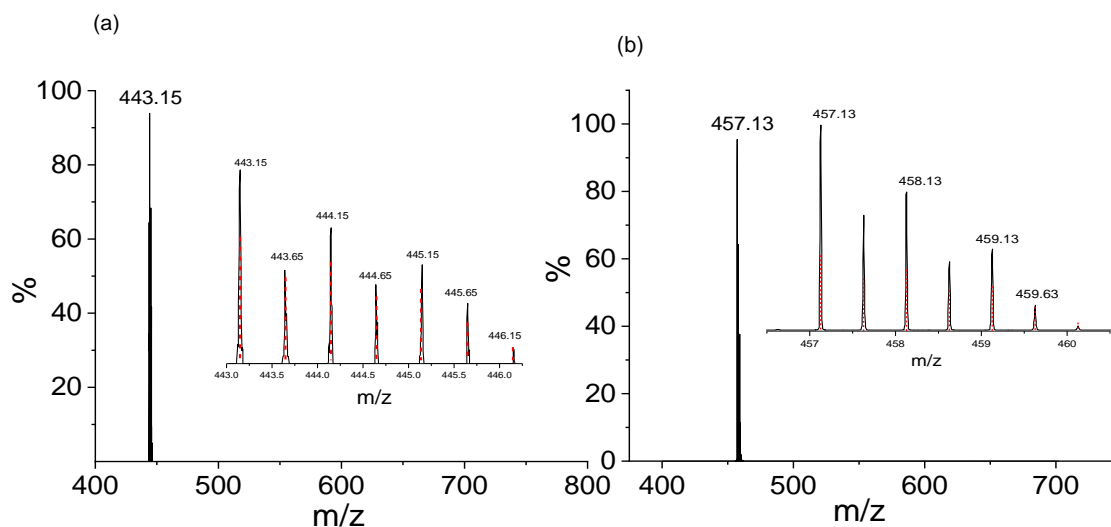


**Fig. 5.2.** ESI mass spectra for  $[\text{Zn}(\text{tpy-pvp-H})_2]^{2+}$  (a) ( $m/z = 443.15$ ) and  $[\text{Zn}(\text{tpy-pvp-CH}_3)_2]^{2+}$  (b) ( $m/z = 457.13$ ) in acetonitrile showing the observed and simulated isotopic distribution pattern.

tridentate manner with two tpy-pvp-X units in the complexes with distorted octahedral geometry. Frontier molecular orbital plots show that with a few exception, the HOMOs are predominantly located on stilbene and *p*-substituted phenyl group (Table 5.3 and Fig. 5.4). LUMOs are mainly located on the tpy motif with small contribution of stilbene moiety with the exception of **3**, where the LUMOs are principally located on either nitrobenzene or tpy unit (Table 5.3 and Fig. 5.4).

TD-DFT calculations are performed by using both B3LYP and CAM-B3LYP level to get the calculated absorption spectra of the complexes and the results are summarized in Fig. 5.5 and Tables 5.4-5.5. The participation of FMOs in their lowest energy band is also displayed in Fig. 5.5. The lowest energy band is principally due to stilbene to terpyridine charge transfer (LLCT) transitions, while the next higher energy band is found to be an admixture of both LLCT and  $\pi-\pi^*$  transitions.

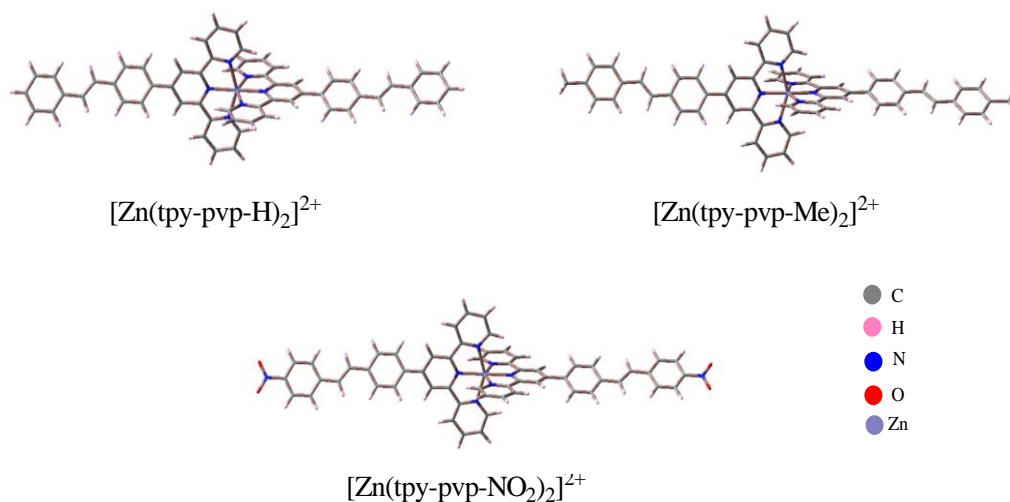


**Fig. 5.3.** Ground state optimized geometries of the *trans-trans* form of Zn(II) complexes of composition  $[\text{Zn}(\text{tpy-pvp-X})_2]^{2+}$  (X= H, Me, and  $\text{NO}_2$ ) in acetonitrile.

**Table 5.1** Selected calculated bond distances (Å) of *trans-trans* form of  $[\text{Zn}(\text{tpy-pvp-X})_2]^{2+}$  where X= H, Me,  $\text{NO}_2$  at TD-DFT/B3LYP level.

<i>trans-trans</i>	
$[\text{Zn}(\text{tpy-pvp-H})_2]^{2+}$	
Zn1-N1	2.235
Zn1-N2	2.126
Zn1-N3	2.233
Zn1-N4	2.233
Zn1-N5	2.126
Zn1-N6	2.235
$[\text{Zn}(\text{tpy-pvp-Me})_2]^{2+}$	
Zn1-N1	2.235
Zn1-N2	2.126
Zn1-N3	2.233
Zn1-N4	2.233
Zn1-N5	2.126
Zn1-N6	2.235
$[\text{Zn}(\text{tpy-pvp-NO}_2)_2]^{2+}$	
Zn1-N1	2.233
Zn1-N2	2.127
Zn1-N3	2.234
Zn1-N4	2.234
Zn1-N5	2.127
Zn1-N6	2.233

**Table 5.2** Selected calculated bond angles (deg) of *trans-trans* form of [Zn(tpy-pvp-H)<sub>2</sub>]<sup>2+</sup>, [Zn(tpy-pvp-CH<sub>3</sub>)<sub>2</sub>]<sup>2+</sup> and [Zn(tpy-pvp-NO<sub>2</sub>)<sub>2</sub>]<sup>2+</sup> at TD-DFT/B3LYP level.

[Zn(tpy-pvp-H) <sub>2</sub> ] <sup>2+</sup>		[Zn(tpy-pvp-CH <sub>3</sub> ) <sub>2</sub> ] <sup>2+</sup>		[Zn(tpy-pvp-NO <sub>2</sub> ) <sub>2</sub> ] <sup>2+</sup>	
N6Zn1N2	104.32	N6Zn1N2	104.33	N6Zn1N2	105.02
N6Zn1N3	93.84	N6Zn1N3	93.84	N6Zn1N3	93.83
N6Zn1N4	149.93	N6Zn1N4	149.93	N6Zn1N4	149.96
N6Zn1N5	74.93	N6Zn1N5	74.93	N6Zn1N5	74.96
N6Zn1N1	93.98	N6Zn1N1	93.98	N6Zn1N1	93.83
N2Zn1N3	74.99	N2Zn1N3	74.99	N2Zn1N3	74.99
N2Zn1N4	105.74	N2Zn1N4	105.73	N2Zn1N4	105.01
N2Zn1N1	74.93	N2Zn1N1	74.93	N2Zn1N1	74.96
N4Zn1N5	74.99	N4Zn1N5	75.00	N4Zn1N5	74.99
N4Zn1N1	93.84	N4Zn1N1	93.84	N4Zn1N1	93.83
N4Zn1N3	93.75	N4Zn1N3	93.75	N4Zn1N3	93.89
N5Zn1N1	104.32	N5Zn1N1	104.34	N5Zn1N1	105.02
N5Zn1N3	105.74	N5Zn1N3	105.72	N5Zn1N3	105.01
N1Zn1N3	149.93	N1Zn1N3	149.93	N1Zn1N3	149.96
N2Zn1N5	178.95	N2Zn1N5	178.97	N2Zn1N5	179.98

The lowest triplet states (T1) of the complexes are also optimized in the solution state by TD-DFT calculation using B3LYP/level methodology. The singly occupied molecular orbitals (SOMOs) which participate in the lowest lying triplet excited state of the complexes are presented in Fig. 5.6 and the singlet-triplet excitation energies at the lowest triplet state are presented in Table 5.6. Upon analysis of the dominant transition, it could be concluded the emission is originated mainly from radiative deactivation of <sup>3</sup>LLCT excited state featuring SOMOs located on the stilbene and tpy unit for **1** and **2**, while on stilbene and nitrobenzene moiety for **3**. In addition to TD-DFT, UKS calculations are also performed directly on the triplet state of the complexes using both B3LYP and CAM- B3LYP methods (Table 5.7-5.8). The emission energies of the complexes are obtained from the energy difference between the ground singlet and the excited lowest triplet state in the optimized geometry. The calculated emission maximum on the basis of TDDFT and UKS are presented in Table 5.6-5.8. The spin density plots for the complexes in their triplet state derived from UKS calculations are also presented in Fig. 5.7 to get an idea about the nature of the emitting excited state in the complexes. In line with TD-DFT calculations, the spin density plots also suggest that the emission is originated from radiative deactivation of the <sup>3</sup>LLCT.

**Table 5.3** Selected MOs along with their energies and compositions in the ground state at the TD-DFT/CAM-B3LYP level for *trans-trans* form of  $[\text{Zn}(\text{tpy-pvp-H})_2]^{2+}$  (**1**),  $[\text{Zn}(\text{tpy-pvp-CH}_3)_2]^{2+}$  (**2**) and  $[\text{Zn}(\text{tpy-pvp-NO}_2)_2]^{2+}$  (**3**) in acetonitrile.

MO	$[\text{Zn}(\text{tpy-pvp-H})_2]^{2+}$ ( <b>1</b> )				
	Energy/ ev	% Compositions			
	<i>Trans-trans</i>	<i>Trans-trans</i>			
		Zn	Tpy	Styryl- benz	Benza l
LUMO+3	-1.35	0.00	99.47	0.52	0.00
LUMO+2	-1.41	0.06	99.42	0.50	0.00
LUMO+1	-1.78	0.68	80.27	16.58	2.45
LUMO	-1.78	0.62	80.46	16.48	2.43
HOMO	-7.31	0.00	4.43	61.84	33.71
HOMO-1	-7.31	0.01	4.39	61.83	33.74
HOMO-2	-8.69	0.00	0.02	0.11	99.86
HOMO-3	-8.69	0.00	0.02	0.11	99.85
	$[\text{Zn}(\text{tpy-pvp-Me})_2]^{2+}$ ( <b>2</b> )				
	<i>Trans-trans</i>	Zn	Tpy	Styryl- benz	Me- Benz
LUMO+3	-1.35	0.00	99.46	0.53	0.00
LUMO+2	-1.40	0.06	99.41	0.51	0.00
LUMO+1	-1.77	0.69	81.13	15.97	2.18
LUMO	-1.77	0.63	81.31	15.88	2.10
HOMO	-7.18	0.00	3.79	56.13	40.06
HOMO-1	-7.18	0.01	3.77	56.12	40.09
HOMO-2	-8.65	0.00	0.00	0.06	99.93
HOMO-3	-8.65	0.00	0.00	0.06	99.93
	$[\text{Zn}(\text{tpy-pvp-NO}_2)_2]^{2+}$ ( <b>3</b> )				
	<i>Trans-trans</i>	Zn	Tpy	Styryl- benz	Nitro- Benz
LUMO+3	-1.74	0.62	78.49	9.64	11.24
LUMO+2	-1.74	0.67	78.31	9.60	11.31
LUMO+1	-2.35	0.03	5.80	14.10	80.05
LUMO	-2.35	0.04	5.82	14.12	80.00
HOMO	-7.65	0.00	5.84	69.35	24.78
HOMO-1	-7.65	0.02	5.80	69.36	24.81
HOMO-2	-8.73	0.01	99.61	0.37	0.00
HOMO-3	-8.73	0.00	99.59	0.40	0.00



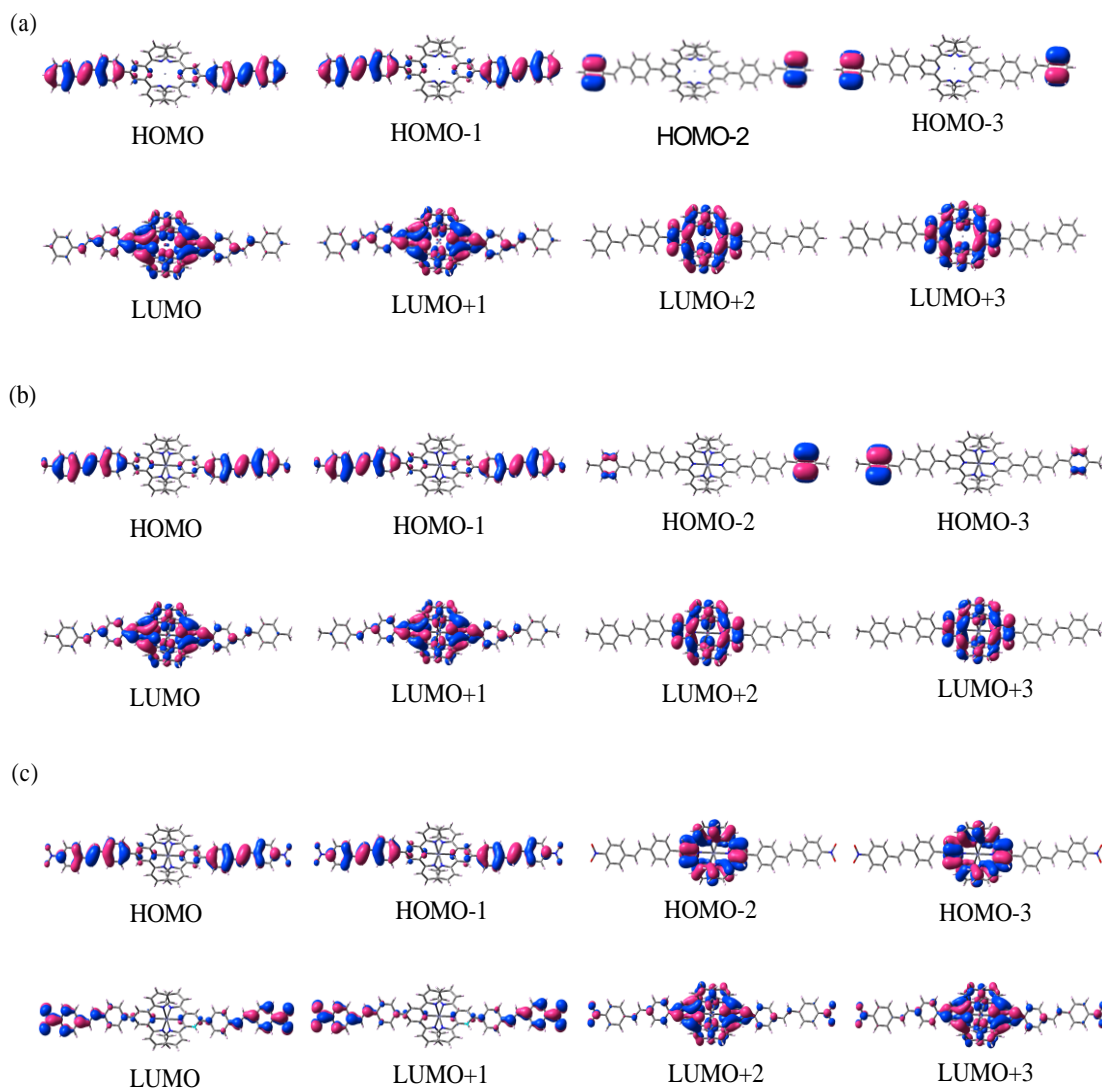


**Fig. 5.4.** Schematic drawings of selective frontier molecular orbitals in the ground state of the *trans-trans* form of  $[\text{Zn}(\text{tpy-pvp-H})_2]^{2+}$  (a),  $[\text{Zn}(\text{tpy-pvp-CH}_3)_2]^{2+}$  (b) and  $[\text{Zn}(\text{tpy-pvp-NO}_2)_2]^{2+}$  (c) in acetonitrile by CAM-B3LYP level calculation.

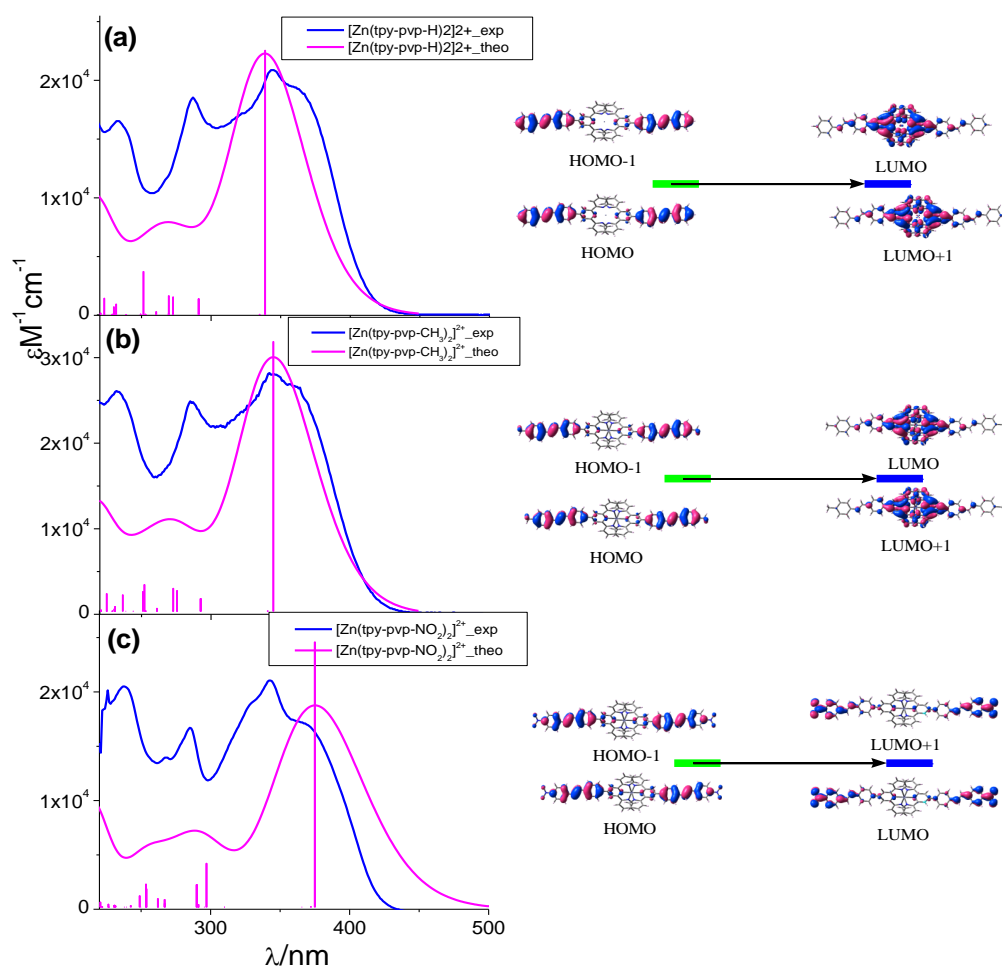


**Fig. 5.5.** The left panel shows the overlay of the calculated (pink lines) and experimental (blue lines) UV-vis absorption spectra of **1** (a), **2** (b) and **3** (c) in acetonitrile. Calculated results are also presented in the sticks form by CAM-B3LYP level of calculation. The right panel shows the frontier molecular orbitals that are involved in the lowest energy absorption band.

## 5.3.5 Absorption and emission spectra

Absorption and emission spectra of the complexes are recorded in three different solvents. The overlay of the experimental and the calculated absorption spectra of the complexes in MeCN are displayed in Fig. 5.5, while the relevant spectral data are presented in Table 5.9. A broad band within the spectral domain of 341-390 nm is observed in all complexes which can be assigned with the aid of TD-DFT calculations as ligand-to-ligand charge transfer (LLCT) from phenyl-vinyl to the coordinated terpyridine moiety. Several bands originate within 291-236 nm region because of  $\pi$ - $\pi^*$  transitions. The position of LLCT band maximum varies to a small extent, depending on the nature of X in the complexes. The outcomes of the TD-DFT calculations obtained by using B3LYP level of theory show a large disparity between experimental and calculated spectra (Table 5.4). Particularly, the huge band within the spectral region of 400-500 nm

**Table 5.4** Selected UV-vis energy transitions at the TD-DFT/B3LYP level for *trans-trans*  $[\text{Zn}(\text{tpy-pvp-H})_2]^{2+}$  (**1**),  $[\text{Zn}(\text{tpy-pvp-CH}_3)_2]^{2+}$  (**2**) and  $[\text{Zn}(\text{tpy-pvp-NO}_2)_2]^{2+}$  (**3**) in acetonitrile.

Excited state	$\lambda_{\text{cal}}/\text{nm}$	Oscillator strength(f)	$\lambda_{\text{expt}}/\text{nm}$	Key transitions	Character
$[\text{Zn}(\text{tpy-pvp-H})_2]^{2+}$					
S <sub>1</sub>	451	1.69	362	H-1→L (50%), H→L+1(49%)	LLCT
S <sub>9</sub>	337	2.13	344	H-1→L+4 (49%), H→L+5(48%)	LLCT, $\pi$ - $\pi^*$
S <sub>46</sub>	278	0.31	288	H-5→L+2 (23%), H-4→L+3(11%)	$\pi$ - $\pi^*$
$[\text{Zn}(\text{tpy-pvp-CH}_3)_2]^{2+}$					
S <sub>1</sub>	469	1.68	363	H-1→L (50%), H→L+1(49%)	LLCT
S <sub>9</sub>	345	2.23	342	H-1→L+4 (49%), H→L+5(48%)	LLCT, $\pi$ - $\pi^*$
S <sub>48</sub>	278	0.26	285	H-4→L+3 (37%), H-5→L+2(15%)	$\pi$ - $\pi^*$
$[\text{Zn}(\text{tpy-pvp-NO}_2)_2]^{2+}$					
S <sub>1</sub>	481	2.78	341	H-1→L+1 (49%), H→L(50%)	ILCT
S <sub>25</sub>	316	0.23	284	H-3→L+2(43%), H-2→L+3 (42%)	ILCT, $\pi$ - $\pi^*$
S <sub>58</sub>	280	0.12	236	H-5→L+4 (23%), H-2→L+5(34%), H-4→L+5 (15%), H-3→L+4(15%)	$\pi$ - $\pi^*$

**Table 5.5** Selected UV-vis energy transitions at the TD-DFT/CAM-B3LYP level for *trans-trans* [Zn(tpy-pvp-H)<sub>2</sub>]<sup>2+</sup> (**1**), [Zn(tpy-pvp-CH<sub>3</sub>)<sub>2</sub>]<sup>2+</sup> (**2**) and [Zn(tpy-pvp-NO<sub>2</sub>)<sub>2</sub>]<sup>2+</sup> (**3**) in acetonitrile.

Excited state	$\lambda_{\text{cal}}/\text{nm}$	Oscillator strength(f)	$\lambda_{\text{expt}}/\text{nm}$	Key transitions	Character
[Zn(tpy-pvp-H) <sub>2</sub> ] <sup>2+</sup>					
S <sub>1</sub>	340	3.53	362	H-1→LUMO (35%), H-1→L+4 (11%), HOMO→L+1 (35%), HOMO→L+5 (11%)	LLCT
S <sub>3</sub>	291	0.21	288	H-5→L+1 (27%), H-4→LUMO (27%), H-1→L+3 (11%), HOMO→L+2 (12%)	LLCT, $\pi$ - $\pi^*$
S <sub>16</sub>	251	0.58	233	H-5→L+2 (39%), H-4→L+3 (30%), H-11→LUMO (6%), H-10→L+1 (6%)	$\pi$ - $\pi^*$
[Zn(tpy-pvp-CH <sub>3</sub> ) <sub>2</sub> ] <sup>2+</sup>					
S <sub>1</sub>	345	3.60	363	H-1→LUMO (34%), H-1→L+4 (11%), HOMO→L+1 (35%), HOMO→L+5 (11%)	LLCT
S <sub>6</sub>	276	0.25	285	H-5→L+1 (17%), H-4→LUMO (17%), H-1→L+3 (20%), HOMO→L+2 (23%)	LLCT, $\pi$ - $\pi^*$
S <sub>22</sub>	236	0.22	236	H-7→LUMO (31%), H-6→L+1 (31%) H-15→L+1 (3%)	$\pi$ - $\pi^*$
[Zn(tpy-pvp-NO <sub>2</sub> ) <sub>2</sub> ] <sup>2+</sup>					
S <sub>1</sub>	375	3.55	370	H-1→L+1 (44%), HOMO→LUMO (44%)	ILCT
S <sub>7</sub>	297	0.58	285	H-1→L+3 (37%), HOMO→L+2 (37%) H-7→L+1 (4%)	ILCT, $\pi$ - $\pi^*$
S <sub>22</sub>	253	0.31	240	H-13→L+3 (17%), H-12→L+2 (15%), H-3→L+4 (16%), H-2→L+5 (13%)	$\pi$ - $\pi^*$

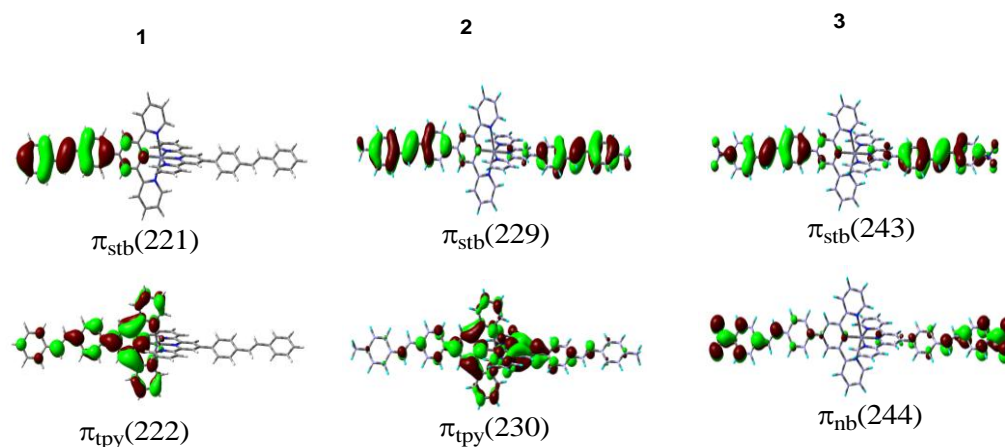


**Fig. 5.6.** Schematic drawings of the molecular orbitals involved in the dominant configuration of the lowest lying triplet excited states of *trans-trans* form of **1**, **2** and **3** in MeCN.

**Table 5.6** Singlet-triplet excitation energies at the lowest triplet state ( $T_1$ ) along with key transitions of the complexes in their *trans-trans* forms of **1**, **2** and **3** in MeCN.

Compounds	Key transition	$E/\text{cm}^{-1}$
<b>1</b>	$\pi_{\text{stb}}(221) \rightarrow \pi_{\text{tpy}}^*(222)$ (98%)	18281
<b>2</b>	$\pi_{\text{stb}}(229) \rightarrow \pi_{\text{tpy}}^*(230)$ (97%)	21692
<b>3</b>	$\pi_{\text{stb}}(243) \rightarrow \pi_{\text{nb}}^*(244)$ (98%)	20790

**Table 5.7** Emission maxima of *trans-trans*  $[\text{Zn}(\text{tpy-pvp-H})_2]^{2+}$  (**1**),  $[\text{Zn}(\text{tpy-pvp-CH}_3)_2]^{2+}$  (**2**) and  $[\text{Zn}(\text{tpy-pvp-NO}_2)_2]^{2+}$  (**3**) in MeCN according to UKS calculations at the TD-DFT/B3LYP level and associated experimental values.

Compounds	$\lambda_{\text{cal}}/\text{nm}$	$\lambda_{\text{exp}}/\text{nm}$
<b>1</b>	494	522
<b>2</b>	500	518
<b>3</b>	551	499

**Table 5.8** Emission maxima of *trans-trans*  $[\text{Zn}(\text{tpy-pvp-H})_2]^{2+}$  (**1**),  $[\text{Zn}(\text{tpy-pvp-CH}_3)_2]^{2+}$  (**2**) and  $[\text{Zn}(\text{tpy-pvp-NO}_2)_2]^{2+}$  (**3**) in MeCN according to UKS calculations at the TD-DFT/CAM-B3LYP level and associated experimental values.

Compounds	$\lambda_{\text{cal}}/\text{nm}$	$\lambda_{\text{exp}}/\text{nm}$
<b>1</b>	599	522
<b>2</b>	604	518
<b>3</b>	654	499

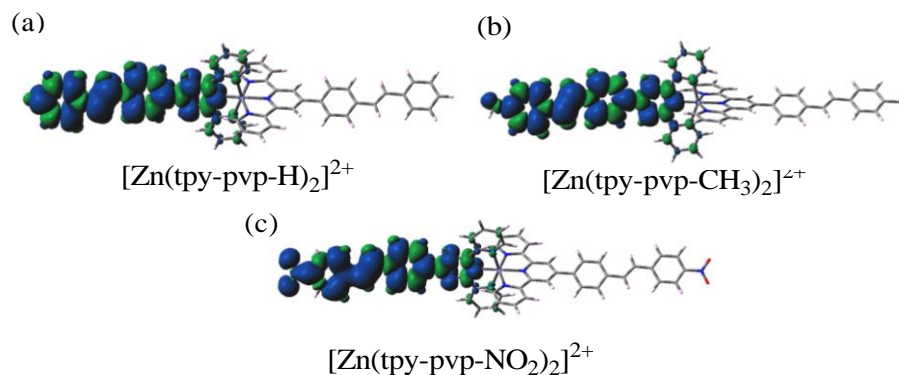


**Fig. 5.7.** Spin density plots for the  $T_1$  state of the *trans-trans* form of **1**(a), **2**(b), and **3**(c) in MeCN.

**Table 5.9** Absorption and emission spectral data of **1-3**.

Compds	Absorption $\lambda_{\text{max}}/\text{nm}$ ( $\epsilon/\text{M}^{-1}\text{cm}^{-1}$ )			Luminescence $\lambda_{\text{max}}/\text{nm}$		
	MeCN	DCM	DMSO	MeCN	DCM	DMSO
<b>1</b>	362(28900), 344(31300), 288(27600)	381(25400), 344(sh)(20800), 322(25600)	347(22700), 291(19400)	522	510	421, 518
<b>2</b>	363(26400), 342(28200), 285(24900)	390(32300), 322(35400), 287(34400)	347(33900), 288(28900)	518	524	435, 535
<b>3</b>	341(44900), 284(34880), 236(41680)	372(39500), 343(42400), 285(32200)	375(28000), 351(27100), 287(26100)	499	503	515

in the calculated spectra is not show off in the experimental spectra. To this end, we again carried out calculations by using CAM-B3LYP level of theory, keeping the basis sets unchanged (Table 5.5). The overlay of the experimental and calculated absorption spectra obtained by the later method is displayed in Fig. 5.5 which shows a good agreement between the calculated and experimental results.

Upon excitation at the LLCT or  $\pi$ - $\pi^*$  band, all the Zn(II) complexes exhibit strong emission band within 420-535 nm, dependent on the electronic nature of the substituent (X) and the solvent used (Fig. 5.8). Good correlation between the experimental observations and theoretical results performed on the triplet state of the complexes also leads us to conclude that the emission arises from radiative deactivation of  $^3\text{LLCT}$  state.

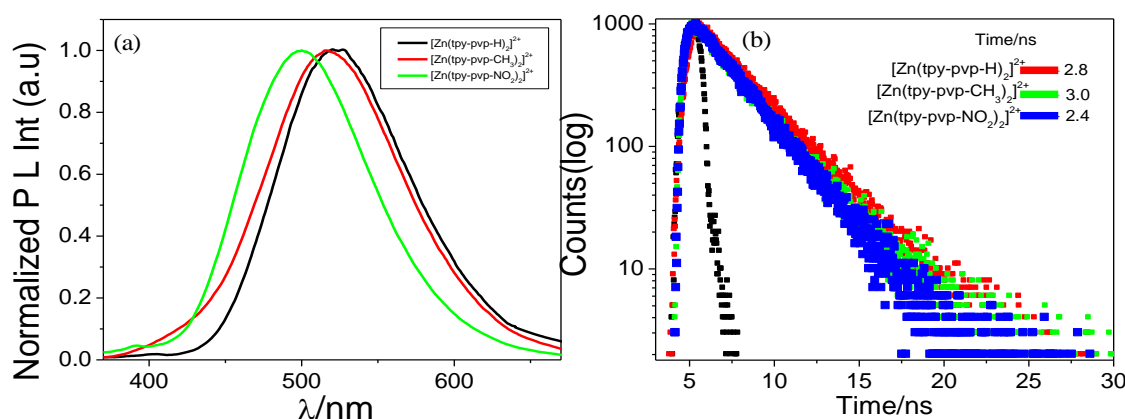


**Fig. 5.8.** Normalized emission ( $\lambda_{\text{ex}} = 330 \text{ nm}$ ) spectra (a) and excited state decay profiles along with the lifetime values of the complexes in MeCN (b).

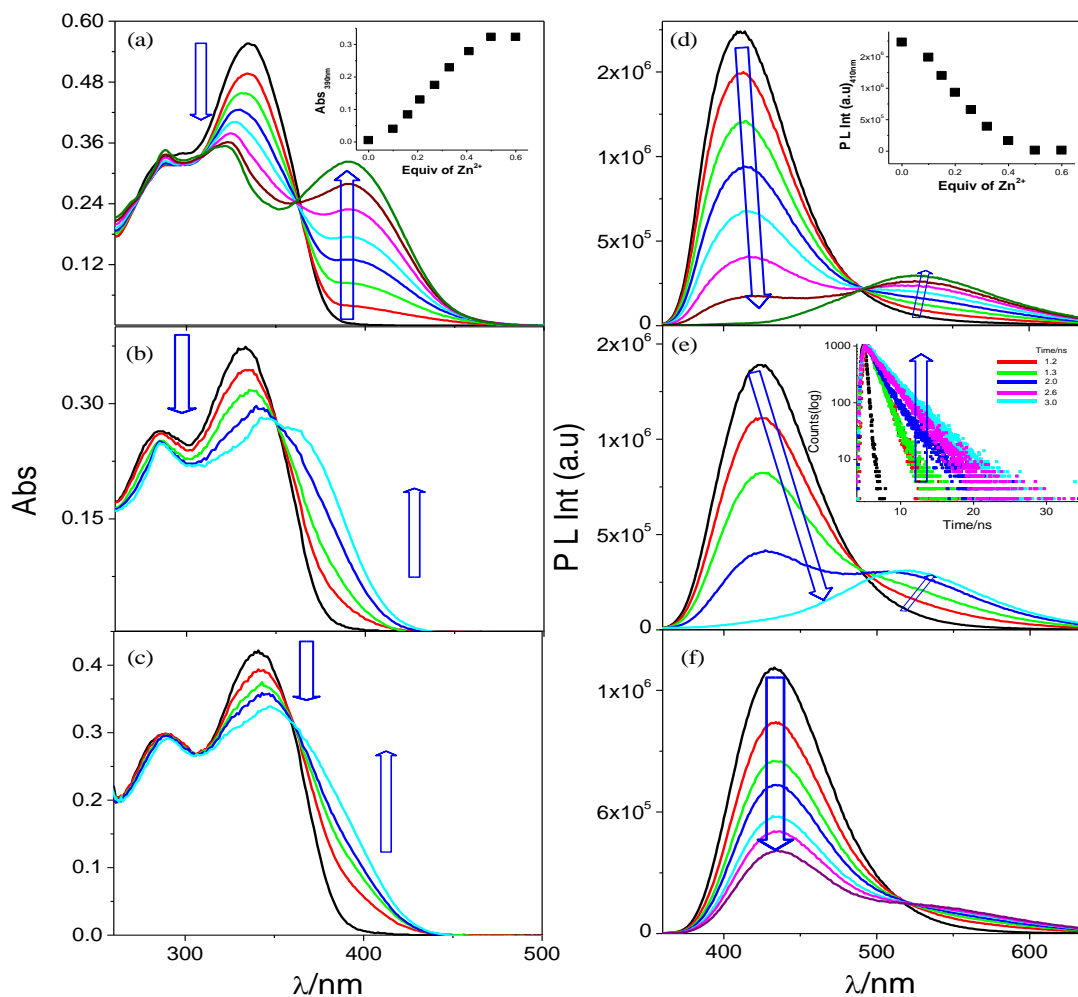


**Fig. 5.9.** UV-vis absorption and emission ( $\lambda_{\text{ex}} = 330$  nm) spectral change of tpy-pvp-CH<sub>3</sub> upon incremental addition of Zn<sup>2+</sup> in DCM (a and d, respectively), MeCN (b and e, respectively) and DMSO (c and f, respectively). The inset to fig. (a) shows the change of absorbance at 390 nm, while the inset to fig. (d) shows the quenching of emission at 410 nm as a function of the equivalent of Zn<sup>2+</sup>.

It is to be noted from Table 5.6-5.8 that as compared with the UKS approach, the calculated values of emission maxima of the complexes obtained by TDDFT method are closer to those of the experimentally observed values.

Lifetime of the complexes was measured through time-correlated single photon counting and the decay profiles together with their lifetime values are presented in Fig. 5.8(b). The complexes display mono-exponential decay profiles and the emission lifetime of the complexes in MeCN increases in the order **3** (2.4 ns) < **1** (2.8 ns) < **2** (3.0 ns).

In-situ generation of Zn(II) complexes are also observed in all the three studied solvents via absorption and emission spectroscopy (Fig. 5.9-5.13). Upon incremental addition of  $\text{Zn}(\text{ClO}_4)_2$ , a new band evolves in the longer wavelength region (341-390 nm), gradually intensifies and finally saturates upon addition of 0.5 equiv of  $\text{Zn}^{2+}$  indicating the formation of  $[\text{Zn}(\text{tpy-pvp-X})_2]^{2+}$  (Inset of Fig. 5.9a-5.11a). In the absorption spectral profiles, several clean isosbestic points (at 361, 307 and 272 nm for tpy-pvp- $\text{CH}_3$  in DCM) clearly suggest the transformation of the free tpy-pvp- $\text{CH}_3$  to  $[\text{Zn}(\text{tpy-pvp-CH}_3)_2]^{2+}$  (Fig. 5.9a). In the emission side, gradual quenching of emission at  $\sim 410$  nm is also accompanied by a distinct emission enhancement at  $\sim 524$  nm upon incremental addition of  $\text{Zn}^{2+}$  (Inset of Fig. 5.9d and Fig. 5.10b-5.13b).

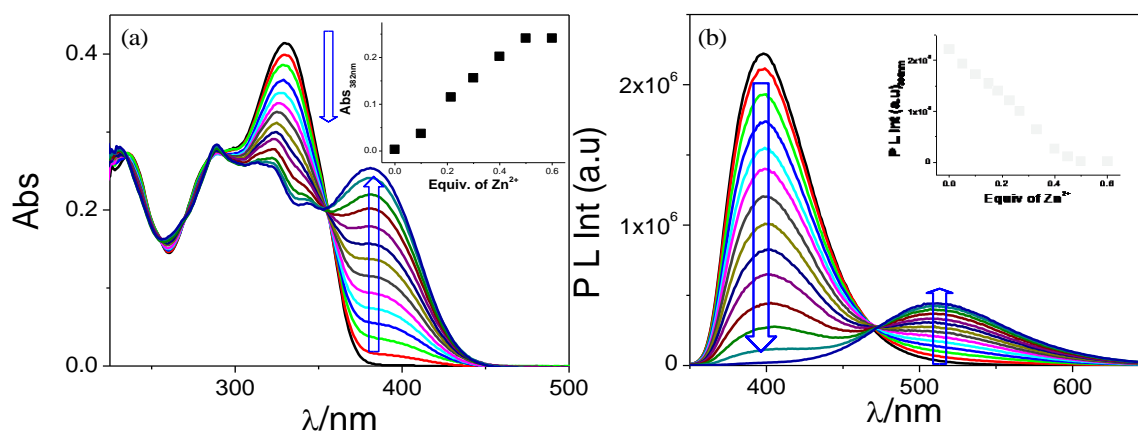


**Fig. 5.10.** UV-vis absorption (a) and emission ( $\lambda_{\text{ex}} = 330$  nm) (b) spectral change of tpy-pvp-H upon incremental addition of  $\text{Zn}^{2+}$  in dichloromethane. Inset to fig. a shows the change of absorbance at 382 nm, while the inset to fig. b shows the emission quenching at 398 nm vs. equivalent of  $\text{Zn}^{2+}$ .



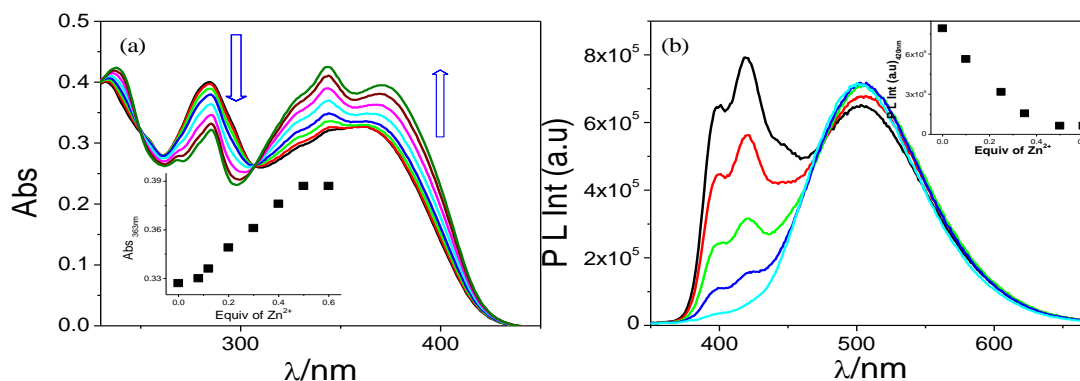


**Fig. 5.11.** UV-vis absorption (a) and emission ( $\lambda_{ex} = 330$  nm) (b) spectral change of tpy-pvp-NO<sub>2</sub> upon incremental addition of  $Zn^{2+}$  in dichloromethane. The inset to fig. a shows the change of absorbance at 363 nm, while the inset to fig. b shows the emission quenching at 420 nm vs. equivalent of  $Zn^{2+}$ .

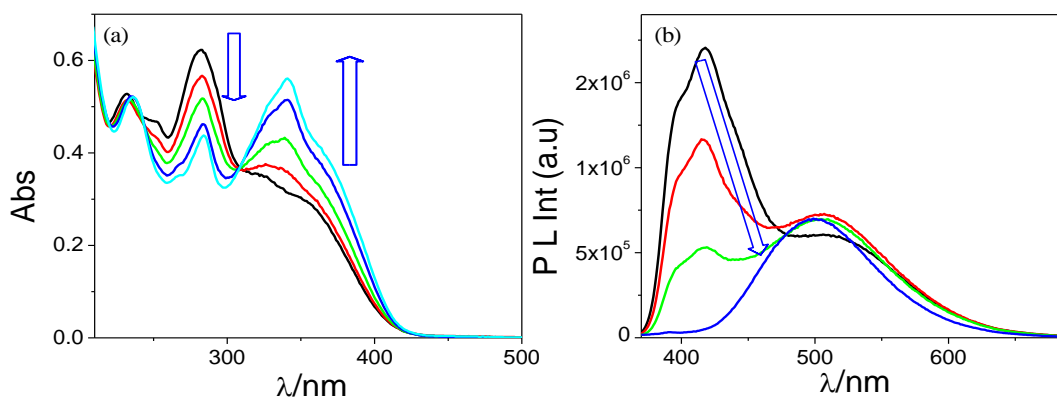


**Fig. 5.12.** UV-vis absorption (a) and emission ( $\lambda_{ex} = 330$  nm) (b) spectral change of tpy-pvp-NO<sub>2</sub> upon incremental addition of  $Zn^{2+}$  in acetonitrile.

### 5.3.6 Photo-isomerization studies of the complexes

As the complexes possess two stilbene motifs, we are interested to undertake their light-induced isomerization behaviors. We performed isomerization studies in three different solvents (DCM, MeCN and DMSO) upon the action of UV (334 nm) as well as visible (405 nm) light sources. The isomerization event was monitored through absorption, emission and time correlated single photon counting measurements. Firstly, the isomerization studies are carried out in acetonitrile and absorption and emission

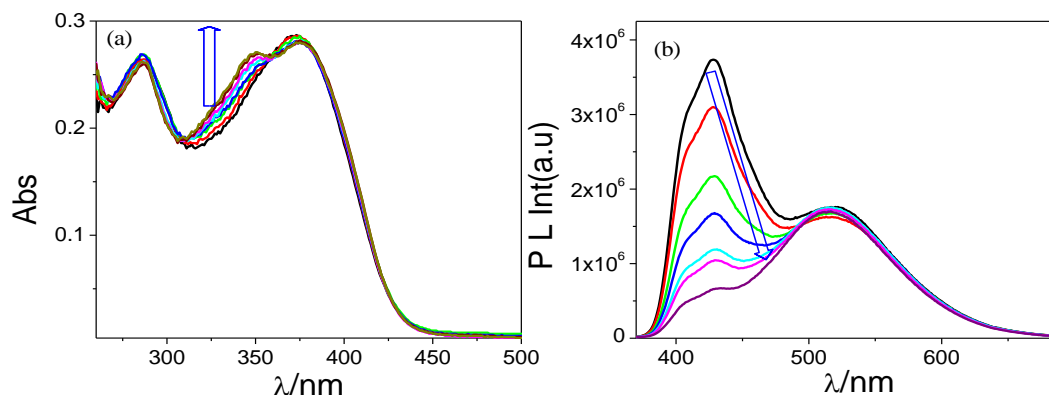


**Fig. 5.13.** UV-vis absorption (a) and emission ( $\lambda_{\text{ex}} = 330$  nm) (b) spectral change of tpy-pvp-NO<sub>2</sub> upon incremental addition of Zn<sup>2+</sup> in dimethylsulfoxide.

spectral changes upon irradiation of UV light are presented in Fig. 5.14. Only one-step change is observed in their absorption and emission spectral profiles. The intensity of LLCT band (at ~345 nm) decreased gradually with simultaneous increase of the  $\pi$ - $\pi^*$  band intensity (~285 nm). The extent of decrease varies in the range of 40-65% for the LLCT, while increases between 15% and 35% for the  $\pi$ - $\pi^*$  band (~285 nm), depending upon the nature of X. During the process, successive absorption lines pass through several well defined isosbestic points (307 nm and 248 nm for **3**). Small blue-shift of the LLCT bands is observed during the isomerization process (Fig. 5.14). Almost complete quenching of emission intensity (~95%) at ~510 nm was noticed for **1-2**, whereas substantial enhancement (~56%) was observed for **3** during photo-irradiation (Fig. 5.14f). In spite of emission quenching, small increase in lifetime is observed during the isomerization processes (inset of Fig. 5.14f). The isomerization studies performed in two other solvents (DCM and DMSO) in presence of UV light also induce one-step change in all the three complexes. The absorption spectral profiles of the complexes in DMSO (Fig. 5.15) are similar to that of MeCN but differ considerably in DCM (Fig. 5.16). In DCM, the intensity of broad LLCT absorption band decreased gradually through several isosbestic points (358, 285 and 237 nm for **1**) with concomitant increase of the  $\pi$ - $\pi^*$  band intensity at ~325 nm. In contrast to the observed behavior in MeCN and DMSO, the

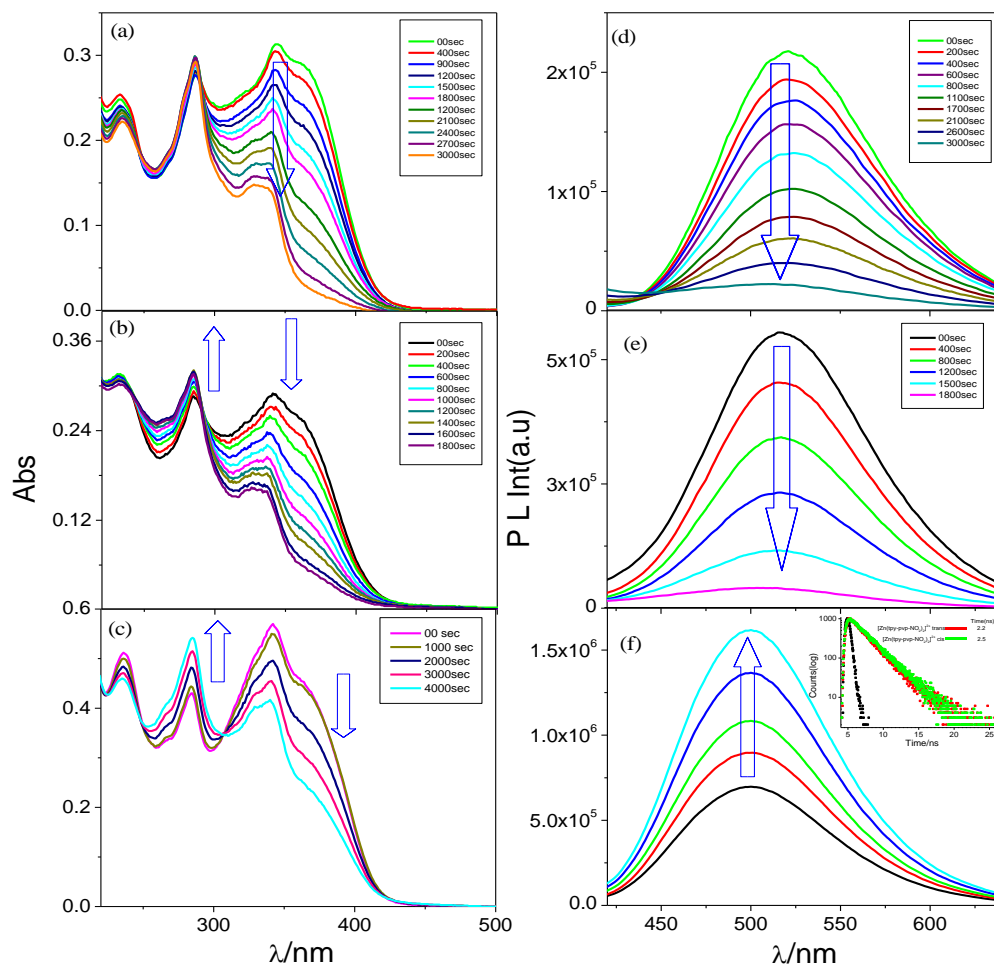


**Fig. 5.14.** Absorption and emission ( $\lambda_{\text{ex}} = 330 \text{ nm}$ ) spectral change of  $[\text{Zn}(\text{tpy-pvp-H})_2]^{2+}$  (a and d, respectively),  $[\text{Zn}(\text{tpy-pvp-Me})_2]^{2+}$  (b and e, respectively) and  $[\text{Zn}(\text{tpy-pvp-NO}_2)_2]^{2+}$  (c and f, respectively) in acetonitrile upon irradiation with UV light. Insets to the figs. a-f indicate the irradiation time. Inset of fig. f shows the excited state decay traces and values of the lifetimes.

emission intensity gradually increases in DCM together with significant blue shift of the emission maximum (510→460 nm for **1**) upon isomerization (Fig. 5.16). In addition, a clean isoemissive point (~499 nm) is observed in all cases except nitro derivative. By contrast, red-shift of the emission maximum is observed (500→510 nm) in the case of nitro-derivative (**3**) (Fig. 5.16f). In order to check the effect of irradiation wavelength on the thermodynamic and kinetic aspects of the isomerization process, we also monitor the spectral change in the complexes in presence of visible light ( $\lambda_{\text{max}}=405 \text{ nm}$ ). One-step

change is also observed with visible light having almost similar spectral profile as noticed with UV irradiation, although the time of irradiation and extent of spectral change differ (Figs. 5.17-5.19). Taking into consideration the one-step change in both absorption and emission spectral profiles, irrespective of solvents and irradiating wavelengths, we surmise a possible mode of conversion could be due to *trans-trans* to the corresponding *trans-cis* form.

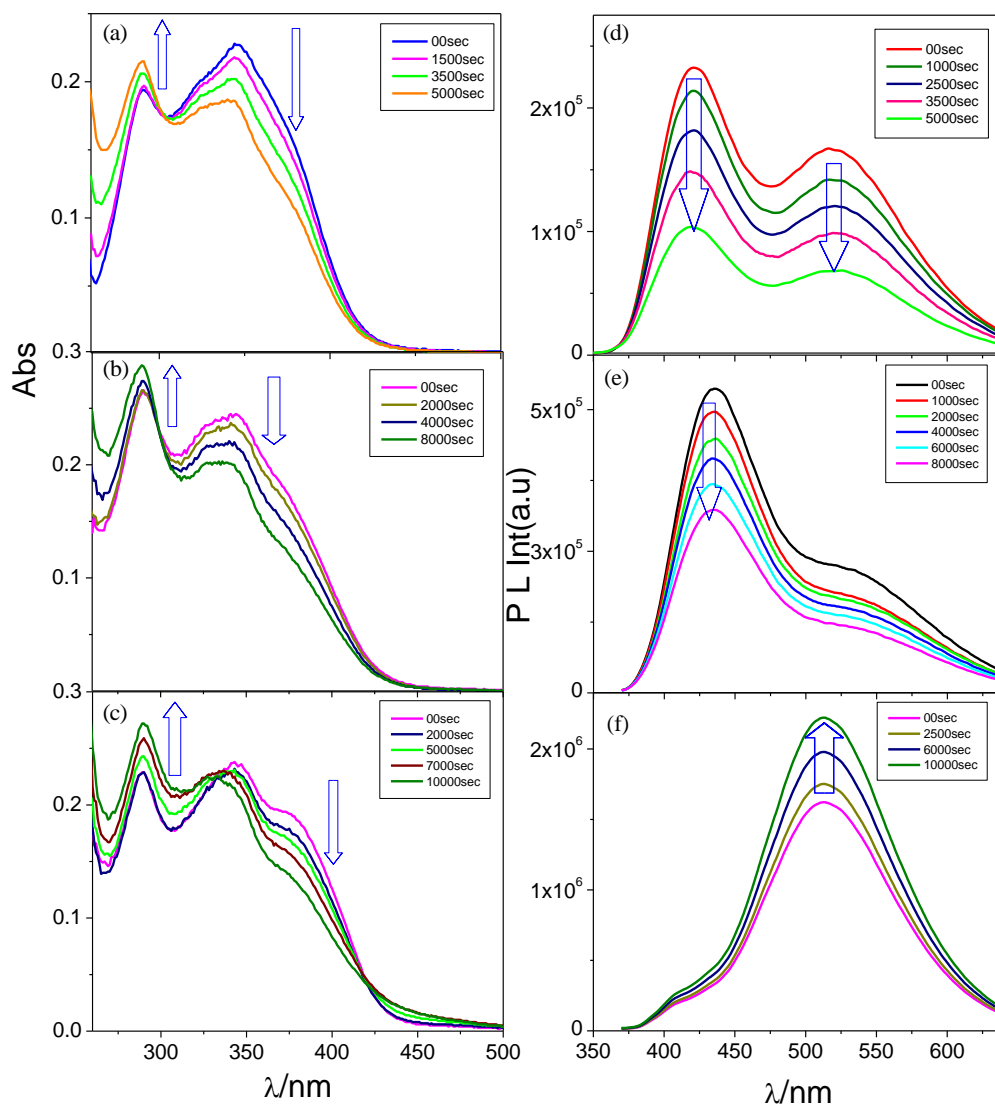


**Fig. 5.15.** Absorption and emission ( $\lambda_{\text{ex}} = 330 \text{ nm}$ ) spectral changes of  $[\text{Zn}(\text{tpy-pvp-H})_2]^{2+}$  (a and d, respectively),  $[\text{Zn}(\text{tpy-pvp-Me})_2]^{2+}$  (b and e, respectively) and  $[\text{Zn}(\text{tpy-pvp-NO}_2)_2]^{2+}$  (c and f, respectively) in dimethylsulfoxide upon irradiation with UV light. Insets to the figs. a-f indicate the irradiation time.

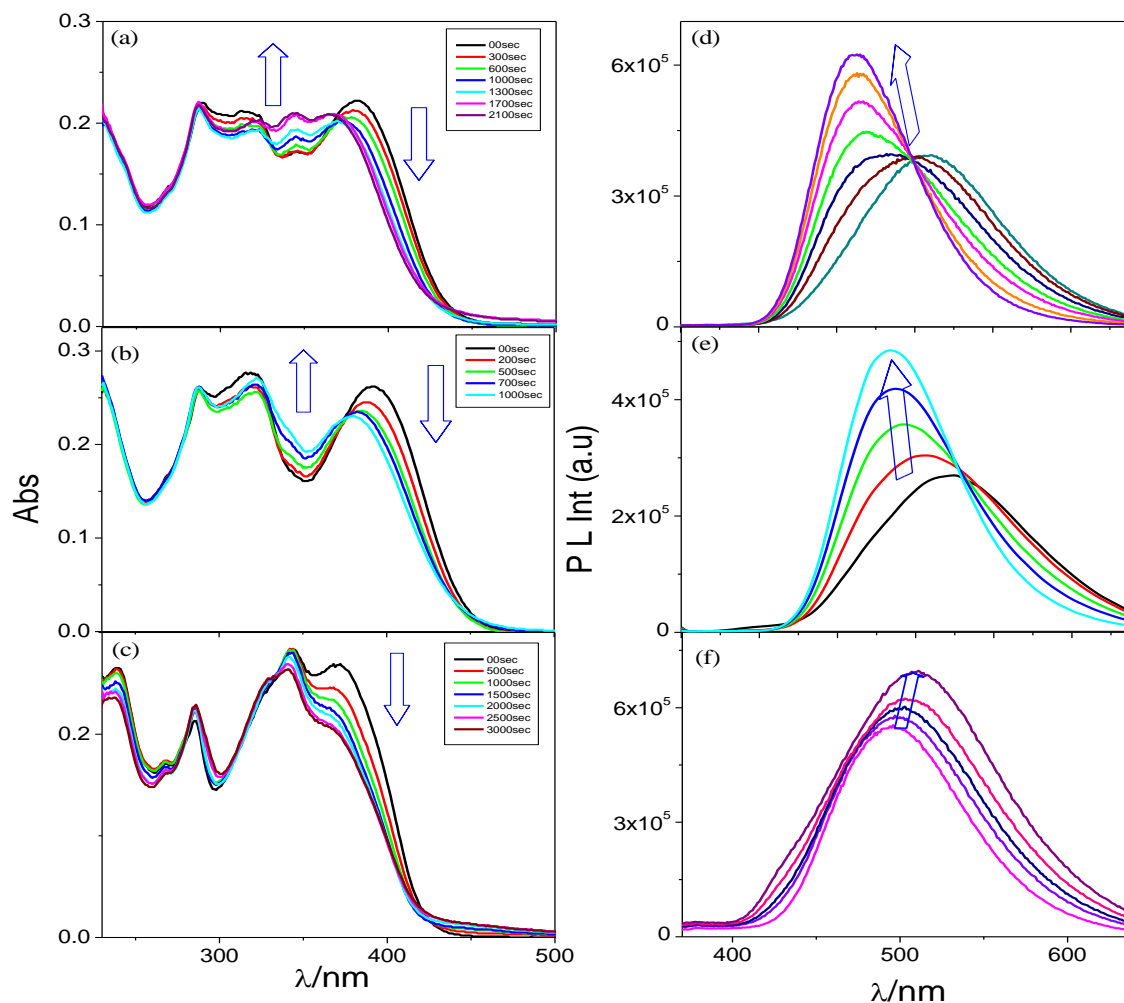


**Fig. 5.16.** The absorption and emission ( $\lambda_{\text{ex}} = 330$  nm) spectral change of **1** (a and d, respectively), **2** (b and e, respectively) and **3** (c and f, respectively) in DCM upon irradiation with UV light. Insets to the figs. a-c indicate the irradiation time.

We also monitored the isomerization behavior through  $^1\text{H}$  NMR spectroscopy in order to ascertain the probable mode of isomerization of the complexes. A representative complex (**2**) is chosen for this purpose as the signals for the isomerizable protons associated with the stilbene bond are clearly observed for this complex.  $^1\text{H}$  NMR spectrum of **2** as a function of irradiation time with 405 nm light is shown in Fig. 5.20. Upon photolysis, we noticed a gradual decrease in intensity of the proton signals associated with stilbene unit ( $\text{H}_9$  and  $\text{H}_{10}$ ) as well as the adjacent protons ( $\text{H}_7$ ,  $\text{H}_8$ ,  $\text{H}_{11}$  and

H<sub>12</sub>). Concomitant growth along with systematic intensification of the said proton signals are observed in the up-field region with time { (H<sub>7'</sub> = 8.25 ppm, J = 7.2 Hz);

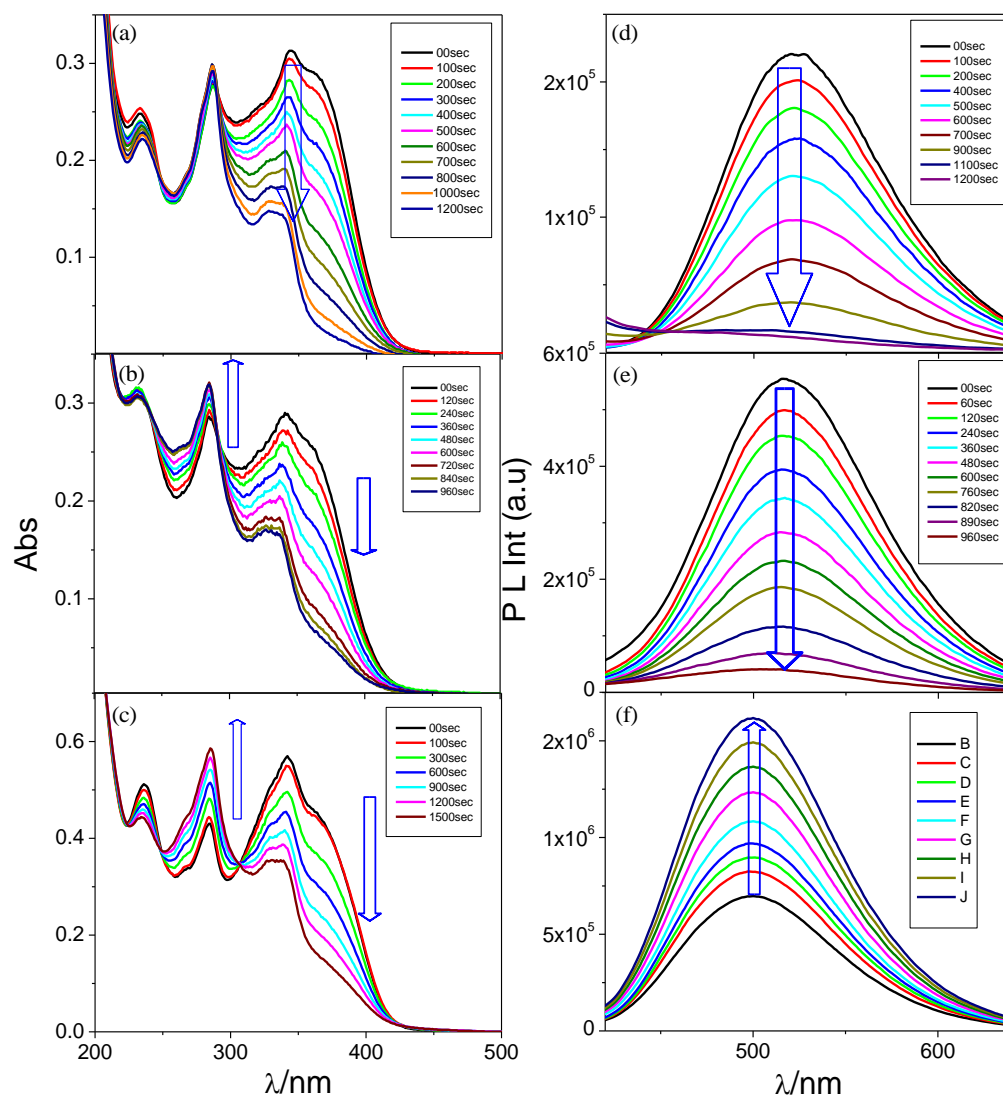


**Fig. 5.17.** Absorption and emission ( $\lambda_{\text{ex}} = 330 \text{ nm}$ ) spectral change of  $[\text{Zn}(\text{tpy-pvp-H})_2]^{2+}$  (a and d, respectively),  $[\text{Zn}(\text{tpy-pvp-Me})_2]^{2+}$  (b and e, respectively) and  $[\text{Zn}(\text{tpy-pvp-NO}_2)_2]^{2+}$  (c and f, respectively) in acetonitrile upon irradiation with visible light. Insets to the figs. a-f indicate the irradiation time.

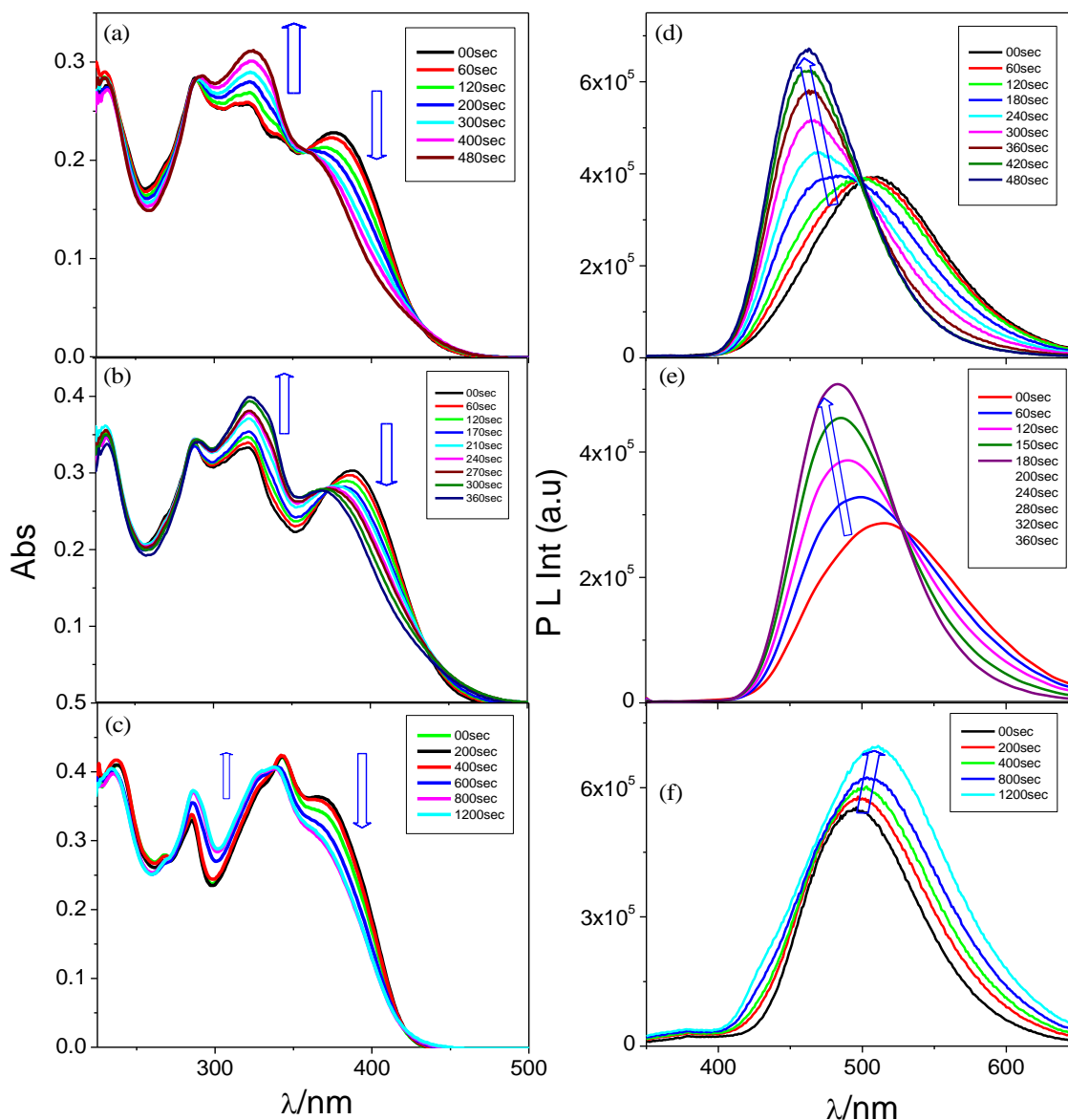


**Fig. 5.18.** Absorption and emission ( $\lambda_{\text{ex}} = 330 \text{ nm}$ ) spectral change of  $[\text{Zn}(\text{tpy-pvp-H})_2]^{2+}$  (a and d, respectively),  $[\text{Zn}(\text{tpy-pvp-Me})_2]^{2+}$  (b and e, respectively) and  $[\text{Zn}(\text{tpy-pvp-NO}_2)_2]^{2+}$  (c and f, respectively) in dichloromethane upon irradiation with visible light. Insets to the figs. a-f indicate the irradiation time.

( $H_{8'} = 8.01 \text{ ppm}$ ,  $J = 7.4 \text{ Hz}$ ); ( $H_{9'} = 6.76 \text{ ppm}$ ,  $J = 12.0 \text{ Hz}$ ); ( $H_{10'} = 6.69 \text{ ppm}$ ,  $J = 12 \text{ Hz}$ ), ( $H_{11'} = 7.77 \text{ ppm}$ ,  $J = 7.9 \text{ Hz}$ );  $H_{12'} = 7.47 \text{ ppm}$ ,  $J = 8.2 \text{ Hz}$ ). It is observed that  $H_9$  and  $H_{10}$  protons experienced an up-field shift  $\{\Delta\delta(H_9) = 0.57 \text{ ppm}$  and  $\Delta\delta(H_{10}) = 0.56 \text{ ppm}\}$  along with remarkable decrease of  $J$  values (from  $\sim 16 \text{ Hz}$  to  $\sim 12 \text{ Hz}$ ). The adjoining

protons ( $H_7$ ,  $H_8$ ,  $H_{11}$  and  $H_{12}$ ) also experienced an up-field shift  $\{\Delta\delta(H_7)=0.07$  ppm,  $\Delta\delta(H_8, H_{11})=0.06$  ppm and  $\Delta\delta(H_{11}, H_{12})=0.04$  ppm $\}$  upon photolysis for 8h. The observed spectral change suggests the isomerization is taking place from *trans-trans* to the corresponding *trans-cis* form [43,52].

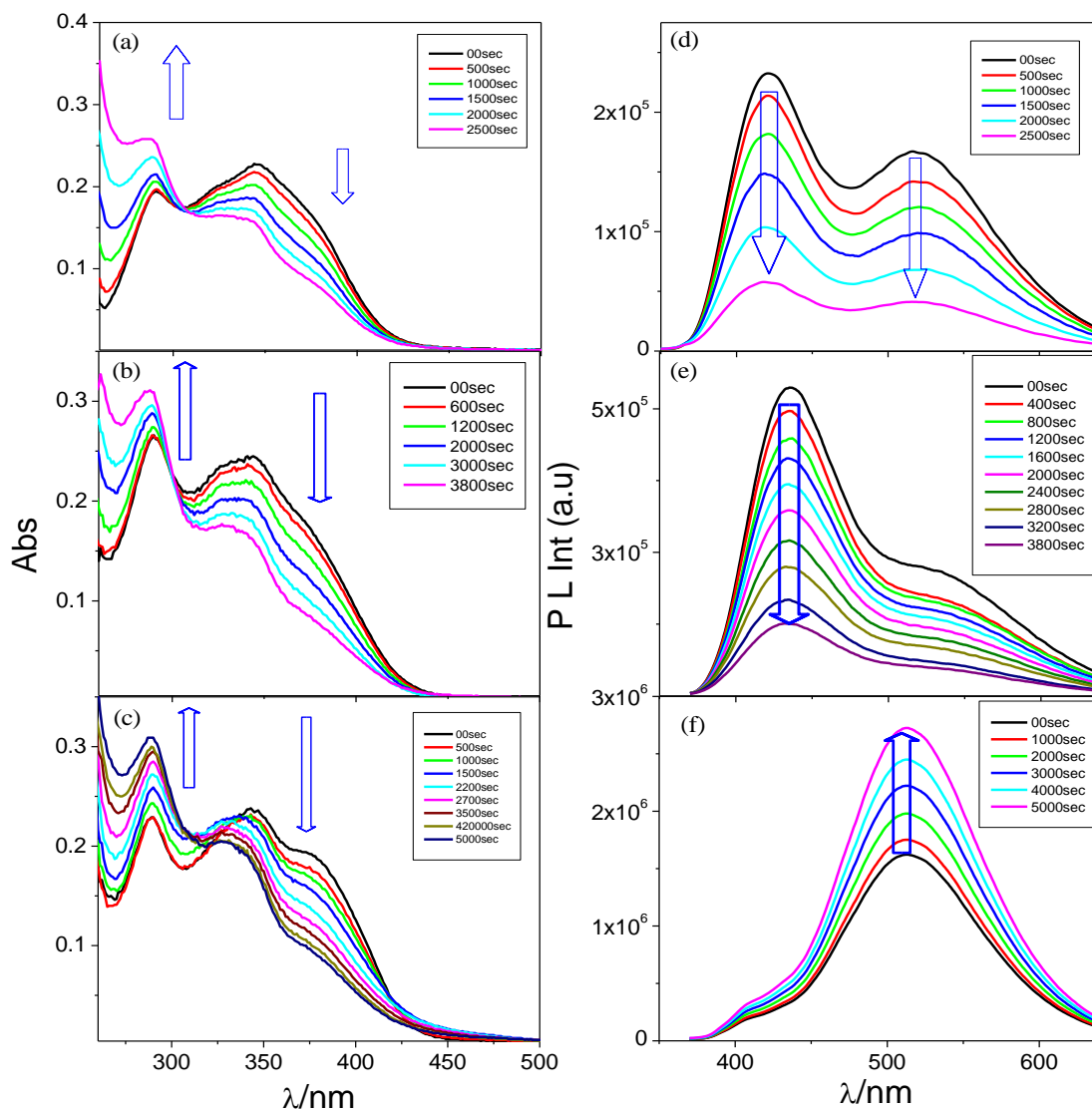


**Fig. 5.19.** Absorption and emission ( $\lambda_{ex} = 330$  nm) spectral change of  $[Zn(tpy-pvp-H)_2]^{2+}$  (a and d, respectively),  $[Zn(tpy-pvp-Me)_2]^{2+}$  (b and e, respectively) and  $[Zn(tpy-pvp-NO_2)_2]^{2+}$  (c and f, respectively) in dimethylsulfoxide upon irradiation with visible light. Insets to the figs. a-f indicate the irradiation time.



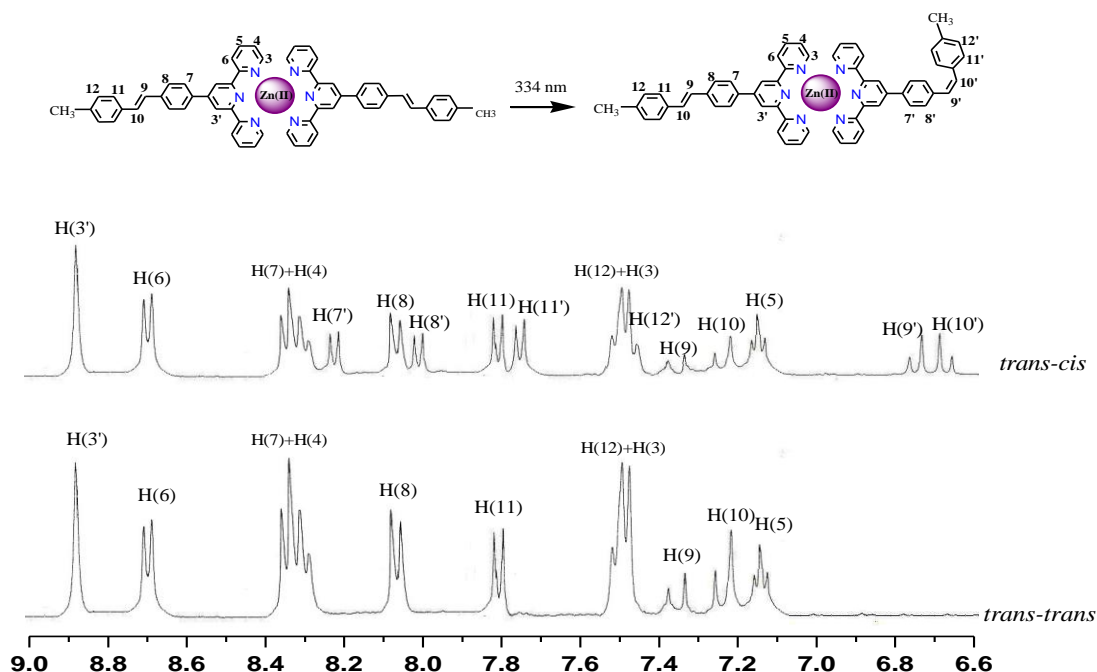


**Fig. 5.20.**  $^1\text{H}$  NMR spectrum of **2** and upon 8h of photo-irradiation with visible light of 405 nm in  $\text{CD}_3\text{CN}$ .

We also carried out TD-DFT calculations on the *trans-cis* forms of the complexes in their singlet and triplet excited states in order to compare the experimental spectra with the calculated results. The calculated results are summarized in Table 5.10-5.15 and Fig. 5.21-5.23. The overlay of the calculated and experimental absorption spectra of the *trans-trans* and *trans-cis* forms of the complexes is displayed in Fig. 5.24-5.25. The agreement between the experimental and calculated results is remarkably good and the trend of the experimentally observed blue-shift in the lowest energy absorption and emission maxima on going from *trans-trans* to *trans-cis* isomer is reproduced in our calculation. The lowest triplet states of the *trans-cis* forms are also optimized through UKS calculations by using both B3LYP and CAM- B3LYP methods and the results are summarized in Table 5.16-5.17. The experimentally observed emission maxima matches better with the results obtained from TD-DFT calculation than that of the UKS calculation.

**Table 5.10** Selected calculated bond distances (Å) of *trans-cis* form of  $[\text{Zn}(\text{tpy-pvp-X})_2]^{2+}$  where X= H, Me, NO<sub>2</sub> at TD-DFT/B3LYP level.

<i>trans-cis</i>	
$[\text{Zn}(\text{tpy-pvp-H})_2]^{2+}$	
Zn1-N1	2.234
Zn1-N2	2.127
Zn1-N3	2.238
Zn1-N4	2.237
Zn1-N5	2.128
Zn1-N6	2.234
$[\text{Zn}(\text{tpy-pvp-Me})_2]^{2+}$	
Zn1-N1	2.113
Zn1-N2	2.018
Zn1-N3	2.112
Zn1-N4	2.112
Zn1-N5	2.018
Zn1-N6	2.113
$[\text{Zn}(\text{tpy-pvp-NO}_2)_2]^{2+}$	
Zn1-N1	2.253
Zn1-N2	2.152
Zn1-N3	2.258
Zn1-N4	2.257
Zn1-N5	2.152
Zn1-N6	2.255

**Table 5.11** Selected calculated bond angles (deg) of *trans-cis* form of  $[\text{Zn}(\text{tpy-pvp-H})_2]^{2+}$ ,  $[\text{Zn}(\text{tpy-pvp-CH}_3)_2]^{2+}$  and  $[\text{Zn}(\text{tpy-pvp-NO}_2)_2]^{2+}$  at TD-DFT/B3LYP level.

$[\text{Zn}(\text{tpy-pvp-H})_2]^{2+}$		$[\text{Zn}(\text{tpy-pvp-CH}_3)_2]^{2+}$		$[\text{Zn}(\text{tpy-pvp-NO}_2)_2]^{2+}$	
N6Zn1N2	105.90	N6Zn1N2	106.01	N6Zn1N2	105.89
N6Zn1N3	93.92	N6Zn1N3	93.91	N6Zn1N3	93.54
N6Zn1N4	149.82	N6Zn1N4	149.82	N6Zn1N4	149.86
N6Zn1N5	74.96	N6Zn1N5	74.95	N6Zn1N5	74.95
N6Zn1N1	93.70	N6Zn1N1	93.86	N6Zn1N1	93.90
N2Zn1N3	74.89	N2Zn1N3	74.89	N2Zn1N3	74.91
N2Zn1N4	105.92	N2Zn1N4	104.16	N2Zn1N4	104.23
N2Zn1N1	74.95	N2Zn1N1	74.96	N2Zn1N1	74.93
N4Zn1N5	74.86	N4Zn1N5	74.87	N4Zn1N5	74.92
N4Zn1N1	93.59	N4Zn1N1	93.56	N4Zn1N1	94.21
N4Zn1N3	94.29	N4Zn1N3	94.17	N4Zn1N3	93.84
N5Zn1N1	105.66	N5Zn1N1	105.51	N5Zn1N1	103.87
N5Zn1N3	104.47	N5Zn1N3	104.62	N5Zn1N3	106.27
N1Zn1N3	149.85	N1Zn1N3	149.85	N1Zn1N3	149.84
N2Zn1N5	178.90	N2Zn1N5	178.91	N2Zn1N5	178.54

The backward *trans-cis* to *trans-trans* conversion proceeds very slowly at ambient condition. We tried to revert back by heating the isomerized solution at ~40°C and observed slow conversion towards their initial form in all the studied solvents. But we are unable to revert back to the exact initial position. The absorption and emission spectral changes of the complexes upon heating at 40 °C are presented in Fig. 5.26-5.31. Emission quenching and red-shifting of the respective band is observed in the reverse process and

**Table 5.12** Selected MOs along with their energies and compositions in the ground state of the *trans-cis* form of  $[\text{Zn}(\text{tpy-pvp-H})_2]^{2+}$  (**1**),  $[\text{Zn}(\text{tpy-pvp-CH}_3)_2]^{2+}$  (**2**) and  $[\text{Zn}(\text{tpy-pvp-NO}_2)_2]^{2+}$  (**3**) in acetonitrile at the TD-DFT/CAM-B3LYP level.

MO	$[\text{Zn}(\text{tpy-pvp-H})_2]^{2+}$ ( <b>1</b> )				
	Energy/ev	% Compositions			
	<i>Trans-cis</i>	<i>Trans-cis</i>			
		Zn	Tpy	Styryl-benz	Benzal
LUMO+3	-1.35	0.00	99.48	0.51	0.00
LUMO+2	-1.40	0.07	99.43	0.49	0.00
LUMO+1	-1.75	0.66	84.49	13.80	1.03
LUMO	-1.75	0.73	84.37	13.80	1.04
HOMO	-7.52	0.00	4.43	61.84	33.72
HOMO-1	-7.52	0.02	4.39	61.83	33.76
HOMO-2	-8.63	0.00	0.56	9.37	90.10
HOMO-3	-8.63	0.00	0.54	9.31	90.14
	$[\text{Zn}(\text{tpy-pvp-Me})_2]^{2+}$ ( <b>2</b> )				
	<i>Trans-cis</i>	Zn	Tpy	Styryl-benz	Me-Benz
LUMO+3	-1.35	0.00	99.50	0.49	0.00
LUMO+2	-1.40	0.06	99.45	0.47	0.00
LUMO+1	-1.75	0.66	85.07	13.29	0.95
LUMO	-1.75	0.73	84.93	13.36	0.96
HOMO	-7.38	0.00	3.41	53.92	42.65
HOMO-1	-7.38	0.01	3.38	53.90	42.69
HOMO-2	-8.56	0.00	2.49	15.09	82.40
HOMO-3	-8.56	0.00	2.40	14.88	82.70
	$[\text{Zn}(\text{tpy-pvp-NO}_2)_2]^{2+}$ ( <b>3</b> )				
	<i>Trans-cis</i>	Zn	Tpy	Styryl-benz	Nitro-Benz
LUMO+3	-1.74	0.66	82.95	10.75	5.60
LUMO+2	-1.74	0.71	82.84	10.75	5.67
LUMO+1	-2.29	0.01	2.91	8.34	88.71
LUMO	-2.29	0.02	2.95	8.35	88.66
HOMO	-7.85	0.00	6.50	71.91	21.57
HOMO-1	-7.85	0.02	6.44	71.92	21.61
HOMO-2	-8.72	0.01	99.51	0.45	0.01
HOMO-3	-8.72	0.00	99.48	0.49	0.01

**Table 5.13** Selected UV-vis energy transitions at the TD-DFT/B3LYP level of *trans-cis* forms of  $[\text{Zn}(\text{tpy-pvp-H})_2]^{2+}$  (**1**),  $[\text{Zn}(\text{tpy-pvp-CH}_3)_2]^{2+}$  (**2**) and  $[\text{Zn}(\text{tpy-pvp-NO}_2)_2]^{2+}$  (**3**) in acetonitrile.

Excited state	$\lambda_{\text{cal}}/\text{nm}$	Oscillator strength(f)	$\lambda_{\text{expt}}/\text{nm}$	Key transitions	Character
<i>Trans-cis</i> $[\text{Zn}(\text{tpy-pvp-H})_2]^{2+}$					
S <sub>1</sub>	433	0.98	338	H-1→L+1 (49%), H→L (50%)	LLCT
S <sub>9</sub>	324	0.97	327	H-1→L+4 (47%), H→L+5 (47%)	LLCT, $\pi$ - $\pi^*$
S <sub>23</sub>	302	0.25	286	H-9→L (31%), H-8→L+1 (31%), H-7→L+1 (14%), H-6→L(16%)	LLCT, $\pi$ - $\pi^*$
<i>Trans-cis</i> $[\text{Zn}(\text{tpy-pvp-CH}_3)_2]^{2+}$					
S <sub>1</sub>	451	0.93	336	H-1→L+1 (49%), H→L (50%)	LLCT
S <sub>9</sub>	323	1.07	326	H-1→L+4 (47%), H→L+5 (47%)	LLCT, $\pi$ - $\pi^*$
S <sub>52</sub>	278	0.47	285	H-9→L+2 (13%), H-8→L+3 (10%), H-7→L+2 (19%), H-6→L+3(45%)	$\pi$ - $\pi^*$
<i>Trans-cis</i> $[\text{Zn}(\text{tpy-pvp-NO}_2)_2]^{2+}$					
S <sub>1</sub>	468	1.76	338	H→L(96%)	LLCT
S <sub>2</sub>	457	0.38	326	H-1→L+1 (96%)	LLCT
S <sub>7</sub>	395	0.22	285	H-1→L+2 (95%)	LLCT, $\pi$ - $\pi^*$
S <sub>27</sub>	312	0.54	235	H-9→L (19%), H→L+6 (76%)	LLCT, $\pi$ - $\pi^*$

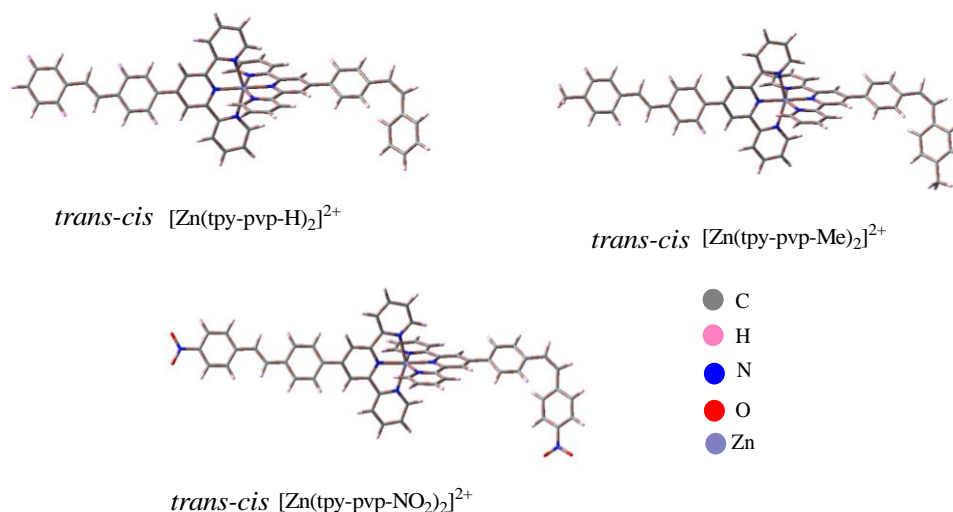


**Fig. 5.21.** Ground state optimized geometries of the *trans-cis* forms of the Zn(II) complexes of composition  $[\text{Zn}(\text{tpy-pvp-X})_2]^{2+}$  (X= H, Me, and NO<sub>2</sub>) in acetonitrile.

**Table 5.14** Selected UV-vis energy transitions at the TD-DFT/CAM-B3LYP level of *trans-cis* forms of  $[\text{Zn}(\text{tpy-pvp-H})_2]^{2+}$  (**1**),  $[\text{Zn}(\text{tpy-pvp-CH}_3)_2]^{2+}$  (**2**) and  $[\text{Zn}(\text{tpy-pvp-NO}_2)_2]^{2+}$  (**3**) in acetonitrile.

Excited state	$\lambda_{\text{cal}}/\text{nm}$	Oscillator strength(f)	$\lambda_{\text{exp}}/\text{nm}$	Key transitions	Character
<i>Trans-cis</i> $[\text{Zn}(\text{tpy-pvp-H})_2]^{2+}$					
S <sub>1</sub>	321	2.07	338	H-1→L+1 (34%), H-1→L+4 (11%), HOMO→LUMO (34%), HOMO→L+5 (11%)	LLCT
S <sub>4</sub>	289	0.28	327	H-5→L+1 (36%), H-4→LUMO (35%), H-1→L+2 (7%), HOMO→L+3 (6%)	LLCT, $\pi$ - $\pi^*$
S <sub>14</sub>	251	0.88	286	H-5→L+2 (40%), H-4→L+3 (31%)H-11→L+1 (7%), H-10→LUMO (6%)	LLCT, $\pi$ - $\pi^*$
<i>Trans-cis</i> $[\text{Zn}(\text{tpy-pvp-CH}_3)_2]^{2+}$					
S <sub>1</sub>	326	1.98	336	H-1→L+1 (33%), H-1→L+4 (12%), HOMO→LUMO (33%), HOMO→L+5 (12%)	LLCT
S <sub>4</sub>	290	0.25	326	H-7→L+1 (34%), H-6→LUMO (33%), H-1→L+2 (8%), HOMO→L+3 (7%)	LLCT, $\pi$ - $\pi^*$
S <sub>16</sub>	252	0.99	285	H-7→L+2 (40%), H-6→L+3 (31%), H-11→L+1 (6%), H-10→LUMO (6%)	$\pi$ - $\pi^*$
<i>Trans-cis</i> $[\text{Zn}(\text{tpy-pvp-NO}_2)_2]^{2+}$					
S <sub>1</sub>	353	1.28	338	H-18→L+1 (35%), H-17→LUMO (35%) H-20→L+1 (7%), H-19→LUMO (7%)	LLCT
S <sub>7</sub>	292	0.45	326	H-9→L+1 (29%), H-8→LUMO (29%)	LLCT
S <sub>9</sub>	290	1.09	285	H-1→L+3 (30%), HOMO→L+2 (31%)	LLCT, $\pi$ - $\pi^*$
S <sub>22</sub>	252	0.65	235	H-3→L+4 (38%), H-2→L+5 (30%), H-11→L+2 (6%), H-10→L+3 (6%)	LLCT, $\pi$ - $\pi^*$

**Table 5.15** Singlet-triplet excitation energies at the lowest triplet state (T<sub>1</sub>) along with key transition of complexes in their *trans-cis* forms of **1**, **2** and **3** in MeCN.

Compounds	Key transitions	$E$ (cm <sup>-1</sup> )
<b>1</b>	$\pi_{\text{stb}}(221) \rightarrow \pi_{\text{tpy}}^*(222)$ (97%)	21097
<b>2</b>	$\pi_{\text{stb}}(229) \rightarrow \pi_{\text{tpy}}^*(230)$ (96%)	19685
<b>3</b>	$\Pi_{\text{stb}}(243) \rightarrow \pi_{\text{nb}}^*(244)$ (97%)	18281

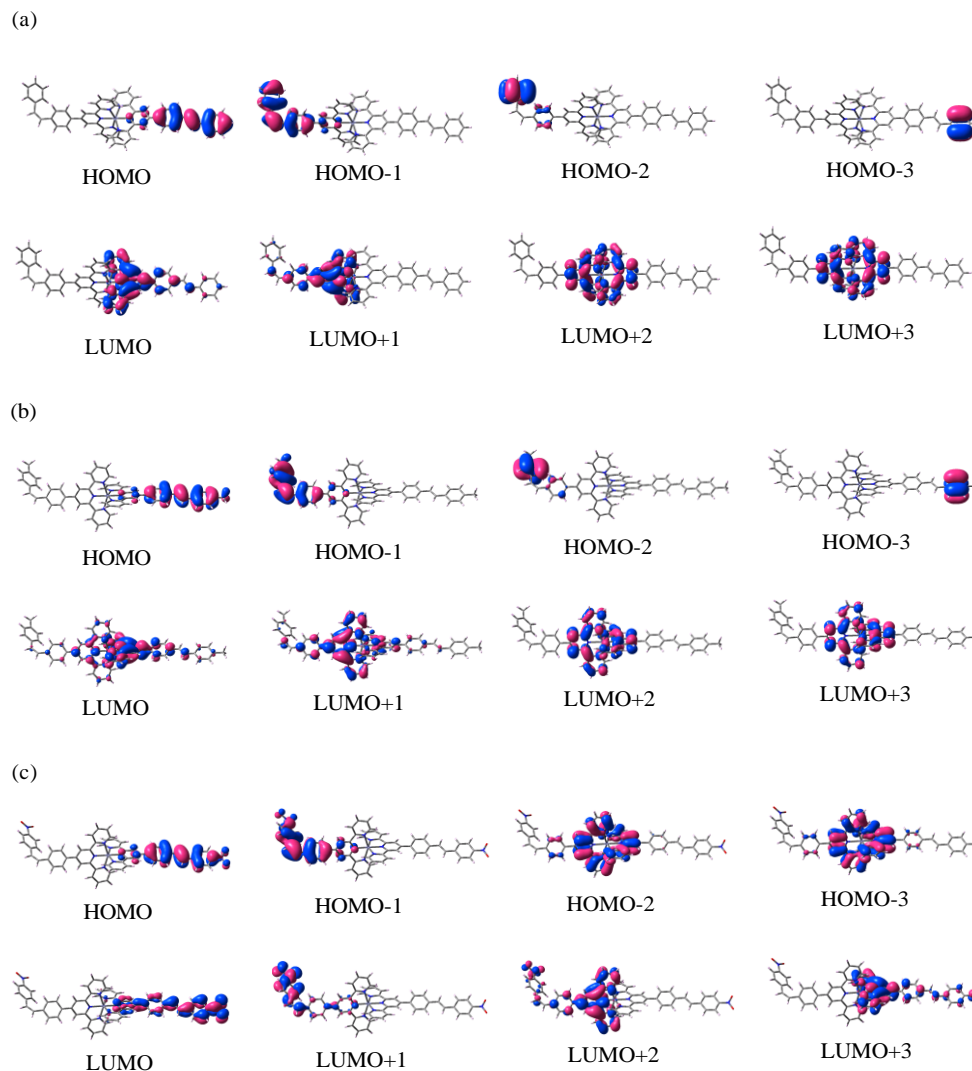


**Fig. 5.22.** Schematic drawings of selective frontier molecular orbitals in the ground state of *trans-cis* form of  $[\text{Zn}(\text{tpy-pvp-H})_2]^{2+}$  (a),  $[\text{Zn}(\text{tpy-pvp-CH}_3)_2]^{2+}$  (b) and  $[\text{Zn}(\text{tpy-pvp-NO}_2)_2]^{2+}$  (c) in acetonitrile by CAM-B3LYP level calculation.

restoration of the original spectra occurs to the extent of ~90% in DCM. In MeCN and DMSO, the original emission was also restored up to the extent of 80% by heating at 40 °C. Thus, successive "on-off" and "off-on" emission switching processes can be achievable by alternative treatment with light and heat.

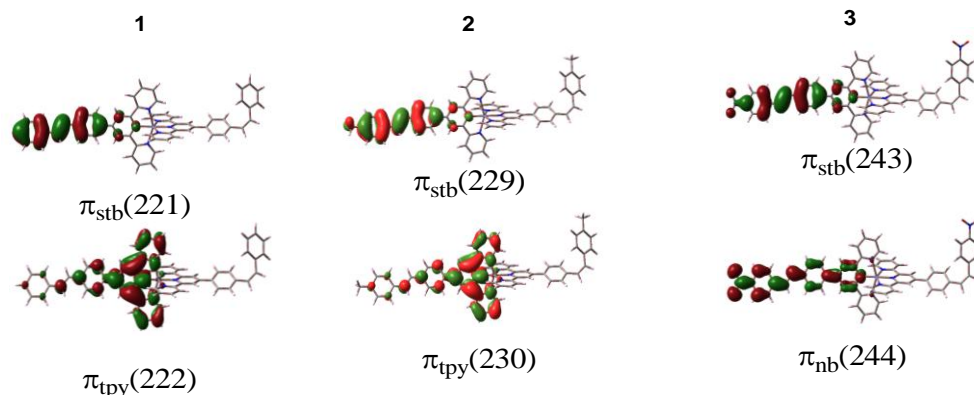


**Fig. 5.23.** Schematic drawings of the molecular orbitals that are involved in the dominant configurations of the lowest lying triplet excited states of *trans-cis* form of **1** (left panel), **2** (middle panel) and **3** (right panel) in MeCN.

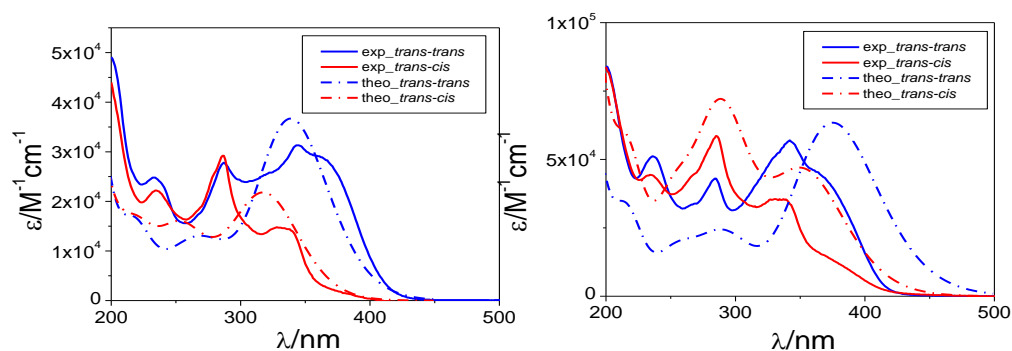


**Fig. 5.24.** The overlay of the calculated (dotted lines) and experimental (solid lines) absorption spectra of *trans-trans* (blue) and *trans-cis* (red) form of **1** (left) and **3** (right) in acetonitrile.

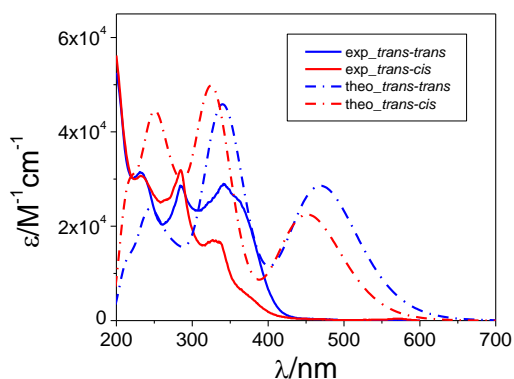


**Fig. 5.25.** Overlay of the calculated (dotted lines) and experimental (solid lines) absorption spectra of *trans-trans* (blue), and *trans-cis* (red) form of  $[\text{Zn}(\text{tpy-pvp-CH}_3)_2]^{2+}$  (**2**) in acetonitrile.

**Table 5.16** Emission maxima of *trans-cis* forms of  $[\text{Zn}(\text{tpy-pvp-H})_2]^{2+}$  (**1**),  $[\text{Zn}(\text{tpy-pvp-CH}_3)_2]^{2+}$  (**2**) and  $[\text{Zn}(\text{tpy-pvp-NO}_2)_2]^{2+}$  (**3**) in MeCN according to UKS calculations at the TD-DFT/B3LYP level and associated experimental values.

Compounds	$\lambda_{\text{cal}}/\text{nm}$	$\lambda_{\text{exp}}/\text{nm}$
<b>1</b>	732	512
<b>2</b>	735	510
<b>3</b>	778	502

**Table 5.17** Emission maxima of the *trans-cis* forms of  $[\text{Zn}(\text{tpy-pvp-H})_2]^{2+}$  (**1**),  $[\text{Zn}(\text{tpy-pvp-CH}_3)_2]^{2+}$  (**2**) and  $[\text{Zn}(\text{tpy-pvp-NO}_2)_2]^{2+}$  (**3**) in MeCN according to UKS calculations at the TD-DFT/CAM-B3LYP level and associated experimental values.

Compounds	$\lambda_{\text{cal}}/\text{nm}$	$\lambda_{\text{exp}}/\text{nm}$
<b>1</b>	734	512
<b>2</b>	735	510
<b>3</b>	765	502

We calculated the "apparent" rate constants ( $k_{\text{iso}}$ ), quantum yield ( $\Phi$ ) and free energy of activation ( $\Delta G^\ddagger$ ) for both the forward and the reverse processes and the values are provided in Table 5.18-5.20. We used the term "apparent rate constant" as it depends on the intensity of light. The  $k_{\text{iso}}$  for the forward process varies between  $1.1 \times 10^{-4} \text{ s}^{-1}$  and  $38.9 \times 10^{-4} \text{ s}^{-1}$ , dependent on the nature of substituent X, solvent and wavelength of light used. The rate constants of the thermal backward process, on the other hand, vary between  $0.5 \times 10^{-5} \text{ s}^{-1}$  and  $9.2 \times 10^{-5} \text{ s}^{-1}$ . absorption peak lying within the range of 330-361 nm, depending upon the nature of X, gradually diminished in intensity together with simultaneous enhancement of peak in the spectral domain of 355-390 nm. The ligands which display intense emission with the maximum lying in the range of 398-420 nm, quenched remarkably upon photo-isomerization. The rate constant of *trans*→*cis* isomerization varies in the range of and  $11.7 \times 10^{-3} \text{ s}^{-1}$ . Thus,  $\text{Zn}^{2+}$  affects the photophysics and isomerization behaviors of tpy-pvp-X motif to a great extent in the present study. Coordination of  $\text{Zn}^{2+}$  induces evolution of an intense absorption band in the near-visible



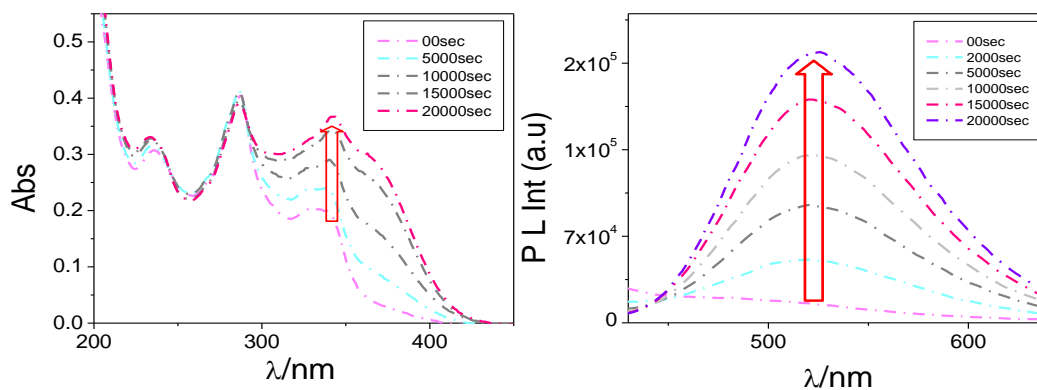


**Fig. 5.26.** The UV-vis absorption (a) and emission ( $\lambda_{\text{ex}}=330$  nm) (b) spectral changes upon heating the photolyzed acetonitrile solution of **1** at 40°C. Insets show the heating time.

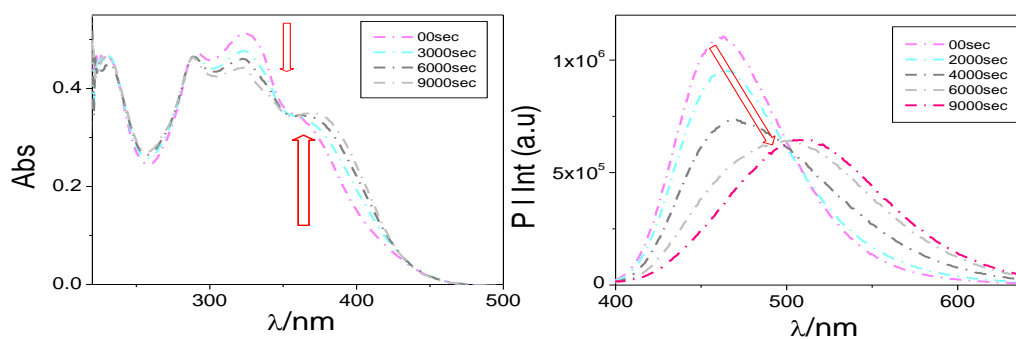


**Fig. 5.27.** The UV-vis absorption (a) and emission ( $\lambda_{\text{ex}}=330$  nm) (b) spectral changes upon heating the photolyzed dichloromethane solution of **1** at 40 °C. Insets show the heating time.

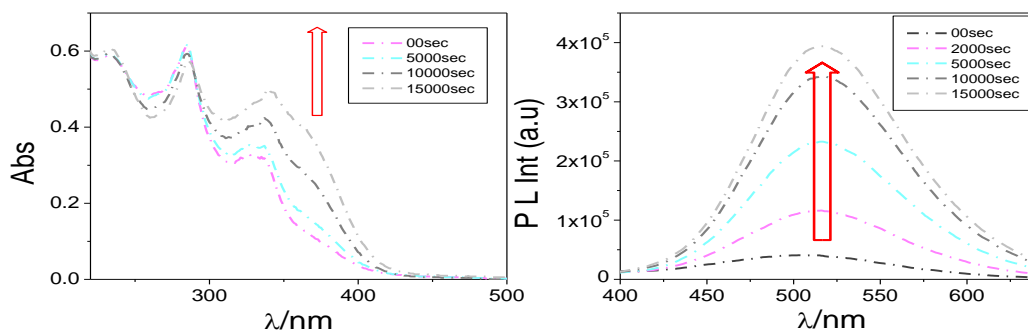


**Fig. 5.28.** UV-vis absorption (a) and emission ( $\lambda_{\text{ex}}=330$  nm) (b) spectral changes upon heating the photolyzed acetonitrile solution of **2** at 40°C. Insets show the heating time.

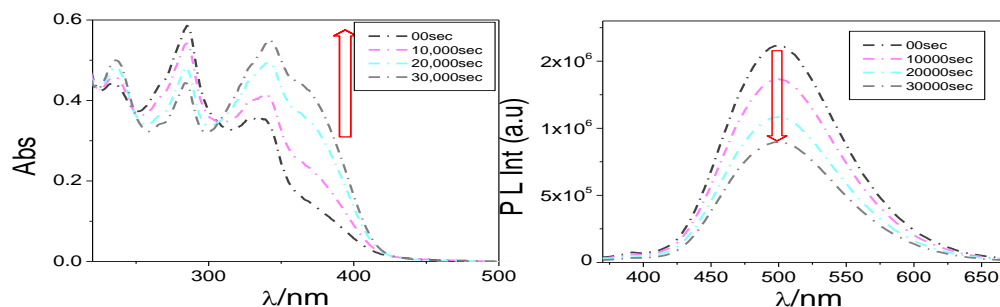


**Fig. 5.29.** UV-vis absorption (a) and emission ( $\lambda_{\text{ex}}=330$  nm) (b) spectral changes upon heating the photolyzed acetonitrile solution of **3** at 40°C. Insets show the heating time.

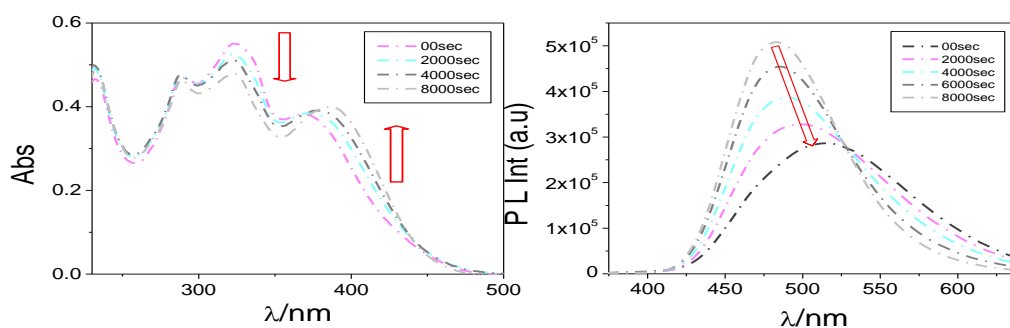


**Fig. 5.30.** UV-vis absorption (a) and emission ( $\lambda_{\text{ex}}=330$  nm) (b) spectral changes upon heating the photolyzed dichloromethane solution of **2** at 40°C. Insets show the heating time.

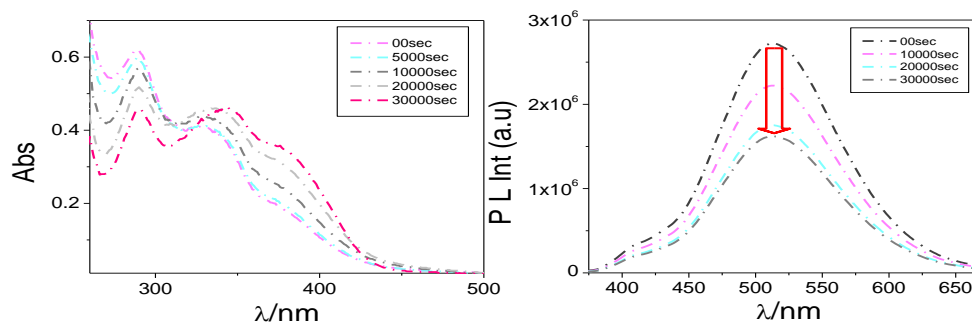


**Fig. 5.31.** UV-vis absorption (a) and emission ( $\lambda_{\text{ex}}=330$  nm) (b) spectral changes upon heating the photolyzed dimethylsulfoxide solution of **3** at 40°C. Insets show the heating time.

**Table 5.18** Apparent rate constants ( $k_{\text{iso}}$ ) and quantum yields ( $\Phi$ ) for the forward photoisomerization processes of the complexes **1-3**.

Compound	UV light (350 nm)						Visible light (405 nm)					
	MeCN		DCM		DMSO		MeCN		DCM		DMSO	
	$k_{\text{iso}}/\text{s}^{-1}$ ( $\times 10^{-4}$ ) $t\text{-}t \rightarrow t\text{-}c$	$\Phi$ ( $\times 10^{-2}$ ) $t\text{-}t \rightarrow t\text{-}c$	$k_{\text{iso}}/\text{s}^{-1}$ ( $\times 10^{-4}$ ) $t\text{-}t \rightarrow t\text{-}c$	$\Phi$ ( $\times 10^{-2}$ ) $t\text{-}t \rightarrow t\text{-}c$	$k_{\text{iso}}/\text{s}^{-1}$ ( $\times 10^{-4}$ ) $t\text{-}t \rightarrow t\text{-}c$	$\Phi$ ( $\times 10^{-3}$ ) $t\text{-}t \rightarrow t\text{-}c$	$k_{\text{iso}}/\text{s}^{-1}$ ( $\times 10^{-4}$ ) $t\text{-}t \rightarrow t\text{-}c$	$\Phi$ ( $\times 10^{-2}$ ) $t\text{-}t \rightarrow t\text{-}c$	$k_{\text{iso}}/\text{s}^{-1}$ ( $\times 10^{-4}$ ) $t\text{-}t \rightarrow t\text{-}c$	$\Phi$ ( $\times 10^{-2}$ ) $t\text{-}t \rightarrow t\text{-}c$	$k_{\text{iso}}/\text{s}^{-1}$ ( $\times 10^{-4}$ ) $t\text{-}t \rightarrow t\text{-}c$	$\Phi$ ( $\times 10^{-3}$ ) $t\text{-}t \rightarrow t\text{-}c$
<b>1</b>	7.6	2.7	11.2	4.5	1.7	7.4	19.7	6.9	33.4	15.1	1.5	6.5
<b>2</b>	13.8	5.1	15.2	5.5	1.1	4.5	26.3	9.8	38.9	14.1	2.2	9.3
<b>3</b>	4.0	2.0	9.2	4.4	1.1	5.6	9.5	4.7	17.6	5.6	2.2	11.1

**Table 5.19** Free energies of activation ( $\Delta G^\ddagger$ ) of the forward photoisomerization processes for **1-3**.

Compounds	UV light (350 nm)			Visible light (490 nm)		
	MeCN	DCM	DMSO	MeCN	DCM	DMSO
	$\Delta G^\ddagger/\text{kJmol}^{-1}$ $t\text{-}t \rightarrow t\text{-}c$	$\Delta G^\ddagger/\text{kJmol}^{-1}$ $t\text{-}t \rightarrow t\text{-}c$	$\Delta G^\ddagger/\text{kJmol}^{-1}$ $t\text{-}t \rightarrow t\text{-}c$	$\Delta G^\ddagger/\text{kJmol}^{-1}$ $t\text{-}t \rightarrow t\text{-}c$	$\Delta G^\ddagger/\text{kJmol}^{-1}$ $t\text{-}t \rightarrow t\text{-}c$	$\Delta G^\ddagger/\text{kJmol}^{-1}$ $t\text{-}t \rightarrow t\text{-}c$
<b>1</b>	90.8	89.8	94.5	88.4	87.1	94.9
<b>2</b>	89.3	89.0	95.7	87.7	86.7	93.8
<b>3</b>	92.3	90.3	95.6	90.2	88.7	93.9

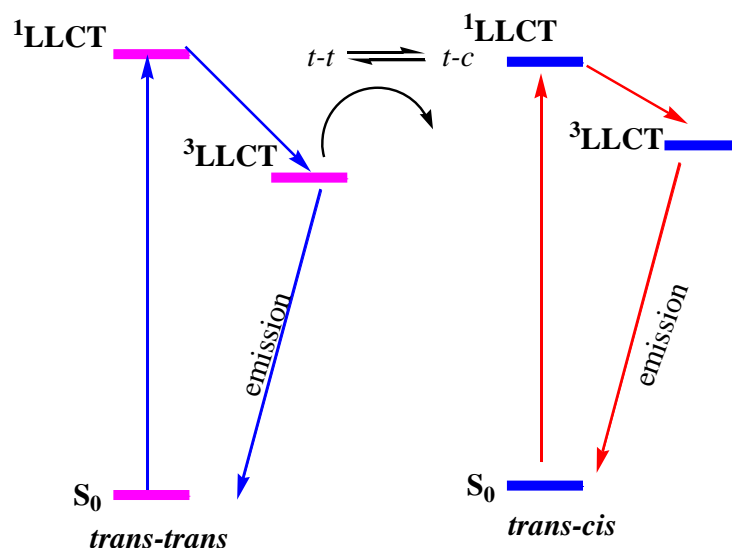
**Table 5.20** Apparent rate constants ( $k_{\text{iso}}$ ), free energies of activation ( $\Delta G^\ddagger$ ) and chemical yield for the backward thermal isomerization processes for **1-3**.

Compound	Heat (40°C)								
	MeCN			DCM			DMSO		
	$k_{\text{iso}}/\text{s}^{-1}$ ( $\times 10^{-5}$ ) $t\text{-}c \rightarrow t\text{-}t$	$\Delta G^\ddagger/\text{kJmol}^{-1}$ $t\text{-}c \rightarrow t\text{-}t$	Chemical Yield ( $\times 10^{-3}$ ) $t\text{-}c \rightarrow t\text{-}t$	$k_{\text{iso}}/\text{s}^{-1}$ ( $\times 10^{-5}$ ) $t\text{-}c \rightarrow t\text{-}t$	$\Delta G^\ddagger/\text{kJmol}^{-1}$ $t\text{-}c \rightarrow t\text{-}t$	Chemical Yield ( $\times 10^{-3}$ ) $t\text{-}c \rightarrow t\text{-}t$	$k_{\text{iso}}/\text{s}^{-1}$ ( $\times 10^{-5}$ ) $c\text{-}c \rightarrow t\text{-}t$	$\Delta G^\ddagger/\text{kJmol}^{-1}$ $c\text{-}c \rightarrow t\text{-}t$	Chemical Yield ( $\times 10^{-3}$ ) $c\text{-}c \rightarrow t\text{-}t$
<b>1</b>	6.0	97.1	5.9	7.6	96.5	3.9	0.8	102.1	0.4
<b>2</b>	9.0	96.1	6.3	9.2	96.0	5.7	0.6	102.8	1.1
<b>3</b>	2.7	99.1	8.9	3.1	98.7	2.5	0.5	103.2	2.1

(~380 nm) region and also causes substantial quenching of ligand-centered emission in the range of 398-420 nm with simultaneous evolution of emission band in the visible spectral domain (500-524 nm).

In chapter 2, we investigated the photoisomerization aspects of tpy-pvp-X ligands upon irradiating with UV light [67]. We observed that the lowest energy LLCT  $1.61 \times 10^{-3}$  The rate constant of photo-isomerization for Zn(II) complexes decreases substantially (between  $1.1 \times 10^{-4}$  and  $38.9 \times 10^{-4} \text{ s}^{-1}$ ). This is most probably due to the presence of a low lying LLCT excited state that efficiently quenches the higher energy phantom  $p^*$  state.

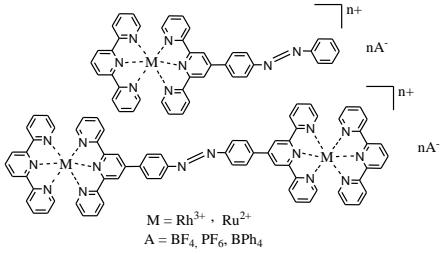
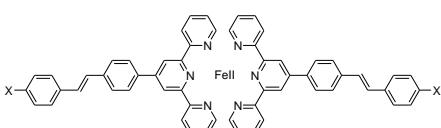
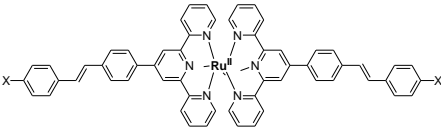
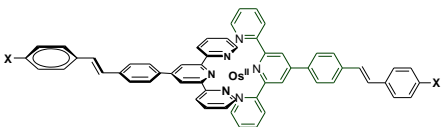
It would be good to provide some insight about the mechanism of the isomerization process. In general, the pure triplet LL state located on the isomerizable ligand plays a crucial role in the photoisomerization event. It should be accessible via  $^1\text{LLCT}$  to  $^3\text{LLCT}$  ISC and/or  $^3\text{LLCT}$ - $^3\text{IL}$  vibronic coupling and there will be a competition between emission and isomerization processes. Although the present data are not at maturity for pushing too far for mechanistic interpretation, we are providing a simplified and tentative energy diagram for the isomerization process of the present Zn(II) complexes (Fig. 5.32).

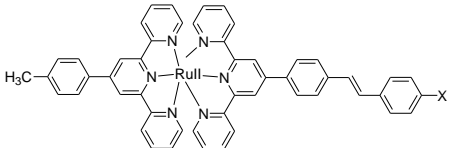
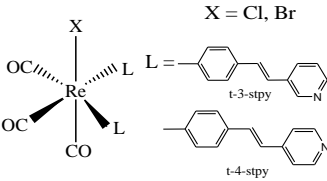
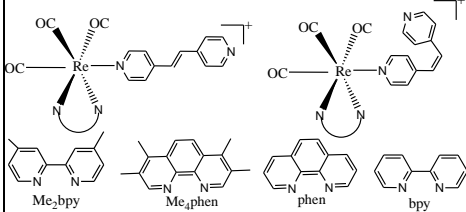
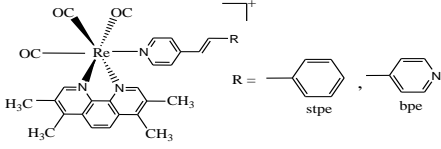
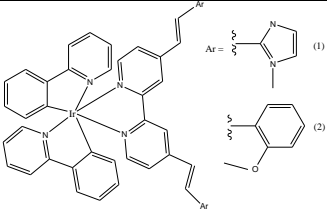


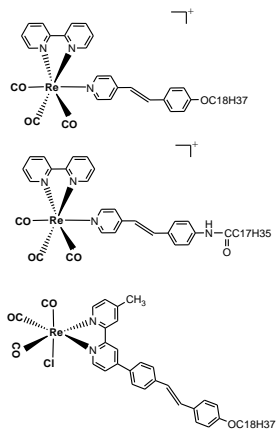
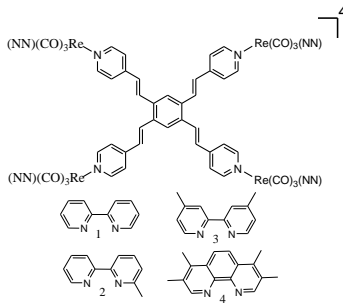
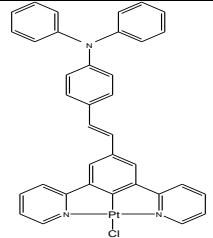
**Fig. 5.32.** Simplified and tentative energy diagram displaying photoisomerization along with competitive photophysical processes in the complexes.

It would be of interest to compare the photoisomerization efficiencies of the present complexes with previously reported polypyridine complexes of heavier transition metals (such as Re, Ru, Rh, Ir, and Pt) appended with stilbene and azo groups. Table 5.21 shows representative examples of metal complexes exhibiting *trans/cis* isomerization at different irradiating wavelengths as well as solvents. It is evident that quite a large number of reports are available on stilbene-appended pyridine or bipyridine-type systems of heavier transition metal complexes but no report is available on stilbene-appended terpyridine systems. Nishihara's group reported some terpyridine complexes of Ru(II) and Rh(III) coupled with photoactive azo unit [68]. Recently, our group initiated the isomerization studies of stilbene-appended terpyridine complexes of Fe(II), Ru(II) and Os(II) metals [30-31,59,33]. Photoisomerization behaviors of various heavier transition metal complexes (Re, Co, Rh, Ir etc.) covalently coupled with stilbene-appended polypyridine complexes are reported by different research groups (Gray, Wrighton, Yam, Lees, Iha and Patricinio, to name a few) and the quantum efficiency of the isomerization process of those systems are summarized in Table 5.21 [22,47,49-51,56,69-70]. It is observed that when the stilbene-appended pyridine unit is coordinated in a monodentate fashion together other co-ligand (CO and/or halide) with the heavier metals such as Re(I), the quantum efficiency of the photoisomerization process is usually high as compared with related systems having bipyridine or phenanthroline type coordination motifs. As compared with Re(I)-carbonyl-stilbene systems, the quantum efficiency of azo-terpyridine conjugate of Ru(II) and Rh(III) is usually small, although exception is there, depending upon specific system and condition used for isomerization. They estimated higher  $\Phi$  values for the Rh(III) azo-terpyridine systems compared with their Ru(II) systems probably because of the increased charge of the metal. The quantum efficiency of our stilbene-appended Ru(II)- terpyridine complexes was found to higher relative to the azo-terpyridine Ru(II) systems. In addition to other factors, the  $\Phi$  value of our stilbene-appended terpyridine systems depends mainly on the nature of metal ion and follows the general trend, Ru(II)<Os(II)<Fe(II)<Zn(II). Among the four types, the Ru(II)

**Table 5.21** Representative metal complexes exhibiting photo-induced *trans/cis* isomerization.

Compounds	Solvent	Irradiating wavelength	$\Phi$	ref
 <p>M = Rh<sup>3+</sup>, Ru<sup>2+</sup> A = BF<sub>4</sub><sup>-</sup>, PF<sub>6</sub><sup>-</sup>, BPh<sub>4</sub><sup>-</sup></p>	MeCN  DMSO  MeCN  DMSO	366 nm ( <i>trans</i> → <i>cis</i> )	(di-Rhtpy.nA <sup>-</sup> )  0.000016(A = BF <sub>4</sub> <sup>-</sup> ), 0.000011(A = PF <sub>6</sub> <sup>-</sup> )  0.00058(A = BF <sub>4</sub> <sup>-</sup> ), 0.0016(A = PF <sub>6</sub> <sup>-</sup> ), 0.0033(A = BPh <sub>4</sub> <sup>-</sup> ).  (di-Rhtpy.nA <sup>-</sup> )  0.0057(A = BPh <sub>4</sub> <sup>-</sup> ).  0.0019(A = BF <sub>4</sub> <sup>-</sup> ), 0.0016(A = PF <sub>6</sub> <sup>-</sup> ), 0.0021(A = BPh <sub>4</sub> <sup>-</sup> ).	68
 <p>[Fe(tpy-pvp-X)<sub>2</sub>]<sup>2+</sup> X = H (1); X = Me (2), and X = NO<sub>2</sub> (3)</p>	DCM MeCN DMSO MeOH DCM MeCN DMSO MeOH	436nm (( <i>trans</i> → <i>cis</i> )    336(( <i>trans</i> → <i>cis</i> )	0.0032(1)  0.0009(1)  0.0005(1)  0.0004(1)  0.0014(1)  0.0002(1)  0.0003(1)  0.00008(1)	59
 <p>[Ru(tpy-pvp-X)<sub>2</sub>]<sup>2+</sup> X = H (1), Me (2), Cl (3), NO<sub>2</sub> (4), Ph (5)</p>	MeCN-DCM	436nm( <i>trans</i> → <i>cis</i> )	0.000036 (1)  0.000046 (2)  0.000029(3)  0.00001 (4)  0.000038 (5)	31
 <p>[Os(tpy-pvp-X)<sub>2</sub>]<sup>2+</sup> X = H (1), Me (2), Cl (3), NO<sub>2</sub> (4), Ph (5)</p>	MeCN-DCM MeCN DMSO  MeCN-DCM	490nm ( <i>trans</i> → <i>cis</i> )    350nm ( <i>trans</i> → <i>cis</i> )	0.00011-0.0012  0.00019-0.00062  0.00013-0.0004  0.00004-0.00010	33

 <p>[(tpy-Ph-CH<sub>3</sub>)Ru(tpy-pvp-X)]<sup>2+</sup> X = H (1), Me (2), Cl (3), NO<sub>2</sub> (4), Ph (5)</p>	MeCN-DCM	UV light	0.00013(1) 0.00012(2) 0.00016(3) 0.0001(4) 0.00012(5)	30
 <p>X = Cl, Br L = t-3-stpy, t-4-stpy</p>	CH <sub>2</sub> Cl <sub>2</sub>	313 nm ( <i>trans</i> → <i>cis</i> )  366 nm ( <i>trans</i> → <i>cis</i> )	0.49 (X = Cl, L = t-4-stpy) 0.64 (X = Br, L = t-4-stpy) 0.60 (X = Cl, L = t-3-stpy) 0.54 (X = Cl, L = t-4-stpy) 0.51 (X = Br, L = t-4-stpy) 0.51 (X = Cl, L = t-3-stpy)	50
 <p>Me<sub>2</sub>bpy, Me<sub>4</sub>phen, phen, bpy</p>		350 nm ( <i>trans</i> → <i>cis</i> )  250 nm ( <i>cis</i> → <i>trans</i> )	0.21 (NN = bpy) 0.23 (NN = Me <sub>2</sub> bpy) 0.22 (NN = phen) 0.21 (NN = Me <sub>4</sub> phen) 0.18 (NN = bpy) 0.18 (NN = Me <sub>2</sub> bpy) 0.18 (NN = phen) 0.16 (NN = Me <sub>4</sub> phen)	56
 <p>H<sub>3</sub>C, CH<sub>3</sub>, R = stpe, bpe</p>	MeCN	365 nm ( <i>trans</i> → <i>cis</i> ) 404 nm ( <i>trans</i> → <i>cis</i> ) 365 nm ( <i>trans</i> → <i>cis</i> ) 404 nm ( <i>trans</i> → <i>cis</i> )	0.33 (R = bpe) 0.29 (R = bpe) 0.57 (R = stpe) 0.35 (R = stpe)	47
 <p>Ar = (1), (2)</p>	DCM	366 nm ( <i>trans</i> → <i>cis</i> )	—	85

	CH <sub>2</sub> Cl <sub>2</sub>	365 nm ( <i>trans</i> → <i>cis</i> )	0.49  0.43  0.42	22
	MeCN	405 nm ( <i>trans</i> → <i>cis</i> )	0.65 (Re-1) 0.45 (Re-1) 0.21 (Re-1) 0.19 (Re-1)	49
	DCM	365nm ( <i>trans</i> → <i>cis</i> )	0.003	86

and Os(II) complexes exhibit emission predominantly from their <sup>3</sup>MLCT state, while the Fe(II) complexes are non-luminescent because of presence of low-lying <sup>3/5</sup>MC state. In case of Ru(II) and Os(II) systems, the isomerization is believed to take place through combined <sup>3</sup>MLCT-<sup>3</sup>LLCT excited states and also the emission is a competitive decay pathway of isomerization. The enhanced quantum efficiency of present Zn(II)-terpyridine complexes is highest as isomerization is believed to take place through <sup>3</sup>LLCT excited states and due to absence of low-lying metal centered excited state. Thus, the present low cost Zn(II)-terpyridine complexes could act as potential photoswitches.



In the previous section, we were successful in modulating the absorption and emission spectral behaviors of the Zn(II) complexes to a significant extent upon irradiating with UV and visible light sources. In case of **1** and **2**, the emission quenching upon irradiation with 334 nm and 405 nm light sources and restoration of the original emission upon heating at 40°C gives rise to “on-off” and “off-on” emission switching. By contrast, for **3**, emission enhancement upon exposing to the said light sources followed by restoration of emission upon heating leads to “off on” and “on-off” emission switching. We can utilize the emission responses of the complexes as function of photonic and thermal inputs to mimic the function of two-input binary logic gates.

### 5.3.7 IMPLICATION Gate

The IMPLICATION logic operation was initiated by Whitehead and Russell along with three fundamental logic operations: AND, OR, and NOT. The function of IMPLICATION gate is very important as well as useful for the material implication. Molecular systems exhibiting excellent implication activity (IMP) are relatively sparse in literature. In order to mimic the function of an IMPLICATION gate, we have selected two stimuli (heat as input 1 and photon as input 2) and the emission maximum at 522 nm was used as the output signal (Fig. 5.33). The truth table in Fig. 5.33 shows that in absence of either of the two inputs, **1** exhibits intense emission at 522 nm corresponding to the “ON” state (1) of the system. By contrast, input 2 (photon) induces decrease in emission intensity below the threshold corresponding to the “OFF” state (0) of the system. In addition, two other possible input combinations as shown in the truth table exhibit the value of the output signals above the threshold energy level and thus corresponds to the “ON” state (1) of the system. Thus, by monitoring the emission maximum at 522 nm by the action of heat and photon, the function of an IMPLICATION gate can be mimicked at the molecular level. Fig. 5.33e shows the reversibility of the system upon alternative action of the two inputs (heat and photon). In absence of two inputs, the emission maximum at 522 nm lies above the threshold energy level indicating the “ON” state of the system. The stepwise interaction of “heat-photon-heat” give rise to the “ON-OFF-ON” state of the system and indicates one complete cycle of this reversible process. With increasing the number of cycles, the emission intensities of the “ON” state decreases and “OFF” state increases as simultaneous

interaction of heat (Input 1) or photon (Input 2) with the solution which was already treated with both the inputs cannot fully restored the original emission in the complex.

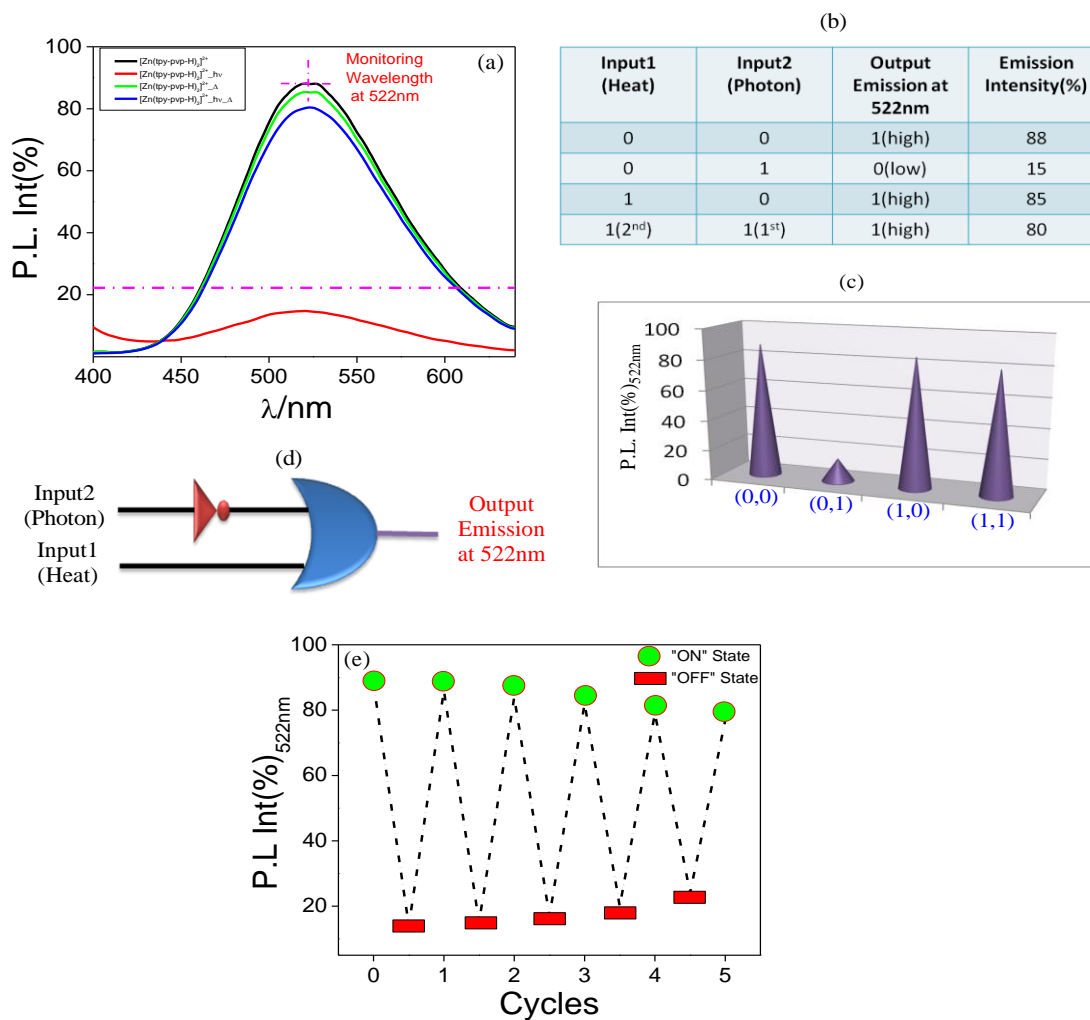


**Fig. 5.33.** (a) The emission ( $\lambda_{ex}=370$  nm) spectral change of **1** upon the action of heat (input 1) and photon (input 2). (b) Corresponding truth table. (c) 3D representation of the changes in emission intensities upon the action of different combinations of stimuli. (d) Schematic representation of an IMPLICATION gate based on the emission at 522 nm for **1** and (e) Diagram showing the reversibility of the system due to stepwise addition of heat and photon.

## 5.3.8 INHIBIT Gate

The term INHIBIT means the gate which produces a certain or fixed output whatever be the inputs or even the inputs are changed. An INHIBIT gate is basically an AND gate with an additional event. To construct an INHIBIT gate, we used the same two inputs (heat as input 1 and photon as input 2) and also used the emission maximum at 500 nm for complex **3** as the output signals (Fig. 5.34). The truth table in Fig. 5.34 indicates that in absence of either of the two inputs, **3** exhibits emission at 500 nm

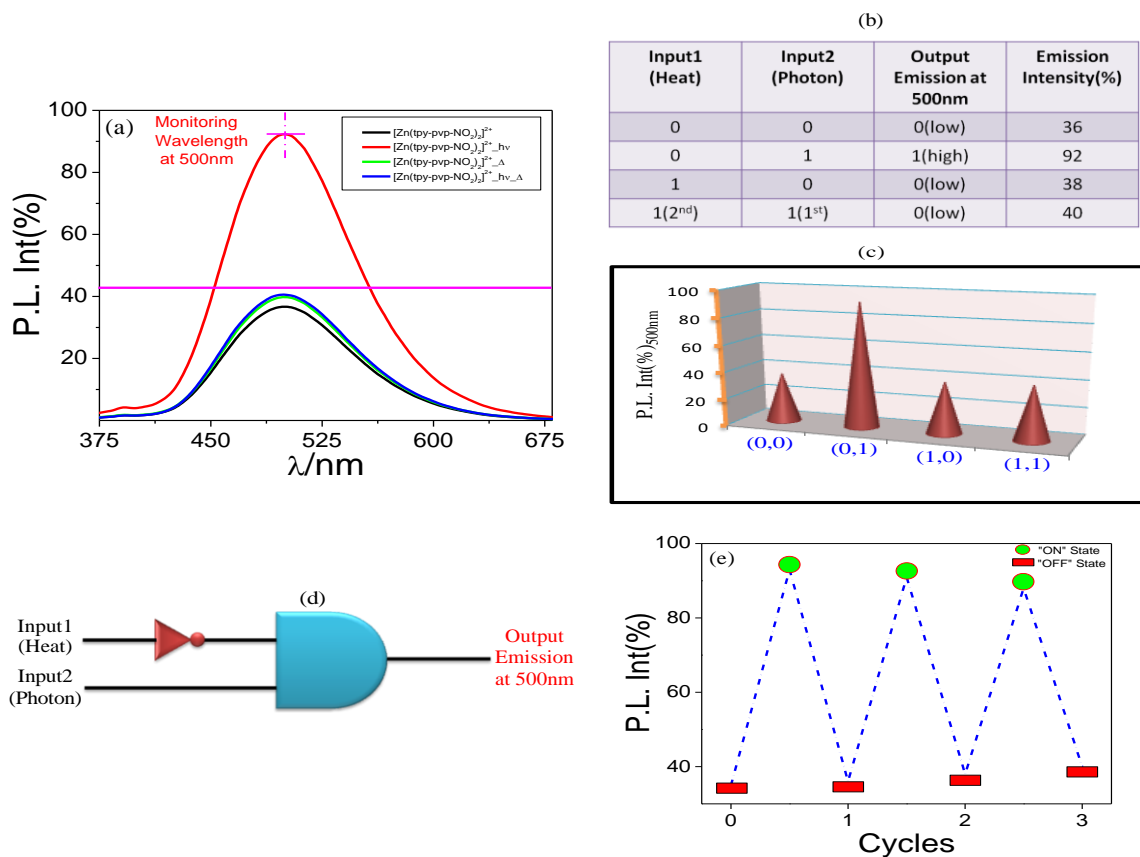


**Fig. 5.34.** (a) The emission ( $\lambda_{\text{ex}}=370$  nm) spectral changes of  $[\text{Zn}(\text{tpy-pvp-NO}_2)_2]^{2+}$  (**3**) upon the action of heat (input 1) and photon (input 2). (b) Corresponding truth table. (c) 3D representation of emission intensities which changes upon addition of different combinations of stimuli. (d) Schematic representation of an INHIBIT gate based on the emission at 500 nm for **3**. (e) Diagram showing the reversibility of the system due to stepwise addition of photon and heat.

which lies below the threshold energy level and corresponds to the “OFF” state (0) of the system. Input 2 (photon) induces substantial increase in emission intensity and corresponds to the “ON” state (1) of the system. In addition, two other possible input combinations also show the output signal below the threshold energy level indicating the “OFF” state (0) of the system. Thus, by monitoring the emission maximum at 500 nm upon the action of heat and photon inputs, an INHIBIT gate can be constructed. Fig. 5.34e shows the reversibility of the system upon alternative addition of the two inputs (heat and photon) can be repeated many times without appreciable loss of emission intensity.

### 5.4 Conclusions

With regard to our objective to design low-cost and easily synthesizable photo-switches, we reported in this work the synthesis, characterization, photophysics, and photo-isomerization behaviors of three Zn(II)-terpyridine complexes covalently tethered with stilbene moiety. The complexes exhibit absorption bands stretching up to the edge of the visible domain due to ligand- ligand charge transfer (LLCT) transition and strong emission at room temperature arising out from radiative deactivation of  $^3\text{LLCT}$  state having lifetime within 1.0-3.0 ns. The electron donating as well as electron withdrawing group was introduced in the complex backbone to modulate their spectral behaviors as well as the kinetic and thermodynamic aspects of the isomerization process. Taking advantage of stilbene moieties, the photo-isomerization studies of the complexes were carried out in three different solvents with both UV and visible light sources to tune the thermodynamic and kinetic aspects of the isomerization process. All the three complexes underwent *trans-trans* to *trans-cis* isomerization with substantial change in their absorption, emission and  $^1\text{H}$  NMR spectral profiles. The reversal from *trans-cis* to *trans-trans* isomerization also occurs, albeit very slowly, on keeping and can be accelerated upon heating. The  $k_{\text{iso}}$  as well as  $\Phi$  is found to be much higher in presence of visible light source in all solvents than that of UV light. The electronic nature of X imparts a dramatic influence on the emission characteristics of their Zn(II) complexes during isomerization process. In case of **1** and **2**, the emission quenching upon irradiation with 336 nm and 405 nm light sources and restoration of original emission upon heating at 40°C gives rise to “on-off” and “off-on” emission switching. By contrast, for **3**, emission enhancement upon

light irradiation followed by restoration of emission upon heating leads to “off-on” and “on-off” emission switching. Another important aspect of the present work is that the emission responses of the complexes as function of photonic and thermal inputs were successfully utilized to construct two-input IMPLICATION and INHIBIT logic gates. Thus, present Zn(II)-terpyridine complexes are quite useful for the fabrication of low-cost molecular photo-switches which in turn could be potential building blocks for information processing at the molecular level.

## 5.5 References

- [1] A. J. McConnell, C. S. Wood, P. P. Neelakandan, J. R. Nitschke, Stimuli-responsive metal-ligand assemblies, *Chem. Rev.* 115 (2015) 7729-7793.
- [2] S. Kobatake, S. Takami, H. Muto, T. Ishikawa, M. Irie, Rapid and reversible shape changes of molecular crystals on photoirradiation, *Nature*. 446 (2007) 778-781.
- [3] M. Kondo, M. Uchikawa, W. W. Zhang, K. Namiki, S. Kume, M. Murata, Y. Kobayashi, H. Nishihara, Protonation-induced cyclocondensation of 1-aryl ethynylantraquinones: expanding the  $\pi$  conjugation, *Angew. Chem. Int. Ed.* 46 (2007) 6271-6274.
- [4] Q. Li (Ed.), *Intelligent Stimuli-Responsive Materials*, John Wiley & Sons, Inc., Hoboken, Nj, 2013.
- [5] S. A. Rommel, D. U. Sorsche, M. Fleischmann, S. Rau, Optical sensing of anions via supramolecular recognition with biimidazole complexes, *Chem. Eur. J.* 23 (2017) 18101-18119.
- [6] S. Kume, H. Nishihara, Photochrome-coupled metal complexes: molecular processing of photon stimuli, *Dalton Trans.* (2008) 3260– 3271.
- [7] B. Valeur, *Molecular Fluorescence: Principles and Applications*; Wiley. 2002.
- [8] L. Prodi, F. Bolletta, M. Montalti, Luminescent chemosensors for transition metal ions, *Coord. Chem. Rev.* 205 (2000) 59-83.
- [9] K. Müllen, U. Scherf, *Organic light emitting devices-synthesis, properties and applications*, Wiley, 2006.

- [10] H. N. Kim, W. X. Ren, J. S. Kim, J. Yoon, Fluorescent and colorimetric sensors for detection of lead, cadmium, and mercury ions, *Chem. Soc. Rev.* 41 (2012) 3210-3244.
- [11] M. Irie, Diarylethenes for memories and switches, *Chem. Rev.* 100 (2000) 1685–1716.
- [12] B. L. Feringa, R. A. van Delden, M. K. J. ter Wiel, *Chiroptical molecular switches*; Wiley-VCH, 2001.
- [13] H. Tian, S. Yang, Recent progresses on diarylethene based photochromic switches, *Chem. Soc. Rev.* 33 (2004) 85–97.
- [14] S. Kawata, Y. Kawata, Three-dimensional optical data storage using photochromic materials, *Chem. Rev.* 100 (2000) 1777–1788.
- [15] H. Rau, H. Dürr, H.B. Laurent (Eds.), *Photochromism: Molecules and Systems*, Elsevier, Amsterdam, 1990, pp. 165–192.
- [16] K. Ichimura, S. K. Oh, M. Nakagawa, Light-driven motion of liquids on a photoresponsive surface, *Science*. 288 (2000) 1624–1626.
- [17] R. Sakamoto, S. Kume, H. Nishihara, Visible-light photochromism of triarylamine- or ferrocene-bound diethynylethenes that switches electronic communication between redox sites and luminescence, *Chem. Eur. J.* 14 (2008) 6978-6986.
- [18] D. H. Waldeck, Photoisomerization dynamics of stilbenes, *Chem. Rev.* 91 (1991) 415–436.
- [19] J. Bossert, C. Daniel, Trans-cis photoisomerization of the styrylpyridine ligand in  $[\text{Re}(\text{CO})_3(2,2'\text{-bipyridine})(\text{t-4-styrylpyridine})]^+$ : role of the metal-to-ligand charge transfer excited states, *Chem. Eur. J.* 12 (2006) 4835–4843.
- [20] D.M. Dattelbaum, M.K. Itokazu, N.Y.M. Iha, T.J. Meyer, Mechanism of metal-to ligand charge transfer sensitization of olefin trans-to-cis isomerization in the *fac*- $[\text{ReI}(\text{phen})(\text{CO})_3(1,2\text{-bpe})]^+$  cation, *J. Phys. Chem. A.* 107 (2003) 4092-4095.
- [21] S. S. Sun, A. J. Lees, Synthesis, photophysical properties, and photoinduced luminescence switching of trinuclear diimine rhenium(I) tricarbonyl complexes linked by an isomerizable stilbene-like ligand, *Organometallics*. 21 (2002) 39-49.

- 
- [22] V. W.-W. Yam, Y. Yang, J. Zhang, B. W.-K. Chu, N. Zhu, Synthesis, characterization, and photoisomerization studies of azo- and stilbene-containing surfactant rhenium(I) complexes, *Organometallics*, 20 (2001) 4911-4918.
- [23] Ko C.-C, V.W.-W. Yam, Coordination compounds with photochromic ligands: ready tunability and visible light-sensitized photochromism, *Acc. Chem. Res.* 51 (2018) 149-159.
- [24] M. Kurihara, H. Nishihara, Azo-and quinone-conjugated redox complexes photo- and proton-coupled intramolecular reactions based on d- $\pi$  interaction, *Coord. Chem. Rev.* 226 (2002) 125-135.
- [25] H. Nishihara, Multi-mode molecular switching properties and functions of azo-conjugated metal complexes, *Chem. Soc. Jpn.* 77 (2004) 407-428.
- [26] H. Nishihara, Y.F. Kodansha (Ed.), *Inorganic Photochromism*, Springer, 2007, pp. 239-257.
- [27] S. Kume, H. Nishihara, Metal-based photoswitches derived from photoisomerization, *Struct. bonding (Berlin, Ger.)*. 123 (2006) 79-112.
- [28] C.-C. Ko, V. W.-W. Yam, Transition metal complexes with photochromic ligands-photosensitization and photoswitchable properties, *J. Mater. Chem.* 20 (2010) 2063-2070.
- [29] C.-C. Ko, L.-X. Wu, K. M.-C. Wong, N. Zhu, V. W.-W. Yam, Synthesis, characterization and photochromic studies of spirooxazine- containing 2,2'-bipyridine ligands and their Rhenium(I) tricarbonyl complexes, *Chem.-Eur. J.* 10 (2004) 766-776.
- [30] P. Pal, S. Mukherjee, D. Maity, S. Baitalik, Synthesis, structural characterization, and luminescence switching of diarylethene-conjugated Ru(II)-terpyridine complexes by trans-cis photoisomerization: experimental and DFT/TD-DFT investigation, *Inorg. Chem.* 57 (2018) 5743-5753.
- [31] P. Pal, S. Mukherjee, D. Maity, S. Baitalik, Synthesis, Photophysics, and switchable luminescence properties of a new class of ruthenium(II)-terpyridine complexes containing photoisomerizable styrylbenzene units, *ACS Omega.* 3 (2018) 14526-14537.

- [32] P. Pal, T. Ganguly, D. Maity, S. Baitalik, Experimental and theoretical exploration of photophysics and trans-cis photoisomerization of styrylbenzene conjugated terpyridine complexes of Ru(II): strong effect of deprotonation from second coordination sphere, *J. Photochem. Photobiol. A.* 392 (2020) 112409.
- [33] P. Pal, T. Ganguly, A. Sahoo, S. Baitalik, Emission switching in the near-infrared by reversible trans-cis photoisomerization of styrylbenzene-conjugated osmium terpyridine complexes, *Inorganic Chemistry.* 60 (2021) 4869-4882.
- [34] E. C. Constable, 2,2':6',20''-Terpyridines: From chemical obscurity to common supramolecular motifs, *Chem. Soc. Rev.* 33 (2007) 246-253.
- [35] H. Hofmeier, U. S. Schubert, Recent developments in the supramolecular chemistry of terpyridine-metal complexes, *Chem. Soc. Rev.* 33 (2004) 373-399.
- [36] E. Baranoff, J. P. Collin, L. Flamigni, J.-P. Sauvage, From ruthenium(ii) to iridium(iii): 15 years of triads based on bis-terpyridine complexes, *Chem. Soc. Rev.* 33 (2004) 147.
- [37] X. Wang, A. Guerzo, S. Baitalik, G. Simon, G. B. Shaw, L. Chen, R. H. Schmehl, The influence of bridging ligand electronic structure on the photophysical properties of noble metal diimine and triimine light harvesting systems, *Photosynth. Res.* 87 (2006) 83-103.
- [38] A. Breivogel, C. Kreitner, K. Heinze, Redox and photochemistry of bis(terpyridine) ruthenium(II) amino acids and their amide conjugates-from understanding to applications, *Eur. J. Inorg. Chem.* (2014) 5468-5490.
- [39] A. Harriman R. Ziessel, Making photoactive, molecular-scale wires, *Chem. Commun.* (1996) 1707-1716.
- [40] E. A. Medlycott, G. S. Hanan, Synthesis and properties of mono- and oligo-nuclear Ru(II) complexes of tridentate ligands: the quest for long-lived excited states at room temperature, *Coord. Chem. Rev.* 250 (2006) 1763.
- [41] E. A. Medlycott, G. S. Hanan, Designing tridentate ligands for ruthenium(ii) complexes with prolonged room temperature luminescence lifetimes, *Chem. Soc. Rev.* 34 (2005) 133.



- [42] X. Chen, Q. Zhou, Y. Cheng, Y. Geng, D. Ma, Z. Xie, L. Wang, Synthesis, structure and luminescence properties of zinc (II) complexes with terpyridine derivatives as ligands, *Journal of Luminescence*. 126 (2007) 81–90.
- [43] F. Tessore, D. Roberto, R. Ugo, M. Pizzotti, Terpyridine Zn(II), Ru(III), and Ir(III) Complexes: The relevant role of the nature of the metal ion and of the ancillary ligands on the second-order nonlinear response of terpyridines carrying electron donor or electron acceptor groups, *Inorg. Chem.* 44 (2005) 8967-8978.
- [44] T. Tsukamoto, K. Takada, R. Sakamoto, R. Matsuoka, R. Toyoda, H. Maeda, T. Yagi, M. Nishikawa, N. Shinjo, S. Amano, T. Iokawa, N. Ishibashi, T. Oi, K. Kanayama, R. Kinugawa, Y. Koda, T. Komura, S. Nakajima, R. Fukuyama, N. Fuse, M. Mizui, M. Miyasaki, Y. Yamashita, K. Yamada, W. Zhang, R. Han, W. Liu, T. Tsubomura, H. Nishihara, Coordination nanosheets based on terpyridine–zinc(II) complexes: as photoactive host materials, *J. Am. Chem. Soc.* 139 (2017) 5359–5366.
- [45] T. Tsukamoto, R. Aoki, R. Sakamoto, R. Toyoda, M. Shimada, Y. Hattori, Y. Kitagawa, E. Nishibori, M. Nakano, H. Nishihara, . Mechano-, thermo-, solvato-, and vapochromism in bis(acetato- $k^1O$ )[4'-(4-(diphenylamino)phenyl)]- 2,2':6',2''-terpyridine- $k^3N,N',N''$ )zinc(II) and its polymer, *Chem. Commun.* 53 (2017) 9805-9808.
- [46] R.C. Amaral, L.S. Matos, K.P.S. Zanoni, N.Y.M. Iha, Photoreversible molecular motion of stpyCN coordinated to fac-[Re(CO)<sub>3</sub>(NN)]<sup>+</sup> complexes, *J. Phys. Chem. A*. 122 (2018) 6071-6080.
- [47] A. S. Polo, M. K. Itokazu, K. M. Frin, A. O. T. Patrocínio, N. Y. M. Iha, Light driven *trans*-to-*cis* isomerization of stilbene-like ligands in fac-[Re(CO)<sub>3</sub>(NN)(*trans*-L)]<sup>+</sup> and luminescence of their photoproducts, *Coord. Chem. Rev.* 250 (2006) 1669-1680.
- [48] L. A. Faustino, A. E. H. Machado, A. O. T. Patrocínio, Photochemistry of fac-[Re(CO)<sub>3</sub>(dcbH<sub>2</sub>)(*trans*-stpy)]<sup>+</sup>: new insights on the isomerization mechanism of coordinated stilbene-like ligands, *Inorg. Chem.* 57 (2018) 2933-2941.

- [49] J. L. Lin, C. W. Chen, S. S. Sun, A. J. Lees, Photoswitching tetranuclear rhenium(I) tricarbonyl diimine complexes with a stilbene-like bridging ligand, *Chem. Comm.* 47 (2011) 6030-6032.
- [50] M. S. Wrighton, D. L. Morse, L. Pdungsap, Intraligand lowest excited states in tricarbonylhalobis(styrylpyridine)rhenium(I) complexes, *J. Am. Chem. Soc.* 97 (1975) 2073-2079.
- [51] V. W. W. Yam, V. C. Y. Lau, L. X. Wu, Synthesis, photophysical, photochemical and electrochemical properties of rhenium(I) diimine complexes with photoisomerizable pyridyl-azo, -ethenyl or -ethyl ligands, *J. Chem. Soc. Dalton Trans.* (1998) 1461-1468.
- [52] L. S. Matos, R. C. Amaral, N. Y. M. Iha, Visible photosensitization of trans-styrylpyridine coordinated to fac-[Re(CO)<sub>3</sub>(dcbH<sub>2</sub>)]<sup>+</sup>: New insights, *Inorg. Chem.* 57 (2018) 9316-9326.
- [53] A. O. T. Patrocinio, N. Y. M. Iha, Photoswitches and luminescent rigidity sensors based on fac-[Re(CO)<sub>3</sub>(Me<sub>4</sub>phen)(L)]<sup>+</sup>, *Inorg. Chem.* 47 (2008) 10851-10857.
- [54] A. J. Vlcek, M. Busby, Ultrafast ligand-to-ligand electron and energy transfer in the complexes fac-[ReI(L)(CO)<sub>3</sub>(bpy)]<sup>n+</sup>, *Coord. Chem. Rev.* 250 (2006) 1755-1762.
- [55] M. Kayanuma, C. Daniel, H. Koppel, E. Gindensperger, Photophysics of isomerizable Re(I) complexes: A theoretical analysis, *Coord. Chem. Rev.* 255 (2011) 2693-2703.
- [56] O. S. Wenger, L. M. Henling, Winkler, M. W. Jay R. Day, H. B. Gray, Photoswitchable luminescence of rhenium(I) tricarbonyl diimines, *Inorg. Chem.* 43 (2004) 2043-2048.
- [57] T. Yutaka, I. Mori, M. Kurihara, N. Tamai, H. Nishihara, Photochemical behavior of azobenzene-conjugated Co<sup>II</sup>, Co<sup>III</sup>, and Fe<sup>II</sup> bis(terpyridine) complexes, *Inorg. Chem.* 42 (2003) 6306-6313.
- [58] Y. Hasegawa, K. Takahashi, S. Kume, H. Nishihara, Complete solid state photoisomerization of bis(dipyrazolylstyrylpyridine)iron(II) to change magnetic properties, *Chem. Commun.* 47 (2011) 6846-6848.

- [59] S. Mukherjee, P. Pal, A. Sahoo, S. Baitalik, Photo-switchable iron-terpyridine complexes functionalized with styrylbenzene unit, *J. Photochem. Photobiol. A*. 407 (2021) 113059.
- [60] Q. Zhang, X. Tian, Z. Hu, C. Brommesson, J. Wu, H. Zhou, S. Li, J. Yang, Z. Sun, Y. Tian, K. Uvdal, A series of Zn(II) terpyridine complexes with enhanced two-photon-excited fluorescence for *in vitro* and *in vivo* bioimaging, *J. Mater. Chem. B*. 3 (2015) 7213-7221.
- [61] Y. Tang, M. Kong, X. Tian, J. Wang, Q. Xie, A. Wang, Q. Zhang, H. Zhou, J. Wu, Y. Tian, A series of terpyridine-based zinc(II) complexes assembled for third-order nonlinear optical responses in the near-infrared region and recognizing lipid membranes, *J. Mater. Chem. B*. 5 (2017) 6348-6355.
- [62] A. P. De Silva, H.Q.N. Gunaratne, C.P. McCoy, A molecular photoionic AND gate based on fluorescent signaling, *Nature*. 364 (1993) 42-44.
- [63] A. P. De Silva, D. P. Fox, A. J. M. Huxley, T. S. Moody, Combining luminescence, coordination and electron transfer for signaling purposes, *Coord. Chem. Rev.* 205 (2000) 41-57.
- [64] E. Katz. Molecular and supramolecular information processing: from molecular switches to logic system, Wiley-VCH Weinheim, Germany, 2012.
- [65] R. Guliyev, S. Ozturk, Z. Kostereli, E. U. Akkaya, From virtual to physical: integration of chemical logic gates, *Angew. Chem Int. Ed.* 50 (2011) 9826-9831.
- [66] S. Karmakar, S. Mardanya, S. Das, S. Baitalik, Efficient deep-blue emitter and molecular-scale memory device based on dipyrityl-phenylimidazole-terpyridine assembly, *J. Phys. Chem. C*. 119 (2015) 6793-6805.
- [67] S. Mukherjee, P. Pal, D. Maity, S. Baitalik, Photophysics and luminescence switching properties of a series of photochromic styrylbenzene-terpyridine conjugate: Experimental and DFT/ TD-DFT investigation, *J. Photochem. Photobiol. A*. 378 (2019) 94-104.
- [68] T. Yutaka, I. Mori, M. Kurihara, J. Mizutani, K. Kubo, S. Furusho, K. Matsumura, N. Tamai, H. Nishihara, Synthesis, characterization, and photochemical properties of azobenzene-conjugated Ru(II) and Rh(III) bis(terpyridine) complexes, *Inorg. Chem.* 40 (2001) 4986-4995.

- [69] S. Sinha, S. Mandal, P. Gupta, Cyclometalated iridium(III) complexes of (aryl)ethenyl functionalized 2,2'-bipyridine: synthesis, photophysical properties and *trans–cis* isomerization behavior, RSC Adv. 5 (2015) 99529-99539.
- [70] F. Nisic, A. Colombo, C. Dragonetti, D. Roberto, A. Valore, J. M. Malicka, M. Cocchi, G. R. Freemane, J. A. G. Williams, Platinum(ii) complexes with cyclometallated 5- $\pi$ -delocalized-donor-1,3-di(2-pyridyl)benzene ligands as efficient phosphors for NIR-OLEDs, J. Mater. Chem. C. 2 (2014) 1791-1800.

\*\*\*\*

## ***Chapter 6***

**Light and cation driven optical switch based  
on a stilbene appended terpyridine system  
for the design of molecular-scale  
logic devices**

## 6.1 Introduction

Information processing and computation at the molecular level has been developing rapidly since the first realization of the principles of storing logical states at the molecular level by de Silva [1-6]. During last two decades, a wide range of molecular and supramolecular systems have been fabricated to strengthen this relatively young field of chemistry [7-18]. Information processing in computers is based on the principles of Boolean algebra and logic gates implement binary arithmetic and logical functions [19-21]. Molecular level computation is thus feasible only with systems which are efficient to integrate simple logic gates into various connective circuits [9,22-25]. In addition, molecular based logic could give rise to smaller and more faster and proficient devices compared with conventional silicon-based circuitries.

Although significant efforts have been given to design molecular systems which are effective of mimicking the actions of different fundamental logic gates together with high order functions, but smart functional systems which have the potentiality to mimic the complicated logic operations as necessitated in various circuits, molecular keypad locks [26-33], half-adder/subtractor [34-36], multiplexer/demultiplexer/exciple [37-39] and memory devices [10,40-48] are relatively less in the literature. Thus, there remains space to tailor design of smart molecules which on interaction with different external stimuli can give rise to multiple optical channels which in turn can perform sequential as well as complicated logic functions. During working last few years in this particular field, we realized that receptors with distinct ion binding sites may be potential candidates for designing complicated logic gates since the optical properties of these receptors can be substantially altered by appropriate combination of different ionic inputs [49-55]. In this work, we have utilized one of our recently reported terpyridine-based receptor, (2-(6-(pyridin-2-yl)-4-(4styrylphenyl)pyridin-2-yl)pyridine (tpy-pvp-H), wherein a terpyridine coordinating motif is covalently coupled with a stilbene unit at its 4'-position for the fabrication of multifunctional logic system (Chart 6.1) [56]. In the design strategy of the ligand, apart from incorporating terpyridine site for binding with cations, an stilbene moiety has also been incorporated which is prone to undergo *trans-cis* isomerization on light irradiation. Although stilbene derivative constitute a very useful group of photo-responsive compounds and one of the well-studied *trans-cis* isomerization systems [57-60],

but the system incorporating ethylenic double bond into the well known and versatile terpyridine coordinating units have never been used for mimicking complicated logic function with regard to computation at the molecular level.

Incorporation of a stilbene unit into the terpyridyl chelating motif also leads to generation of intra-ligand charge transfer (ICT)-sensitive photo-switchable chromophoric and fluorophoric receptor. Thus, the present system can act as bifunctional receptor whose optical properties such absorption, emission, and lifetime could be significantly tuned by light of specified wavelength as well as selected cationic guests. In the present study, based on response profiles of the receptor toward selected cations (such as  $\text{Fe}^{2+}$  and  $\text{Zn}^{2+}$ ) as well as light of specific wavelength, we are able to successfully demonstrate multiple Boolean logic functions such as INHIBIT, IMPLICATION, OR, NOR and NAND as well as various combinations of them. Moreover, we utilized the present compound for the design of a molecular level keypad lock by maintaining proper sequence of inputs ( $\text{Zn}^{2+}$  and light) and monitoring the emission output signal of the receptor. A keypad lock is able to generate a secret password which provides a secure way to protect information [26-33]. In addition, we are also able to construct a memory device which can display Set-Reset (S-R logic) logic operation showing “write–read–erase–read” like reversible and reconfigurable functions at molecular level [44-48].

The operation in Boolean logic systems is based on switching of the output response among the two extreme domains, viz. "0" or "1". But in reality, the presence of some intermediate states in between "0" and "1" are evident in majority of the systems. The fuzzy logic system (FLS) is believed to become a probable substitute of the Boolean logic to identify the in-between states [61-65]. The inspiration in implementing FLS is rest on the perception that human thinking and decision taking mechanism is too complicated to be accurately expressed and believed to operate as an automatic fine-controlling administer which deals with several intermediate steps with varied order of truths. FLS is composed of non-linear scaling of the input data vectors into the scalar outputs. Significant emphasis is currently been given to prosper artificial intelligence with vague and imprecise inputs. In reality, only a limited number of FLS have been reported to date [66-69]. In the present paper, we also implemented fuzzy logic for generating an infinite-valued logic

scheme based on the emission spectral response of the receptor as a function of selected cations ( $\text{Fe}^{2+}$  and/or  $\text{Zn}^{2+}$ ) and anion ( $\text{CN}^-$ ).

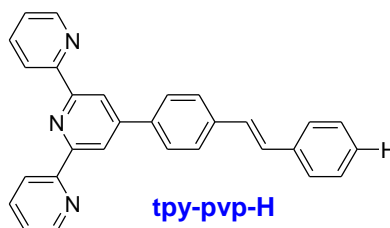


**Chart 6.1.** Chemical structure of the stilbene-appended terpyridine receptor.

## 6.2 Materials and methods

The materials that are employed to synthesize the ligand are described in [chapter 2](#). The description of instruments and physico-chemical measurements are provided in previous chapters.

## 6.3 Results and discussion

### 6.3.1 Synthesis, characterization and overview of photoisomerization and complexation-decomplexation process

Synthesis, characterization, and photo-isomerization behavior of stilbene-terpyridine ligand (tpy-pvp-H) and its Fe(II) complex of the type  $[\text{Fe}(\text{tpy-pvp-H})_2]^{2+}$  have been reported in [chapter 2](#) and [chapter 3](#). An overview of the photophysical, photoisomerization and ion-binding behavior of tpy-pvp-H is again presented here for the benefit of the readers. Tpy-pvp-H exhibits intense absorption band at 330 and 288 nm in DCM primarily due to styrylbenzene $\rightarrow$ terpyridine intra ligand charge transfer transition (ILCT) and  $\pi$ - $\pi^*$  transition, respectively and a strong emission band at 398 nm with quantum yield 0.33 and lifetime 1.05 ns [56]. The absorption and emission maximum of the ligand differs to a little stretch depending upon the nature of the solvent. The ligand undergoes *trans-cis* isomerization induced by UV light accompanied with substantial alteration of absorption and emission spectral behaviors ([Fig. 6.1](#)) [56]. The intensity of the band at 330 nm gradually decreases together with a little bathochromic-shift and at its expense a broad tail stretching within the range of 360-420 nm evolved, gradually intensified and finally saturated upon photolysis of ~22 minutes. Quenching of emission



together with red-shift of the emission band is observed upon photolysis. The backward *cis*→*trans* isomerization is also feasible upon irradiation with visible light ( $\lambda_{\text{ex}}=400$  nm) and the initial spectrum get almost restored in the reverse process.

Due to the presence of terpyridine site, the ligand is capable to interact with metal ions through coordination. The absorption and emission spectrum profile of *trans* tpy-pvp-H upon gradual addition of  $\text{Fe}^{2+}$  and  $\text{Zn}^{2+}$  ions are presented in Fig. 6.2 and Fig. 6.3.  $\text{Fe}^{2+}$  leads to the generation of a peak at ~575 nm with development of brilliant violet color assignable as  $\text{Fe}(\text{d})\rightarrow\text{tpy}(\pi^*)$  MLCT transition, while  $\text{Zn}^{2+}$  induces generation of a band at 380 nm due to intra-ligand charge transfer from stilbene to the coordinated terpyridine moiety [70]. Systematic change in the spectral profile of tpy-pvp-X as a function of  $\text{Fe}^{2+}$  and  $\text{Zn}^{2+}$  ions are presented in Fig. 6.2 and Fig. 6.3, respectively.

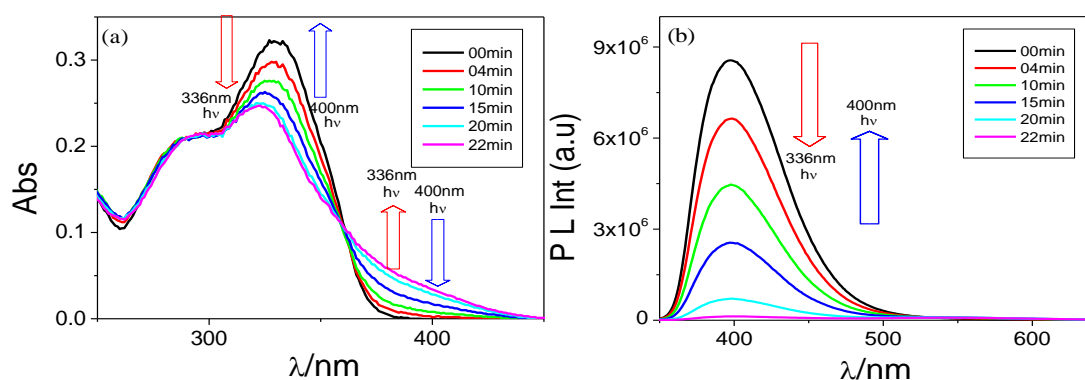


**Fig. 6.1.** UV-vis absorption (a) and emission ( $\lambda_{\text{ex}}=330$  nm) (b) spectrum of tpy-pvp-H in DCM upon irradiation of UV ( $\lambda_{\text{max}}=336$  nm) followed by visible ( $\lambda_{\text{max}}=400$  nm) light.

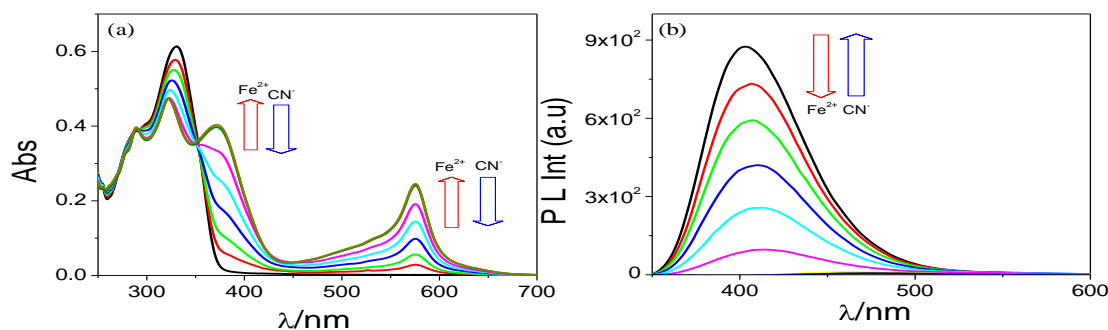


**Fig. 6.2.** UV-vis absorption (a) and emission ( $\lambda_{\text{ex}}=330$  nm) (b) spectrum of tpy-pvp-H in DCM upon incremental addition of  $\text{Fe}^{2+}$  followed by  $\text{CN}^-$ .

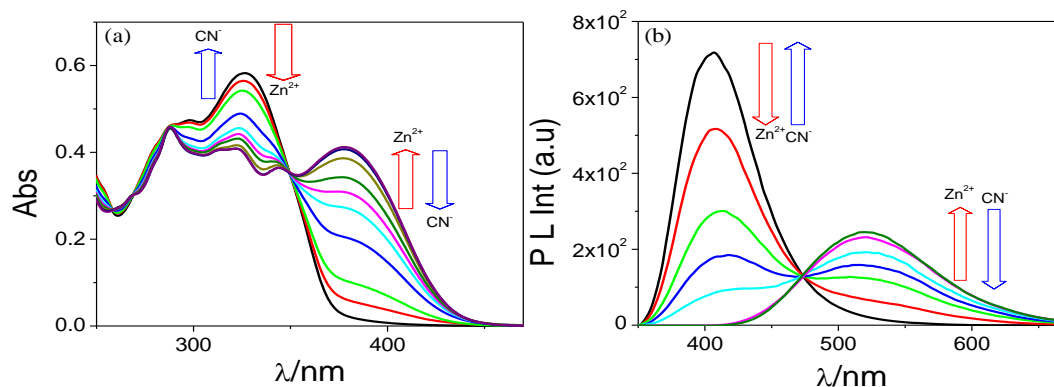


**Fig. 6.3.** UV-vis absorption (a) and emission ( $\lambda_{\text{ex}}=330$  nm) (b) spectrum of tpy-pvp-H in DCM upon incremental addition of  $\text{Zn}^{2+}$  followed by  $\text{CN}^-$ .

Considerable quenching of emission was observed in both cases, but in case of  $\text{Zn}^{2+}$ , gradual quenching of emission at 398 nm is also accompanied by an emission augmentation at 512 nm. The saturation of both absorption and emission spectrum takes place after inclusion of 0.5 equivalent of ions indicating the generation of  $[\text{M}(\text{tpy-pvp-H})_2]^{2+}$  species. It is to be mentioned here that the *cis* form of tpy-pvp-H cannot form bis-terpyridine ( $[\text{M}(\text{tpy-pvp-H})_2]^{2+}$ ) type complexes upon addition of the respective metal ions probably because of the strain that is developed in the *cis*-isomer does not allow to convert the *transoid* conformation of the three nitrogen atoms of the terpyridine motif to the *cisoid* form which is necessary to coordinate with the bivalent 3d metals. We would also like to point out that upon excitation at the MLCT band at 575 nm, the Fe(II) complex ( $[\text{Fe}(\text{tpy-pvp-H})_2]^{2+}$ ) does not display any emission band in the red region because of the existence of low-lying metal-centered ( $^3/5\text{MC}$ ) excited states.

Interestingly, addition of  $\text{CN}^-$  leads to the de-complexation of both Fe(II) and Zn(II) complexes and eventually regenerates the free ligand in presence of excess  $\text{CN}^-$ . The decomplexation process has also been monitored through absorption and emission spectroscopic techniques. The titration data clearly indicate that addition of  $\text{CN}^-$  prompts sequestering of the metal ions ( $\text{Fe}^{2+}$  and  $\text{Zn}^{2+}$  ions) from the respective complex and produces more steady ion-pair or complex cation of the type  $[\text{Fe}(\text{CN})_6]^{4-}$  and  $\text{Zn}(\text{CN})_4^{4-}$  in solution leading to regeneration of the free ligand. Moreover, complexation of the receptor by the said metals and their decomplexation by  $\text{CN}^-$  is reversible and can be repeated many times. This reversible complexation and decomplexation behavior together with reversible

*trans-cis* photo-isomerization aspect of the ligand will be utilized for the construction of various logic gates and complicated circuits. Importantly, tpy-pvp-H is capable to mimic several fundamental as well as complicated logic functions by monitoring the output absorption and emission spectral responses upon sequential use of appropriate combination of the ionic inputs ( $\text{Fe}^{2+}$  and  $\text{Zn}^{2+}$ ) and light of specific wavelength.

### 6.3.2 Key-pad lock

Key pad lock device is used mainly for the security purpose at the molecular level. In order to develop a security key pad lock, the emission intensity at 525 nm of tpy-pvp-H is used as the output signal in presence of two stimuli, viz.  $\text{Zn}^{2+}$  and light of  $\lambda_{\text{ex}} = 336$  nm (photon), in appropriate sequence. In Fig. 6.4, the input  $\text{Zn}^{2+}$  is assigned as “R”, whereas the input photon ( $\lambda_{\text{ex}} = 336$  nm) is assigned as “A”. On the other hand, “T” and

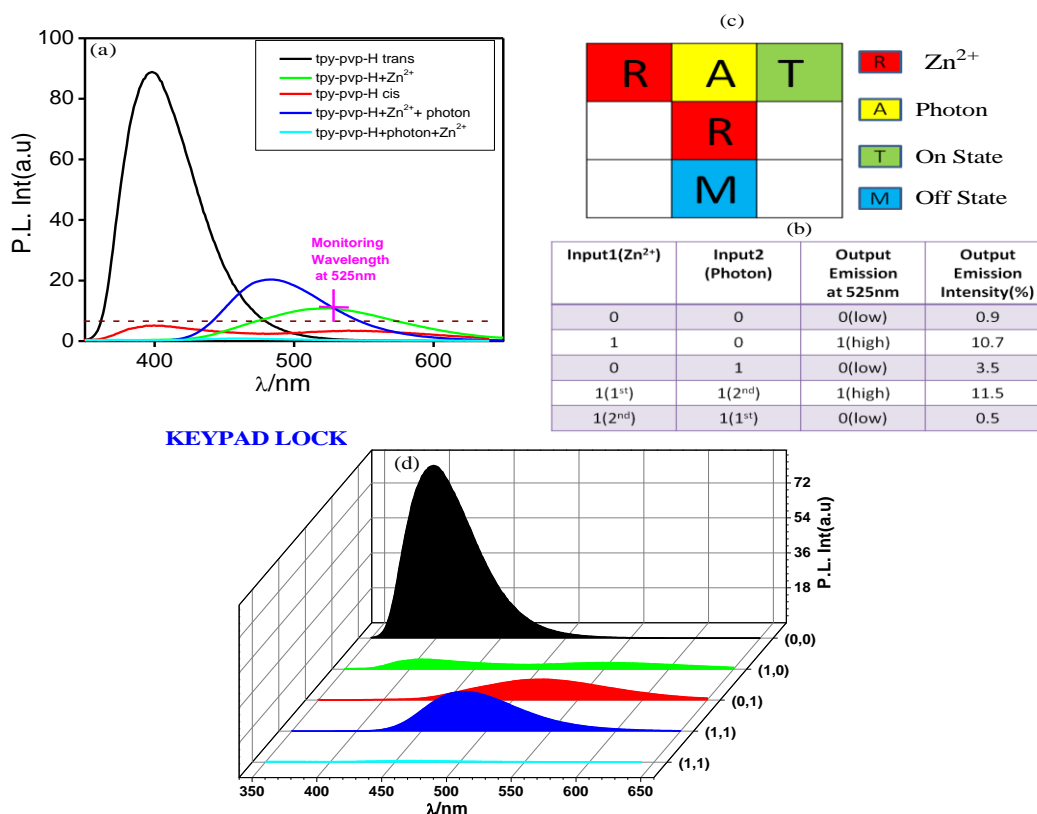


**Fig. 6.4.** (a) Emission spectral changes of tpy-pvp-H upon interaction with  $\text{Zn}^{2+}$  (0.5 equiv) and photon. Truth table and schematic presentation for the security keypad lock (b and c, respectively). (d) 3d presentation for the change in emission intensity as function of inputs.

“**M**” implies the “ON-state” and “OFF-state”, respectively. In absence of both the inputs, there is no emission at 525 nm implying the “OFF-state”. Addition of “**R**” followed by interaction with “**A**” induces a considerable increase in emission intensity at the said wavelength indicating the “ON-state” and generates a secret password “**RAT**”. Alteration of this sequence (“**A**” followed by “**R**”) leads to sharp fall of emission below the threshold level which designates the “OFF-state” resulting in the generation of password “**ARM**”. Thus, the wrong password “**ARM**” will not be able to unlock the keypad lock. Therefore, to construct a keypad lock at the molecular level the sequence dependent stimuli play a very crucial role. Thus, only the legalized user can unlock this system and it is a novel way to secure the information at the molecular level and superior over conventional number-based PIN.

### 6.3.3 Combination of IMPLICATION and INHIBIT logic gates

To mimic the said logic functions,  $\text{Zn}^{+2}$  and  $\text{CN}^-$  is utilized as two different ionic inputs, while the emission intensity at either 512 or 398 nm of *tpy-pvp-H* was utilized as the output signal. Inclusion of  $\text{Zn}^{+2}$  induces significant augmentation of the emission at 512 nm, while almost complete quenching at 398 nm. Sequential inclusion of  $\text{Zn}^{+2}$  followed by  $\text{CN}^-$  gives rise to turn-off of the emission at 512 nm, whereas turn-on at 398 nm (Fig. 6.5). Thus, by maintaining appropriate sequence of the addition of  $\text{Zn}^{+2}$  (input 1) and  $\text{CN}^-$  (input 2) and utilizing the emission intensity at 512 nm and 398 nm, it is possible to mimic the combined operations of INHIBIT and IMPLICATION gates. The emission over the threshold barrier relates to the ON-state (1), whereas the low emission beneath the threshold relates to OFF-state (0). In absence of both the inputs, the output at 512 nm is low showing the OFF-state (0). IMPLICATION logic gate can also be constructed by using the same stimuli and observing the output emission signal at 398 nm. Without any inputs, the free receptor displays high emission at 398 nm and relates to the ON-state (1). Input 1 prompts quenching of emission and accordingly relates to the OFF-state (0). The inclusion of either input 2 or input 1 followed by input 2 prompts to enhance the signal at 398 nm and again suggests the ON-state (1). In essence, the function of IMPLICATION logic gate is mimicked (Fig. 6.5).

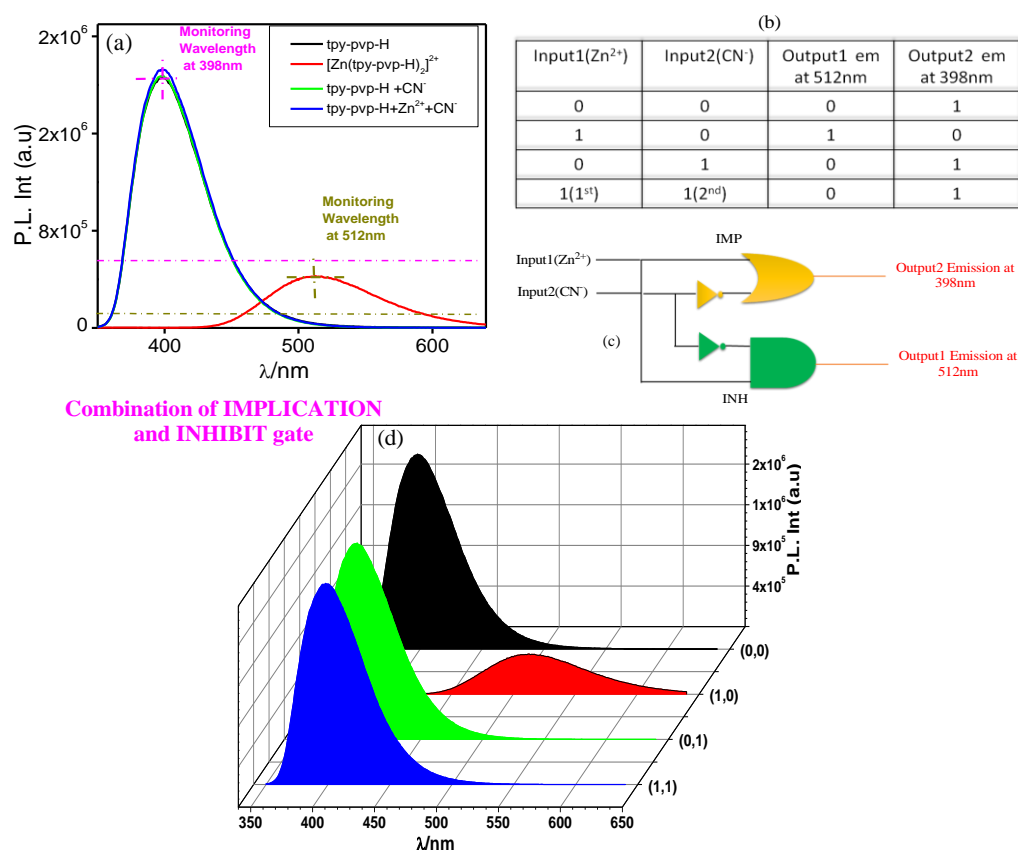


**Fig. 6.5.** (a) Emission spectral changes of tpy-pvp-H upon interaction with  $\text{Zn}^{2+}$  (0.5 equiv) and  $\text{CN}^-$ . Truth table and schematic presentation for combined IMPLICATION and INHIBIT gates (b and c, respectively). (d) 3d presentation for the change in emission intensity as function of inputs.

## 6.3.4 Construction of set-reset flip-flop circuit (memory devices)

From the previous section, it appears that INHIBIT and IMPLICATION logic gates are complementary to each other and comparable to IF-THEN and NOT functions. The memory device, useful for storing information, could be fabricated by performing sequential logic operations. The operation of a memory device occurs via a feedback loop where one of the outputs also functions as the input and is memorized as “memory element”. Here, we can fabricate sequential logic circuit, “Write-Read-Erase-Read” by utilizing the emission output signal at 512 nm for tpy-pvp-H upon the action of  $\text{Zn}^{2+}$  (input 1) and  $\text{CN}^-$  (input 2).

In the present case, input 1 and input 2 also corresponds to Set (S) and Reset (R) process, respectively and emission intensity at 512 nm above threshold represents the ON-state (1), whereas below the threshold designates the OFF-state (0). At high concentration of Set input ( $S=1$ ), the system writes and memorizes the binary state “1”. The stored data then can be erased upon the action of the Reset input giving rise to OFF-state. The Set/Reset events could be represented in the mould of a feedback loop as presented in Fig. 6.6 and the loop can be repeated multiple times.

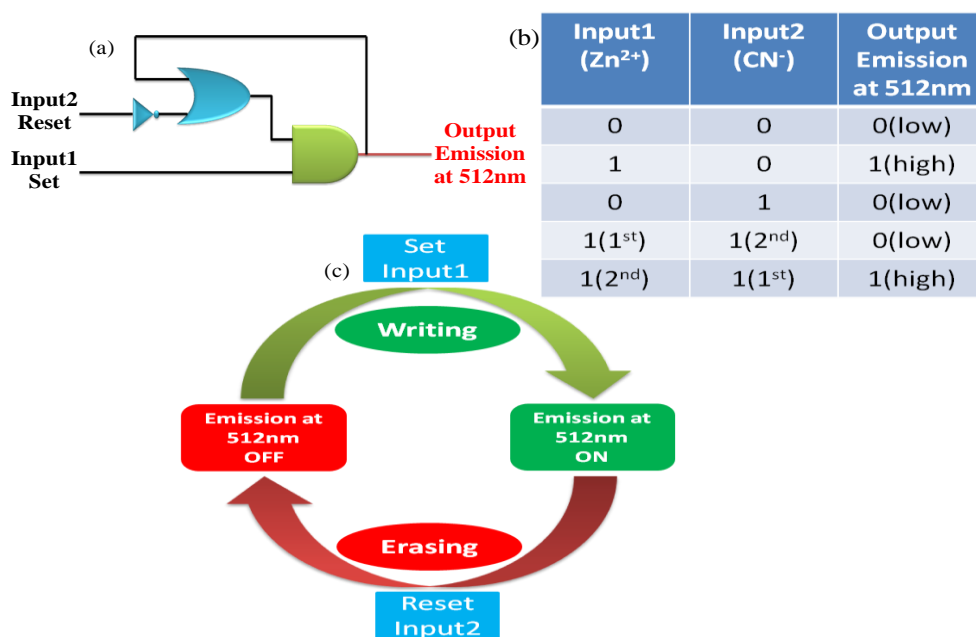


**Fig. 6.6.** (a) Schematic presentation of reversible and reconfigurable set-reset flip-flop logic functions of the memory element with “writing-reading-erasing-reading” sort of performance (a and c). Corresponding truth table is presented in (b).

### 6.3.5 Combination of NOR and INHIBIT logic gates

To mimic the said logic functions, light of  $\lambda_{ex}= 336$  nm is used as input 1, while the  $Zn^{+2}$  ion acts the input 2. The emission intensity at 522 nm and 409 nm of tpy-pvp-H in acetonitrile is taken as the output signal. Under UV light irradiation, the emission intensity at 409 nm is quenched substantially below the threshold representing the OFF-state (0). Addition of  $Zn^{+2}$  gives rise to the evolution and intensification of the emission band at 522 nm (ON-state) while substantial quenching of the emission band at 409 nm

(OFF-state) (Fig. 6.7). Upon addition of  $\text{Zn}^{2+}$  to the photo-irradiated solution of tpy-pvp-H, no change takes place in its emission spectrum and the emission intensity at both 409 and 522 nm lies below the threshold and thus represents the OFF-state. Thus, by the use of appropriate sequence of action of these selected stimuli, a function of the combined NOR and INHIBIT logic gates could be mimicked (Fig. 6.7).

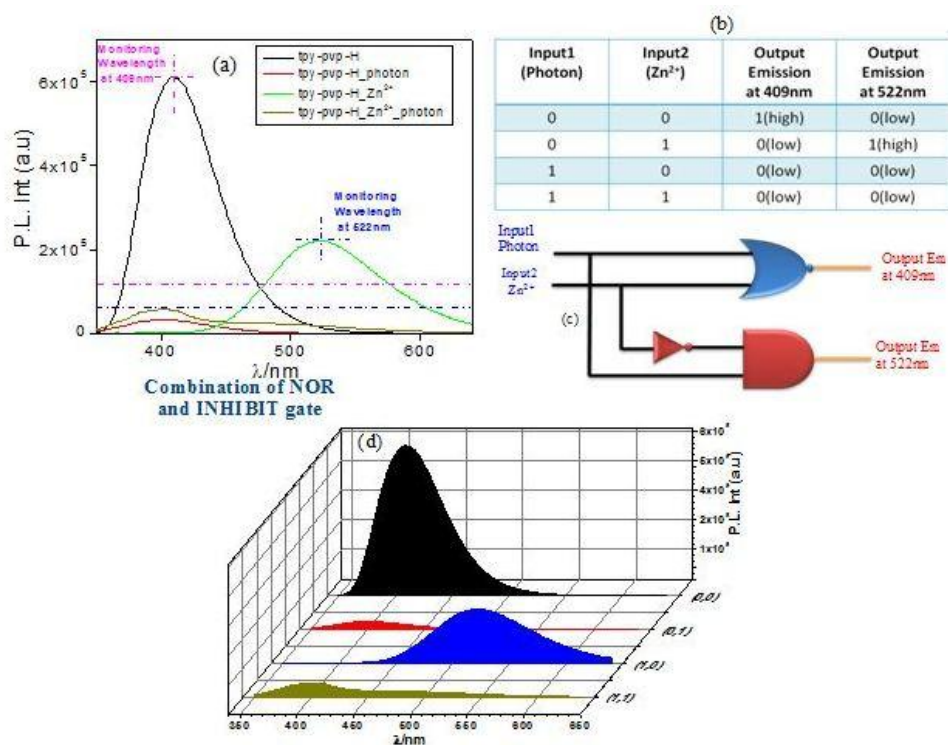


**Fig. 6.7.** (a) Emission spectral changes of tpy-pvp-H in MeCN at 409 nm and 522 nm in presence of photon and  $\text{Zn}^{2+}$  (0.5 equiv). Truth table and schematic presentation for combined NOR and INHIBIT gate (b and c, respectively). (d) 3d presentation for the change in emission intensity as function of inputs.

### 6.3.6 Combination of OR and INHIBIT logic gates

To mimic the functions of the said logic gates,  $\text{Fe}^{2+}$  is taken as input 1, while UV light was used as input 2 and absorption maxima at 370 and 575 nm were considered as the output signals. Free tpy-pvp-H possesses no absorption at both the wavelengths in DCM. In presence of  $\text{Fe}^{2+}$  (input 1), strong absorption band at both 370 and 575 nm was observed with concomitant development of deep violet color which corresponds to the ON-state. By contrast, upon treatment with input 2 (light), no such signal was observed at



575 nm indicating the OFF-state. When these two inputs are applied successively (input 1 followed by input 2), no signal at 575 nm is observed upon prolonged irradiated with UV light photon which indicates the OFF-state (Fig. 6.8). So, it is possible to mimic an INHIBIT gate upon applying these two inputs. On the other side, when we choose the monitoring wavelength at 370 nm, the compound gives rise to on-state upon applying either input 1 or input 2 or both. These confirmed the possibility of formation of OR gate. Thus, here we can mimic the combination of INHIBIT and OR gate (Fig. 6.8).

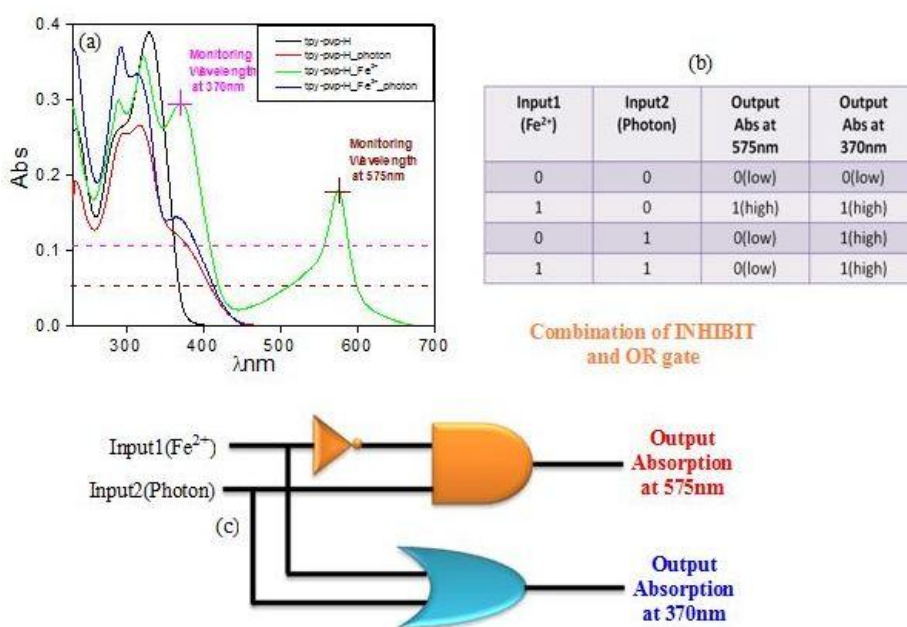


**Fig. 6.8.** (a) Absorption spectral changes of tpy-pvp-H in DCM at 575 and 370 nm in presence of Fe<sup>2+</sup> (0.5 equiv) and photon. Truth table and schematic presentation for combined OR and INHIBIT gate (b and c, respectively).

### 6.3.7 Combination of OR and NOR logic gates

In order to display combinational functions of OR and NOR logic gates, the absorbance of tpy-pvp-H at 380 nm and the emission at 398 nm is monitored upon the action of UV light of  $\lambda_{\text{ex}} = 336$  nm as input 1, while the Zn<sup>2+</sup> ion as the input 2. Inclusion of Zn<sup>2+</sup> ion leads to significant increment of absorbance at 380 nm representing the on-state, whereas remarkable quenching of emission at 398 nm indicating the off-state. Upon the action of light, no such enhancement in the absorption maximum is observed, but the



emission spectral change is found to be almost same as that is observed under the influence of input 2 (Fig. 6.9). But sequential action of  $\text{Zn}^{2+}$  followed by light gives rise to turn-on of absorption at 380 nm whereas turn-off of emission at 398 nm. Thus, by following proper sequence for the action of the said inputs and upon monitoring the absorbance at 380 nm and emission at 398 nm, the combined functions of OR and NOR gates are mimicked (Fig. 6.9).

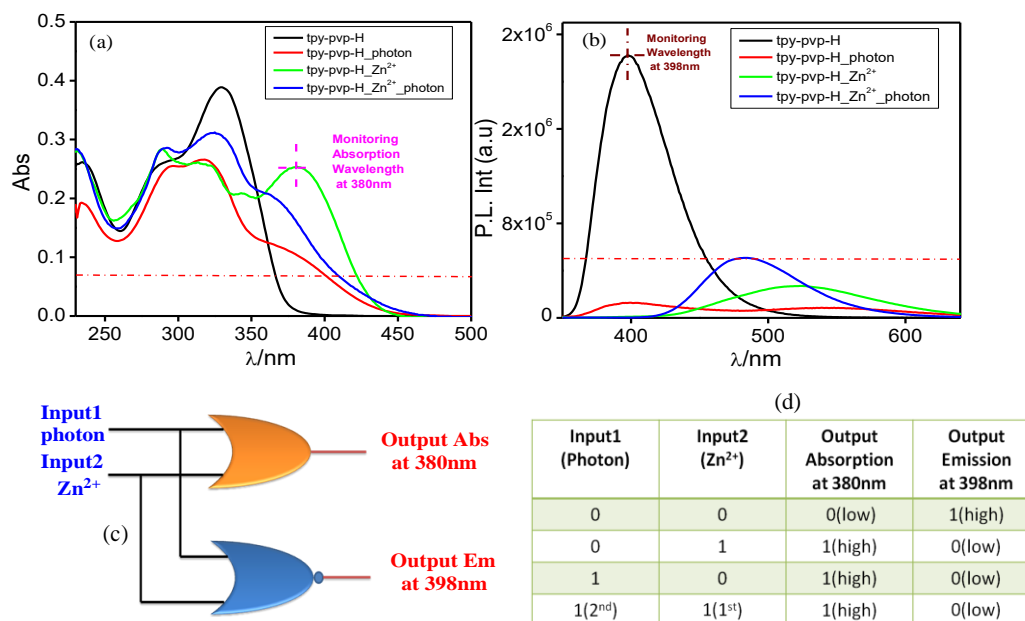


**Fig. 6.9.** Absorption and emission spectral changes of tpy-pvp-H in DCM at 380 and 398 nm, respectively in presence and  $\text{Zn}^{2+}$  (0.5 equiv) and photon (a and b, respectively). Schematic presentation and truth table for combined OR and NOR gate are presented in part c and d, respectively.

There is another possibility to construct a combination of OR and NOR logic gates by applying a three input logic system. In this case, we used  $\text{Zn}^{2+}$ ,  $\text{Fe}^{2+}$  and light as input 1, input 2 and input 3, respectively. The absorbance at 375 nm and emission at 410 nm of tpy-pvp-H is used as the output signal (Fig. 6.10). In absence of any of these three inputs, there is no appreciable absorbance at 375 nm implying the OFF-state, but intense emission band at 410 nm give rise to the ON-state. If we allow tpy-pvp-H to interact with any of three inputs (singly, doubly or triply) and irrespective of their sequence, we noticed appreciable absorbance at 375 nm in each case which demonstrates the ON-state,

while substantial emission quenching at 410 nm below the threshold indicates the off-state in all cases. In essence, three input combined OR and NOR logic gates are constructed (Fig. 6.10).

### 6.3.8 Construction of NAND logic gate

Upon using UV light as input 1 and  $\text{Zn}^{2+}$  as the input 2 and by monitoring the emission intensity at 419 nm in DMSO, the function of NAND gate can be mimicked. The output of NAND gate is usually turn-ON in presence of any single input or without both of the two inputs. In the absence of any of these inputs, the emission intensity at 419 nm is very high (output 1). But in presence of  $\text{Zn}^{2+}$  (input 2) if we interact the receptor with photon (input 1), the emission intensity is dramatically quenched implying the OFF state of this system. Thus, the construction of two input NAND logic gate is feasible as shown in the truth table of Fig. 6.11.

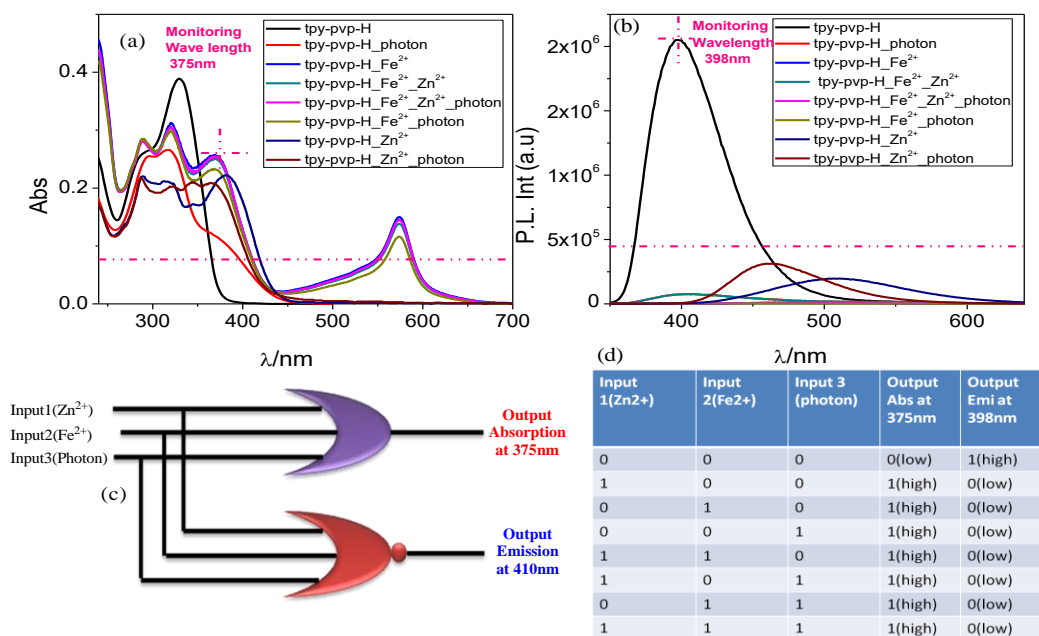


**Fig. 6.10.** Absorption and emission spectral changes of tpy-pvp-H in DCM at 375 and 410 nm, respectively in presence of  $\text{Zn}^{2+}$  (input 1),  $\text{Fe}^{2+}$  (input 2) and photon (input 3) (a and b, respectively). Schematic presentation and truth table for combined OR and NOR gate are presented in part c and d, respectively.

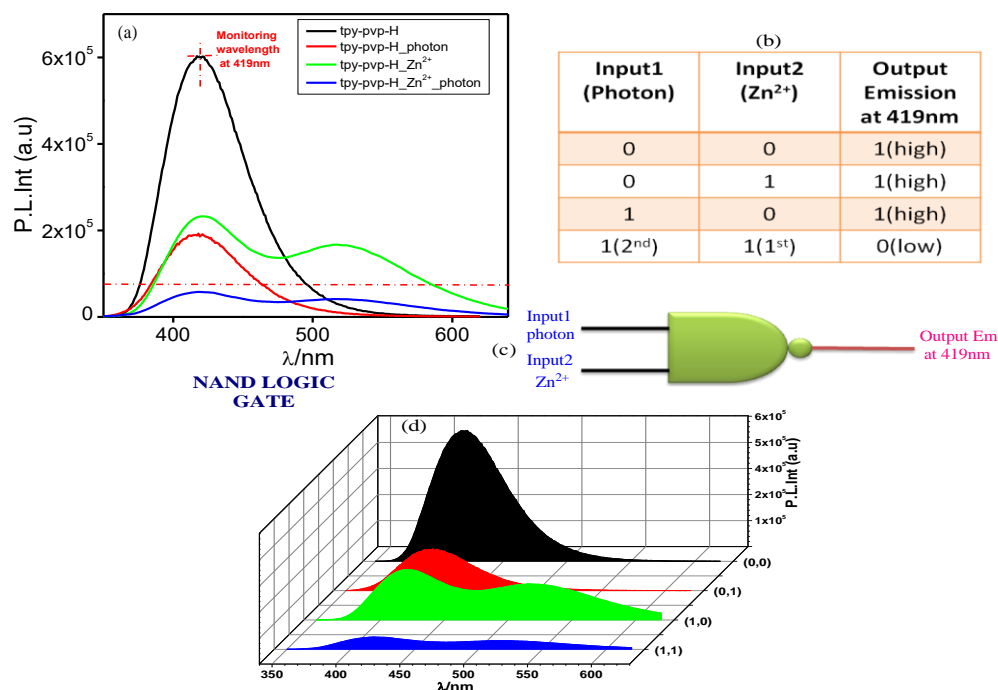


**Fig. 6.11.** (a) Emission spectral changes of tpy-pvp-H in DMSO at 419 nm in presence of photon and Zn<sup>2+</sup> (0.5 equiv). Truth table and schematic presentation for NAND gate (b and c, respectively). (d) 3d presentation for the change in emission intensity as function of inputs.

NAND gate can be made by combining an AND gate and a NOT gate. It behaves inverse of an AND gate. We can see this action in an analog circuit as presented in Fig. 6.12. Either input 1 or input 2 has to be high for the power to go to the light outputting 1 (“ON” state). If both input 1 (photon) and input 2 (Zn<sup>2+</sup>) is high, power is routed away from the light giving output 0 indicating the “OFF” state of the system. If both the input is low then the “ON” state of the system will be generated.

### 6.3.9 Construction of INHIBIT logic gate

We can mimic the function of INHIBIT logic gate upon using UV light as input 1 and Zn<sup>2+</sup> as the input 2 and utilizing the absorption output signal at 365 nm in MeCN (Fig. 6.13). This system gives rise to the “ON-State” only in presence of a particular input. It is to mention here that this particular type of gate can be mimicked in MeCN

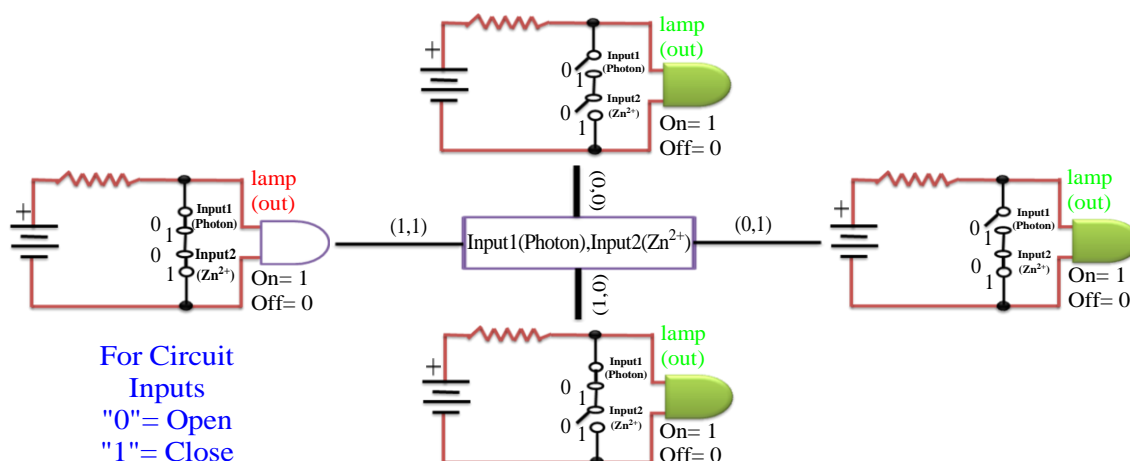


**Fig. 6.12.** NAND analog circuit exhibited by tpy-pvp-H based on its emission spectral response at 419 nm in DMSO upon the action of photon and  $\text{Zn}^{2+}$  (0.5equiv).

only and thus is solution specific. Without the action of two selected inputs, no absorbance at 365 nm corresponds to the “OFF-state”. In presence of photon or in combination of photon and  $\text{Zn}^{2+}$ , again no absorption signal in the said wavelength is observed which corresponds to the OFF-state. In the presence of only  $\text{Zn}^{2+}$ , a strong

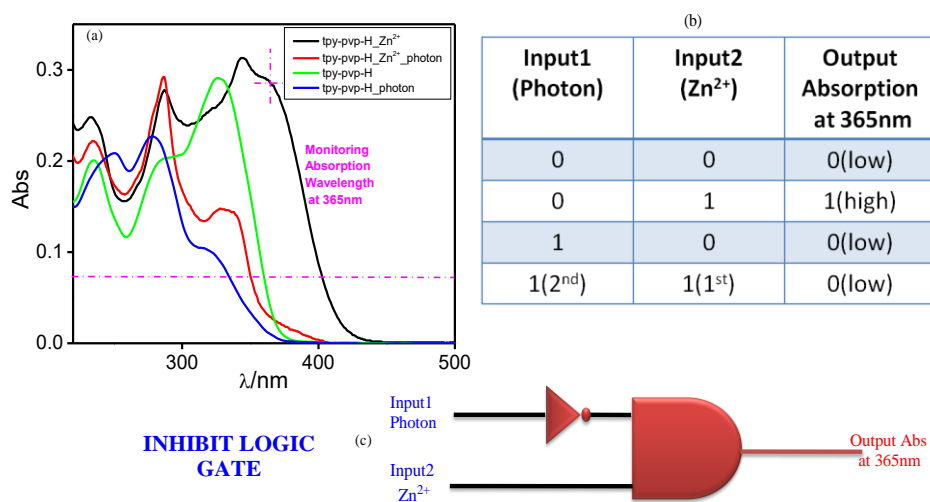


**Fig. 6.13.** (a) Absorption spectral changes of tpy-pvp-H in MeCN at 365 nm in presence of photon and  $\text{Zn}^{2+}$  (0.5 equiv). The truth table and schematic presentation for INHIBIT gate are presented in part b and c, respectively.

absorbance at 365 nm is observed which corresponds to the ON-state. As a result, a two input INHIBIT logic gate is fabricated as displayed in the truth table of Fig. 6.13.

### 6.3.10 Fuzzy logic operations

Although Boolean logic is simple as well as effective in discriminating true and false interactions, it is not competent enough to represent multi-valued systems and the degree of the truthfulness of the intermediate states. Because of the imprecise nature of most of the chemical reactions, the FLS is believed to be a probable substitute for expressing the imprecise information in the analogue domain. Without the specific values of input and output parameters, one could deliberate the variables in some linguistic characters, viz. low, medium, or high (Table 6.1-6.2). In the present case, the inputs ( $\text{Fe}^{2+}/\text{Zn}^{2+}$  and  $\text{CN}^-$ ) and the output (emission quantum yield,  $\Phi$ ) variables are presented in the form of fuzzy sets {( Fig. 6.14 for  $\text{Fe}^{2+}/\text{CN}^-$ ) and Fig.6.15 for  $\text{Zn}^{2+}/\text{CN}^-$  (SI)}. A

**Table 6.1** Values of emission quantum yield ( $\Phi$ ) as a function of  $n_{\text{Fe}^{2+}}/n_{\text{tpy-pvp-H}}$  and  $n_{\text{CN}^-}/n_{\text{tpy-pvp-H}}$ .

$\text{Fe}^{2+}(\text{eq})$	$\text{CN}^-(\text{eq})$	Output	Emission Quantum yield ( $\Phi$ )
0	0	high	0.33
0.1	0	high	0.31
0.3	1	medium	0.27
0.5	3	medium	0.26
0	4	high	0.31
0	6	high	0.32
0.7	0.4	low	0.08
0.8	0	low	0.06
1	0.9	low	0.07
0	6	high	0.32
1	6	medium	0.22
1	0	low	0.03

summary of various IF-THEN comments encompassing the inference rules is presented in Fig. 6.15 and Table 6.3-6.4. The IF-part correlates to the antecedent, whereas the THEN-part conforms to the consequence. The surmise tool of FLS worked out to convert the inputs into the output fuzzy sets. The defuzzifier then converts the outputs into the

crisp numbers which plays a key role in forecasting the output variable such as  $\Phi$ . Following the same procedure, the input ( $\text{Zn}^{2+}$ ) and output ( $\Phi$ ) variables are presented in terms of fuzzy logic (Fig. 6.15 and Table 6.4).

**Table 6.2** Values of emission quantum yield ( $\Phi$ ) as a function of  $n_{\text{Zn}^{2+}}/n_{\text{tpy-pvp-H}}$  and  $n_{\text{CN}^-}/n_{\text{tpy-pvp-H}}$ .

$\text{Zn}^{2+}(\text{eq})$	$\text{CN}^-(\text{eq})$	Output	Emission Quantum yield ( $\phi$ )
0	0	high	0.33
0.1	0	high	0.31
0.3	1	high	0.29
0.5	3	high	0.28
0	4	high	0.33
0	2	high	0.31
0.7	0.2	low	0.11
0.8	0.3	low	0.10
1	4	medium	0.21
0	2.5	high	0.30
1	3	medium	0.20
1	0	low	0.05

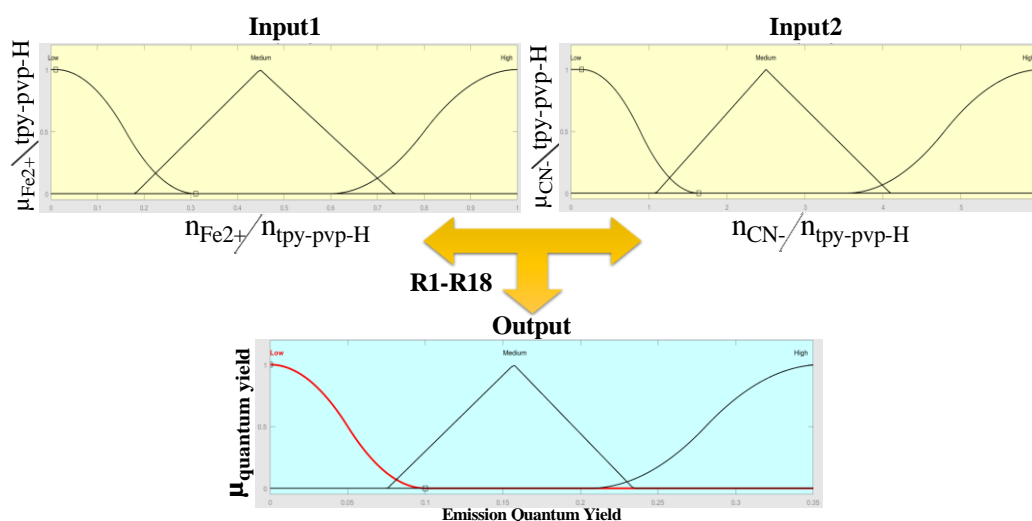


**Fig. 6.14.** Diagrammatic demonstration of fuzzy correlations based on FIS upon considering  $\text{Fe}^{2+}$  as input 1 and  $\text{CN}^-$  as input 2, while the emission quantum yield ( $\Phi$ ) as the output.

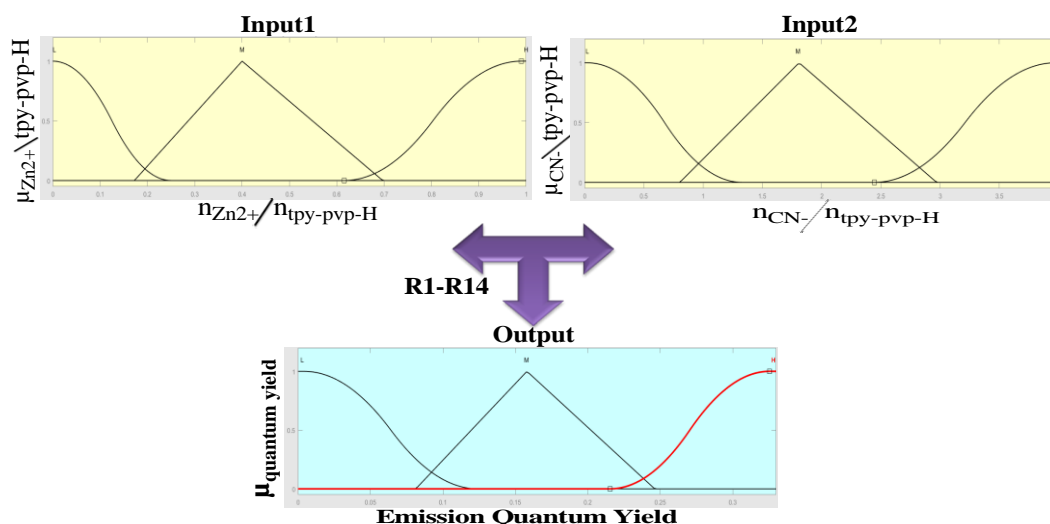


**Fig. 6.15.** Diagrammatic demonstration of fuzzy correlations based on FIS upon considering  $\text{Zn}^{2+}$  as input 1 and  $\text{CN}^-$  as input 2, while the emission quantum yield ( $\Phi$ ) as the output.

$\text{Fe}^{2+}$  induces emission quenching in  $\text{tpy-pvp-H}$ , whereas concurrent inclusion of both  $\text{Fe}^{2+}$  and  $\text{CN}^-$  might give rise to either enhancement or quenching of emission. To this end,  $\text{tpy-pvp-H}$  is exposed to carry out fuzzy logic functions with changing equivalent of  $\text{Fe}^{2+}$  and  $\text{CN}^-$  ions and treating  $\Phi$  as the output (Table 6.1). In FLS, the rules are “IF..., THEN...” comments with various antecedents comprising the OR and AND operators. Plausible merging of inputs yields eighteen different combinations for  $\text{Fe}^{2+}/\text{CN}^-$  (Table 6.3) and fourteen combinations for  $\text{Zn}^{2+}/\text{CN}^-$  (Table 6.4). The molar proportion of input and receptor ( $n_{\text{Fe}^{2+}}/n_{\text{tpy-pvp-H}}$  and  $n_{\text{CN}^-}/n_{\text{tpy-pvp-H}}$ ) is disintegrated to three fuzzy sets: (i) low ( $\mu_L$ ) bearing the symbol zmf, (ii) medium ( $\mu_M$ ) with the symbol trimf, and (iii) high ( $\mu_H$ ) having symbol smf. In the same way, the output ( $\Phi_F$ ) is stretched into three fuzzy sets: (i) low with a zmf $\mu_L$ , (ii) medium with a trimf $\mu_M$ , and (iii) high with a smf $\mu_H$ . We can now devise the fuzzy rules upon enforcing Mamdani’s FLS [71]. Because of the coactive role of  $\text{Fe}^{2+}$  and  $\text{CN}^-$ , the dual inputs are associated here via the OR and AND operator. A 3D plot showing the variation of  $\Phi$  with varying equivalent of  $\text{Fe}^{2+}$  and  $\text{CN}^-$  is displayed in Fig. 6.16, while for  $\text{Zn}^{2+}/\text{CN}^-$  conjugate is presented in Fig. 6.17.

**Table 6.3** Rules for the fuzzy logic system (FLS) taking  $\text{Fe}^{2+}$  and  $\text{CN}^-$  as inputs and emission quantum yield ( $\Phi$ ) as the output. The rules consist of the following statements.

(1)	IF $n_{\text{Fe}^{2+}} / n_{\text{ipy-pvp-H}}$ is low AND $n_{\text{CN}^-} / n_{\text{ipy-pvp-H}}$ is null, THEN quantum yield is high
(2)	IF $n_{\text{Fe}^{2+}} / n_{\text{ipy-pvp-H}}$ is medium AND $n_{\text{CN}^-} / n_{\text{ipy-pvp-H}}$ is null, THEN quantum yield is medium
(3)	IF $n_{\text{Fe}^{2+}} / n_{\text{ipy-pvp-H}}$ is high AND $n_{\text{CN}^-} / n_{\text{ipy-pvp-H}}$ is null, THEN quantum yield is low
(4)	IF $n_{\text{Fe}^{2+}} / n_{\text{ipy-pvp-H}}$ is null AND $n_{\text{CN}^-} / n_{\text{ipy-pvp-H}}$ is low, THEN quantum yield is high
(5)	IF $n_{\text{Fe}^{2+}} / n_{\text{ipy-pvp-H}}$ is null AND $n_{\text{CN}^-} / n_{\text{ipy-pvp-H}}$ is medium, THEN quantum yield is high
(6)	IF $n_{\text{Fe}^{2+}} / n_{\text{ipy-pvp-H}}$ is null AND $n_{\text{CN}^-} / n_{\text{ipy-pvp-H}}$ is high, THEN quantum yield is high
(7)	IF $n_{\text{Fe}^{2+}} / n_{\text{ipy-pvp-H}}$ is low AND $n_{\text{CN}^-} / n_{\text{ipy-pvp-H}}$ is low, THEN quantum yield is high
(8)	IF $n_{\text{Fe}^{2+}} / n_{\text{ipy-pvp-H}}$ is low AND $n_{\text{CN}^-} / n_{\text{ipy-pvp-H}}$ is medium, THEN quantum yield is high
(9)	IF $n_{\text{Fe}^{2+}} / n_{\text{ipy-pvp-H}}$ is low AND $n_{\text{CN}^-} / n_{\text{ipy-pvp-H}}$ is high, THEN quantum yield is high
(10)	IF $n_{\text{Fe}^{2+}} / n_{\text{ipy-pvp-H}}$ is medium AND $n_{\text{CN}^-} / n_{\text{ipy-pvp-H}}$ is low, THEN quantum yield is medium
(11)	IF $n_{\text{Fe}^{2+}} / n_{\text{ipy-pvp-H}}$ is medium AND $n_{\text{CN}^-} / n_{\text{ipy-pvp-H}}$ is medium, THEN quantum yield is medium
(12)	IF $n_{\text{Fe}^{2+}} / n_{\text{ipy-pvp-H}}$ is medium AND $n_{\text{CN}^-} / n_{\text{ipy-pvp-H}}$ is high, THEN quantum yield is medium
(13)	IF $n_{\text{Fe}^{2+}} / n_{\text{ipy-pvp-H}}$ is high AND $n_{\text{CN}^-} / n_{\text{ipy-pvp-H}}$ is low, THEN quantum yield is low
(14)	IF $n_{\text{Fe}^{2+}} / n_{\text{ipy-pvp-H}}$ is high AND $n_{\text{CN}^-} / n_{\text{ipy-pvp-H}}$ is medium, THEN quantum yield is medium
(15)	IF $n_{\text{Fe}^{2+}} / n_{\text{ipy-pvp-H}}$ is high AND $n_{\text{CN}^-} / n_{\text{ipy-pvp-H}}$ is high, THEN quantum yield is medium
(16)	IF $n_{\text{Fe}^{2+}} / n_{\text{ipy-pvp-H}}$ is medium AND $n_{\text{CN}^-} / n_{\text{ipy-pvp-H}}$ is medium, THEN quantum yield is medium
(16)	IF $n_{\text{Fe}^{2+}} / n_{\text{ipy-pvp-H}}$ is high AND $n_{\text{CN}^-} / n_{\text{ipy-pvp-H}}$ is medium, THEN quantum yield is medium
(18)	IF $n_{\text{Fe}^{2+}} / n_{\text{ipy-pvp-H}}$ is high AND $n_{\text{CN}^-} / n_{\text{ipy-pvp-H}}$ is low, THEN quantum yield is low

At this point we would like to mention that the Mamdani's FLS procedure is a coarse one and is not sufficiently smart to figure out the input-output connections quite methodically and efficiently. The more state-of-art way is to adopt a neuro computing blended fuzzy logic system (ANFIS) that not only takes into account the lingual variables but also accommodates the experimentally noticed input-output data set [72]. In this context, a FIS achieved by Sugeno's approach has been endorsed [73]. To implement FIS by



Sugeno's method, we have taken  $\Phi$  as the output signal and molar ratio of  $\text{CN}^-$  and  $\text{tpy-pvp-H}$  or  $\text{Zn}^{2+}$  and  $\text{tpy-pvp-H}$  as the inputs.

The inputs are disintegrated into three range of values (low, medium and high) possessing trapezoidal and triangular membership functions. The input-output chart for the designed ANFIS is presented schematically in Fig. 6.18-6.19. The outcomes obtained by ANFIS is more authentic to gauge any of the input equivalence for different  $\Phi$  over a fixed equivalent of another input.

**Table 6.4** Rules for the fuzzy logic system (FLS) taking  $\text{Zn}^{2+}$  and  $\text{CN}^-$  as inputs and emission quantum yield ( $\Phi$ ) as the output. The rules consist of the following statements.

(1)	IF $n_{\text{Zn}^{2+}} / n_{\text{tpy-pvp-H}}$ is low AND $n_{\text{CN}^-} / n_{\text{tpy-pvp-H}}$ is null, THEN quantum yield is high
(2)	IF $n_{\text{Zn}^{2+}} / n_{\text{tpy-pvp-H}}$ is medium AND $n_{\text{CN}^-} / n_{\text{tpy-pvp-H}}$ is null, THEN quantum yield is medium
(3)	IF $n_{\text{Zn}^{2+}} / n_{\text{tpy-pvp-H}}$ is high AND $n_{\text{CN}^-} / n_{\text{tpy-pvp-H}}$ is null, THEN quantum yield is low
(4)	IF $n_{\text{Zn}^{2+}} / n_{\text{tpy-pvp-H}}$ is null AND $n_{\text{CN}^-} / n_{\text{tpy-pvp-H}}$ is low, THEN quantum yield is high
(5)	IF $n_{\text{Zn}^{2+}} / n_{\text{tpy-pvp-H}}$ is null AND $n_{\text{CN}^-} / n_{\text{tpy-pvp-H}}$ is medium, THEN quantum yield is high
(6)	IF $n_{\text{Zn}^{2+}} / n_{\text{tpy-pvp-H}}$ is null AND $n_{\text{CN}^-} / n_{\text{tpy-pvp-H}}$ is high, THEN quantum yield is high
(7)	IF $n_{\text{Zn}^{2+}} / n_{\text{tpy-pvp-H}}$ is low AND $n_{\text{CN}^-} / n_{\text{tpy-pvp-H}}$ is low, THEN quantum yield is high
(8)	IF $n_{\text{Zn}^{2+}} / n_{\text{tpy-pvp-H}}$ is low AND $n_{\text{CN}^-} / n_{\text{tpy-pvp-H}}$ is medium, THEN quantum yield is high
(9)	IF $n_{\text{Zn}^{2+}} / n_{\text{tpy-pvp-H}}$ is low AND $n_{\text{CN}^-} / n_{\text{tpy-pvp-H}}$ is high, THEN quantum yield is high
(10)	IF $n_{\text{Zn}^{2+}} / n_{\text{tpy-pvp-H}}$ is low AND $n_{\text{CN}^-} / n_{\text{tpy-pvp-H}}$ is low, THEN quantum yield is high
(11)	IF $n_{\text{Zn}^{2+}} / n_{\text{tpy-pvp-H}}$ is medium AND $n_{\text{CN}^-} / n_{\text{tpy-pvp-H}}$ is low, THEN quantum yield is medium
(12)	IF $n_{\text{Zn}^{2+}} / n_{\text{tpy-pvp-H}}$ is high AND $n_{\text{CN}^-} / n_{\text{tpy-pvp-H}}$ is low, THEN quantum yield is low
(13)	IF $n_{\text{Zn}^{2+}} / n_{\text{tpy-pvp-H}}$ is high AND $n_{\text{CN}^-} / n_{\text{tpy-pvp-H}}$ is medium, THEN quantum yield is medium
(14)	IF $n_{\text{Zn}^{2+}} / n_{\text{tpy-pvp-H}}$ is medium AND $n_{\text{CN}^-} / n_{\text{tpy-pvp-H}}$ is medium, THEN quantum yield is medium

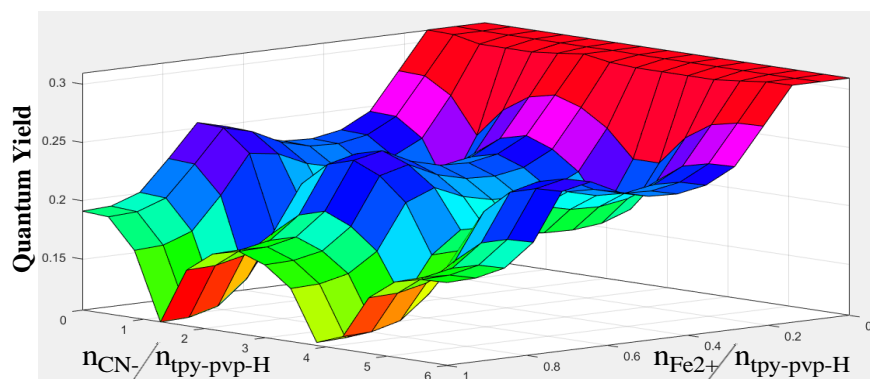


**Fig. 6.16.** A 3D display of the dependence of  $\Phi$  of tpy-pvp-H upon simultaneous injection of  $\text{Fe}^{2+}$  and  $\text{CN}^-$  inputs.

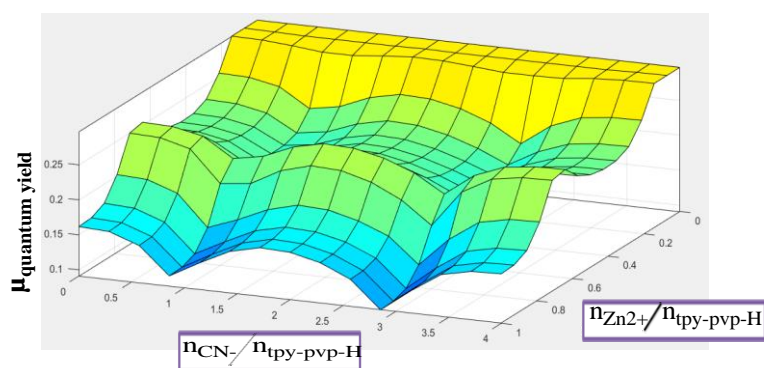


**Fig. 6.17.** A 3D display of the dependence of  $\Phi$  of tpy-pvp-H upon simultaneous injection of  $\text{Zn}^{2+}$  and  $\text{CN}^-$  inputs.

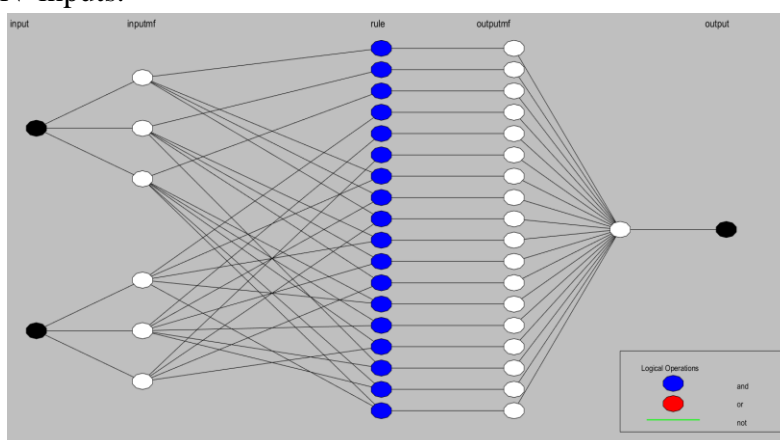


**Fig. 6.18.** Schematic representation of ANFIS by adopting Sugeno's method to map  $\Phi$  of tpy-pvp-H with  $\text{CN}^-$  and  $\text{Fe}^{2+}$  inputs.

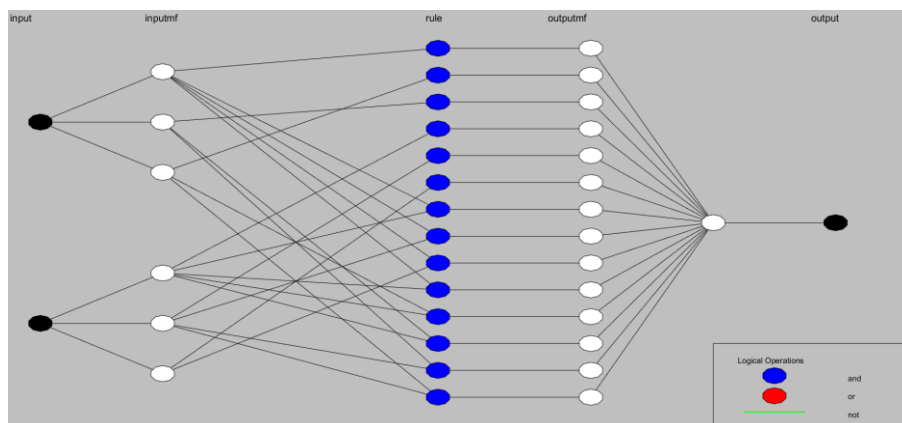


**Fig. 6.19.** Schematic representation of ANFIS by adopting Sugeno's method to map  $\Phi$  of tpy-pvp-H with  $\text{CN}^-$  and  $\text{Zn}^{2+}$  inputs.

## 6.4 Conclusions

With regard to our continued effort to develop smart molecular systems capable of processing information and computation at the molecular level, we have successfully utilized in this work a terpyridine-based receptor incorporating styrylbenzene moiety as the photo-switchable unit. The terpyridine motif is a versatile tridentate coordinating moiety so that the optical properties of the receptor could be significantly modulated by the presence of incoming cationic guests. The styrylbenzene moiety, on the other hand, can give rise to switching of the optical properties of both the free receptor as well as its cationic adduct upon interaction with light. Interestingly, on the basis of the optical response profiles of the receptor toward selected cations as well as light of specific wavelength, we are able to demonstrate multiple Boolean logic functions such as INHIBIT, IMPLICATION, OR, NOR and NAND as well as various combinations of them. Of particular interest, we utilized the present systems for the construction of security keypad locks and memory devices by maintaining proper sequence of the inputs and monitoring either absorption or emission at a specific wavelength as the output signal. In addition, fuzzy logic approach is accomplished to design an infinite-valued system for locating the imprecise values between completely true (1) and completely false (0). Thus, the present photo-switchable terpyridine based receptors can act as potential building blocks for information processing and computation at the molecular level.

## 6.5 References

- [1] A.P. de silva, H. Q. N. Gunaratne, C.P. McCoy, A molecular photoionic AND gate based on fluorescent signaling, *Nature*. 364 (1993) 42-44.
- [2] J. Ling, B. Daly, V. A. D. Silversen, A. P. de Silva, Taking baby steps in molecular logic-based computation, *Chem. Commun.* 51 (2015) 8403-8409.
- [3] A. P. de Silva, N. D. McClenaghan, Molecular-scale Logic Gates, *Chem. Eur. J.* 10 (2004) 574-586.
- [4] A. P. de Silva, Molecular logic gate arrays, *Chem. Asian J.* 6 (2011) 750-766.
- [5] A. P. de Silva, D. P. Fox, A. J. M. Huxley, T. S. Moody, Combining luminescence, coordination and electron transfer for signalling purposes, *Coord. Chem. Rev.* 205(2000) 41-57.
- [6] B. Daly, J. Ling, A. P. de Silva, Current developments in fluorescent PET (photoinduced electron transfer) sensors and switches, *Chem. Soc. Rev.* 44 (2015) 4203-4211.
- [7] E. Katz, (Ed.) *Molecular and supramolecular information processing: from molecular switches to logic systems*; Wiley-VCH, Weinheim, Germany, 2012.
- [8] E. Katz, S. Minko, Enzyme-based logic systems interfaced with signal-responsive materials and electrodes, *Chem. Commun.* 51(2015) 3493-3500.
- [9] G. Strack, M. Ornatska, M. Pita, E. Katz, Biocomputing security system: Concatenated enzyme-based Logic Gates operating as a biomolecular keypad lock, *J. Am. Chem.* 130 (2008) 4234-4235.
- [10] K. Mac Vittie, J. Halament, E. Kartz, Enzyme-based D-flop memory system, *Chem. Commun.* 48 (2012) 11742-11744.
- [11] D. Gust, J. Andréasson, U. Pischel, T. A. Moore, A. L. Moore, Data and signal processing using photochromic molecules, *Chem. Commun.* 48 (2012) 1947-1957.
- [12] G. de Ruiter, M. E. van der Boom, Surface-confined assemblies and polymers for molecular logic, *Acc. Chem. Res.* 44 (2011) 563-573.
- [13] J. Andréasson, U. Pischel, Smart molecules at work mimicking advanced logic operations, *Chem. Soc. Rev.* 39 (2010) 174-188.

- [14] A. Credi, Molecules that make decisions, *Angew. Chem. Int. Ed.* 46 (2007) 5472-5475.
- [15] S. Sreejith, A. Ghosh, Molecular logic gates: recent advances and perspectives, *Indian J. Chem.* 51A (2012) 47-56.
- [16] P. L. Gentili, The fundamental fuzzy logic operators and some complex boolean logic circuits implemented by the chromogenism of a spirooxazine, *Phys. Chem. Chem. Phys.* 13 (2011) 20335-20344.
- [17] P. L. Gentili, Boolean and fuzzy logic gates based on the interaction of flindersine with bovine serum albumin and tryptophan, *J. Phys. Chem. A.* 112 (2008) 11992-11997.
- [18] P. L. Gentili, Boolean and fuzzy logic implemented at the molecular level, *Chem. Phys.* 336 (2007) 64-73.
- [19] M. Ben-Ari, *Mathematical Logic for Computer Science*, Prentice-Hall, Hemel Hempstead, 1993.
- [20] R. J. Mitchell, *Microprocessor Systems; An Introduction*; Macmillan: London, 1995.
- [21] P. Ball, Chemistry meets computing, *Nature.* 406 (2000) 118–120.
- [22] S. Erbas-Cakmak, E. U. Akkaya, Cascading of molecular logic gates for advanced functions: a self-reporting, activatable photosensitizer, *Angew. Chem. Int. Ed.* 52 (2013) 11364-11368.
- [23] R. Guliyev, S. Ozturk, Z. Kostereli, E. U. Akkaya, From virtual to physical: integration of chemical logic gates, *Angew. Chem. Int. Ed.* 50 (2011) 9826-9831.
- [24] T. Gupta, Boom, M. E. vander Boom, Redox-active monolayers as a versatile platform for integrating boolean logic gates, *Angew. Chem. Int. Ed.* 47 (2008) 5322-5326.
- [25] J. Chen, S. Zhou, J. Wen, Concatenated logic circuits based on a three-way DNA junction: a keypad-lock security system with visible readout and an automatic reset function, *Angew. Chem. Int. Ed.* 54 (2015) 446-450.

- [26] S. Kumar, V. Luxami, R. Saini, D. Kaur, Superimposed molecular keypad lock and half-subtractor implications in a single fluorophore, *Chem. Commun.* 21 (2009) 3044-3046.
- [27] J. Andrasson, S. Straight, D. T. Moore, A. Moore, D. Gust, An all-photonic molecular keypad lock, *Chem. Eur. J.* 15 (2009) 3936-3939.
- [28] D. Margulies, C. E. Felder, G. Melman, A. Shanzer, A molecular keypad lock: a photochemical device capable of authorizing password entries, *J. Am. Chem. Soc.* 129 (2007) 347-354.
- [29] Z. Guo, W. Zhu, L. Shen, H. Tian, A fluorophore capable of crossword puzzles and logic memory, *Angew. Chem. Int. Ed.* 46 (2007) 5549-5553.
- [30] V. Bhalla, Roopa, M. Kumar, Fluoride triggered fluorescence “turn on” sensor for  $\text{Zn}^{2+}$  ions based on pentaquinone scaffold that works as a molecular keypad lock, *Org. Lett.* 14 (2012) 2802-2805.
- [31] Qi. Zou, X. Li, J. Zhang, J. Zhou, B. Sun, H. Tian, Unsymmetrical diarylethenes as molecular keypad locks with tunable photochromism and fluorescence via  $\text{Cu}^{2+}$  and  $\text{CN}^-$  coordinations, *Chem. Commun.* 48 (2012) 2095-2097.
- [32] C. P. Carvalho, Z. Dominguez, J. P. Da Silva, U. Pischel, A supramolecular keypad lock, *Chem. Commun.* 51 (2015) 2698-2701.
- [33] X.-J. Jiang, D. K. P. Ng, Sequential logic operations with a molecular keypad lock with four inputs and dual fluorescence outputs, *Angew. Chem.* 126 (2014) 10649 - 10652.
- [34] M. Suresh, D. A. Jose, A. Das, [2,2'-Bipyridyl]-3,3'-diol as a molecular half-subtractor, *Org. Lett.* 9 (2007) 441-444.
- [35] A. Coskun, E. Deniz, E. U. Akkaya, Effective PET and ICT switching of boradiazaindacene emission: a unimolecular, emission-mode, molecular half-subtractor with reconfigurable logic gate, *Org. Lett.* 7 (2005) 5187-5189.
- [36] D. Margulies, G. Melman, A. Shanzer, Molecular full-adder and full-subtractor, an additional step toward a molecular logic, *J. Am. Chem. Soc.* 128 (2006) 4865-4871.

- [37] J. Andrasson, S. D. Straight, S. Bandyopadhyay, R. H. Mitchell, T. A. Moore, A. L. Moore, D. Gust, Molecular 2:1 digital multiplexer, *Angew. Chem. Int. Ed.* 46 (2007) 958-961.
- [38] S. Erbas-Cakmak, O. A. Bozdemir, Y. Cakmak, E. U. Akkaya, Proof of principle for a molecular 1:2 demultiplexer to function as an autonomously switching theranostic device, *Chem. Sci.* 4 (2013) 858-862.
- [39] S. Xu, Y.-X. Hao, W. Sun, C.-J. Fang, X. Lu, M.-N. Li, M. Zhao, S.-Q. Peng, C.-H. Yan 2:1 Multiplexing function in a simple molecular system, *Sensors*. 12 (2012) 4421-4430.
- [40] N. Kaur, S. Kumar, Aminoanthraquinone-based chemosensors: colorimetric molecular logic mimicking molecular trafficking and a set–reset memorized device, *Dalton Trans.* 41 (2012) 5217-5224.
- [41] H. Zhuang, Q. Zhou, Q. Zhang, H. Li, N. Li, Q. Xu, J. Lu, Effects of aromatic spacers on film morphology and device memory performance based on imidazole- $\pi$ -triphenylamine derivatives, *J. Mater. Chem. C*, 3 (2015) 416-422.
- [42] S. Mardanya, S. Karmakar, D. Mondal, S. Baitalik, An imidazolyl-pyreno-imidazole conjugate as a cyanide sensor and a set–reset memorized sequential logic device, *Dalton Trans.* 44 (2015) 15994-16012.
- [43] S. Karmakar, S. Mardanya, S. Das, S. Baitalik, Efficient deep-blue emitter and molecular-scale memory device based on dipyrrolyl-phenylimidazole-terpyridine assembly, *J. Phys. Chem. C* 119 (2015) 6793-6805.
- [44] Q. Hao, Z.J. Li, B. Bai, X. Zhang, Y.W. Zhong, L.J. Wan, D. Wang, Covalent organic framework film for three-state near-infrared electrochromism and molecular logic gate, *Angew. Chem. Int. Ed.* 60 (2021) 12498-12503.
- [45] J.Y. Shao, B.B. Cui, J.H. Tang, Y.W. Zhong, Resistive memory switching of transition-metal complexes controlled by ligand design, *Coord. Chem. Rev.* 393 (2019) 21-36.
- [46] J.H. Tang, T.G. Sun, J.Y. Shao, Z.L. Gong, Y.W. Zhong, Resistive memory devices based on a triphenylamine-decorated non-precious cobalt(II) bis-terpyridine complex, *Chem. Commun.* 53 (2017) 11925-11928.

- [47] B.B. Cui, J.H. Tang, J. Yao, Y.W. Zhong, A molecular platform for multistate near infrared electrochromism and flip-flop, flip-flap-flop, and ternary memory, *Angew. Chem. Int. Ed.* 54 (2015) 9192-9197.
- [48] B.B. Cui, Y.W. Zhong, J. Yao, Three-state near-infrared electrochromism at the molecular scale, *J. Am. Chem. Soc.* 137 (2015) 4058-4061.
- [49] D. Mondal, M. Bar, D. Maity, S. Baitalik, Anthraimidazoledione-terpyridine-based optical chemosensor for anions and cations that works as molecular half subtractor, key-pad lock, and memory device, *J. Phys. Chem. C.* 119 (2015) 25429–25441.
- [50] S. Karmakar, D. Maity, S. Mardanya, S. Baitalik, Demonstration of multiple logic operations in a heteroditopic pyrene-phenylimidazole-terpyridine conjugate based on optical responses by selective anions and cations: an experimental and theoretical investigation, *J. Phys. Chem A.* 118 (2014) 9397-9410.
- [51] S. Karmakar, S. Mardanya, P. Pal, S. Baitalik, Design of multichannel osmium-based metalloreceptor for anions and cations by taking profit from metal-ligand interaction and construction of molecular keypad lock and memory device, *Inorg. Chem.* 54 (2015) 11813-11825.
- [52] S. Mardanya, D. Mondal, S. Karmakar, S. Baitalik, Smart ruthenium and osmium complexes mimic the complicated functions of traffic signal and memory device, *Sens. Actuators B.* 239 (2017) 635-641.
- [53] D. Mondal, P. Pal, S. Baitalik, Anthraquinone-biimidazole based ruthenium(II) complexes as selective multichannel anion sensors and multi-readout molecular logic gates and memory devices: combined experimental and DFT/TD-DFT study, *Sens. Actuators B.* 242 (2017) 746-759.
- [54] L. S. Natrajan, A. Toulmin, A. Chewa, S. W. Magennis, Two-photon luminescence from polar bis-terpyridyl-stilbene derivatives of Ir(III) and Ru(II), *Dalton Trans.* 39 (2010) 10837-10846.
- [55] Y. M. Liu, Y. C. Lin, W. C. Chen, J. H. Cheng, Y. L. Chen, G. P. A. Yap, S. S. Sun, T. G. Ong, Synthesis and characterization of para-pyridine linked NHC palladium complexes and their studies for the Heck-Mizoroki coupling reaction, *Dalton Trans.* 41 (2012) 7382-7389.



- [56] S. Mukherjee, P. Pal, D. Maity, S. Baitalik, Photophysics and luminescence switching properties of a series of photochromic styrylbenzene-terpyridine conjugate: Experimental and DFT/ TD-DFT investigation, *J. Photochem. Photobiol. A*. 378 (2019) 94-104.
- [57] J. J. Santos, S. H. Toma, P. M. Lalli, M. F. Riccio, M. N. Eberlin, H. E. Toma, K. Araki, Exploring the coordination chemistry of isomerizable terpyridine derivatives for successful analyses of cis and trans isomers by travelling wave ion mobility mass spectrometry, *Analyst* 137 (2012) 4045-4051.
- [58] D. H. Waldeck, Photoisomerization dynamics of stilbenes, *Chem. Rev.* 91 (1991) 415-436.
- [59] A. Momotake, T. Arai, Photochemistry and photophysics of stilbene dendrimers and related compounds, *J. Photochem. Photobiol. C* 5 (2004) 1-25.
- [60] F. D. Lewis, Formation and reactions of stilbene exciplexes, *Acc. Chem. Res.* 12 (1979) 152-158.
- [61] P. L. Gentili, The Fuzziness of the molecular world and Its perspectives, *Molecules*. 23 (2018) 2074.
- [62] L.A. Zadeh, Outline of a new approach to the analysis of complex systems and decision processes, *IEEE Trans. Syst. Man Cyb.* 3 (1973) 28-44.
- [63] L. A. Zadeh, Toward human level machine intelligence-is it achievable? the need for a paradigm shift, *IEEE Comput. Intell. Mag.* 3 (2008) 11-22.
- [64] P. L. Gentili, A strategy to face complexity: the development of chemical artificial intelligence. In *advances in artificial life, evolutionary computation, and systems chemistry*; Rossi, F., Piotto, S., Concilio, S., Eds.; Springer: Cham, Switzerland; New York, NY, USA, 708 (2017) 151-160.
- [65] P.L. Gentili, The human sensory system as a collection of specialized fuzzifiers: a conceptual framework to inspire new artificial intelligent systems computing with words, *J. Intell. Fuzzy Syst.* 27 (2014) 2137-2151.
- [66] P.L. Gentili, The fundamental fuzzy logic operators and some complex boolean logic circuits implemented by the chromogenism of a spirooxazine, *Phys. Chem. Chem. Phys.* 13 (2011) 20335-20344.

- [67] P.L. Gentili, M.S. Giubila, B.M. Heron, Processing binary and fuzzy logic by chaotic time series generated by a hydrodynamic photochemical oscillator, *ChemPhysChem*. 18 (2017) 1831-1841.
- [68] P.L. Gentili, M.S. Giubila, R. Germani, A. Romani, A. Nicoziani, A. Spalletti, B.M. Heron, Optical communication among oscillatory reactions and photo-excitabile systems: uv and visible radiation can synchronize artificial neuron models, *Angew. Chem. Int. Ed.* 56 (2017) 7535-7540.
- [69] P.L. Gentili, A.L. Rightler, B.M. Heron, C.D. Gabbutt, Extending human perception of electromagnetic radiation to the UV region through biologically inspired photochromic fuzzy logic (BIPFUL) systems, *Chem. Commun.* 52 (2016) 1474-1477.
- [70] S. Mukherjee, P. Pal, A. Sahoo, S. Baitalik, Photo-switchable iron terpyridine complexes functionalized with styrylbenzene unit, *J. Photochem. Photobiol. A*. 407 (2021) 113059.
- [71] E. H. Mamdani, Application of fuzzy logic to approximate reasoning using linguistic synthesis, *IEEE Trans. Comput.* 26 (1977) 1182-1191.
- [72] J. S. R. Jang, C. T. Sun, Neuro-fuzzy modeling and control, *Proc. IEEE*. 83 (1995) 378-405.
- [73] M. Sugeno, T. Yasukhiro, A fuzzy-logic-based approach to qualitative modeling, *IEEE Trans. Fuzzy Syst.* 1 (1993) 7-31.

\*\*\*\*\*

### List of Publications

- [1] **S. Mukherjee**, P. Pal, M. Bar, S. Baitalik, Chromogenic and fluorogenic detection of selected anions by bis-terpyridine Fe(II) complex through displacement approach, *J. Chem. Sci.* 130 (2018) 84.
- [2] **S. Mukherjee**, P. Pal, D. Maity, S. Baitalik, Photophysics and luminescence switching properties of a series of photochromic styrylbenzene-terpyridine conjugate: experimental and DFT/TD-DFT investigation, *J. Photochem. Photobiol. A.* 378 (2019) 94-104.
- [3] **S. Mukherjee**, P. Pal, A. Sahoo, S. Baitalik, Photo-switchable iron-terpyridine complexes functionalized with styrylbenzene unit, *J. Photochem. Photobiol. A.* 407 (2021) 113059.
- [4] **S. Mukherjee**, P. Pal, A. Sahoo, S. Baitalik, Low-cost photo switches based on stilbene-appended Zn(II)-terpyridine complexes, *Photochem. Photobiol. Sci.* 20 (2021) 1125–1145.
- [5] **S. Mukherjee**, A. Sahoo, S. Deb, S. Baitalik, Light and cation-driven optical switch based on a stilbene-appended terpyridine system for the design of molecular-scale logic devices, *J. Phys. Chem. A.* 125 (2021) 8261-8273.
- [6] D. Mondal, M. Bar, **S. Mukherjee**, S. Baitalik, Design of Ru(II) complexes based on anthraimidazoledione-functionalized terpyridine ligand for improvement of room-temperature luminescence characteristics and recognition of selective anions: experimental and DFT/TD-DFT study, *Inorg. Chem.* 55 (2016) 9707-9724.
- [7] S. Karmakar, M. Nandi, **S. Mukherjee**, S. Baitalik, Polypyridyl-imidazole based smart Ru(II) complex mimicking advanced Boolean and Fuzzy logic functions, *Inorg. Chim. Acta.* 454 (2017) 76-78.
- [8] P. Pal, **S. Mukherjee**, D. Maity, S. Baitalik, Synthesis, structural characterization, and luminescence switching of diarylethene-conjugated Ru(II)-terpyridine complexes by trans-cis photoisomerization: experimental and DFT/TD-DFT investigation, *Inorg. Chem.* 57 (2018) 5743–5753.

- [9] P. Pal, **S. Mukherjee**, D. Maity, S. Baitalik, Synthesis, photophysics, and switchable luminescence properties of a new class of ruthenium(II)–terpyridine complexes containing photoisomerizable styrylbenzene units, ACS Omega. 3(2018) 14526–14537.
- [10] M. Bar, S. Deb, **S. Mukherjee**, S. Baitalik, Stimuli-responsive near-infrared emissive Os(II)–terpyridine complexes with a sense of logic, ACS Omega. 4 (2019) 2241-2255.

*Publications 1-5 are included in the thesis*

\*\*\*\*\*